



UNIVERSIDAD DE GRANADA

Facultad de Ciencias

Departamento de Química Orgánica

Programa de Doctorado en Química

*DISEÑO, SÍNTESIS Y EVALUACIÓN DE LAS PROPIEDADES FÍSICAS
DE NANOGRAFENOS DISTORSIONADOS QUE INCLUYEN
HEPTÁGONOS*

*DESIGN, SYNTHESIS AND PHYSICAL PROPERTIES EVALUATION OF
HEPTAGON-CONTAINING DISTORTED NANOGRAFENES*

MEMORIA DE TESIS DOCTORAL

presentada por

CARLOS MORENO CRUZ

para optar al título de

DOCTOR EN QUÍMICA

con mención INTERNACIONAL

Editor: Universidad de Granada. Tesis Doctorales
Autor: Carlos Moreno Cruz
ISBN: 978-84-1306-483-3
URI: <http://hdl.handle.net/10481/62243>

RESUMEN / SUMMARY

RESUMEN

La siguiente tesis doctoral recoge el trabajo realizado por el doctorando **Carlos Moreno Cruz** durante su etapa predoctoral. Los datos recogidos en esta tesis se han estructurado en los siguientes apartados: i) introducción general, ii) objetivos, iii) resultados y discusión, iv) parte experimental, y v) conclusiones.

El primer apartado se basa en una introducción general, con el fin de contextualizar el trabajo realizado dentro del campo de aplicación de la tesis. Así mismo, describe los ejemplos más relevantes en el apartado en el que se ubica la presente tesis doctoral. De este modo, esta introducción se inicia con una descripción estructural de los principales alótopos del carbono, prestando especial interés al **grafeno**. La estructura química del grafeno así como la presencia de **defectos** en su estructura se verá en profundidad.

Tras una breve descripción de los métodos de preparación de grafeno, se introduce al lector las **nanocintas de grafeno**. En concreto, se hace especial hincapié en la preparación de nanocintas de grafeno mediante técnicas "*bottom-up*" en disolución aunque también se mencionan tanto técnicas "*top-down*" y en superficie. Esta sección permite indirectamente la introducción de las estructuras de polifenilenos, estructuras que serán descritas en la siguiente sección.

La sección principal de la introducción se centra en la estructura y síntesis de **nanografenos**. Primeramente se hablará sobre la estructura, síntesis y propiedades de estos. En este apartado se describen los **métodos sintéticos** basados en reacciones de ciclotrimerización de alquinos o reacciones de Diels-Alder en combinación con reacciones de tipo Scholl. Intercaladas en esta sección aparecen las descripciones de los mecanismos de reacción de las reacciones de ciclotrimerización de alquinos y de la reacción de Scholl. Del mismo modo, se introducen las bases de la técnica de **absorción de doble fotón**. Seguidamente se describen ejemplos de nanografenos extendidos de gran interés y relacionados estructuralmente con los estudiados en esta tesis doctoral. Por último, se introducen ejemplos de metodologías alternativas para la preparación de Nanografenos.

Seguidamente, se describe la estructura de los carbo[*n*]helicenos y dos de las **propiedades quirópticas** más importantes en este trabajo, asociadas a ellos: i) el dicroísmo circular y ii) la luminiscencia circularmente polarizada. La estructura y propiedades de los ejemplos más

relevantes de helicenos tanto simples como extendidos ocupan el siguiente apartado, desembocando en la introducción de una nueva familia de nanografenos helicoidales, los **superhelicenos**. Como extensión a las estructuras con un heliceno, se describen las estructuras y las propiedades de múltiples helicenos comparando las propiedades de análogos simples con sus respectivas estructuras π -extendidas. Esta sección termina con los ejemplos más relevantes y actuales de nanografenos extendidos que presentan múltiples helicenos.

Para finalizar la introducción, se describe la estructura de nanografenos que incorporan **anillos no hexagonales** en su estructura, desde las estructuras más simples como los $[n]$ circulenos hasta ejemplos de nanografenos extendidos. A su vez, se describen las metodologías descritas para la preparación de estos nanografenos distorsionados.

A continuación se recogen los objetivos planteados, los **resultados y la discusión** de estos. En este apartado se describen: i) las metodologías usadas para la preparación de distintos nanografenos distorsionados que combinan tanto anillos heptagonales como helicenos, ii) la caracterización estructural de estos, iii) el estudio de sus propiedades ópticas y quirópticas, iv) el estudio de sus propiedades electroquímicas, v) el estudio de otras propiedades como imagen en superficie.

Por último, el apartado de **parte experimental** recoge los datos de interés correspondientes a las técnicas utilizadas durante la realización de la presente tesis, así como la descripción detallada de las síntesis de los compuestos preparados y su caracterización estructural. En último lugar, se pueden encontrar las conclusiones obtenidas tras el trabajo realizado.

En forma de anexos, se han incluido otros resultados obtenidos durante la elaboración de esta tesis doctoral, presentados de manera resumida.

SUMMARY

The present doctoral thesis gathers the research work carried out by the PhD candidate **Carlos Moreno Cruz** during his predoctoral stage. The data reported on this thesis has been structured in the next sections: i) introduction and background, ii) objectives, iii) results and discussion, iv) experimental section, and v) conclusions.

The first section is based on a general introduction, in order to contextualize the work carried out into the field where the thesis is located. Likewise, the most relevant examples on the field are described. In this sense, this introduction is started with a structural description of the main carbon allotropes, focusing on **graphene**. An in-depth report on the chemical structure of graphene as well as the presence of defects on graphene will be found.

After a short description of the graphene preparation methodologies, the **graphene nanoribbons** are introduced. Particularly, a strong emphasis on the in solution "*bottom-up*" preparation of graphene nanoribbons is made, although "*top-down*" and on-surface techniques are also mentioned. This section also allows to introduce the structure of polyphenylene compounds, key structures on the next section.

The main part of the introduction section is focused on the structure and synthesis of **nanographenes**. Firstly, their structure, synthesis and properties will be reported. In this section, the **synthetic methodologies** based on alkyne cyclotrimerization reactions or Diels-Alder reactions in combination with Scholl-type reaction will be described. Among these methodologies, an explanation of the mechanism of the alkyne cyclotrimerization reaction and the Scholl reaction will be found. Likewise, the basis of the **two-photon absorption** technique are detailed followed by examples of structurally related extended nanographenes as a background on the field were this thesis is found. Lastly, alternative methodologies for the preparation of nanographenes are described.

Subsequently, a description of the structure of carbo[*n*]helicenes can be found along with two of the most important associated **chiroptical properties**: i) circular dichroism, and ii) circularly polarized luminescence. The structure and properties of the most relevant helicenes, both simple and extended take up the next section, ending on the introduction of a new family of helical nanographenes, the **superhelicenes**. As extension for the structures containing one helicene, the

structure and properties of multiple-helicene compounds are described, comparing the properties of simple compounds with their π -extended analogues. This section ends with the most relevant and actual examples of extended nanographenes bearing multiple helicenes.

The introduction and background ends talking about non-hexagonal ring-containing nanographenes, from the simplest structures such as $[n]$ circulenes to examples of extended nanographenes. At the same time, the reported methodologies for the preparation of this family of nanographenes are described.

Regarding the background on the field, the objectives of the thesis are disclosed. The results and discussion of the information obtained is structured as follows for each prepared compound: i) the methodology applied for the preparation of the different nanographenes combining both heptagons and helicenes, ii) the structural characterization of these compounds, iii) the study of their optical and chiroptical properties, iv) the study of their electrochemical properties, and v) the study of other properties such as surface imaging.

The last section gathers the **experimental** data corresponding to the used techniques during the thesis, as well as a detailed description of the synthesis of the prepared compounds and its structural characterization. Lastly, the obtained conclusions of the work developed in this thesis can be found.

Additionally, we have included other results obtained during the development of this thesis that can be found as annexes.

ABBREVIATIONS AND ACORNIMS

ABBREVIATIONS AND ACORNIMS

| | |
|-----------|---|
| 2D | Two-dimension(al) |
| 3D | Three-dimension |
| AB | Anodic Bonding |
| AC-HRTEM | Aberration-corrected High Resolution Transmission Electron Microscopy |
| AC-STEM | Aberration-corrected scanning transmission Electron Microscopy |
| AFM | Atomic force microscopy |
| Anh. | Anhydrous |
| APEX | Annulative Pi Extension |
| ca. | Circa |
| CD | Circular dichroism |
| CNT | Carbon nanotube |
| COSY | Correlation spectroscopy |
| CPL | Circularly polarized luminescence |
| CSP-HPLC | Chiral stationary phase High Performance Liquid Chromatography |
| CV | Cyclic Voltammetry |
| CVD | Chemical Vapor Deposition |
| DBATT | 2,3,8,9-dibenzanthanthrene |
| DBBA | 10,10'-dibromo-9,9'-bianthryl |
| DBU | 1,8-Diazabicyclo[5.4.0]undec-7-ene |
| DDQ | 2,3-Dichloro-5,6-dicyano-1,4-benzoquinone |
| DEPT | Distortionless Enhancement by Polarization Transfer |
| DFT | Density Functional Theory |
| DMAP | 4-Dimethylaminopyridine |
| DMF | Dimethylformamide |
| DPEX | Dehydrative Pi Extension |
| ECD | Electronic Circular Dichroism |
| <i>ee</i> | Enantiomeric excess |
| ESI | Electrospray ionization |
| Fc | Ferrocene |

| | |
|--------|---|
| GNR | Graphene Nanoribbon |
| GQD | Graphene quantum dot |
| HBC | Hexa- <i>peri</i> -hexabenzocoronene |
| HBT | Hexabenzotriphenylene |
| HMBC | Heteronuclear Multiple Bond Correlation |
| HOMO | Highest Occupied Molecular Orbital |
| HPLC | High Performance Liquid Chromatography |
| HRTEM | High-resolution Transmission Electron Microscopy |
| HSQC | Heteronuclear single quantum correlation spectroscopy |
| IRF | Instrumental response function |
| LAGB | Large-angle grain boundary |
| LPE | Liquid-phase exfoliation |
| LQY | Low quantum yield |
| LUMO | Lowest Unoccupied Molecular Orbital |
| MALDI | Matrix-assisted Laser Desorption/Ionization |
| MC | Micromechanical Cleavage |
| MLG | Multilayer graphene |
| MS | Mass spectrometry |
| MWCNT | Multi-walled carbon nanotube |
| NC-AFM | Non-contact atomic force microscopy |
| NIR | Near Infrared |
| NIT | Nitronyl-nitroxide |
| NMR | Nuclear Magnetic Resonance |
| OLED | Organic Light-emitting Diode |
| OPA | One-photon absorption |
| OPE | One-photon excitation |
| PAH | Polycyclic aromatic hydrocarbon |
| PEM | Photoelastic modulator |
| PIFA | (Bis(trifluoroacetoxy)iodo)benzene |
| ROESY | Rotating frame nuclear Overhauser effect spectroscopy |
| RSE | Ring strain energy |

| | |
|--------|---|
| RT | Room temperature |
| Sat. | Saturated |
| SCXRD | Single-crystal X-ray diffraction |
| SLG | Single-layer graphene |
| STEM | Scanning Transmission Electron Microscopy |
| STM | Scanning Tunneling Microscopy |
| SWV | Square-wave voltammetry |
| TBAF | Tetra-n-butylammonium fluoride |
| TBTQ | Tribenzotriquinacene |
| TD-DFT | Time-dependent Density functional theory |
| TEM | Transmission Electron Microscopy |
| THF | Tetrahydrofuran |
| TLC | Thin layer chromatography |
| TMS | Trimethylsilane |
| TMSA | Trimethylsilylacetylene |
| TNT | Trinaphtotriphenylene |
| TOF | Time of flight |
| TPA | Two-photon absorption |
| TPE | Two-photon excitation |
| TPIF | Two-photon induced fluorescence |
| UC | Upconversion |
| UHV | Ultra-high vacuum |
| UV-vis | Ultraviolet-visible |

TABLE OF CONTENTS

TABLE OF CONTENTS

| | |
|---|-----------|
| 1. BACKGROUND..... | 23 |
| 1.1. Graphene..... | 27 |
| 1.1.1. General description, structure and properties..... | 27 |
| 1.1.2. Defects in graphene..... | 31 |
| 1.1.2.1. <i>Point defects</i> | 32 |
| 1.1.2.2. <i>One-dimensional defects</i> | 35 |
| 1.1.2.3. <i>Defects-property relationships</i> | 36 |
| 1.1.3. Preparation of graphene..... | 37 |
| 1.1.3.1. <i>Top-down strategies</i> | 38 |
| 1.1.3.2. <i>Bottom-up strategies</i> | 39 |
| 1.2. Graphene nanoribbons..... | 41 |
| 1.2.1. General description, structure and properties..... | 42 |
| 1.2.2. Preparation of graphene nanoribbons..... | 43 |
| 1.2.2.1. <i>Top-down strategies</i> | 43 |
| 1.2.2.2. <i>Bottom-up strategies</i> | 44 |
| <i>On surface synthesis</i> | 45 |
| <i>Solution synthesis</i> | 47 |
| 1.3. Nanographenes..... | 55 |
| 1.3.1. Structure, synthesis and properties..... | 55 |
| 1.3.1.1. <i>Nanographene synthesis by Diels-Alder/cyclotrimerization and Scholl reactions</i> | 56 |
| <i>Alkyne cyclotrimerization reaction – a first approach</i> | 58 |
| <i>Scholl reaction – the key step</i> | 60 |
| <i>Functionalization on HBC derivatives – tuning the properties</i> | 62 |
| <i>Non-linear optical properties on HBC and nanographenes – Two-photon absorption</i> | 64 |
| <i>Functionalization and expansion – toward larger graphene molecules</i> | 65 |
| 1.3.1.2. <i>Other approaches for nanographene synthesis</i> | 75 |
| 1.3.2. Helicene-containing nanographenes..... | 81 |
| <i>Circular Dichroism and Circularly Polarized Luminescence – key chiroptical properties</i> | 82 |
| <i>Instrumentation for CPL measurements</i> | 86 |
| 1.3.2.1. <i>CPL-active helical- and helicene-based compounds</i> | 87 |
| 1.3.2.2. <i>Laterally-extended helicenes as contorted nanographenes</i> | 88 |
| 1.3.2.3. <i>Multiple helicenes as contorted nanographenes</i> | 93 |
| 1.3.3. Nanographenes containing non-hexagonal rings..... | 101 |
| 1.3.3.1. <i>[n]circulenes</i> | 103 |
| 1.3.3.2. <i>Synthetic strategies towards heptagon-containing nanographenes</i> | 105 |
| 1.3.3.3. <i>Reported heptagon-containing nanographenes</i> | 109 |

| | |
|--|-----|
| 2. OBJECTIVES | 117 |
| 3. RESULTS AND DISCUSSION | 121 |
| 3.1. Ribbon-shaped nanographene combining TPA-UC and CPL | 123 |
| 3.1.1. Synthesis and structural characterization..... | 124 |
| 3.1.2. Optical properties..... | 130 |
| 3.1.3. Chiroptical properties..... | 135 |
| 3.1.4. Electrochemical properties..... | 139 |
| 3.1.5. On surface study..... | 140 |
| 3.2. Extended ribbon-shaped saddle-helix hybrid nanographene | 142 |
| 3.2.1. Synthesis and structural characterization..... | 142 |
| 3.2.2. Optical properties..... | 148 |
| 3.2.3. Electrochemical properties..... | 152 |
| 3.3. Undecabenzo[7] superhelicenes | 154 |
| 3.3.1. Synthesis and structural characterization..... | 154 |
| 3.3.2. Optical properties..... | 163 |
| 3.3.3. Chiroptical properties..... | 166 |
| 3.3.4. Electrochemical properties..... | 170 |
| 3.4. Multiple helicene distorted saddle-helix hybrid nanographene | 171 |
| 3.4.1. Synthesis and structural characterization..... | 171 |
| 3.4.2. Optical properties..... | 177 |
| 3.4.3. Chiroptical properties..... | 179 |
| 3.5. Triskelion-shaped saddle-helix hybrid nanographene | 181 |
| 3.5.1. Synthesis and structural characterization..... | 181 |
| 3.5.2. Optical properties..... | 187 |
| 3.5.3. Chiroptical properties..... | 192 |
| 4. EXPERIMENTAL SECTION | 197 |
| 4.1. General information | 199 |
| 4.2. Synthesis and characterization of the prepared compounds | 202 |
| 4.3. X-Ray diffraction structures | 242 |
| 4.4. Representative NMR spectra of prepared compounds | 246 |
| 5. CONCLUSIONS | 285 |
| 6. ANNEXES | 289 |

1. BACKGROUND

Carbon represents the fourth most abundant element both in the Milky Way Galaxy and in the Solar System after hydrogen, helium and oxygen whilst on Earth, it only represents a small piece of the planet total mass. It can be found as a native mineral (graphite or diamond), charcoal, or taking part on different compounds in combination with other elements such as oxygen (CO, CO₂ or CO₃²⁻) or hydrogen (CH₄ and hydrocarbons) among others at the Earth's crust.

Clearly, the preeminent characteristic of carbon atoms is their easiness to form covalent bonds with almost the rest of elements of the periodic table (either electronegative or electropositive). However, its catenation ability, the capacity to form long chains between carbon atoms, is the most important from a chemical point of view. This feature is not only key for the biosynthesis of physiologically relevant compounds such as sugars or proteins but it is also fundamental on purely carbon-based compounds like carbon allotropes.

Allotropy is described as the property of some elements to exist in two or more different forms, known as allotropes. Regarding carbon, its allotropy is directly related to its valence and catenation ability. Hybridization of carbon atoms allows to form different kind of bonds (simple, double or triple) with other carbon atoms and, together with its catenation ability, a wide variety of carbon allotropes can be formed.

Diamond and graphite were the first carbon allotropes discovered and have been studied for centuries. The former exhibits a tetragonal arrangement of carbon atoms with sp³ hybridization while the latter is based on stacked sheets of carbon atoms in a hexagonal disposition with sp² hybridization.

Nevertheless, it was on 1985 when H. W. Kroto, R. F. Curl, R. E. Smalley and co-workers detected a new carbon allotrope, the C₆₀ or Buckminsterfullerene, by mass spectrometry after the laser-irradiation of a graphite disk, adding a new member to the list.¹ The authors proposed a spheroidal soccer-ball-type structure for C₆₀ where each carbon atom is placed on the vertices of a truncated icosahedron, even evidences of C₇₀ fullerene could be found on the reported mass spectrum. This new allotrope was the first one constituted by a defined number of carbon atoms

¹ H. W. Kroto, J. R. Heath, S. C. O'Brien, R. F. Curl, R. E. Smalley, *Nature* **1985**, *318*, 162-163.

and drew the beginning of a new research era based on carbon allotropes.² Up to date, an extensive research in the field of fullerenes has been carried out, being employed in a wide variety of fields, from medical applications³ to new composites for energy storage.⁴ Moreover, their properties can be easily tuned by its functionalization through synthetic chemistry.⁵

Following the timeline on the era of carbon allotropes, the next milestone was reached by S. Iijima in 1991 who reported the first evidence of a new finite carbon allotrope, the carbon nanotubes (CNTs).⁶ CNTs are graphitic-like structures arranged in a tubular form, which were firstly prepared by using similar instrumentation than that of C₆₀ mass production.⁷ Structurally, CNTs can be found as Single Walled Carbon Nanotubes (SWCNTs) or as Multi-Walled Carbon Nanotubes (MWCNTs). Furthermore, this one-dimensional carbon allotrope also exhibits different conformations such as zigzag, armchair or even chirality. As for fullerenes, CNTs have been extensively studied during the last decades finding applications in a wide range of fields.⁸

The last candidate to reach the carbon allotropes *hall of fame* was graphene, a two dimensional atomic crystal which consists of carbon atoms arranged in a hexagonal lattice, in other words, a graphite monolayer. Envisioned and attempted to be isolated from the last century, its isolation and primary study of their properties were finally reported by K. S. Novoselov, A. K. Geim and co-workers in 2004.⁹ Nowadays an intensive effort on the new preparation and isolation of carbon allotropes is still being carried out around the world, where new allotropes such as C₁₈, the first isolated cyclo[*n*]carbon, have been recently reported, following the seminal works of Diederich.¹⁰

² A. Hirsch, *Nat. Mater.* **2010**, *9*, 868-871.

³ N. Panwar, A. M. Soehartono, K. K. Chan, S. Zeng, G. Xu, J. Qu, P. Coquet, K.-T. Yong, X. Chen, *Chem. Rev.* **2019**, *119*, 9559-9656.

⁴ a) C. Cui, Y. Li, Y. Li, *Adv. Energy Mater.* **2017**, *7*, 1601251; b) T. Gatti, E. Menna, M. Meneghetti, M. Maggini, A. Petrozza, F. Lamberti, *Nano Energy* **2017**, *41*, 84-100.

⁵ a) A. A. Popov, S. Yang, L. Dunsch, *Chem. Rev.* **2013**, *113*, 5989-6113; b) M. A. Lebedeva, T. W. Chamberlain, A. N. Khlobystov, *Chem. Rev.* **2015**, *115*, 11301-11351; d) W. Yan, S. Seifermann, P. Pierrat, S. Bräse, *Org. Biomol. Chem.* **2015**, *13*, 25-54; c) E. E. Maroto, M. Izquierdo, S. Reboredo, J. Marco-Martínez, S. Filippone, N. Martín, *Acc. Chem. Res.* **2014**, *47*, 2660-2670.

⁶ S. Iijima, *Nature* **1991**, *354*, 56-58.

⁷ W. Krätschmer, L. D. Lamb, K. Fostiropoulos, D. R. Huffman, *Nature* **1990**, *347*, 354-358.

⁸ M. F. L. De Volder, S. H. Tawfick, R. H. Baughman, A. J. Hart, *Science* **2013**, *339*, 535-539.

⁹ K. S. Novoselov, A. K. Geim, S. V. Morozov, D. Jiang, Y. Zhang, S. V. Dubonos, I. V. Grigorieva, A. A. Firsov, *Science* **2004**, *306*, 666-669.

¹⁰ a) Y. Rubin, F. Diederich, *J. Am. Chem. Soc.* **1989**, *111*, 6870-6871; b) K. Kaiser, L. M. Scriven, F. Schulz, P. Gawel, L. Gross, H. L. Anderson, *Science* **2019**, *365*, 1299-1301.

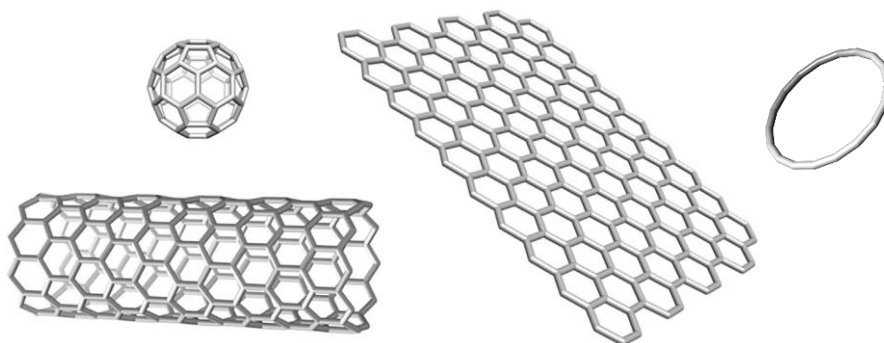


Figure 1. Last carbon allotropes isolated and studied. Left-top: fullerenes; Left-bottom: nanotubes; Middle: graphene. Right: C₁₈.¹¹

1.1. Graphene

1.1.1. General description, structure and properties

Graphene is the latest carbon allotrope isolated and prepared in a sufficient scale for an intensive research since the communication of K. S. Novoselov, A. K. Geim and co-workers in 2004, where the authors isolated graphene and studied the electric field effect in atomically thin carbon films.⁸ This fact, and its subsequent research, resulted in the Nobel Prize in physics in 2010.¹² During the last fifteen years, graphene has attracted much more attention than the previously isolated carbon allotropes (fullerenes and CNTs) due to its revolutionary properties.

The structure of graphene could be defined as: a monolayer of carbon atoms disposed in a flat honeycomb-like hexagonal lattice, where each carbon atom possess sp^2 hybridization and bonded directly with other three identical carbon atoms. Regarding the orbitals that take part on the carbon-carbon bonds, each carbon is linked thrice through their sp^2 orbitals forming three σ bonds, while each atom exhibits a non-hybridized p orbital, perpendicular to the sp^2 hybrid orbitals, which takes part on a π bond. This fact results on a delocalization of the electrons along the surface of the hexagonal lattice as a delocalized π orbital.

¹¹ N. Martín, *Chem* **2019**, *5*, 733-738.

¹² a) A. K. Geim, *Angew. Chem. Int. Ed.* **2011**, *50*, 6966-6985; b) K. S. Novoselov, *Angew. Chem. Int. Ed.* **2011**, *50*, 6986-7002.

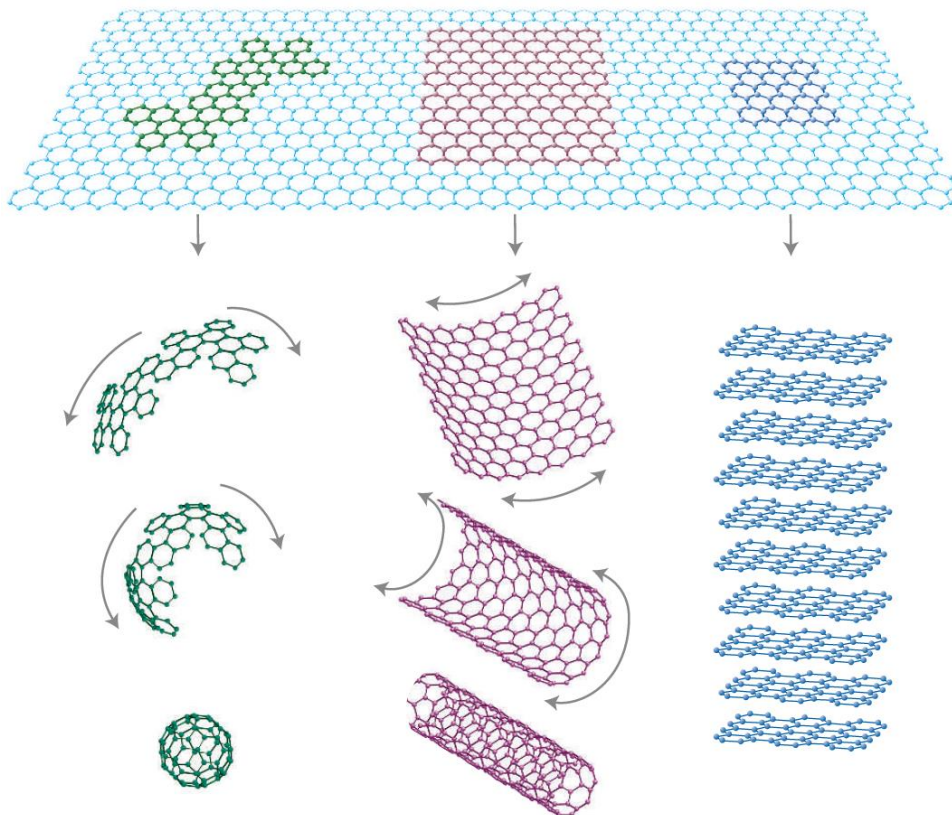


Figure 2. Graphene, the 2D carbon allotrope as precursor for all graphitic carbon allotropes such as 0D fullerenes, 1D CNTs or 3D graphite.¹³

It would be expected that singular electronic properties may arise from this electron delocalization. Since 1947, many attempts have been done in order to explain the electronic properties of graphite and its band theory was discerned taking a monolayer (graphene) as model.¹⁴ From the point of view of its electronic properties, graphene is a zero-gap semiconductor, in other words, the conduction band and the valence band are encountered in one point (Dirac point) in coincidence with each carbon atom. The valence band is full of electron density meaning that the Fermi level is located at the Dirac Point (Figure 3), which results in changes at the Fermi level (E_F) when changing gate voltage (V_g) with a rapid decrease in resistivity (ρ), showing an ambipolar electric field effect.⁹

¹³ A. K. Geim, K. S. Novoselov, *Nat. Mater.* **2007**, *6*, 183-191.

¹⁴ a) P. R. Wallace, *Phys. Rev.* **1947**, *71*, 622-634; b) J. W. McClure, *Phys. Rev.* **1956**, *104*, 666-671; c) J. C. Slonczewski, P. R. Weiss, *Phys. Rev.* **1958**, *109*, 272-279.

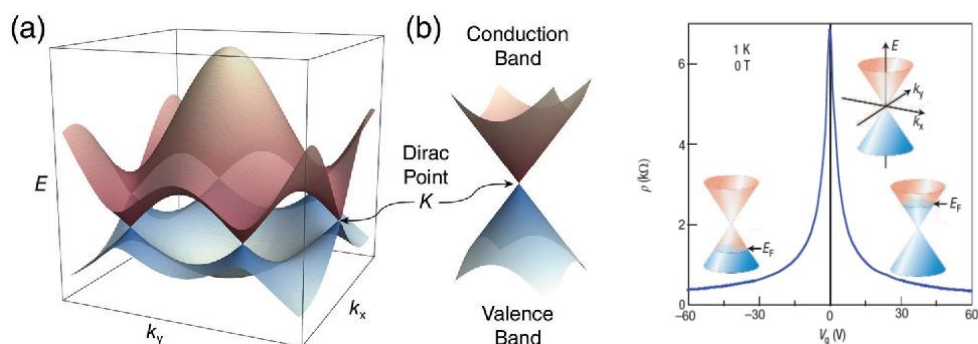


Figure 3. Valence band (blue) and conduction band (red) of graphene, note the six Dirac points coinciding with each carbon atom on each hexagonal ring.¹³

This singular fact could be considered as a drawback rather than a benefit for its application in electronics as semiconductor for information storage, since devices made of graphene cannot be switched off and, therefore, are not suitable for logic applications. Nevertheless, the band structure of graphene can be modified, being possible to open a band gap in three ways: (i) arranging graphene in a ribbon shaped (graphene nanoribbons); (ii) by biasing bilayer graphene and; (iii) by applying strain to graphene (Figure 4).¹⁵ Regarding graphene nanoribbons (GNRs), two different types were postulated accordingly to the disposition of the carbon atoms at their edges: zigzag or armchair. Theoretically, both types of GNRs were presumed to exhibit a band gap that is inversely proportional to the width of the nanoribbon. This fact has been verified experimentally for width down to 1 nm.¹⁶

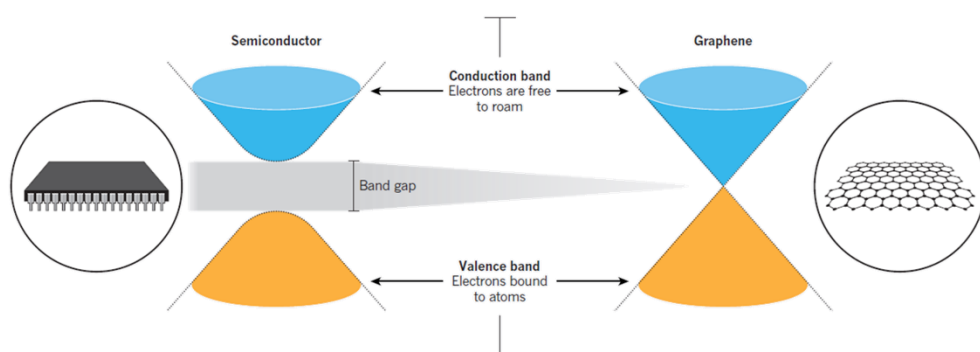


Figure 4. Schematic representation of the valence and conduction band on a semiconductor in comparison with that of graphene.

¹⁵ F. Schwierz, *Nat. Nanotechnol.* **2010**, *5*, 487-496.

¹⁶ X. Li, X. Wang, L. Zhang, S. Lee, H. Dai, *Science* **2008**, *319*, 1229-1232.

1. Background

However, these structural features are not only observable on GNRs since they are also found on graphene flakes. Armchair and zigzag edges are, basically, different kind of crystal faces (do not forget that graphene is a 2D crystal).¹⁷ Nevertheless, not only these two edge types can be found on graphene, a wide variety of structural features have been found on graphene edges, known as cove, gulf, bay or fjord (Figure 5).¹⁸ The properties have been found to be different on dependence of the edge type.¹⁹ Thus, edge modifications are supposed to be an interesting observable from a possible tuning of graphene properties.

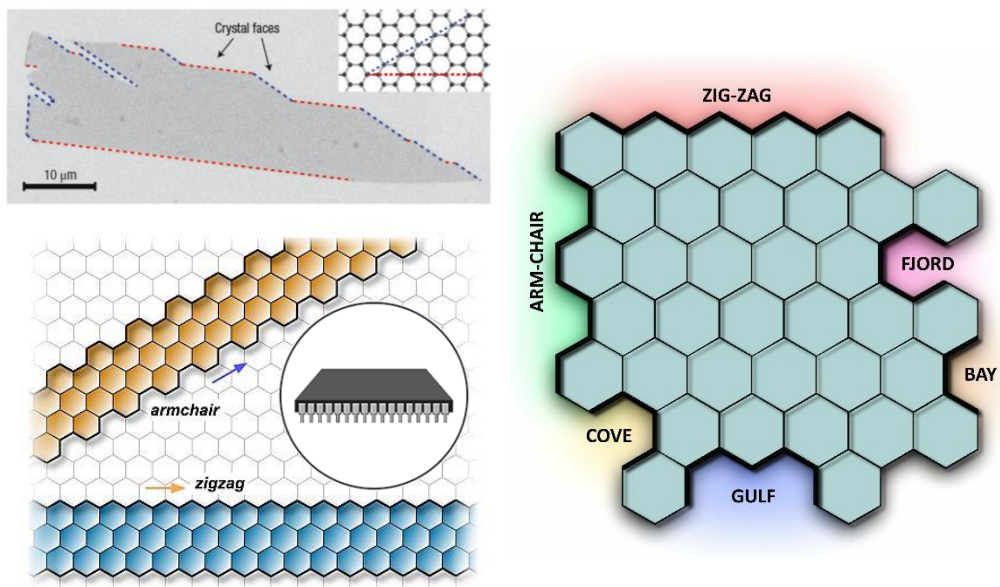


Figure 5. Left-top: Different crystal faces found on a graphene flake; Left-down: armchair (orange) and zigzag (blue) GNRs; Right: Edge variety on graphene and their different names.⁹

¹⁷ Ç. Ö. Girit, J. C. Meyer, R. Erni, M. D. Rossell, C. Kisielowski, L. Yang, C.-H. Park, M. F. Crommie, M. L. Cohen, S. G. Louie, A. Zettl, *Science* **2009**, 323, 1705-1708.

¹⁸ D. Lungerich, O. Papaianina, M. Feofanov, J. Liu, M. Devarajulu, S. I. Toyonov, S. Maier, K. Amsharov, *Nat. Commun.* **2018**, 9, 4756.

¹⁹ H. Goto, E. Uesugi, R. Eguchi, A. Fujiwara, Y. Kubozono, *Nano Lett.* **2013**, 13, 1126-1130.

1.1.2. Defects in graphene

Edge topology is not only the main interesting structural feature on graphene. As a crystal, graphene can incorporate defects into the crystal lattice.²⁰ These defects could alter its properties since the predicted extraordinary properties can only be observed at graphene sheets with extremely low defect concentration. Despite the presence of defects, graphene remains unusual since it is a 2D crystal able to host lattice defects. This could be related to the different hybridization of carbon atoms and the flexibility on the angle between bonds, arranging carbons into a variety of geometrical shapes, not only hexagons, to form different structures. Non-hexagonal rings may introduce curvature on a graphene sheet or maintain the flatness when combining in a way that satisfies certain symmetry rules.²¹ This fact cannot be found on other 3D crystals, however, topological defects in bulk graphite have been detected and studied since 1960 where the presence of dislocations was found by using transmission electron microscopy (TEM).²² Nowadays, with modern microscopy methods, such as aberration-corrected high-resolution transmission electron microscopy (AC-HRTEM), aberration-corrected scanning transmission electron microscopy (AC-STEM) or scanning tunneling microscopy (STM), the exact atomic structure of graphene can be resolved and its crystallographic defects studied.²³ In spite of this, defects on graphene have been also studied by computational methods, quantifying defect formation in terms of activation energies,²⁴ underpinning experimental observations that confirm the non-stationary behavior of defects.²⁵ Defects can be produced during the formation of graphene, as grain boundaries on polycrystalline graphene,²⁶ or by deliberate introduction via electronic beam impacts or chemical treatment. Different techniques or treatments over pristine graphene will lead on a wide variety of lattice defects. Thus, defects on graphene can be classified as point defects (zero-dimensional) or one-dimensional.

²⁰ A. Hashimoto, K. Suenaga, A. Gloter, K. Urita, S. Iijima, *Nature* **2004**, *430*, 870-873.

²¹ F. Banhart, J. Kotakoski, A. V. Krasheninnikov, *ACS Nano* **2011**, *5*, 26-41.

²² a) S. Amelinckx, P. Delavignette, *Phys. Rev. Lett.* **1960**, *5*, 50-51; b) P. Delavignette, S. Amelinckx, *J. Nucl. Mater.* **1962**, *5*, 17-66.

²³ J. C. Meyer, C. Kisielowski, R. Erni, M. D. Rossell, M. F. Crommie, A. Zettl, *Nano Lett.* **2008**, *8*, 3582-3586.

²⁴ S. T. Skowron, I. V. Lebedeva, A. M. Popov, E. Bichoutskaia, *Chem. Soc. Rev.* **2015**, *44*, 3143-3176.

²⁵ O. Lehtinen, S. Kurasch, A.V. Krasheninnikov, U. Kaiser, *Nat. Commun.* **2013**, *4*, 2098.

²⁶ O. V. Yazyev, Y. P. Chen, *Nat. Nanotechnol.* **2014**, *9*, 755-767.

1. Background

1.1.2.1. Point defects

- *Stone-Wales defect*: the simplest example of defects on a graphene lattice is the Stone-Wales defect, which does not involve any removed or added atom. This particular defect is based on the reconstruction of the hexagonal lattice to form non-hexagonal rings, where four hexagons are transformed into two pentagons and two heptagons by the rotation of one C-C bond 90° .²⁷ The resulting structure retains the same number of atoms and planarity as purely hexagonal graphene showing also an energy barrier high enough for being stable at room temperature (Figure 6).²³

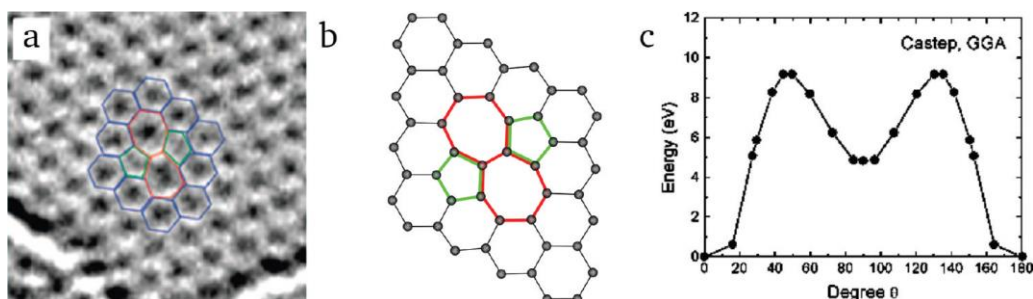


Figure 6. a) TEM image of a Stone-Wales defect on a graphene sheet; b) DFT calculated structure of a Stone-Wales defect; c) Calculated energy barrier for bond rotation.²¹

- *Single vacancies*: a missing atom in a lattice is the simplest defect in any material. Single vacancies have been observed in graphene by TEM and STM. This missing leads to the formation of a five-membered and a nine-membered ring, this vacancy is also called $V_1(5-9)$. The dangling atom on the nine-membered ring (Figure 7b) is easily observable on STM images due to an increase on the local electron density (Figure 7c).²³

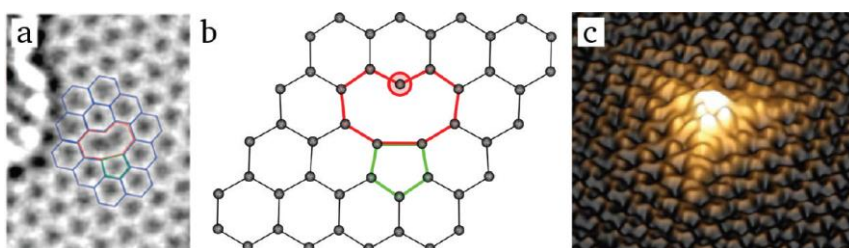


Figure 7. a) TEM image of a $V_1(5-9)$ vacancy on a graphene sheet; b) DFT calculated structure of a $V_1(5-9)$ vacancy; c) experimental STM image of a single vacancy.²¹

²⁷ A. J. Stone, D. J. Wales, *Chem. Phys. Lett.* **1986**, *128*, 501-503.

- *Multiple vacancies*: double vacancies can be interpreted either as the coalescence of two single vacancies or as the removal of two neighboring carbon atoms. In this case, no dangling atoms are present on the structure which can be observed as a combination of one eight-membered ring and two five-membered rings, coined as $V_2(5-8-5)$ (Figure 8a). The $V_2(5-8-5)$ is not the only combination that accommodates a double vacancy, because if one bond is reoriented (as for Stone-Wales defect), the $V_2(5-8-5)$ defect would be rearranged into an energetically favored $V_2(555-777)$ showing three pentagons and three heptagons (Figure 8b).²⁸ One step further would be the transformation of the $V_2(555-777)$ into a $V_2(5555-6-7777)$ defect by a bond rotation (Figure 8c). The mobility on multiple vacancies is higher than for single vacancies, being these almost immobile up to very high temperature.

The removal of a large number of atoms may lead to larger and more complex defect configurations and a reconstruction of the layer would be required, bending or warping the surface since the lattice is reduced. If the number of removed atoms is too high, the healing of the graphene surface would not be achieved and a hole will remain on the hexagonal lattice.

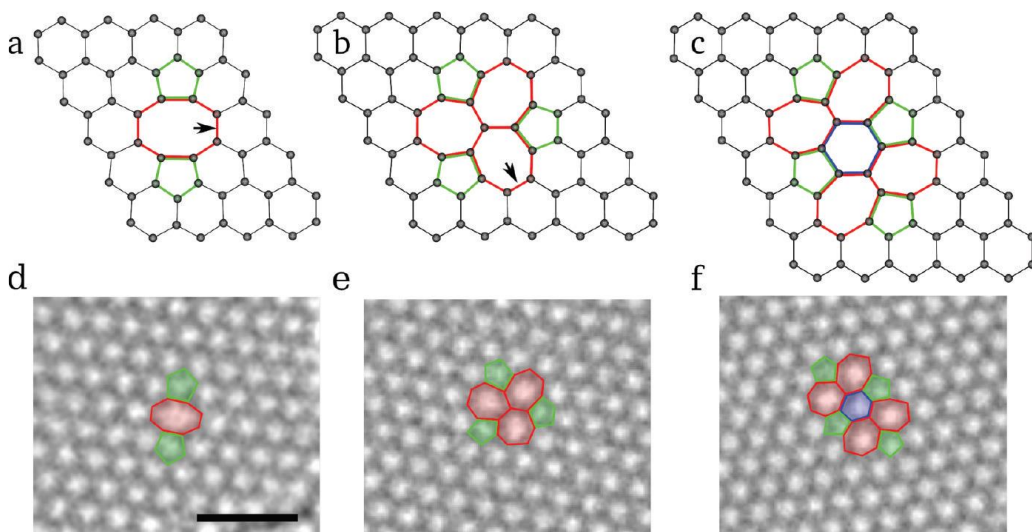


Figure 8. a-c) DFT calculation of double vacancies and their reconstruction; d-f) experimental TEM images of the same double vacancies. Rotating bonds are highlighted.²¹

²⁸ G. -D. Lee, C. Z. Wang, E. Yoon, N. -M. Hwang, D. -Y. Kim, K. M. Ho, *Phys. Rev. Lett.* **2005**, *95*, 205501.

1. Background

- *Self-Interstitials*: the introduction of two extra carbon atoms on the graphene lattice is only possible after treatment of pristine graphene, *i.e.* after sublimation of graphite in presence of graphene²⁹ or by focused electron beam exposure.³⁰ The new extra carbon atoms rearrange the hexagonal lattice forming combination of heptagons and pentagons and originates a high local curvature, leading to blister-like structures (Figure 9).

- *Carbon and foreign adatoms*: a single carbon atom would not be introduced into the hexagonal lattice of graphene due to a high energetic cost, rather than straining the structure out of the plane, the extra atom would be placed on top of a carbon-carbon bond (bridge configuration) since it is energetically favored. This adatom can migrate easily over the graphene surface and if two migrating adatoms meet each other and form a dimer, they can be incorporated into the hexagonal lattice as a self-interstitial defect (Figure 9). On the other hand, the incorporation of foreign adatoms to graphene is ruled by the energy of the bond formed, increasing the mobility over the graphene surface when is weakly physisorbed. During this migration, foreign adatoms such as metals can be trapped on vacancies defects by forming covalent bonds between them.³¹

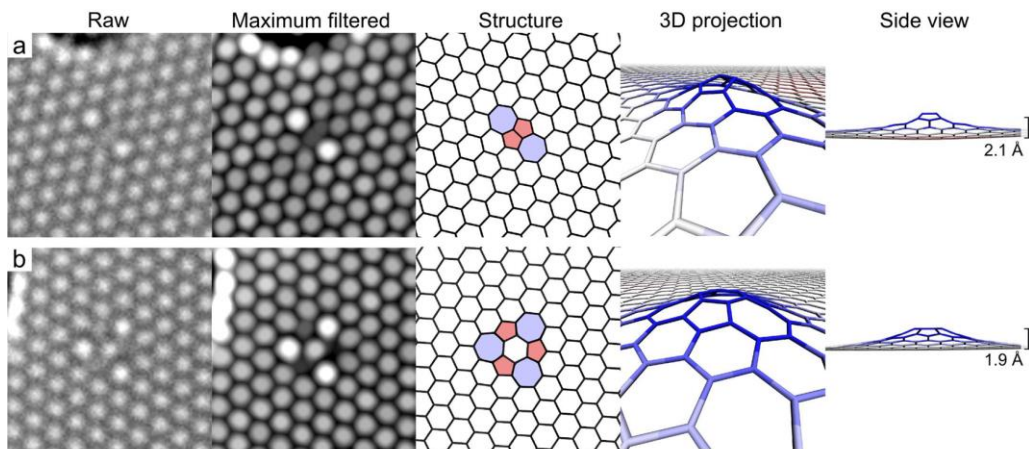


Figure 9. a) AC-HRTEM image, idealized structure and 3D modelling of an inverse Stone-Thrower-Wales defect; b) AC-HRTEM image, idealized structure and 3D modelling of self-interstitial dimers.²⁹

²⁹ O. Lehtinen, N. Vats, G. Algara-Siller, P. Knyrim, U. Kaiser, *Nano Lett.* **2015**, *15*, 235-241.

³⁰ A. W. Robertson, K. He, A. I. Kirkland, J. Warner, *Nano Lett.* **2014**, *14*, 908-914.

³¹ O. Cretu, A. V. Krasheninnikov, J. A. Rodríguez-Manzo, L. Sun, R. Nieminen, F. Banhart, *Phys. Rev. Lett.* **2010**, *105*, 196102.

1.1.2.2. One-dimensional defects

- *Disclinations*: as the elementary topological defect, it can be visualized as the presence of one non-hexagonal ring into the hexagonal lattice, that means the introduction (or removal) of a semi-infinite wedge of material to an ideal 2D structure. The introduction of an isolated heptagon or a pentagon results in the addition or removal of a 60° wedge respectively, meaning a positive (five-membered ring) or negative (seven-membered ring) disclination.³² The presence of isolated disclinations in graphene is not very common as it inevitably results in non-planar structures.³³

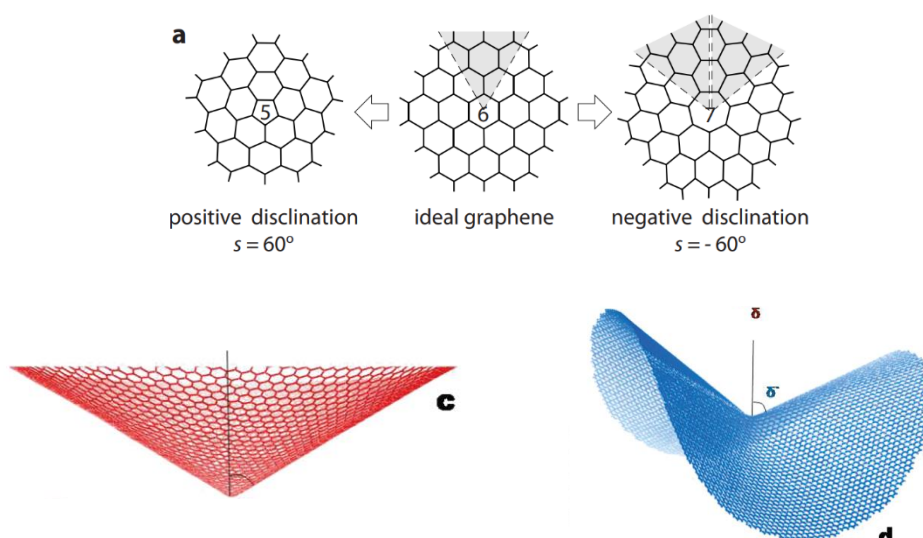


Figure 10. a) Positive and negative disclinations in graphene; b) Graphene lattice containing a five- or seven-membered ring becomes a bowl or a saddle respectively.^{32, 33}

- *Dislocations*: dislocations can be described as the introduction of a strip on the hexagonal lattice and, are caused by the combination of pairs of complementary disclinations, *i.e.* combination of heptagons and pentagons. The Burgers vector (\vec{b} , Figure 11) is the parameter that describes the size of the extra strip and characterizes the different types of dislocations. An edge sharing heptagon-pentagon is a dislocation in graphene with the smallest possible Burgers vector (Figure 11a).^{26, 32}

³² O. V. Yazyev, S. G. Louie, *Phys. Rev. B* **2010**, *81*, 195420.

³³ Y. Liu, B. I. Yakobson, *Nano Lett.* **2010**, *10*, 2178-2183.

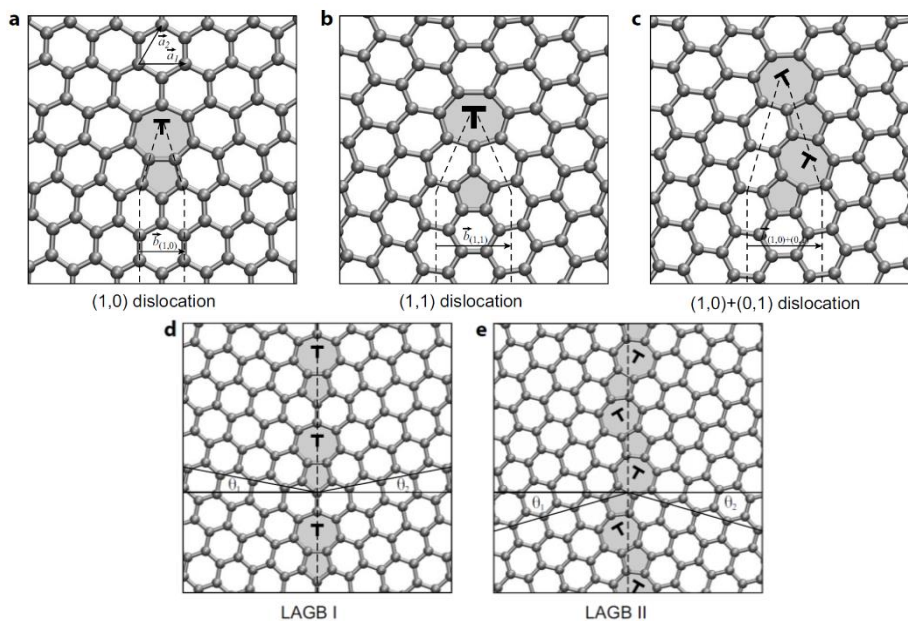


Figure 11. a-c) Atomic structures of different dislocations with different Burgers vectors values. Dashed lines represent the extra strip on the lattice; d-e) Atomic structures of two kind of large angle grain boundaries (LAGB).³²

- *Grain boundaries:* during the preparation of graphene, the resulting sheet is usually polycrystalline, meaning that it is formed by the junction of different domains of single crystals with varying lattice orientation.³⁴ Grain boundaries on a graphene sheet represent a type of topological defect and are based on chains of aligned dislocations. Different types of grain boundaries have been found depending on the misorientation angle formed between two different domains (θ , Figure 11d,e) exhibiting alternating five- and seven-membered rings or alternating eight- and two five-membered rings among others.

1.1.2.3. Defects-property relationships

The outstanding properties of graphene are directly related to the perfect arrangement of carbon atoms and the presence of a delocalized π -orbital all over the hexagonal lattice. Thus, modifications of this periodicity are presumed to modify its properties. Regarding the reactivity

³⁴ a) P. Y. Huang, C. S. Ruiz-Vargas, A. M. van der Zande, W. S. Whitney, M. P. Levendorf, J. W. Kevek, S. Garg, J. S. Alden, C. J. Hustedt, Y. Zhu, J. Park, P. L. McEuen, D. A. Muller, *Nature* **2011**, *469*, 389-393; b) K. Kim, Z. Lee, W. Regan, C. Kisielowski, M. F. Crommie, A. Zettl, *ACS Nano* **2011**, *5*, 2142-2146.

of graphene, it is expected that defects exhibiting dangling atoms or bonds will show a different reactivity in comparison with pristine graphene. Theoretical calculations have demonstrated that vacancy-type defects are able to attach hydroxyl or carboxyl groups and the same is true for graphene edges.³⁵

Electronic properties on defective graphene are also suitable for being modified. The presence of defects modifies the overlap of the p-orbitals since their inclusion leads to a local rehybridization of σ and π -orbitals. The Dirac equation that governs the band theory on graphene would be modified when defects are in the lattice. Thus, grain boundaries introduce large transport gaps into graphene.³⁶

The modification of the π -electron system by doping graphene with defects modifies the charge carrier both by “self-doping”,³⁷ where intrinsic defects modify the band structure locally, or by adding foreign atoms as metals.³⁸

1.1.3. Preparation of graphene

After the first isolation of graphene in 2004, its preparation and isolation in a way to obtain enough quantities, reliable quality and proper size for further improvement and understanding of its properties have been inspiringly progressing. Nowadays, the preparation methods of considerable large fragments of graphene could be summarized on Figure 12 and are divided following two mainly strategies called top-down or bottom-up.³⁹ These two definitions are referred to the nature of the starting material: top-down strategies are referred to production of graphene from macroscopic starting materials such as graphite, whilst bottom-up strategies are based on the construction of graphene fragments from molecular building blocks such as low molecular weight hydrocarbons or polycyclic aromatic hydrocarbons.

³⁵ D. W. Boukhvalov, M. I. Katsnelson, *Nano Lett.* **2008**, *8*, 4373-4379.

³⁶ O. V. Yazyev, S. G. Louie, *Nat. Mater.* **2010**, *9*, 806-809.

³⁷ A. H. Castro Neto, F. Guinea, N. M. R. Peres, K. S. Novoselov, A. K. Geim, *Rev. Mod. Phys.* **2009**, *81*, 109-162.

³⁸ G. Giovanetti, P. A. Khomyakov, G. Brocks, V. M. Karpan, J. van den Brink, P. J. Kelly, *Phys. Rev. Lett.* **2008**, *101*, 026803.

³⁹ F. Bonaccorso, A. Lombardo, T. Hasan, Z. Sun, L. Colombo, A. C. Ferrari, *Mater. Today* **2012**, *15*, 564-589.

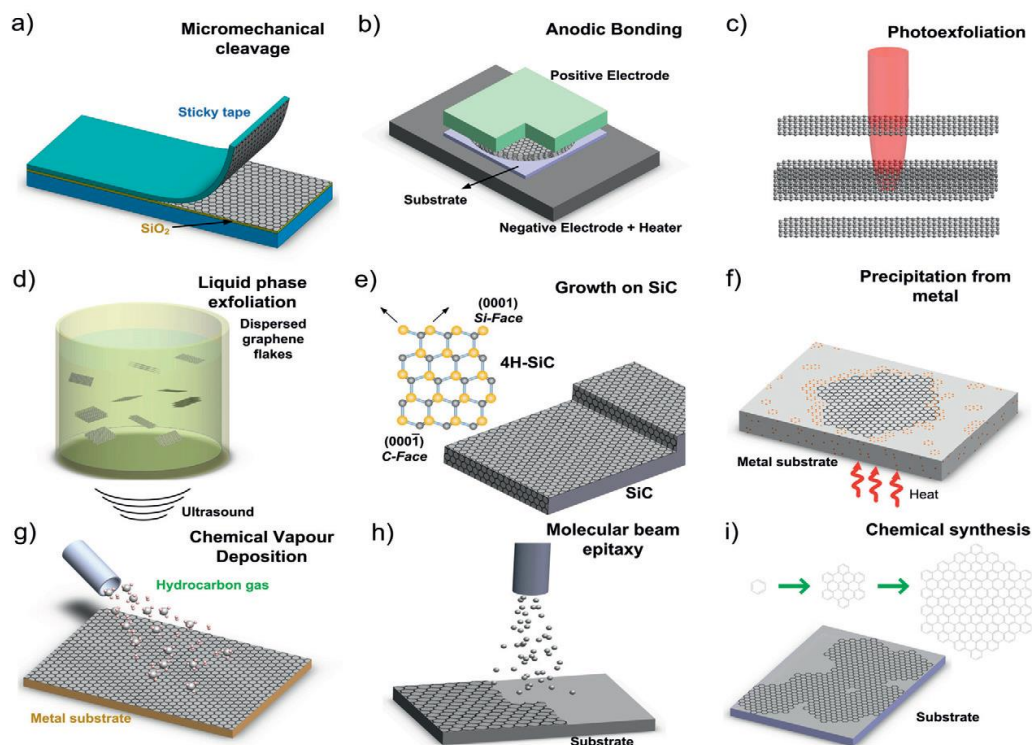


Figure 12. Summary of the top-down and bottom-up strategies for the preparation of graphene; a) Micromechanical cleavage; b) Anodic Bonding; c) Photoexfoliation; d) Liquid phase exfoliation (LPE); e) Growth on SiC; f) Precipitation from metal; g) Chemical vapour deposition (CVD); h) Molecular beam epitaxy (MBE); i) Chemical synthesis.³⁹

1.1.3.1. Top-down strategies

- *Micromechanical cleavage (MC)*: based on the repeated peeling of graphite by using a sticky tape. It has been used by crystallographers for decades and allows the isolation of few layers thick graphene flakes and even single layer graphene (SLG) flakes. This methodology was followed by K. S. Novoselov, A. K. Geim and co-workers in 2004 when they reported the isolation of graphene from highly oriented pyrolyzed graphite for the first time.⁹ The micromechanical cleavage is impractical for large scale applications, however the vast majority of basic research are developed on MC obtained graphene flakes (Figure 12a).

- *Anodic bonding (AB)*: the preparation of SLG by AB is based on pressing graphene onto a glass substrate followed by the application of a high voltage of few kVs (0.5 – 2 kV) between the graphite and a metal back contact. The glass substrate is heated at *ca.* 200°C for 10 – 20 minutes,

then if a positive voltage is applied to the top contact, a negative charge accumulates in the glass side facing the positive electrode. A few layers of graphite, including SLGs, stick to the glass by electrostatic interaction and can then be cleaved off (Figure 12b).⁴⁰

- *Laser ablation and photoexfoliation*: laser pulses can be used to exfoliate graphite flakes. The number of layers obtained can be modified by tuning the laser energy density. This methodology is still underexplored and needs further development since the process is only affordable on inert or vacuum conditions (Figure 12c).⁴¹

- *Liquid-phase-exfoliation (LPE)*: graphite can also be exfoliated in liquid environments exploiting ultrasounds to extract individual layers. The LPE process generally involves three steps: i) dispersion of graphite in a solvent; ii) exfoliation; iii) purification. The third step is necessary to separate exfoliated from un-exfoliated flakes, and is usually carried out via ultracentrifugation (Figure 12d).⁴²

- *Growth on SiC*: graphene can be growth on 4H-SiC or 6H-SiC (different SiC polytypes). This methodology is usually referred as “epitaxial growth” even though there is a very large lattice mismatch between SiC (3.073 Å) and graphene (2.46 Å). The carbon atoms rearrange themselves in a hexagonal structure as Si evaporates from the SiC substrate at high temperatures (>1000°C, Figure 12e).⁴³

1.1.3.2. Bottom-up strategies

- *Growth on metals by precipitation*: as for iron during the formation of steel, metals can dissolve small amounts of carbon into their structures. A supersaturated solution of a metal with carbon can produce the precipitation of this excess of carbon into metal surface forming graphite or graphene. To that end, the use of non-carbide forming metals *e.g.* Cu, Ni, Au, Pt or Ir is preferred since other metals form thermally stable carbides that are not ideal for graphite/graphene

⁴⁰ T. Moldt, A. Eckmann, P. Klar, S. V. Morozov, A. A. Zhukov, K. S. Novoselov, C. Casiraghi, *ACS Nano* **2011**, *5*, 7700-7706.

⁴¹ S. Dhar, A. R. Barman, G. X. Ni, X. Wang, X. F. Xu, Y. Zheng, S. Tripathy, Ariando, A. Rusydi, K. P. Loh, M. Rubhausen, A. H. C. Neto, B. Özyilmaz, T. Venkatesan, *AIP Adv.* **2011**, *1*, 022109.

⁴² A. Ciesielski, P. Samori, *Chem. Soc. Rev.* **2014**, *43*, 381-398.

⁴³ K. V. Emtsev, A. Bostwick, K. Horn, J. Jobst, G. L. Kellogg, L. Ley, J. L. McChesney, T. Ohta, S. A. Reshanov, J. Röhrl, E. Rotenberg, A. K. Schmid, D. Waldmann, H. B. Weber, T. Seyller, *Nat. Mater.* **2009**, *8*, 203-207.

1. Background

growth. This methodology requires careful control of metal thickness, temperature, annealing time, cooling rate and metal microstructure (Figure 12f).

- *Chemical vapor deposition (CVD)*: there are many different types of CVD processes depending on the conditions used. The growth mechanism is understood as follows: carbon atoms, after decomposition from hydrocarbons (gaseous precursors are the most commonly used, such as methane, ethylene or acetylene), nucleate on Cu, and the nuclei grow into large domains (Figure 12g). However, when the Cu surface is fully covered, the films become polycrystalline, consisting of numerous grains of graphene. These areas of monocrystalline graphene with various orientations of the crystal lattice are covalently grown together at their boundaries, introducing a particular type of defect into the graphene structure.⁴⁴

- *Molecular beam epitaxy (MBE)*: used to grow graphitic layers from high purity carbon sources on a variety of substrates such as SiC, Al₂O₃, Mica, SiO₂, etc., in the 400-1100°C range. MBE relies on atomic beams of carbon impinging on the substrate. This fact difficult the deposition of carbon on areas where graphene has already grown. Therefore, it is unlikely that MBE can be used to grow SLG of high enough quality to compete with, for example, CVD.

- *Chemical synthesis*: last but not least, graphene fragments can be also chemically synthesized from low molecular weight precursors as polycyclic aromatic hydrocarbons (PAHs). The preparation could be carried out through organic synthesis in solution or on-surface-assisted chemistry. The former has been found as an efficient methodology for the preparation of nanometer-size graphene molecules called nanographenes while the latter has been widely used on the preparation of both nanographenes and GNRs.⁴⁵

⁴⁴ a) S. Bae, H. Kim, Y. Lee, X. Xu, J.-S. Park, Y. Zheng, J. Balakrishnan, T. Lei, H. R. Kim, Y. I. Song, Y.-J. Kim, K. S. Kim, B. Özyilmaz, J.-H. Ahn, B. H. Hong, S. Iijima, *Nat. Nanotechnol.* **2010**, *5*, 574-578; b) J. Plutnar, M. Pumera, Z. Sofer, *J. Mater. Chem. C* **2018**, *6*, 6082-6101.

⁴⁵ L. Chen, Y. Hernandez, X. Feng, K. Müllen, *Angew. Chem. Int. Ed.* **2012**, *51*, 7640-7654.

1.2. Graphene nanoribbons

Graphene can be envisioned as a periodic arrangement of benzene molecules linked themselves by covalent bonds. Benzene is the main building block graphene, but also of polycyclic aromatic hydrocarbons (PAHs), nanographenes, graphene nanoribbons (GNRs) and graphene quantum dots (Figure 13).

PAHs are aromatic hydrocarbons with two or more fused benzene rings (even though benzene-based molecules with the presence of non-hexagonal rings or even heteroatoms are also considered as PAHs) where all the atoms exhibit sp^2 hybridization. As described for graphene, the p_z orbital of each carbon atom is overlapped with his neighbor ones forming alternated double bonds in a conjugated system.

When the number of fused benzene rings increases up to certain number and the length of the molecule exceeds 1 nm (but not more than 5 nm), the resulting compounds can be considered as graphene molecules. Hexa-*peri*-hexabenzocoronene (HBC) is considered as the smallest graphene molecule, consisting on thirteen fused benzene rings. These nanometer size molecules are part of a bigger family of compounds called nanographenes that includes graphene nanoribbons and graphene quantum dots up to 100 nm size.⁴⁵

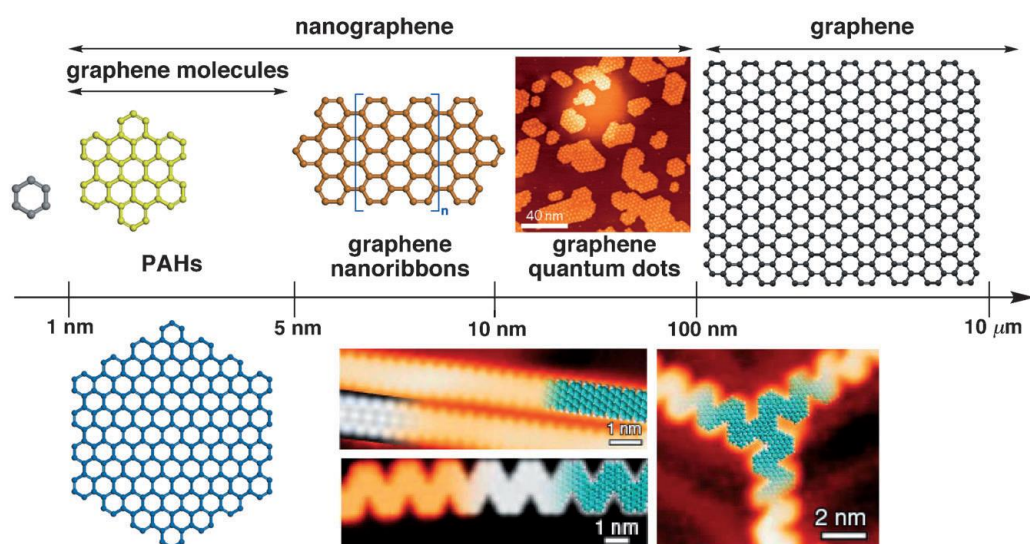


Figure 13. Schematic representation of graphene terminology defined according to their size scale.⁴⁵

1.2.1. General description, structure and properties

GNRs were introduced on section 1.1.1 and are defined as graphene strips with a width of less than 10 nm and with a large aspect ratio (length/width ratio higher than 10).⁴⁵ GNRs can be classified in two types depending on their edge topology; 1) armchair and 2) zigzag (though many others types exist as combination of these two) and are defined with the N number that determines its width (Figure 14). It is fundamental to know the width and the edge topology of the GNRs since, according to theoretical calculations, their electronic properties are directly related to them, including band gaps and charge mobility.³⁷

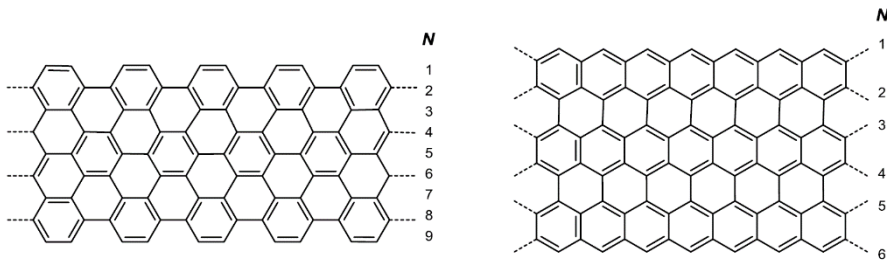


Figure 14. Left: armchair-edged GNR; Right: zigzag-edged GNR. The width of a GNR is defined by N .

Armchair GNRs would exhibit similar properties to non-magnetic semiconductors with relative high band gaps, which increase as the width (N) decreases.⁴⁶ Furthermore, armchair GNRs are predicted to show an extraordinary charge mobility, opening a new route towards ballistic device applications.⁴⁷

Zigzag GNRs are expected to show a metallic character with a zero band gap, with no width relationship. However, previous studies suggest the presence of a finite and width dependent band gap. In contrast to armchair GNRs, zigzag GNRs would show unique magnetic properties for their application in spintronics.⁴⁸

⁴⁶ a) Y.-W. Son, M. L. Cohen, S. G. Louie, *Phys. Rev. Lett.* **2006**, *97*, 216803; b) V. Barone, O. Hod, G. E. Scuseria, *Nano Lett.* **2006**, *6*, 2748-2754.

⁴⁷ D. A. Areshkin, D. Gunlycke, C. T. White, *Nano Lett.* **2007**, *7*, 204-210.

⁴⁸ O. Y. Yazyev, *Rep. Prog. Phys.* **2010**, *73*, 056501.

These properties have been experimentally proven, confirming the band gap theory for armchair GNRs⁴⁹ and the magnetic properties of zigzag GNRs.⁵⁰ Thus, small variations on the width or edge shape would afford a wide variety of GNRs with different properties. For this reason, it is necessary a full control on the final structure in order to ensure the reproducibility of the (opto)electronic and magnetic properties on GNRs.

1.2.2. Preparation of graphene nanoribbons

As described for graphene, the preparation of GNRs can be achieved by two different strategies depending on the starting material. If the chosen starting material is macroscopic, such as graphene or graphite we will describe the methodology as top-down, conversely, if the starting material is composed by low molecular weight building blocks that are subsequently connected by chemical reactions we will use the bottom-up terminology.

1.2.2.1. Top-down strategies

These methodologies are based on the processing (mechanical or chemical) of graphite and other graphitic derivatives such as carbon nanotubes. There are three main top-down methodologies for the preparation of GNRs: i) lithography, or cutting of a graphene/graphite precursor to give rise narrow GNRs; ii) liquid phase exfoliation of graphite via sonication; iii) unzipping of carbon nanotubes.

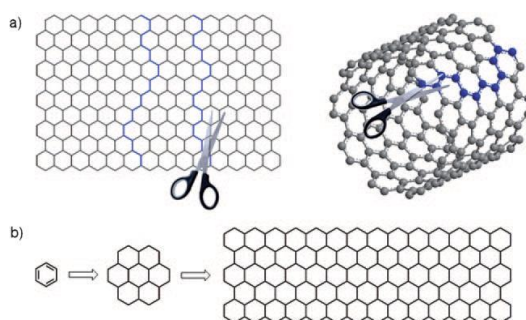


Figure 15. Schematic overview of the a) top-down and b) bottom-up fabrication of GNRs.⁵¹

⁴⁹ N. Merino-Díez, A. García-Lekue, E. Carbonell-Sanromà, J. Li, M. Corso, L. Colazzo, F. Sedona, D. Sanchez-Portal, J. I. Pascual, D. G. de Oteyza, *ACS Nano* **2017**, *11*, 11661-11668.

⁵⁰ G. Z. Magda, X. Jin, I. Hagymási, P. Vancsó, Z. Osváth, P. Nemes-Incze, C. Hwang, L. P. Biró, L. Tapasztó, *Nature* **2014**, *514*, 608-611.

⁵¹ L. Dössel, L. Gherher, X. Feng, K. Müllen, *Angew. Chem. Int. Ed.* **2011**, *50*, 2540-2543.

Lithography is based on the degradation of graphene with oxygen plasma. Graphene deposited over a Si substrate is then protected with Si nanowires before the irradiation with oxygen plasma. The areas that are not protected with Si nanowires are eliminated and only the graphene regions under the Si nanowires remains (acting as a template), obtaining GNRs of different length depending on the length of the used Si nanowire.⁵²

Liquid phase exfoliation of graphite was reported as an efficient way for the preparation of GNRs with less than 10 nm width.¹⁶ The methodology is based on a first exfoliation of graphite under high temperatures (>1000°C) followed by the dispersion of the formed nanoribbons in an organic solvent with the presence of a polymer. Sonication favors the intercalation of the polymer between the GNRs avoiding further self-interactions.

The treatment of carbon nanotubes with highly oxidant reagents or plasma is the third alternative to obtain GNRs. Carbon nanotubes are treated with concentrated sulfuric acid and potassium permanganate at 55 - 70°C or with Ar plasma. In both cases the longitudinal unzipping of carbon nanotubes is produced, obtaining GNRs with functionalized edges.⁵³

Methodologies abovementioned show different crucial drawbacks related to the structure of the resulting GNRs. First, there is no control over the length or width of the resulting GNRs, followed by a non-selectivity on the edge topology and finishing with the observation of undesired functionalization of graphene (*i.e.* when unzipping carbon nanotubes).

1.2.2.2. Bottom-up strategies

Once observed the dramatic structure-property relationships on graphene-related materials, the non-control on the structure of the resulting GNRs involves a huge disadvantage on top-down methodologies. The structural perfection on GNRs is indeed an essential issue, therefore, the chemical synthesis of GNRs has emerged as a reliable method to reproducibly provide GNRs with precise atomic control.⁵⁴ Within the bottom-up strategies for the chemical synthesis of GNRs, two different methodologies can be found: i) on-surface synthesis, and ii) solution synthesis.

⁵² J. Bai, X. Duan, Y. Huang, *Nano Lett.* **2009**, *9*, 2083-2087.

⁵³ D. V. Kosynkin, A. L. Higginbotham, A. Sinitskii, J. R. Lomeda, A. Dimiev, B. K. Price, J. M. Tour, *Nature* **2009**, *458*, 872-877.

⁵⁴ a) A. Narita, X. Feng, K. Müllen, *Chem. Rec.* **2015**, *15*, 295-309; b) A. Narita, Z. Chen, Q. Chen, K. Müllen, *Chem. Sci.* **2019**, *10*, 964-975.

On-surface synthesis

This is a powerful technique for the preparation and the image-tracking of well-defined structures. This methodology is based on the deposition of previously prepared precursors on the surface of a noble metal, such as Au, Ag, Cu, Pt or Ru. These precursors are tailor-made compounds prepared by organic synthesis showing substructures and functionalization at the desired positions for further chemical reactions. Generally, these precursors are sublimated at ultra-high vacuum (UHV) conditions and adsorbed onto the metal surface. The final step is the application of energy, required in order to trigger the desired reactions.⁵⁵

The deposition under UHV conditions (or by CVD at ambient-pressure)⁵⁶ of the synthesized precursors is also a key step on on-surface assisted methodologies. The precursors must be adsorbed on the metal surface, having in mind that the precursors for the on-surface preparation of GNRs are solid polyphenylenes, sublimation at high temperature is mandatory. Thus, labile precursors may suffer decomposition, fragmentation or polymerization. Nowadays, the spray deposition has grown as an alternative for the adsorption of temperature-labile or high sublimation temperature compounds. In this case, a highly diluted solution of the desired precursor is used in order to form a thin film of deposited precursor, avoiding the above-mentioned drawbacks.⁵⁷

As cited before, the last step on the on-surface synthesis is to provide the necessary energy to induce the chemical reaction. The energy is usually thermal, although the catalytic behavior of the metal surface reduces the amount needed to trigger the reaction. Moreover, the required temperature depends directly on what kind of reaction are pursued.

The first report of an on-surface prepared GNR involved the polymerization of a carefully designed molecule that determined the width of the GNR. In that case, 10,10'-dibromo-9,9'-bianthryl (DBBA) was subsequently dehalogenated and polymerized via Ullman coupling. Dehalogenation takes place at 200°C, enough energy to form a biradical intermediate and to

⁵⁵ a) J. Méndez, M. F. López, J. A. Martín-Gago, *Chem. Soc. Rev.* **2011**, *40*, 4578-4590; b) P. H. Jacobse, M.-E. Moret, R. J. M. K. Gebbink, I. Swart, *Synlett* **2017**, *28*, 2509-2516.

⁵⁶ Z. Chen, W. Zhang, C. A. Palma, A. L. Rizzini, B. Liu, A. Abbas, N. Richter, L. Martini, X.-Y. Wang, N. Cavani, H. Lu, N. Mishra, C. Coletti, R. Berger, F. Klappenberger, M. Kläui, A. Candini, M. Affronte, C. Zhou, V. De Renzi, U. del Pennino, J. V. Barth, H. J. Räder, A. Narita, X. Feng, K. Müllen, *J. Am. Chem. Soc.* **2016**, *138*, 15488-15496.

⁵⁷ Z. Chen, R. Berger, K. Müllen, A. Narita, *Chem. Lett.* **2017**, *46*, 1476-1478.

1. Background

favor the diffusion over the metal surface to link the monomers. After the first polymerization reaction, a cyclodehydrogenation reaction was carried out at higher temperature (400°C) to give rise a well-defined armchair GNR with $N = 7$ whose structure was confirmed in terms of STM images (Figure 16a, compound 3). Not only linear armchair-edged GNRs are reported on this work, also chevron-type GNRs were reported following the same methodology, just changing the monomer for a hexaphenylbenzene derivative (Figure 16b).⁵⁸

After the first report, a number of research groups successfully replicated the on-surface synthesis of GNRs, based on the combination of Ullman coupling and cyclodehydrogenation reactions, developing novel designs with different widths as well as cove-edge, zigzag⁵⁹ (Figure 16c) or heteroatom-doped GNRs (Figure 16).⁶⁰

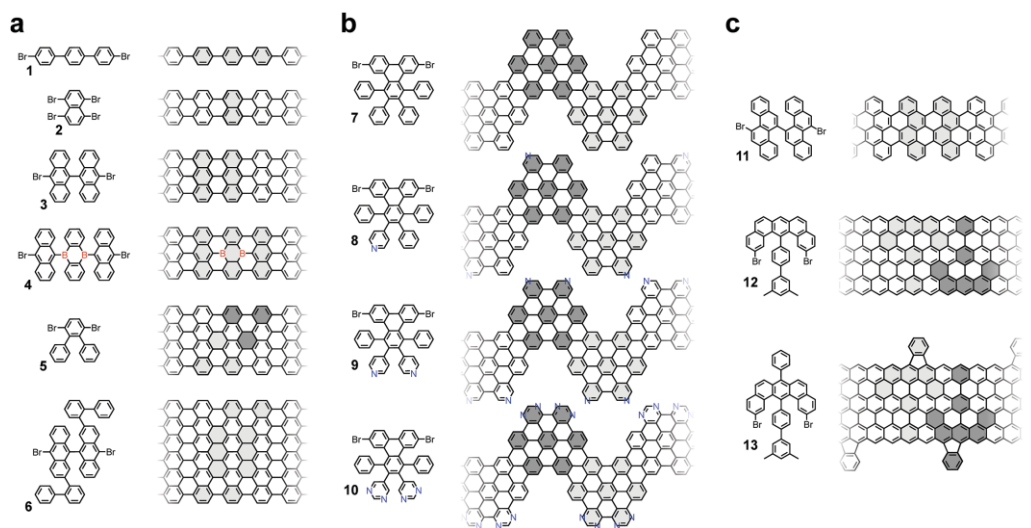


Figure 16. Selected examples of molecular precursors for the on-surface synthesis and their corresponding GNRs.⁶⁰

Despite the success of the Ullmann coupling for the on-surface synthesis of GNRs, other strategies are being actively explored including Glaser coupling, Bergman coupling as well as cycloaddition and cyclotrimerization reactions. Simultaneously, new image tracking techniques

⁵⁸ J. Cai, P. Ruffieux, R. Jaafar, M. Bieri, T. Braun, S. Blankenburg, M. Muoth, A. P. Seitsonen, M. Saleh, X. Feng, K. Müllen, R. Fasel, *Nature* **2010**, *466*, 470-473.

⁵⁹ P. Ruffieux, S. Wang, B. Yang, C. Sánchez-Sánchez, J. Liu, T. Dienel, L. Talirz, P. Shinde, C. A. Pignedoli, D. Passerone, T. Dumslaff, X. Feng, K. Müllen, R. Fasel, *Nature* **2016**, *531*, 489-492.

⁶⁰ L. Talirz, P. Ruffieux, R. Fasel, *Adv. Mater.* **2016**, *28*, 6222-6231.

are also being applied to this methodology. Originally, STM was the most used scanning probe technique, in contrast, noncontact AFM techniques have emerged as a powerful tool for imaging the chemical structure of molecules with atomic resolution.^{55b}

Moreover, computational studies are basic on the study of reaction mechanisms on metal surfaces,⁶¹ the comparison between models and experimental images and the study of the electronic structure.⁵⁹ However, the cornerstone on the preparation of GNRs is the shape of the monomer. The organic synthesis in solution of tailor made PAHs leads to different functionalized precursors that govern the final widths, edge topologies, doping or polymerization reaction.

Solution synthesis

On the other hand, it has recently been probed that solution synthesis of GNRs is indeed possible. Solution synthesis can be scaled up to gram scale and are able to produce GNRs that are longer than 100 nm and dispersible in organic solvents for their characterization and processing in liquid phase. Different edge topologies can be achieved depending on the structure of the monomers used.^{54, 62}

The first attempt to synthesize GNRs in solution dates back to 1970, when J. K. Stille and co-workers reported a fully conjugated bidimensional polymer containing both hexagonal and pentagonal rings.⁶³ This work was completed in 1994 by A. D. Schlüter and co-workers, who introduced flexible alkyl loops to fully characterize the structures by means of NMR, UV-vis and elemental analysis.⁶⁴ During the next decade many attempts to form well defined GNRs were reported based on Diels-Alder reactions, however mixtures of different structural isomers were obtained.

It was more than ten years ago, when researchers focused again on the solution synthesis of GNRs. In the modern synthetic pathways, polymerization step involves cross-coupling reactions (A₂B₂-type, such as palladium-catalyzed Suzuki reactions), nickel-catalyzed AA-type Yamamoto coupling or AB-type Diels-Alder reaction. In all cases, a final Scholl reaction is required in order to

⁶¹ J. Björk, F. Hanke, S. Stafström, *J. Am. Chem. Soc.* **2013**, *135*, 5768-5775.

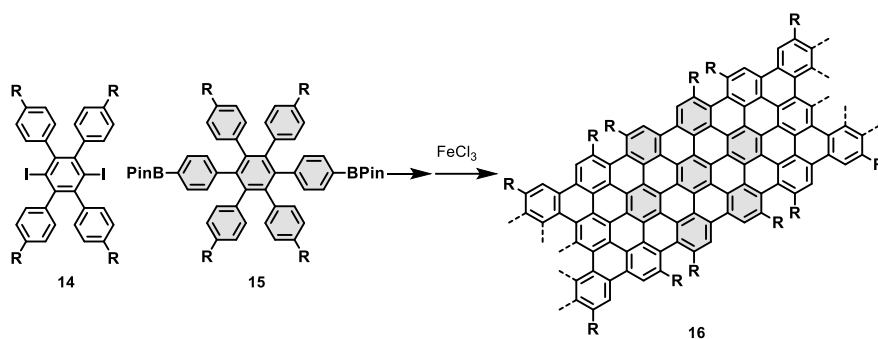
⁶² A. Narita, X.-Y. Wang, X. Feng, K. Müllen, *Chem. Soc. Rev.* **2015**, *44*, 6616-6643.

⁶³ J. K. Stille, G. K. Noren, L. Green, *J. Polym Sci., Part A-1: Polym. Chem.* **1970**, *8*, 2245-2254.

⁶⁴ A. D. Schlüter, M. Löffler, V. Enkelmann, *Nature* **1994**, *368*, 831-834.

form the final fully aromatic structure from polyphenylene precursors. Below, the main polymerization strategies are briefly discussed:

A₂B₂-type polymerization Suzuki reaction was employed firstly in 2008 when K. Müllen and co-workers reported the synthesis of a *N* = 9 armchair GNR by the polymerization of two different kinds of monomers by Suzuki cross coupling reaction: 1,4-diiodo-2,3,5,6-tetraphenylbenzene (**14**) and the *bis*-boronic-ester derivative of the hexaphenylbenzene (**15**) bearing bulky alkyl chains at the peripheral positions. A final intramolecular Scholl reaction leads to the desired GNRs with lengths up to 12 nm (**16**).⁶⁵



Scheme 1. Synthesis of GNR **16**.

The coupled monomers were pointed as a disadvantage on the polymerization step due to the steric hindrance between them and the low flexibility of the final polymer. Thus, the same authors decided to use a more flexible polymer based on the Suzuki coupling of *o*-dibromobenzene (**17**) derivatives and benzene-1,4-diboronic ester (**18**) (Scheme 2). In this case, longer polymer chains of about 25 nm were detected after size exclusion chromatography.⁶⁶ In 2013, Jo and co-workers prepared extended derivatives of **20** by using naphthalene diboronic ester (**21**) and anthracene diboronic ester (**24**) instead of benzene-1,4-diboronic ester (**18**).⁶⁷ Moreover the same authors reported the preparation of N-doped GNRs with the same geometry of those prepared by using **17** as precursor, in this case 2,3-dibromo-5,6-*bis*-dodecyloxy-pyrazine (**27**) was used. By changing the mixing ratio between **27** and **17**, GNRs with different degrees of

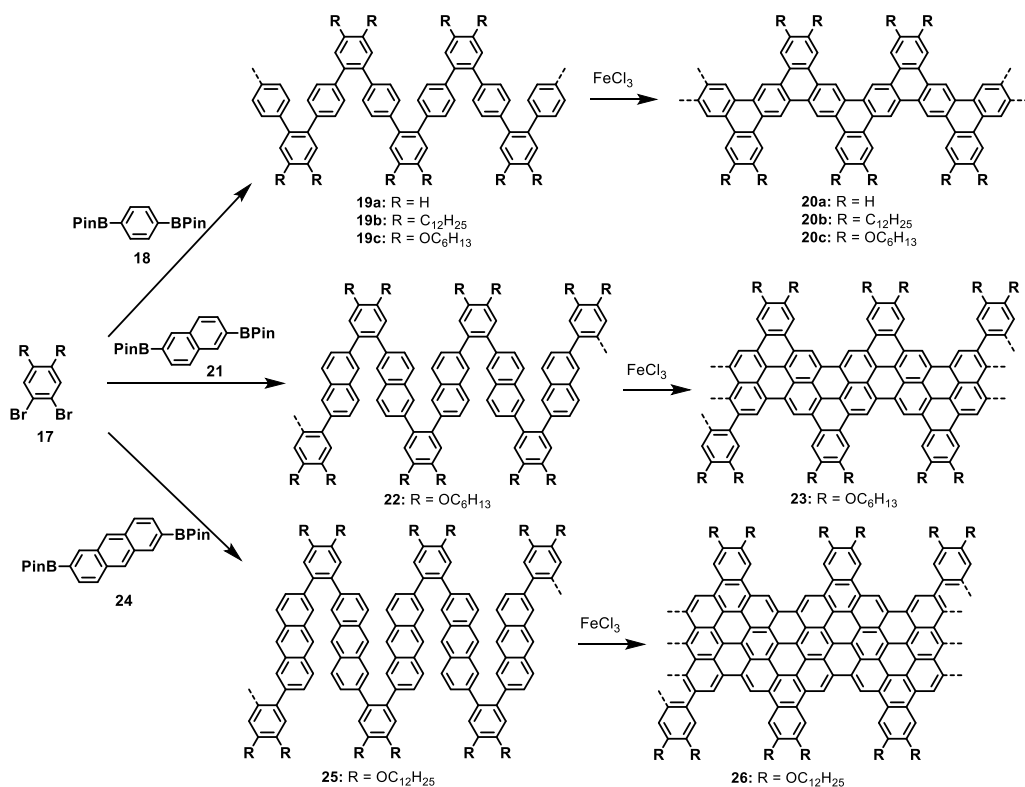
⁶⁵ X. Yang, X. Dou, A. Rouhanipour, L. Zhi, H. J. Räder, K. Müllen, *J. Am. Chem. Soc.* **2008**, *130*, 4216-4217.

⁶⁶ L. Dössel, L. Gherghel, X. Feng, K. Müllen, *Angew. Chem. Int. Ed.* **2011**, *50*, 2540-2543.

⁶⁷ K. T. Kim, J. W. Jung, W. H. Jo, *Carbon* **2013**, *63*, 202-209.

N-doping can be obtained (Scheme 3). N-doped GNRs exhibit reduced hole mobility and increased electron mobility.⁶⁸

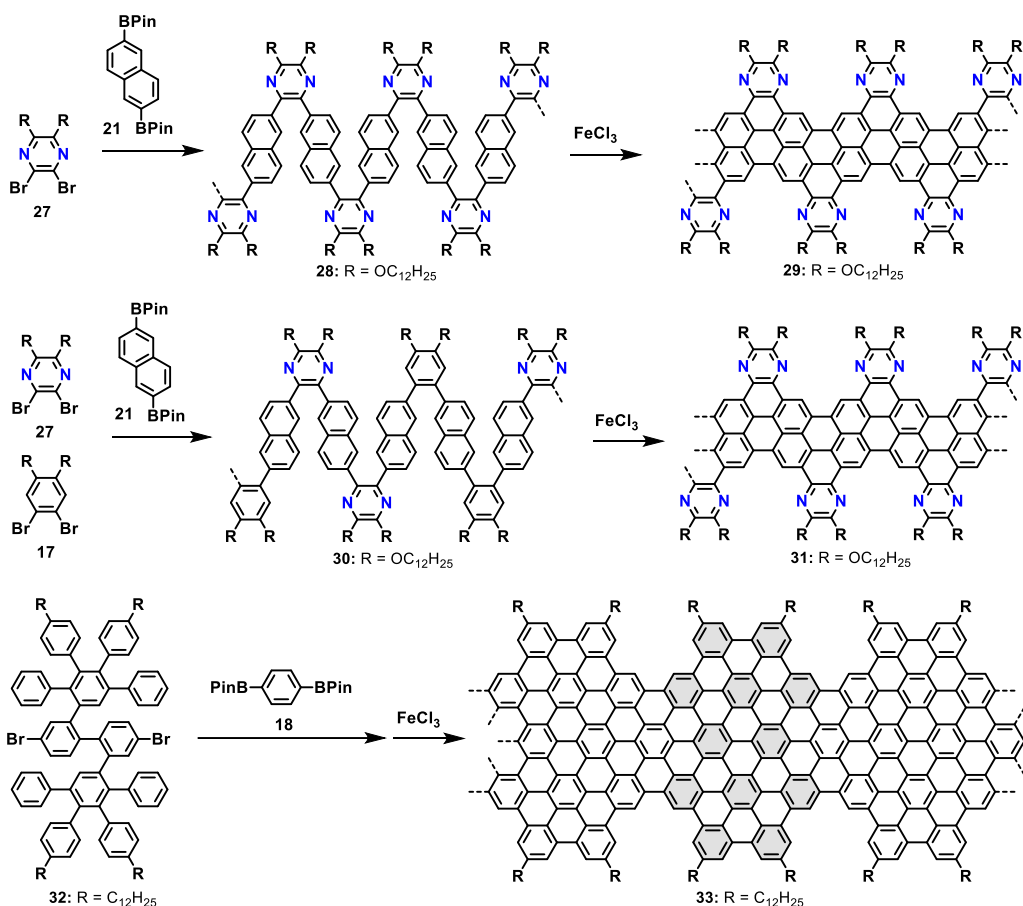
Finally, the last example of GNRs prepared by A₂B₂ polymerization type was the necklace-type GNR reported by K. Müllen and co-workers. This GNR was prepared from the 4,4'-dibromobiphenyl-based precursor **32** and benzene-1,4-diboronic ester **18** (Scheme 3). The final length of the reported GNR was about 13 nm.⁶⁹



Scheme 2. Synthesis of GNRs **20**, **23** and **26**.

⁶⁸ K. T. Kim, J. W. Lee, W. H. Jo, *Macromol. Chem. Phys.* **2013**, *214*, 2768-2773.

⁶⁹ M. G. Schwab, A. Narita, S. Osella, Y. Hu, A. Maghsoumi, A. Mavrinsky, W. Pisula, C. Castiglioni, M. Tommasini, D. Beljonne, X. Feng, K. Müllen, *Chem. Asian J.* **2015**, *10*, 2134-2138.

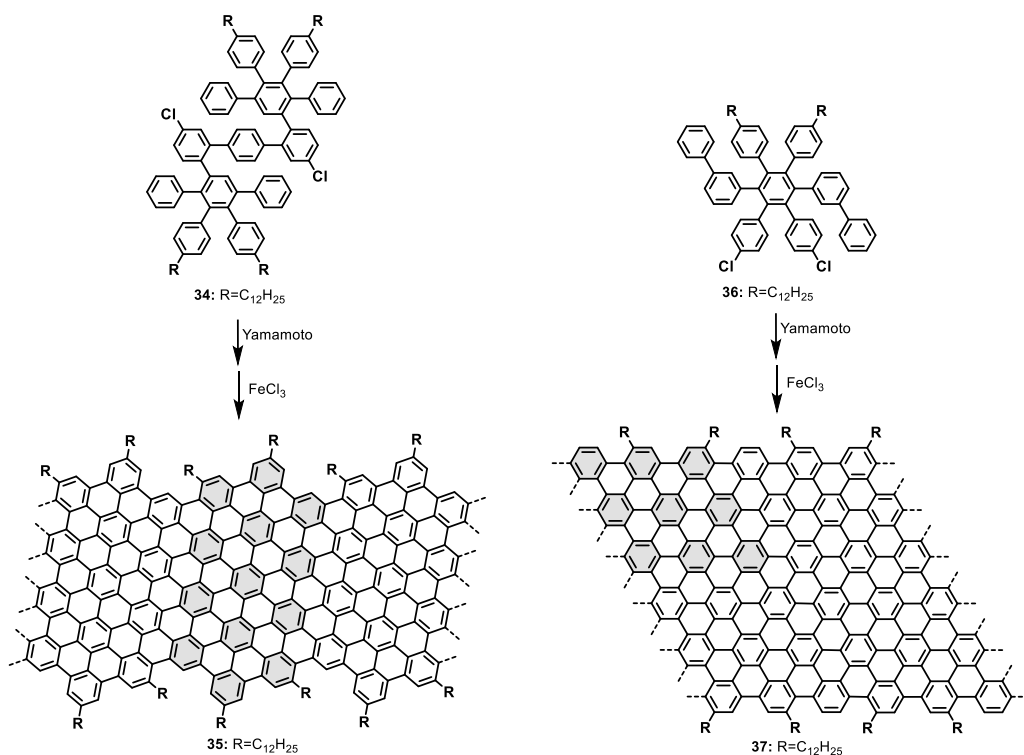


Scheme 3. Synthesis of GNRs 29, 31 and 33.

AA-type Yamamoto polymerization was reported as an alternative for A₂B₂-type Suzuki coupling since the former is based on the use of only one type of monomer, while the latter have a polymerization step directly dependent on the monomers ratio. Thus, small changes on the stoichiometry of monomers lead to an inefficient polymerization step and lowering the length of the final GNR. Yamamoto polymerization was considered to be more advantageous because this method requires only one dihalogenated monomer and is thus free of the ratio problem. Moreover, Yamamoto coupling is also known for being highly efficient in sterically hindered substrates, remarkable fact on the preparation of GNR precursors.

The laterally extended GNR **35** was synthesized through the AA-type Yamamoto polymerization of dichlorinated monomer **34** (Scheme 4). The final GNR exhibits an estimated width of 1.54 – 1.98 nm and an optical bandgap of 1.1 eV with broad absorption into the near-infrared region.⁷⁰

In a next step for the preparation of wider GNRs, the same methodology was applied obtaining GNR **37**. GNR **37** is an armchair-edged GNR possessing an estimated width of 2.1 nm, corresponding to $N = 18$. In this example, the arrangement of the monomer during the polymerization reaction plays a key role, and the resulting GNR shows twice the width of the monomer. The optical bandgap of **37** was found to be approximately 1.6 eV.⁷¹

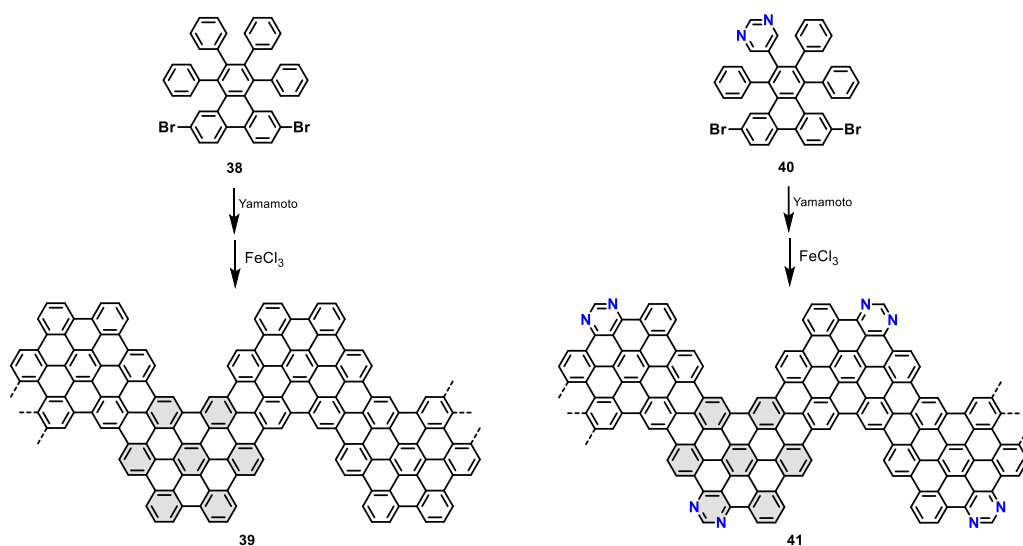


Scheme 4. Synthesis of GNRs **35** and **37**.

⁷⁰ M. G. Schwab, A. Narita, Y. Hernandez, T. Balandina, K. S. Mali, S. De Feyter, X. Feng, K. Müllen, *J. Am. Chem. Soc.* **2012**, *134*, 18169-18172.

⁷¹ M. El Gemayel, A. Narita, L. F. Dössel, R. S. Sundaram, A. Kiersnowski, W. Pisula, M. R. Hansen, A. C. Ferrari, E. Orgiu, X. Feng, K. Müllen, P. Samori, *Nanoscale* **2014**, *6*, 6301-6314.

Chevron-type GNRs have been reported to be prepared not only by on surface assisted synthesis, but also by in solution synthesis. Efficient methodologies for the solution synthesis of both non-doped and N-doped chevron type GNRs can be found on literature. Their structures were confirmed by means of STM analysis, revealing a defined structure for GNRs **39** and **41** (Scheme 5). Regarding their electronic properties, both chevron type GNRs exhibit similar bandgap of approximately 1.6 eV derived from its UV-Vis absorption spectrum.⁷² Extended chevron-type GNRs prepared by the same methodology have been recently reported, exhibiting improved electrical conductivity and application on gas sensing.⁷³



Scheme 5. Synthesis of chevron-type GNR **39** and **41** by AA-type Yamamoto coupling and subsequent cyclodehydrogenation reaction.

AB-type Diels-Alder polymerization reaction is the third methodology used for the preparation of well-defined GNRs in solution. It represents an advantage in comparison with the previously cited methodologies since the Diels-Alder reaction is not subordinated to the use of expensive catalysts. AB-type Diels-Alder polymerization involves the head-tail reaction of particular

⁷² T. H. Vo, M. Shekhirev, D. A. Kunkel, M. D. Morton, E. Berglund, L. Kong, P. M. Wilson, P. A. Dowben, A. Enders, A. Sinitskii, *Nat. Commun.* **2014**, *5*, 3189.

⁷³ M. M. Pour, A. Lashkov, A. Radocea, X. Liu, T. Sun, A. Lipatov, R. A. Korlacki, M. Shekhirev, N. R. Aluru, J. W. Lyding, V. Sysoev, A. Sinitskii, *Nat. Commun.* **2017**, *8*, 820.

monomers, in particular, cyclopentadienone derivatives have been widely used for the preparation of GNR with different widths.

By using tetraphenylcyclopentadienone derivatives as the diene (head) and an ethynyl group as the dienophile (tail), the polymerization reaction takes place simply by heating in a diphenyl ether solution in the absence of any catalyst or reagent, giving polyphenylene precursors of $>600,000 \text{ g}\cdot\text{mol}^{-1}$. Subsequent cyclodehydrogenation led to GNRs with gulf-type edges.

The first example of a GNR prepared under this methodology was reported in 2014 by K. Müllen and co-workers (Scheme 6).⁷⁴ The prepared gulf-edged GNR (**44a**), alternating $N = 12$ and $N = 8$, was found to be long enough ($>200 \text{ nm}$) for their electronic applications. Despite its large size, the resulting GNR was processable on liquid phase, being possible to evaluate its optical band gap as 1.88 eV . The width of the prepared GNRs by the AB-type Diels-Alder polymerization is only dependent on the monomer size. Therefore, if additional phenyl rings are added to the monomer (**45a**), a wider gulf-edged GNR can be obtained with alternating widths of 1.98 and 1.54 nm .⁷⁵

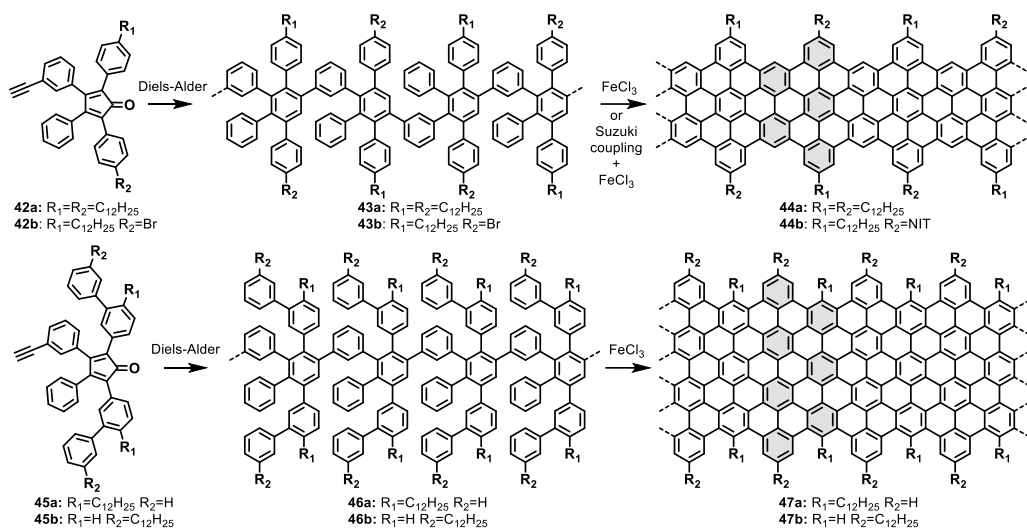
Recently, a general strategy for the edge substitution of GNRs has been developed by using monomers bearing both long alkyl chains and bromine groups (**42b**).⁷⁶ The functionalization takes place after the polymerization step via Suzuki cross coupling reactions. A handful of GNRs derivatives have been prepared modifying the properties of the resulting GNRs, in this sense, magnetic properties can arise from the introduction of nitronyl-nitroxide (NIT) radical groups (**44b**), introducing magnetic edge states beyond zigzag-edged GNRs.⁷⁷

⁷⁴ A. Narita, X. Feng, Y. Hernandez, S. A. Jensen, M. Bonn, H. Yang, I. A. Verzhbitskiy, C. Casiraghi, M. R. Hansen, A. H. R. Koch, G. Fytas, O. Ivasenko, B. Li, K. S. Mali, T. Balandina, S. Mahesh, S. De Feyter, K. Müllen, *Nat. Commun.* **2014**, *6*, 126-132.

⁷⁵ A. Narita, I. A. Verzhbitskiy, W. Frederickx, K. S. Mali, S. A. Jensen, M. R. Hansen, M. Bonn, S. De Feyter, C. Casiraghi, X. Feng, K. Müllen, *ACS Nano* **2014**, *8*, 11622-11630.

⁷⁶ A. Keerthi, B. Radha, D. Rizzo, H. Lu, V. D. Cabanes, I. C.-Y. Hou, D. Beljonne, J. Cornil, C. Casiraghi, M. Baumgarten, K. Müllen, A. Narita, *J. Am. Chem. Soc.* **2017**, *139*, 16454-16457.

⁷⁷ M. Slota, A. Keerthi, W. K. Myers, E. Tretyakov, M. Baumgarten, A. Ardavan, H. Sadeghi, C. J. Lambert, A. Narita, K. Müllen, L. Bogani, *Nature* **2018**, *557*, 691-695.



Scheme 6. Synthesis of gulf-edged GNRs **44** and **47** by AB-type Diels-Alder polymerization and subsequent cyclodehydrogenation reaction.

In addition, two different kinds of monomers can be prepared depending on the location of the long alkyl chains. The introduction of long chains at the inside part of the gulf edge led to a distortion of the resulting GNR which exhibits lower band gap⁷⁸ than those with the alkyl chains on the outer part of the gulf.⁷⁹

In summary, solution-phase synthesis of GNRs has received considerable attention owing to its high potential of controlling width and edge structures of GNRs, especially with respect to top-down strategies. Despite the benefits of solution synthesis, the short length and the lack of orientation control are still considered as the main disadvantages. Thus, new methodologies have emerged to solve these inconveniences,⁸⁰ such as the recently coined APEX methodology developed by K. Itami and co-workers,⁸¹ previously used on the preparation of nanographenes.

⁷⁸ Y. Hu, P. Xie, M. De Corato, A. Ruini, S. Zhao, F. Megendorfer, L. A. Straasø, L. Rondin, P. Simon, J. Li, J. J. Finley, M. R. Hansen, J.-S. Lauret, E. Molinari, X. Feng, J. V. Barth, C.-A. Palma, D. Prezzi, K. Müllen, A. Narita, *J. Am. Chem. Soc.* **2018**, *140*, 7803-7809.

⁷⁹ I. Ivanov, Y. Hu, S. Osella, U. Beser, H. I. Wang, D. Beljonne, A. Narita, K. Müllen, D. Turchinovich, M. Bonn, *J. Am. Chem. Soc.* **2017**, *139*, 7982-7988.

⁸⁰ A. Jolly, D. Miao, M. Daigle, J.-F. Morin, *Angew. Chem. Int. Ed.* **2019**, *58*, 2-12.

⁸¹ Y. Yano, N. Mitoma, K. Matsushima, F. Wang, K. Matsui, A. Takakura, Y. Miyauchi, H. Ito, K. Itami, *Nature* **2019**, *571*, 387-391.

1.3. Nanographenes

1.3.1. Structure, synthesis and properties

Nanographenes are defined as nanometer-size well-defined PAHs with a size between 1 and 100 nm according to the classification made by K. Müllen and co-workers.⁴⁵ Thus PAHs, consisting of sp^2 carbon frameworks can be regarded as the smallest possible graphene molecules with a size between 1 and 5 nm (see Figure 13). Therefore, they can serve as a model system for graphene studies and recent studies suggest their great potential in future applications, such as in nanoelectronics, optoelectronics and spintronics.

On section 1.1.1. (Figure 5) the different edge topologies on graphene were introduced. Thus, as model graphene molecules, the same nomenclature is applied for nanographenes and PAHs. Edge topology and properties are also linked on nanographenes and PAHs, finding that armchair-type PAHs are more stable than zigzag-type ones. On the other hand, cove and fjord topologies are characterized for inducing an out-of-plane distortion. Remarkably, fjord regions can be envisioned as helicenes, where the steric hindrance cause the twist.

Stability on PAHs plays a key role on their preparation and applicability. This can be explained by the Clar's sextet rule, where π -electrons on a hexagonal ring form groups of six known as Clar's sextets, this group of delocalized electrons can be drawn as a circle into the hexagonal ring. Therefore, expanded PAHs could be drawn with a different number of Clar's sextets, where the structure with more sextets would be the most stable one. This fact is not only perceptible on stability, but also in reactivity where it would be possible to predict reaction products.

Regarding their synthesis, as for graphene or graphene nanoribbons, nanographenes can be also prepared following two different methodologies (top-down or bottom-up). A handful of top-down strategies have been reported since 2001 when the preparation of a single nanographene was prepared by a combination of electrophoretic deposition and heat-treatment of diamond nanoparticles.⁸²

⁸² A. M. Affoune, B. L. V. Prasad, H. Sato, T. Enoki, Y. Kaburagi, Y. Hishiyama, *Chem. Phys. Lett.* **2001**, *348*, 17-20.

These methodologies are characterized by the lack of size control and the difficult functionalization of the resulting structure. Therefore, bottom-up chemical synthesis emerged as the main tool for the tailor-made preparation of graphene molecules. A wide spectrum of well-defined nanographenes have been prepared during the last decades, being possible to draw a direct relationship between their structure and their properties.

The chemistry of nanographenes experimented a tremendous progress since the first experimental demonstration of graphene. Although the laboratory synthesis of nanographenes dates back to the beginning of the last century, new methodologies for the preparation of nanographenes have emerged in order to improve their efficiency or to overcome new challenges.

Thus, new nanographenes with novel geometries have emerged during the last years exhibiting new structural features, such as non-hexagonal rings or helicenes, and bringing new properties to an old family of compounds.

1.3.1.1. Nanographene synthesis by Diels-Alder/cyclotrimerization and Scholl reactions

Different methods have been reported for the preparation of well-defined nanographenes. Among them, Scholl and Kovacic-type reactions, based on the use of Lewis acid-oxidant combinations as reagents for intramolecular cyclodehydrogenation, are used as a key step for the aromatization of different precursors. Besides, a wide spectrum of chemical reactions have been reported for the preparation of different precursors.

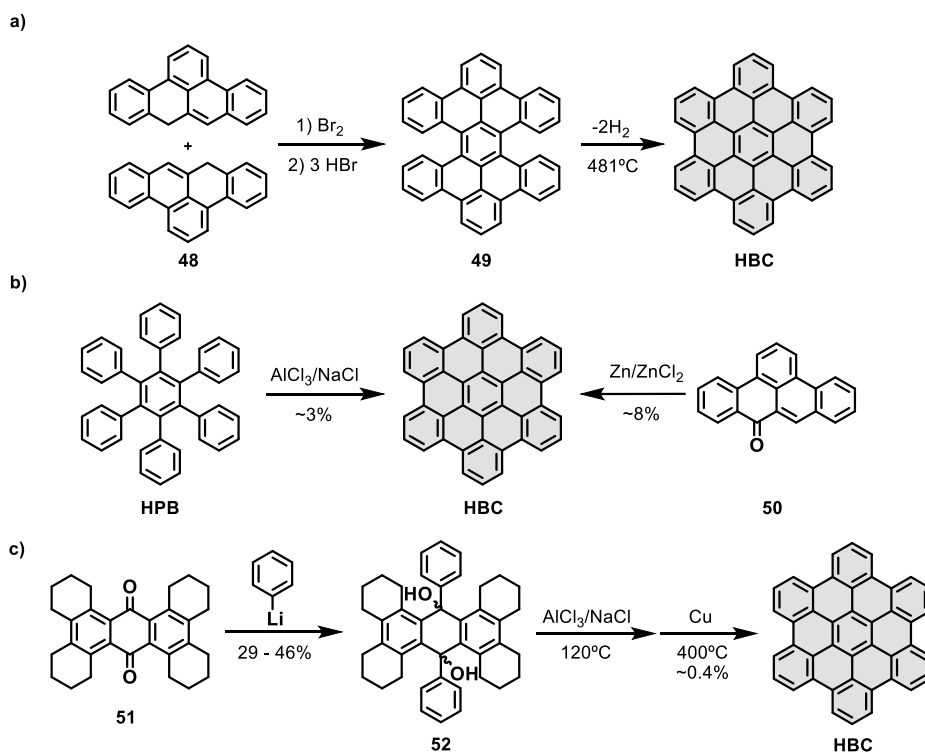
Hexa-*peri*-hexabenzocoronene (HBC), with 42 conjugated sp² carbon atoms in a planar disposition can be envisioned as the smallest nanographene. HBC is based on fused benzene rings arranged in a hexagonal shape of *ca.* 1.4 nm width and it can be regarded as the main building block in the preparation of larger graphene molecules. The synthesis of HBC dates back to the beginning of the last century, and its synthesis have been improved over the years.

The first synthesis of HBC was reported by E. Clar and co-workers in 1958.⁸³ Later, Halleux, Schmidt and co-workers described alternative methods toward HBC. Clar's methodology was based on the bromitaion of 2:3-7:8-dibenzo-*peri*-naphthene (**48**) in benzene, where the resulting

⁸³ a) E. Clar, C. T. Ironside, *Proc. Chem. Soc.* **1958**, 150; b) E. Clar, C. T. Ironside, *J. Chem. Soc.* **1959**, 142.

brown precipitate was heated at 153°C to form tetrabenzoperopyrene (**49**). A final heating at 481°C led to HBC as a pale yellow solid (Scheme 7a).

Halleux and co-workers reported the synthesis of HBC through two different methods: i) the cyclodehydrogenation of hexaphenylbenzene (HPB) by treatment with AlCl_3 and NaCl and ii) the reaction of dibenzo-1,9;2,3-anthrone (**50**) with Zn/ZnCl_2 (Scheme 7b).⁸⁴ In 1986, W. Schmidt and co-workers reported a new synthesis of HBC. As depicted in Scheme 7c, reaction of the quinone **51** with phenyllithium give rise the diol **52** in 29-46% yield. **52** was subsequently cyclized in melt $\text{AlCl}_3/\text{NaCl}$ and then subjected to aromatization with Cu at 400°C affording HBC in 0.4% (Scheme 7c).⁸⁵



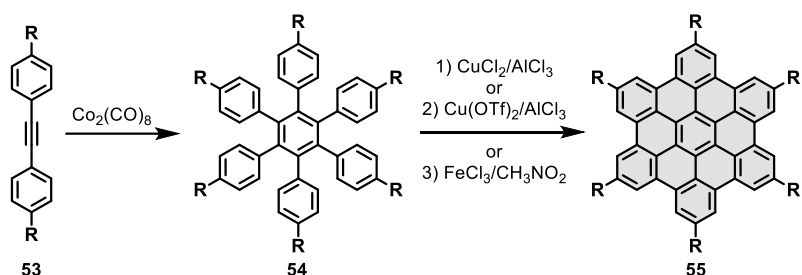
Scheme 7. First reported methodologies for the synthesis of HBC.

⁸⁴ A. Halleux, R. H. Martin, G. S. D. King, *Helv. Chim. Acta* **1958**, *41*, 1177-1183

⁸⁵ W. Hendel, Z. H. Khan, W. Schmidt, *Tetrahedron* **1986**, *42*, 1127-1134.

Alkyne cyclotrimerization reaction – a first approach

An efficient way to prepare HBC and related structures by Scholl-type oxidative cyclodehydrogenation of branched oligophenylenes was reported by K. Müllen and co-workers in 1998 (Scheme 8). The employment of Cu(II) salts such as CuCl_2 or $\text{Cu}(\text{OTf})_2$ catalyzed by AlCl_3 is reported as well as weaker Lewis acid such as FeCl_3 . The preparation of hexaphenylbenzene precursors (**54**) can be achieved by $\text{Co}_2(\text{CO})_8$ -catalyzed alkyne cyclotrimerization of different functionalized diphenylacetylenes. Final cyclodehydrogenation of **54** leads to different functionalized HBCs (Scheme 8).⁸⁶



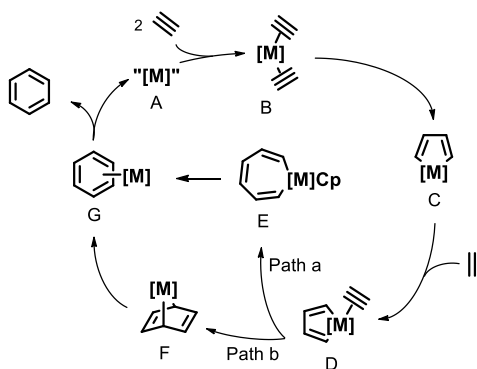
Scheme 8. Alkyne cyclotrimerization methodology for the preparation of HPB precursors.

In this case, the [2+2+2] cycloaddition reaction of alkynes was found as a powerful tool for the synthesis of hexaphenylbenzene derivatives. This pericyclic reaction in which three components, *i.e.* alkynes, contribute with two electrons each is remarkable in terms of synthetic power and scope. However, it is mandatory the use of transition-metal complexes as catalysts, most of them correspond to the late transition metals especially those of group 9 (Co, Rh, Ir). Among all the available catalyst, η^5 -cyclopentadienyl-dicarbonyl cobalt ($\text{CpCo}(\text{CO})_2$) has proved the most popular and versatile reagent for the [2+2+2] cyclotrimerization of alkynes followed by $\text{CpCp}(\text{PPh}_3)_2$. For intermolecular stoichiometric reactions, cobalt carbonyl ($\text{Co}_2(\text{CO})_8$) has also been used. Generally, refluxing conditions in xylenes, toluene or THF in the presence of 5 mol% of $\text{CpCo}(\text{CO})_2$ give good to excellent results. However, some cases require 1 equivalent or even an excess of cobalt complex.

The mechanism of the [2+2+2] cycloaddition is well established and the most important features are shared by the majority of catalytic systems. These mechanistic steps were postulated mainly

⁸⁶ M. Müller, C. Kübel, K. Müllen, *Chem. Eur. J.* **1998**, *4*, 2099-2109.

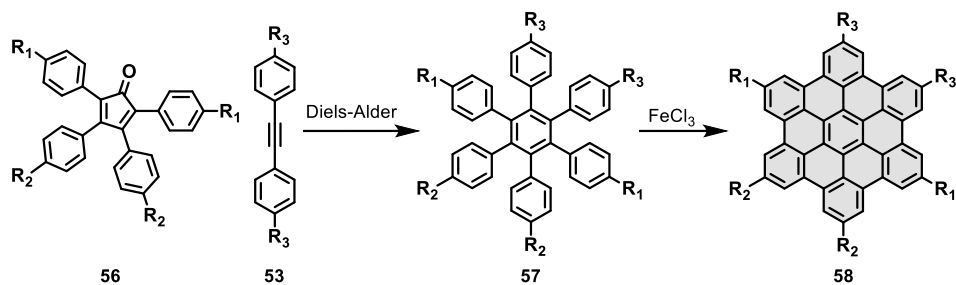
from the isolation of reaction intermediates since experimental results, such as NMR experiments, are difficult to obtain due to the presence of paramagnetic species. On the other hand, computational studies have been a crucial tool to elucidate these mechanism. Thus, a general pathway for Cp-coordinating metals can be proposed (Scheme 9) where, in a first instance, two alkyne partners coordinate to the metal (A) and the resulting complex B forms metallacyclopentadiene C by subsequent oxidative coupling. Then, the third unsaturated partner coordinates to give D, which follows two possible paths: insertion into the M-C bond to give cycloheptametallacycle E, which after reductive elimination gives complex G, or intramolecular [4+2] cycloaddition to form bicyclic complex F, which after isomerization affords complex G. Affording the final cycloadduct after decooordination of the metal (Scheme 9).



Scheme 9. General mechanistic cycle for the metal catalyzed [2+2+2] alkyne cyclotrimerization.

The approaches using this reaction for the preparation of hexaphenylbenzene derivatives lacks regioselectivity of the insertion of the third alkyne and, therefore, on the introduced substituents. To overcome this fact, an alternative for the preparation of HBCs derivatives was introduced. In this case, Diels-Alder cycloadditions between appropriate tetraphenylcyclopentadienone (**56**) derivatives and substituted dephenylacetylenes (**53**) afforded the hexaphenylbenzene derivatives (**57**), which led to the fused HBC after oxidative cyclodehydrogenation with FeCl_3 (Scheme 10).⁸⁶

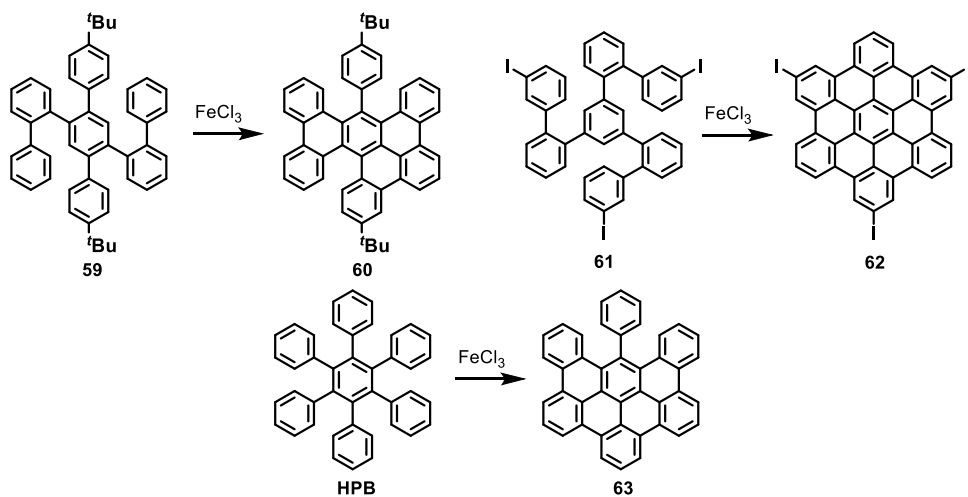
Moreover, the Diels-Alder methodology also allows to introduce both alkyl chains and bromo substituents, and these halogenated positions can be further derivatized creating a wide variety of decorated HBCs. However, the introduced group is limited by its compatibility with the final cyclodehydrogenation step.



Scheme 10. Diels-Alder methodology for the preparation of HPB precursors.

Scholl reaction – the key step

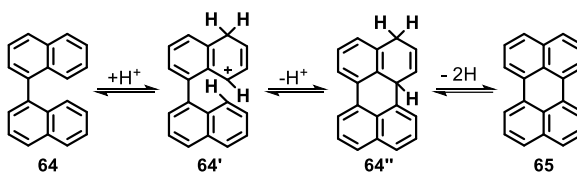
The architectures that theoretically led to HBC are not only reduced to hexaphenylbenzene derivatives. Hence, properly connected benzene rings in a way to undergo cyclodehydrogenation reactions are supposed to form HBC. However, partially fused compounds have been found after treatment with FeCl₃. For example, compound **59** afforded partially ring closing product **60** in good yield, whereas similar triiodinated precursor **61** led to the formation of the corresponding HBC (**62**). This fact suggest an intrinsic relationship between the substituents and the cyclodehydrogenation reaction (Scheme 11). Moreover, when non-functionalized HPB was subjected to Scholl reaction, different stable intermediates were isolated such as compound **63**, suggesting a stepwise cyclization mechanism.



Scheme 11. Precursors and partially fused isolated compounds after Scholl reaction.

There is no a fully accepted mechanism to explain Scholl reaction outcome. Nowadays, researchers around the globe struggle to figure out the mechanism that govern this reaction. However, two different mechanism have been proposed; i) the arenium cation mechanism and ii) the cationic radical mechanism.

The arenium cation mechanism is based on a first protonation of the aromatic compound generating the mentioned arenium cation which is strongly σ -electrophile. This cation can react with a neighbor aromatic ring creating a new carbon-carbon bond, followed by deprotonation. Finally a dehydrogenation step is needed, obtaining the reaction product (Scheme 12).



Scheme 12. Arenium cation proposed mechanism for the Scholl reaction.

Numerous experimental studies support this mechanism, *e.g.* the isolation of an analogous to the intermediate **64''** was described by E. Clar in 1930.⁸⁷ Moreover, some research groups have proposed that Bronsted acids take part as catalysts in the Scholl reaction, finding that traces of HCl or water accelerate the reaction by the formation of $H[AlCl_3OH]$ complexes after its combination with $AlCl_3$.⁸⁸ On the other hand, cyclodehydrogenation reactions may occur over anhydrous HF (non-oxidant acid), conditions where a cation radical could not be formed.⁸⁹ However, the arenium cation intermediate could be formed in the presence of either Lewis or Bronsted acids.

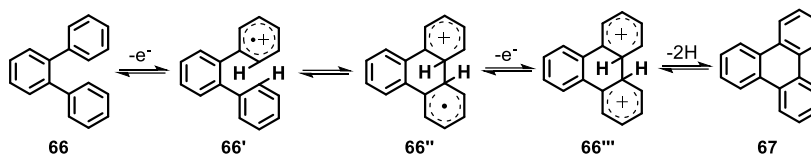
The second suggested mechanism entails the formation of a radical cation after the monoelectronic oxidation of the substrate. Firstly, a radical cation is formed from the starting aromatic compound (**66**) by monoelectronic oxidation. Followed by the formation of a new carbon-carbon bond with a neighbor aromatic ring and subsequent monoelectronic oxidation to

⁸⁷ E. Clar, *Ber. Dtsch. Chem. Ges.* **1930**, 63, 112-120.

⁸⁸ a) G. Baddeley, J. Kenner, *J. Chem. Soc.* **1935**, 303-309; b) G. Baddeley, *J. Chem. Soc.* **1950**, 994-997.

⁸⁹ J. H. Simons, R. E. McArthur, *J. Ind. Eng. Chem.* **1947**, 39, 364-367.

form a dication specie (**66'''**). This double charged specie evolves to the final product (**67**) by losing two hydrogen atoms (Scheme 13).



Scheme 13. Radical cation proposed mechanism for the Scholl reaction.

Functionalization on HBC derivatives – tuning the properties

The introduction of halogen groups in the structure of HBCs opens the door to a further functionalization and expansion of the aromatic backbone. Despite being highly insoluble, iodine and bromine derivatives undergo cross-coupling reactions such as Buchwald-Hartwig, Sonogashira, Suzuki or Kumada reactions.⁹⁰

Thus, a wide variety of decorated HBCs have been prepared during the last years. Although these HBC derivatives exhibit enhanced solubility for their handling, they tend to form stacked structures. In this sense, the group of K. Müllen has studied the formation of highly ordered columnar liquid crystalline phases and their charge transport along the stacking axis, being possible their application on hole transporting materials for organic electronics applications.^{90b,91}

Whereas non-functionalized HBC is planar, the permethoxylated HBC (**68**) is a non-planar nanographene due to the steric hindrance between the substituents at the bay positions (Figure 17). The molecule was prepared by the alkyne cyclotrimerization of the corresponding diphenylacetylene. As depicted in Figure 17, the X-ray structure of **68** reveals that the outer phenyl rings flip up and down in an alternating manner, resulting in a double-concave conformation. Moreover, **68** can act as host for fullerenes or benzene derivatives. The cocrystal obtained after the crystallization of **68** and fullerene revealed a columnar arrangement of alternating fullerene and **68** molecules due to this double-concave conformation.⁹²

⁹⁰ a) J. Wu, M. D. Watson, K. Müllen, *Angew. Chem. Int. Ed.* **2003**, *42*, 5329-5333; b) J. Wu, M. D. Watson, L. Zhang, Z. Wang, K. Müllen, *J. Am. Chem. Soc.* **2004**, *126*, 177-186.

⁹¹ J. Wu, M. Baumgarten, M. G. Debije, J. M. Warman, K. Müllen, *Angew. Chem. Int. Ed.* **2004**, *53*, 5331-5335.

⁹² Z. Wang, F. Dötz, V. Enkelman, K. Müllen, *Angew. Chem. Int. Ed.* **2005**, *44*, 1247-1250.

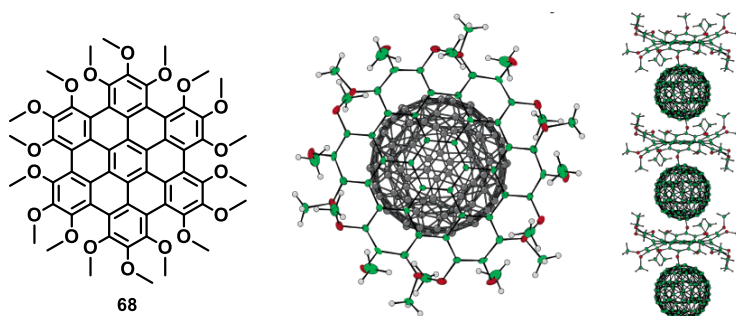


Figure 17. Permethoxylated HBC **68** and its complex with C_{60} .⁹²

More recently, the same group has reported an efficient methodology for the edge perchlorination of parent HBC,⁹³ this methodology was also applied to extended nanographenes and GNRs. The chlorinated products showed a bathochromic shift of 40-50 nm with respect to the hydrogen-terminated compounds, suggesting a decrease on the HOMO-LUMO gap. This fact, was also supported by TD-DFT calculation which showed a decrease on the HOMO and LUMO energies of the chlorinated compounds.

Therefore, the introduction of functional groups at the outer positions of HBC has been proved to have an effect on the electronic properties of the nanographenes. In this sense, it was reported that the decoration of HBC with amino and cyano groups intensifies the fluorescence quantum yield of the parent HBC.⁹⁴ Importantly, the effect of the substituents significantly depends on their relative position, being *para*-substituted HBCs the ones with higher substituent effect.

The most recent work reporting the influence of the relative position of the substituents on HBC units is that reported by N. Jux and co-workers in 2019.⁹⁵ Therein, a family of disubstituted HBCs with Zn-porphyrin groups at *ortho*-, *meta*- and *para*- positions were prepared and their optical and electrochemical properties studied. This study revealed an angle-dependent electronic communication on HBC with attached Zn-porphyrins.

⁹³ Y.-Z. Tan, B. Yang, K. Parvez, A. Narita, S. Osella, D. Beljonne, X. Feng, K. Müllen, *Nat. Commun.* **2013**, *4*, 2646.

⁹⁴ R. Yamaguchi, S. Ito, B. S. Lee, S. Hiroto, D. Kim, H. Shinokubo, *Chem. Asian J.* **2013**, *8*, 178-190.

⁹⁵ M. M. Martin, D. Lungerich, P. Haines, F. Hampel, N. Jux, *Angew. Chem. Int. Ed.* **2019**, *58*, 8932-8937.

Non-linear optical properties on HBC and nanographenes – Two-photon absorption

Not only linear optical properties such as absorption or fluorescence are modified after the introduction of functional groups into the structure of HBC. Non-linear optical properties such as two-photon absorption are also tuned on HBC derivatives by the combination of donor and acceptor groups as reported by J. Wu, Q.-H Xu and co-workers in 2011.⁹⁶

Two-photon absorption is described as: “the process by which a molecule or material absorbs a pair of photons, the sum of whose energy equals the transition energy” according to literature.⁹⁷ This process was firstly described theoretically in 1931 by M. Göppert-Mayer,⁹⁸ and involves the simultaneous absorption of two photons (of energies E_1 and E_2) by a molecule that occurs when $E_1 + E_2$ is in resonance with one of the electronic states of the system, bringing the molecule to an excited state (f , Figure 18). This process can be envisioned as a first absorption of a photon with energy E_1 that lead the system to a temporary virtual state of energy E_1 above the ground state (g). This virtual state is not a real state and only exists for a short time, if during this time a second photon interacts with the molecule, this can be excited to the state f .

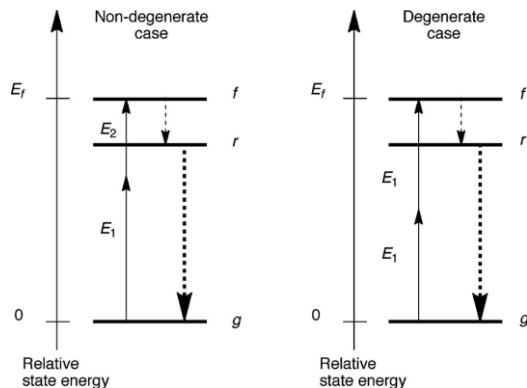


Figure 18. Schematic energy level diagram showing the excitation of a molecule from a ground level g to a excited state f by absorbing two photons of different (left) or equal (right) energies.

The double photon absorption condition described could be satisfied either by the absorption of two photons of different energy ($E_1 \neq E_2$) (Figure 18, left) or by two photons of the same energy

⁹⁶ Z. Zeng, Z. Guan, Q.-H. Xu, J. Wu, *Chem. Eur. J.* **2011**, *17*, 3837-3841.

⁹⁷ M. Rumi, J. W. Perry, *Adv. Opt. Photonics* **2010**, *2*, 451-518.

⁹⁸ M. Göppert-Mayer, *Ann. Phys.* **1931**, *401*, 273-294.

($E_1 = E_2$) (Figure 18, right). Moreover, this thesis will be focused on the measurement of TPA caused by the absorption of two photons of energy E_1 .

Two different methodologies are described for the experimental evaluation of two-photon absorption and are categorized as *direct* or *indirect*. Direct methods are based on the measurement of the beam attenuation after passing through the sample. On the other hand, in indirect methods the quantity to be measured is one of the effects caused by the generation of population in the excited state r , such as fluorescence emission or heat produced.

Regarding direct methods, Z-scan is the mostly common used technique in this category. In a Z-scan experiment, the pulse energy is kept constant and the change in intensity is achieved by moving the sample along the propagation direction z . On the other hand, indirect methods are mainly based on the *two-photon-induced fluorescence* method, in which the intensity of the fluorescence emission induced by TPA is measured. By monitoring the intensity of the fluorescence signal, it is possible to obtain relative or absolute TPA spectra. This method is, indeed, the two-photon analogue of a fluorescence excitation experiment. Thus, the collected spectra by using this technique are often called *two-photon induced fluorescence excitation spectra* (TPIF).

The applications of TPA-based materials have been proven from long time ago. On compounds with a red-shifted one photon absorption, the excitation with two photons would be located at the near infrared (NIR) region. Thus, the incident photons would possess very low energy and were able to, *i.e.* penetrate deeper on living tissues. This is the foundation of the two-photon absorption microscopy, which can be considered a similar technique to confocal laser scanning microscopy. The use of NIR radiation on TPA microscopy minimizes scattering while the background signal is strongly suppressed. Nowadays, the searching for highly TPA active materials is a hot topic in the chemistry of materials due to their promising applications.

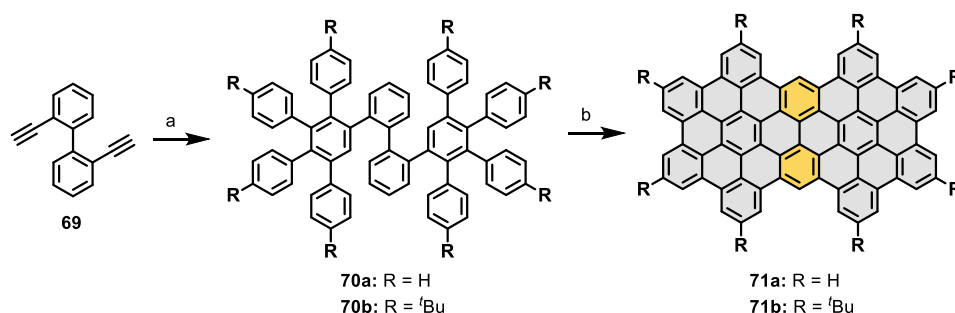
Functionalization and expansion – toward larger graphene molecules

Following the reported strategies for the preparation of HBC derivatives, but simply changing the nature of the starting materials, larger graphene molecules may arise. As mentioned before, Scholl reaction is the key step on the preparation of graphene molecules. Therefore, the

complete cyclodehydrogenation of larger oligophenylene precursors needs careful control of the experimental conditions (such as time, oxidants and stoichiometry), and the structure of the final expanded nanographenes should be determined by different characterization techniques.

Thus, nanographenes consisting of two fused HBCs have been prepared long time ago. Two different structures may arise after fusing two HBC units depending on the number of shared rings. When two rings are shared, a structure formed by 60 sp^2 carbon atoms and exhibiting a combination of armchair- and gulf-type edges is obtained. The synthesis of this nanographene has been reported by following different synthetic pathways.

In 1997, K. Müllen and co-workers reported two different synthesis.⁹⁹ Firstly a two-fused HBC structure was prepared by a two-fold Diels-Alder reaction between the biphenyl derivative **69** and different tetraphenyl-cyclopentadienones (R = H or ^tBu) where the obtained oligophenylene (**70**) was finally subjected to Scholl reaction by using either $CuCl_2/AlCl_3$ or $FeCl_3$ (Scheme 14).

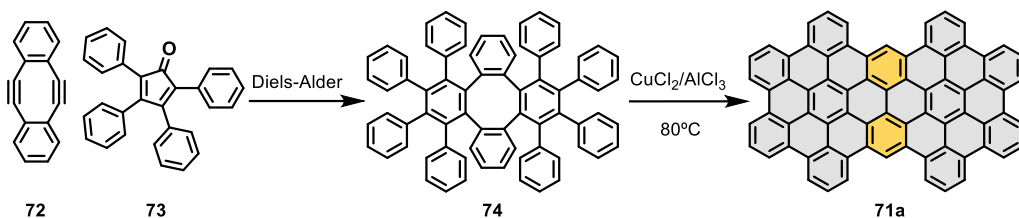


Scheme 14. Synthesis of C₆₀ nanographene **71**. a) Diels-Alder reaction, b) Scholl reaction.

Secondly, another methodology was reported. Based on a two-fold Diels-Alder reaction between a highly strained cyclooctadiyne derivative (**72**) and the corresponding cyclopentadienone (**73**), final cyclodehydrogenation reaction, promoted by the combination of $CuCl_2$ and $AlCl_3$ at 80°C, afforded the planar structure (**71a**) (Scheme 15). The final compound was characterized by LD-TOF-MS confirming the rearrangement of the eight-membered ring.¹⁰⁰

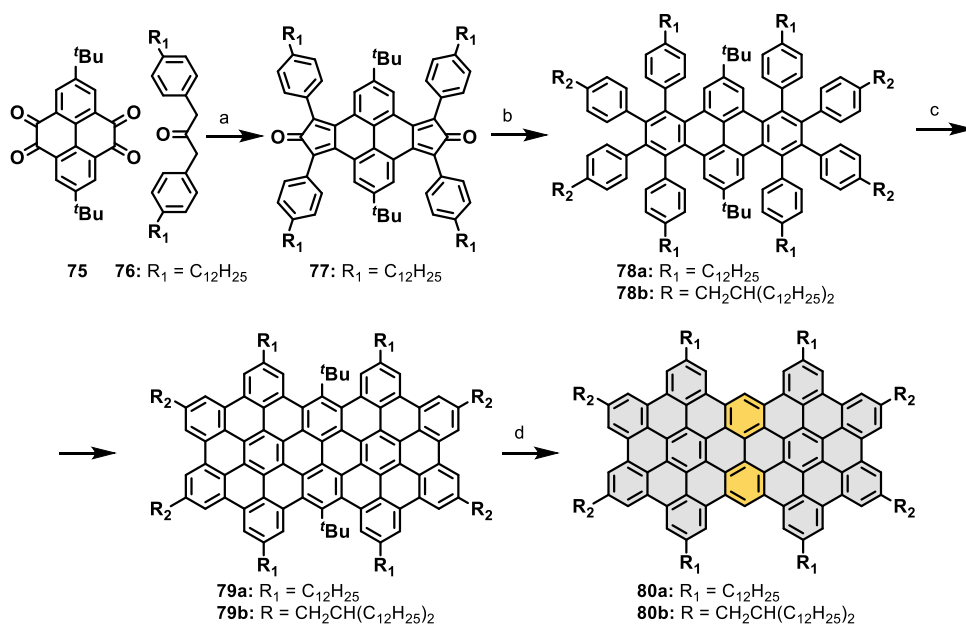
⁹⁹ V. S. Iyer, M. Wehmeier, J. D. Brand, M. A. Keegstra, K. Müllen, *Angew. Chem. Int. Ed.* **1997**, *36*, 1604-1607.

¹⁰⁰ M. Müller, V. S. Iyer, C. Kübel, V. Enkelmann, K. Müllen, *Angew. Chem. Int. Ed.* **1997**, *36*, 1607-1610.



Scheme 15. Synthesis of C60 nanographene **71a**.

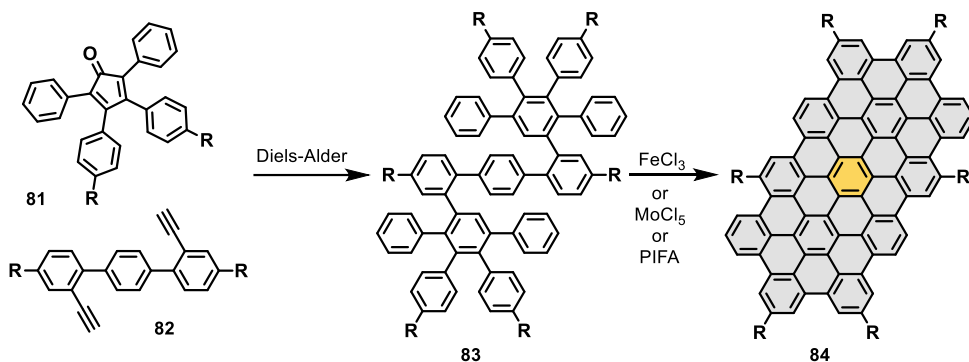
More recently, in 2006, an alternative synthetic route for the preparation of an analogue to compound **71a** was reported by the same group. This analogue exhibits long alkyl chains that allows its characterization by NMR. Moreover, the reported synthetic route was based on the Diels-Alder reaction rather than ring contraction (Scheme 16). Remarkably, the *tert*-butyl groups placed at the gulf region may induce a distortion out of the plane due to steric repulsions as supported by DFT calculations.¹⁰¹



Scheme 16. Synthesis of nanographene **80**. a) Aldol condensation, b) Diels-Alder reaction, c) FeCl₃, Scholl reaction d) Benzene, oleum.

¹⁰¹ D. Wasserfallen, M. Kastler, W. Pisula, W. A. Hofer, Y. Fogel, Z. Wang, K. Müllen, *J. Am. Chem. Soc.* **2006**, *128*, 1334-1339.

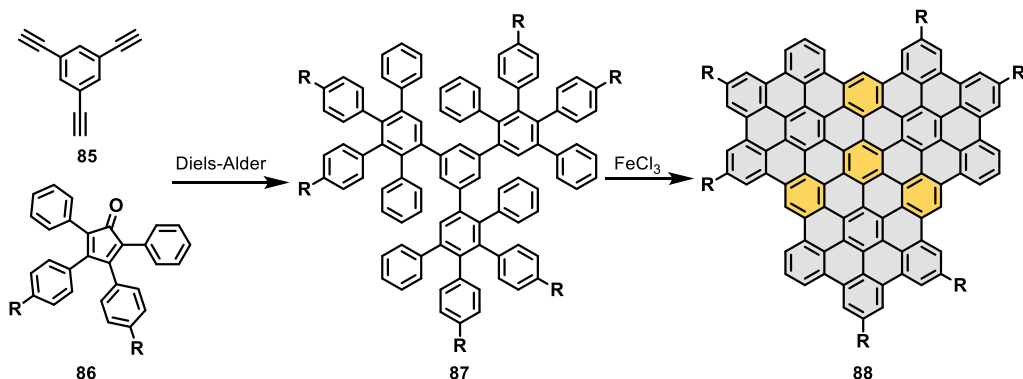
On the other hand, when only one ring is shared by the two HBC units, a larger planar structure containing 78 aromatic carbon atom can be synthesized (**84**, Scheme 17). Although its preparation was reported more than twenty years ago,¹⁰⁰ an elegant synthesis was reported in 2012 where compound **84** was prepared as the smallest section of its corresponding staggered GNR (**35**).⁷⁰ Starting from 2,2''-diethynylterphenyl and through a two-fold Diels-Alder reaction, the oligophenylene precursor can be prepared. The final Scholl reaction can be carried out by using three different reagents (FeCl_3 , MoCl_5 or *Bis*(trifluoroacetoxy)iodobenzene also known as PIFA) affording exclusively **84**, which was characterized in terms of NMR, MALDI-TOF MS and STM (Scheme 17). According to the authors, **84** was reported as the largest PAH that allowed for structural characterization by $^1\text{H-NMR}$ at that moment, nevertheless the $^1\text{H-NMR}$ was reported at high temperatures (170°C) probably due to the strong aggregation and, therefore, broadening on the signals at room temperature. The isotopic distribution at the obtained MS spectrum confirmed the monodispersity and the absence of chlorinated products on the final compound. Moreover, STM images of **84**, after physisorption on Au(111)/1,2,4-trichlorobenzene solid-liquid interface, suggested the formation of well-ordered films.



Scheme 17. Synthesis of nanographene **84** ($\text{R} = \text{C}_{12}\text{H}_{25}$).

As an extension of the described methodologies, nanographene **88** with three HBC units in a trefoil shape, an aromatic surface consisting on 96 sp^2 carbon atoms was prepared by K. Müllen and co-workers. The reported nanographene was prepared by the triple Diels-Alder reaction between the trialkyne derivative **85** and different functionalized tetraphenyl-cyclopentadienones bearing either aryl or long alkyl chains, followed by a final cyclodehydrogenation reaction promoted by FeCl_3 (Scheme 18). The authors characterized the structures in terms of MALDI-TOF

mass spectrometry, differential scanning calorimetry (DSC), polarized optical microscopy (POM) and wide-angle X-ray diffraction (WAXD). However, no NMR spectra were reported due to problems related to dynamic aggregation.¹⁰²



Scheme 18. Synthesis of nanographene **88** (R = Ar or alkyl chains).

HBC can be also envisioned as an extended benzene due to its hexagonal geometry, therefore, HBC units are able to be linked in a similar way to PAHs arrange benzene rings. Thus, **71** and **80** may be defined as “supernaphthalenes” (Figure 19).

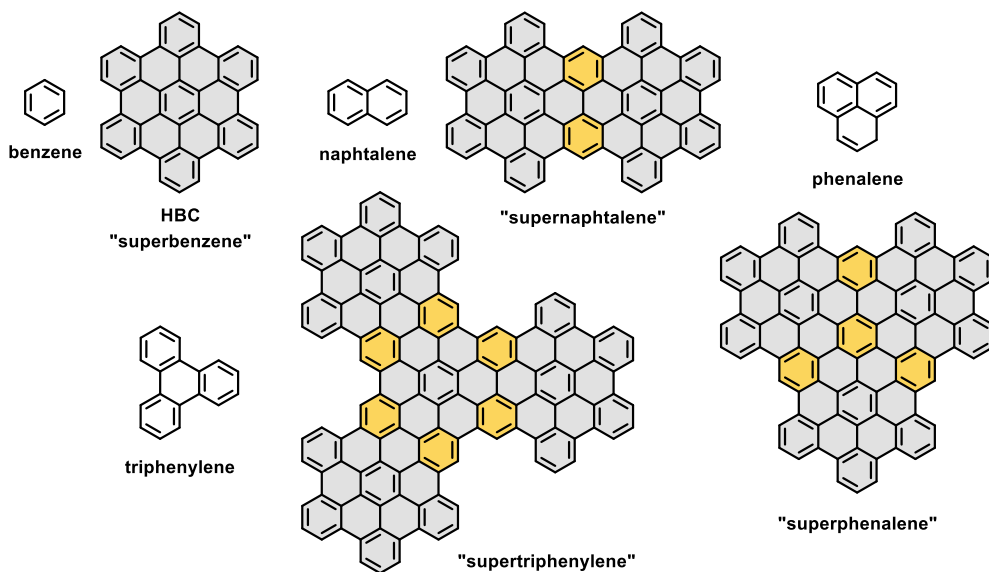


Figure 19. Benzene, different PAHs and their related “superacenes”.

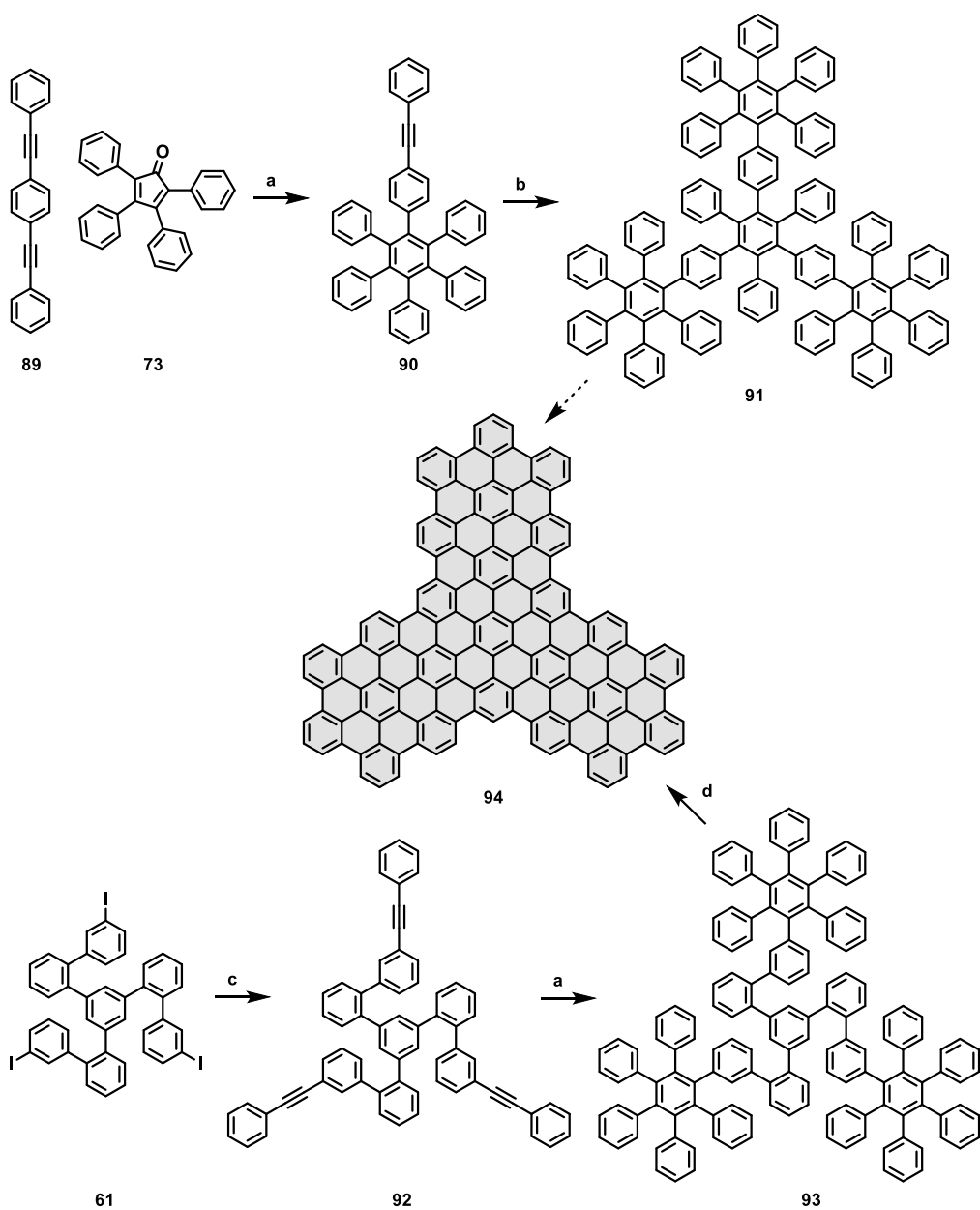
¹⁰² Ž. Tomović, M. D. Watson, K. Müllen, *Angew. Chem. Int. Ed.* **2004**, *43*, 755-758.

Similarly, **88** would be the extended analogous to phenalene, hence “superphenalene”. This terminology, coined by K. Müllen and co-workers in 1997, defines this group of extended nanographenes as “superacenes” (Figure 19).⁹⁹

Larger trefoil nanographenes have been also prepared fifteen years before, thus a graphene molecule containing 150 sp² carbon atoms was prepared by two different synthetic routes. The first one is based on the mono Diels-Alder reaction between 1,4-*bis*(phenylethynyl)benzene (**89**) and tetraphenylcyclopentadienone (**73**) followed by a Co₂(CO)₈-catalyzed alkyne cyclotrimerization reaction (Scheme 19). However, the authors reported the formation of two inseparable structural isomers after this reaction. To overcome this obstacle, they suggested a second synthetic methodology. This new route was based on the preparation of a C₃-symmetric precursor (**93**), synthesized from triiododerivative **61**. The three-fold Sonogashira reaction over **61** with phenylacetylene afforded **92**, which was subjected to a triple Diels-Alder reaction with three equivalents of tetraphenylcyclopentadienone. **93** was finally treated with FeCl₃ to obtain **94** as the only one Scholl reaction product (Scheme 19).

Nevertheless, NMR characterization failed due to the very poor solubility of **94** and elemental analysis could not provide reliable information about the elemental composition because the incomplete combustion during the measurements. Thus, MALDI-TOF was found to be the only methodology that confirms the formation of the final compound, although the presence of chlorinated species was observed due to the *in situ* formation of HCl when using FeCl₃ (Figure 20a). This low solubility limited its conventional spectroscopic characterization in solution, alternatively solid-state UV-Vis and Raman spectroscopy were measured. The UV-Vis spectra were recorded on mechanically “smeared” films on quartz (Figure 20b).¹⁰³

¹⁰³ J. Wu, Ž. Tomović, V. Enkelmann, K. Müllen, *J. Org. Chem.* **2004**, 5179-5186.



Scheme 19. Synthetic route to nanographene **94**; a) Diels-Alder reaction, b) alkyne cyclotrimerization, c) Sonogashira coupling, d) Scholl reaction.

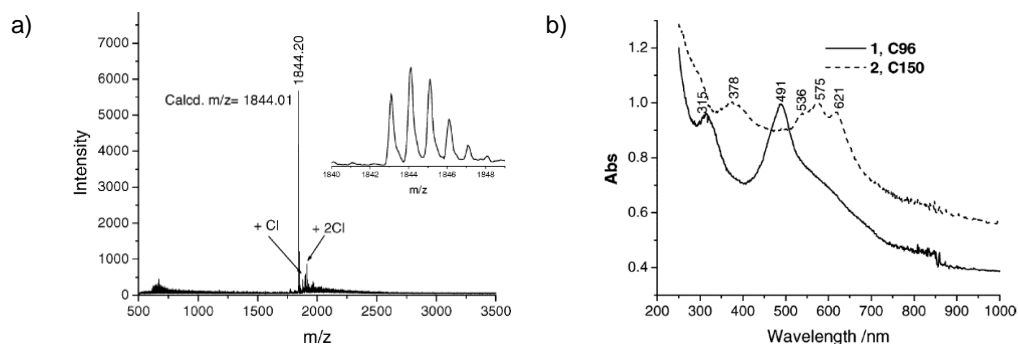
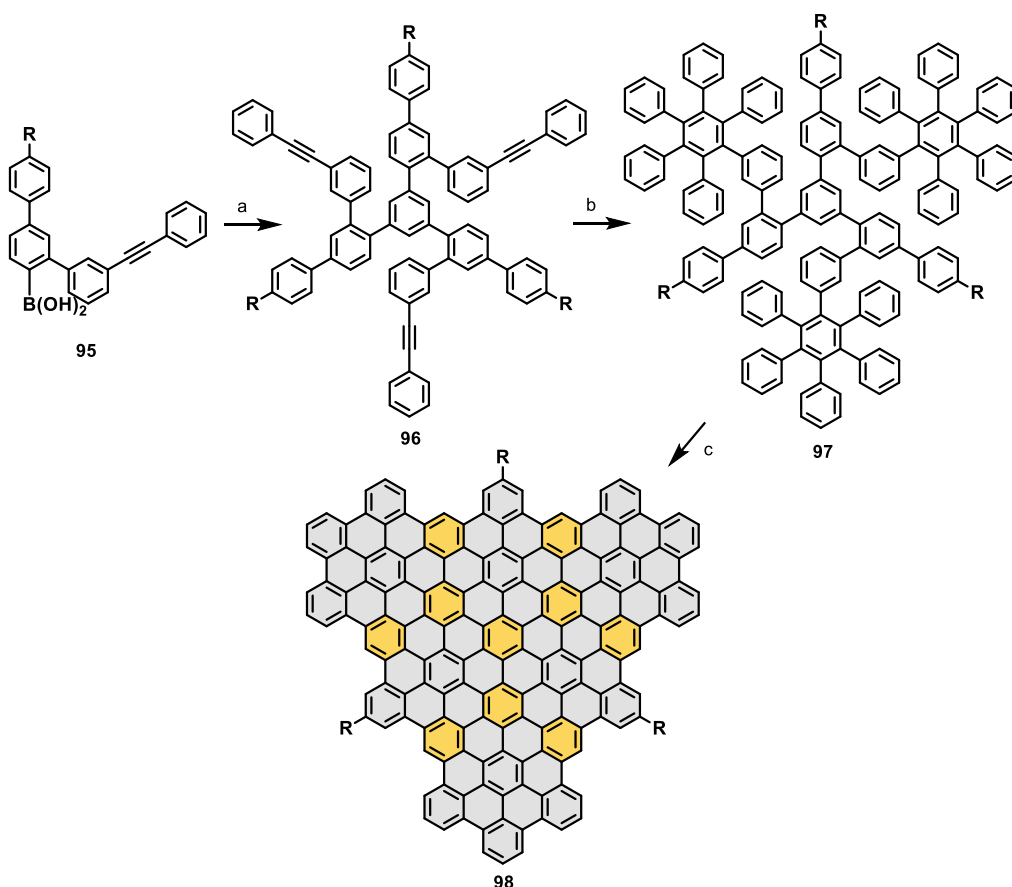


Figure 20. Left: MALDI-TOF spectrum of compound **94**; Right: solid-state UV-Vis of **88** (solid line) and **94** (dotted line).¹⁰³

As mentioned above, the introduction of long alkyl substituents into the periphery of a nanographene has been extensively used in order to increase its solubility. Conversely, for nanographenes with increasing size, the intermolecular attraction rapidly overtakes the solubilization forces, making this strategy less and less effective. Thus, an efficient strategy for the exploration of the optical properties of such extended graphene molecules was reported by L.-s. Liu and co-workers,¹⁰⁴ where the covalently attaching of multiple 1,3,5-trialkyl-substituted phenyl moieties permitted the optical evaluation of a 168 conjugated carbon nanographene. The geometry of the attached substituents force the long chains to be placed over and above the aromatic surface, increasing the distance between the nanographenes and reducing the π - π interactions.

The synthesis of **98** was achieved following the combination of Suzuki couplings and Diels-Alder reactions to form a precursor similar to **93** and ending with typical Scholl reaction conditions that lead to the elimination of 72 aromatic hydrogen atoms (Scheme 20). The structure of **98** was confirmed by means of MALDI-TOF MS and its high solubility (up to 30 mg/mL) allowed its spectroscopic characterization and its use on nanocrystalline solar cells.

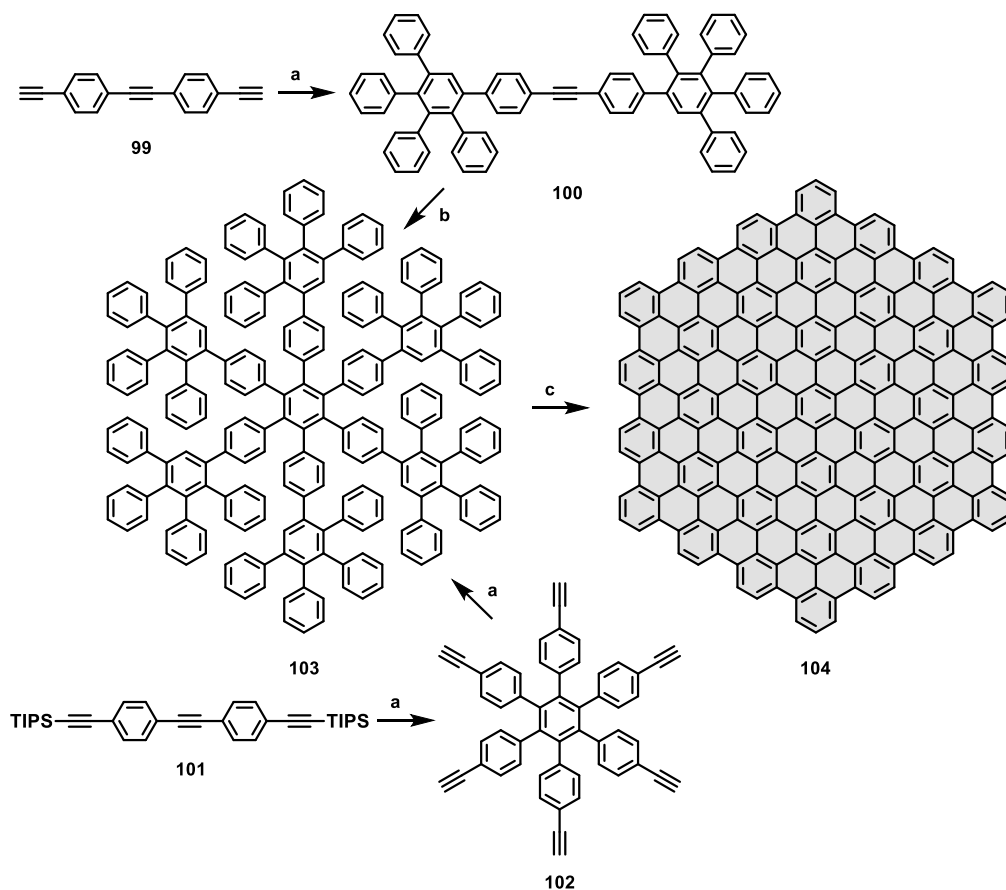
¹⁰⁴ X. Yan, X. Cui, B. Li, L.-s. Li, *Nano Lett.* **2010**, 1869-1873.



Scheme 20. Synthetic route toward soluble nanographene **98** reported on literature (R = 1,3,5-trialkylphenyl).

Finally, the flagship compound prepared following the methodology developed by K. Müllen and co-workers was the giant graphite sheet consisting on 222 carbon atoms **104** (Scheme 21). As for the previously abovementioned nanographenes, the preparation of this hexagonal graphene flake was achieved by combining Diels-Alder and Scholl reactions or alkyne cyclotrimerization and Scholl reactions. Precursors **100** and **102** could be prepared by double and simple Diels-Alder reaction over the corresponding trialkyne **99** and **101**, respectively. Terminal alkynes derivative led to **100** through double Diels-Alder whereas (bulky-substituent) protected alkynes forced the central alkyne to undergo the cycloaddition. Both **100** and **102** were transformed into **103** by alkyne cyclotrimerization from **100** or Diels-Alder reaction from **102**, respectively. Final Scholl reaction led to **104** by losing 108 hydrogen atoms and forming 54 new carbon-carbon bonds in

one single step. The structure of oligophenylene **103** was evaluated in terms of X-Ray diffraction, conversely compound **104** was completely insoluble and only a MALDI-TOF spectrum was obtained confirming the structure. Moreover, a solid-state UV-Vis spectrum was measured exhibiting a broad absorption band up to 2200 nm.¹⁰⁵



Scheme 21. Synthetic routes towards nanographene **104**; a) Diels-Alder reaction, b) alkyne cyclotrimerization, c) Scholl reaction.

¹⁰⁵ C. D. Simpson, J. D. Brand, A. J. Berresheim, L. Przybilla, H. J. Räder, K. Müllen, *Chem. Eur. J.* **2002**, *8*, 1424-1429.

Summary

The preparation of oligophenylene as precursors for nanographenes by the [4+2] cycloaddition or alkyne cyclotrimerization by using different alkynes and cyclopentadienones led to soluble oligomers easily evaluated by means of spectroscopic techniques. The final Scholl reaction to planarize and obtain the aromatic compounds has been extensively studied finding FeCl₃ or the combination of Cu(II) salts and AlCl₃ as the most effective reagents. Thus, the group of K. Müllen has reported a broad family of graphene molecules of different sizes and shapes following this methodology.

Despite the wide variety of compounds, the majority show limited of solubility and, therefore, a unequivocal characterization of their structure by means of NMR is missing. Moreover, this methodology reached its limit when the number of carbon-carbon bonds formed on the last step is too high due to mismatching of topology for large oligophenylenes leading to partial cyclodehydrogenated products.¹⁰⁶

Although the introduction of long alkyl chains enhances their solubility and processability,¹⁰⁷ the π - π stacking between larger compounds remains a problem for a proper handling and evaluation of their properties. Nevertheless, the alignment and self-assembly of these graphene molecules have been found as benefits for the preparation of thin-film devices with applications in electronics due to their good charge transport.¹⁰⁸

1.3.1.2. Other approaches for nanographene synthesis

The synthetic routes commented above have proven to be efficient tools for the preparation of nanographenes. However, the final structure is directly related to the aspect of the oligophenylene acting as precursor. Thus, different kind of nanographenes, exhibiting new geometries remains unexplored due to the sophisticated oligophenylene precursors that might require which are often inaccessible. Therefore, it is essential to develop new synthetic strategies

¹⁰⁶ C. D. Simpson, G. Mattersteig, K. Martin, L. Gherghel, R. E. Bauer, H. J. Räder, K. Müllen, *J. Am. Chem. Soc.* **2004**, *126*, 3139-3147.

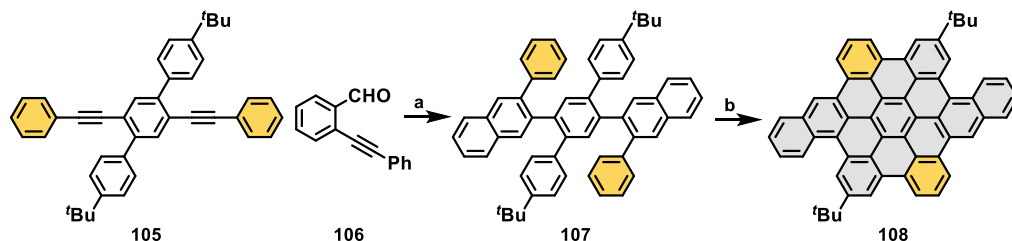
¹⁰⁷ M. G. Debije, J. Piris, M. P. de Haas, J. M. Warman, Ž. Tomović, C. D. Simpson, M. D. Watson, K. Müllen, *J. Am. Chem. Soc.* **2004**, *126*, 4641-4645.

¹⁰⁸ J. Wu, W. Pisula, K. Müllen, *Chem. Rev.* **2007**, *107*, 718-747.

1. Background

for the synthesis of nanographenes to enable the preparation of graphene molecules with tailorable geometries and modulable (opto-)electronic properties.

The first remarkable work that broke the established methodologies for the preparation of extended nanographenes was the sequential benzannulation and cyclodehydrogenation reported by Dichtel and co-workers in 2013.¹⁰⁹ In this work, the authors reported the preparation of dibenzo-fused *p*-HBC (**108**) starting from readily accessible di(arylethynyl)-benzene derivatives (**105**) and followed by the benzannulation reaction with 2-(phenylethynyl)benzaldehyde (Scheme 22). Remarkably, the last step could be performed in a controlled manner, selectively yielding partially fused product (in a shorter reaction time) or the fully conjugated compound (in longer reaction times).

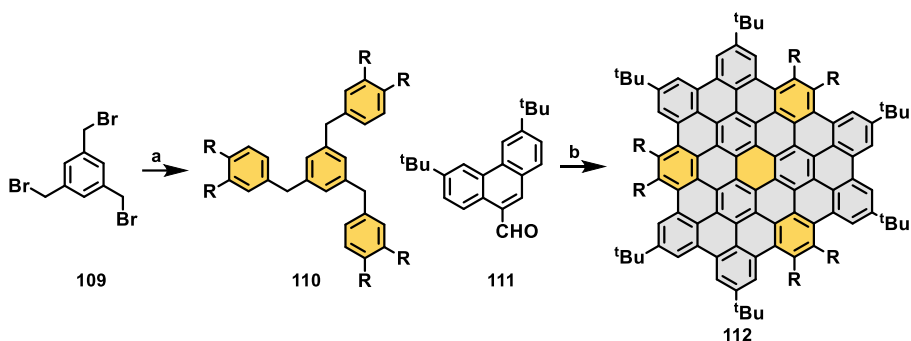


Scheme 22. Sequential benzannulation and cyclodehydrogenation methodology reported by Dichtel *et al.*; a) $\text{Cu}(\text{OTf})_2$, $\text{CF}_3\text{CO}_2\text{H}$; b) FeCl_3 .

More recently, Wei and co-workers reported the two step synthetic route for obtaining C_3 symmetrically *c*-HBC and expanded derivatives (Scheme 23). Starting from 1,3,5-tribenzylbenzene derivatives (**110**) (prepared from 1,3,5-tri(bromomethyl)-benzene, **109**) and after treatment with three equivalents of phenanthraldehyde (**111**) under the presence of FeCl_3 and acetic anhydride as oxidant/Lewis acid and dehydrating agent. The final product (**112**) containing 72 sp^2 carbon atoms was confirmed by X-Ray crystallographic studies.¹¹⁰

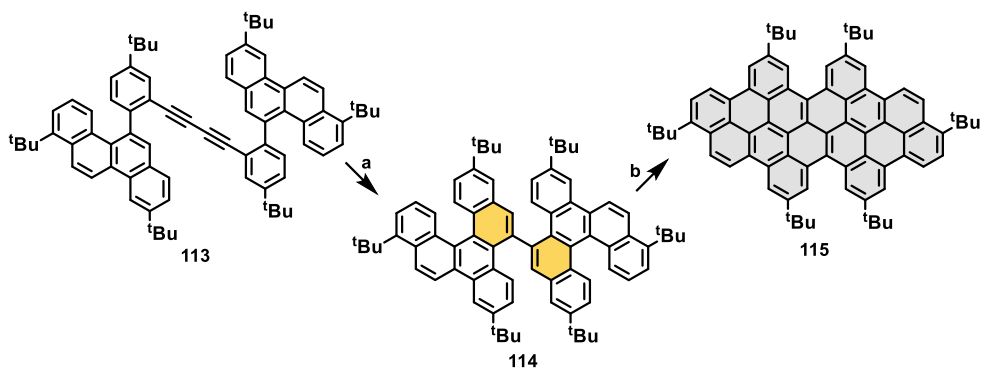
¹⁰⁹ H. Arslan, F. J. Uribe-Romo, B. J. Smith, W. R. Dichtel, *Chem. Sci.* **2013**, *4*, 3973-3978.

¹¹⁰ Q. Zhang, H. Peng, G. Zhang, Q. Lu, J. Chang, Y. Dong, X. Shi, J. Wei, *J. Am. Chem. Soc.* **2014**, *136*, 5057-5064.



Scheme 23. Reported synthesis of compound **112**; a) Suzuki coupling, b) FeCl_3 , Ac_2O .

Furthermore, electrophilic cycloaromatization of *o*-alkynylated biaryls is a versatile method to prepare phenanthrene structures. Thus, its combination with Scholl reaction enables the synthesis of expanded PAHs. Either ruthenium- or platinum-mediated cycloaromatization methods have been reported, even though, metal-free methods based on the use of ICl allow the same transformation.¹¹¹ Remarkably, this methodology has been recently reported as a useful tool for the preparation of cove-edged GNRs precursors (Scheme 24).¹¹²



Scheme 24. Reported synthesis of compound **115**; a) ICl , then *n*- BuLi ; b) DDQ/H^+ .

Another efficient methodology for the preparation of PAHs is that based on the chemistry of short-lived aryne intermediates. In particular, palladium-catalyzed [2+2+2] cycloadditions of aryne derivatives have proven as a versatile transformation for the preparation of large PAHs and

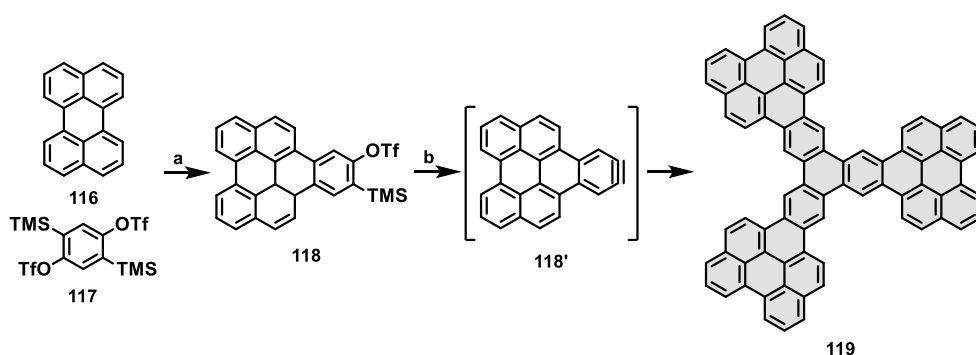
¹¹¹ a) T.-A. Chen, R.-S. Liu, *Chem. Eur. J.* **2011**, *17*, 8023-8027; b) T.-A. Chen, R.-S. Liu, *Org. Lett.* **2011**, *13*, 4644-4647.

¹¹² J. Liu, B.-W. Li, Y.-Z. Tan, A. Giannakopoulos, C. Sanchez-Sanchez, D. Beljonne, P. Ruffieux, R. Fasel, X. Feng, K. Müllen, *J. Am. Chem. Soc.* **2015**, *137*, 6097-6103.

1. Background

nanographenes. In this field, an intensive research has been carried out during the last decades by E. Guitián, D. Pérez and D. Peña, who have reported the preparation of a wide variety of trefoil-shaped PAHs by the aryne chemistry.¹¹³

The ready availability of *o*-(trimethylsilyl)aryl triflates and the mild conditions required to form aryne derivatives allowed them to exploit the synthesis of triphenylene derivatives. A remarkable example was the preparation of an extended nanographene with up to 22 fused benzene rings by means of palladium-catalyzed [2+2+2] cyclotrimerization (Scheme 25).¹¹⁴ Remarkably, the necessary *o*-(trimethylsilyl)aryl triflate was prepared from perylene through a [4+2] cycloaddition of arynes. The final compound was extremely insoluble for conventional characterization methods such as NMR spectroscopy. Thus, NC-AFM with CO functionalized tip was the selected technique for the visualization of nanographene **119**. Moreover, STM allowed the visualization of HOMO and LUMO densities of this molecule.



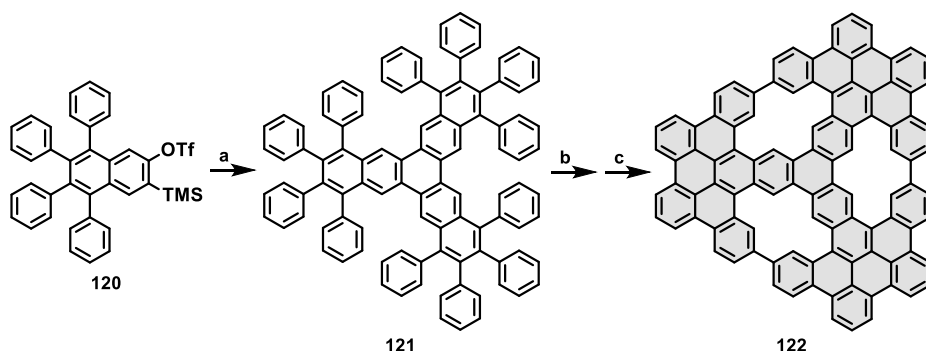
Scheme 25. Reported synthesis of the trefoil nanographene **119** via aryne chemistry; a) CsF, [4+2] cycloaddition, b) CsF, Pd₂(dba)₃, [2+2+2] cycloaddition.

Among many other examples, the abovementioned authors have recently proved that aryne chemistry could be an excellent technique in combination with on-surface synthesis. The preparation of sophisticated precursors with an appropriate geometry to be subjected to a final cyclodehydrogenation reactions on a metal surface can be prepared in a straightforward manner

¹¹³ a) D. Pérez, D. Peña, E. Guitián, *Eur. J. Org. Chem.* **2013**, 5981-6013; b) I. Pozo, E. Guitián, D. Pérez, D. Peña, *Acc. Chem. Res.* **2019**, *52*, 2472-2481.

¹¹⁴ B. Schuler, S. Collazos, L. Gross, G. Meyer, D. Pérez, E. Guitián, Diego Peña, *Angew. Chem. Int. Ed.* **2014**, *53*, 9004-9006.

by aryne chemistry rather than using traditional reactions such as Suzuki coupling.¹¹⁵ Thus, the authors have recently reported the combination of aryne chemistry and on-surface assisted synthesis for the preparation of a porous nanographene (**122**, Figure 26) consisting on 102 carbon atoms,¹¹⁶ or the nanoporous graphene selected “molecule of the year” in 2018.¹¹⁷



Scheme 26. Reported synthesis of the porous nanographene **122** via aryne chemistry; a) CsF, [Pd], [2+2] cycloaddition, b) Au(111), 300°C, c) Au(111), 370°C.

The latest reported strategy with high potential for the preparation of extended PAHs was developed by K. Itami and co-workers. Coined as APEX (Annulative π -extension), this novel methodology can be regarded as the direct C-H arylation of unfunctionalized arenes or heteroarenes with simultaneous construction of one or more fused aromatic rings. Edge topology is a key point on APEX, since this methodology is selective for K-regions (convex armchair edge). Thus, APEX methodology have been applied over a wide spectrum of PAHs exhibiting K-region/s even including heteroaromatic compounds and can be carried out either by one or two steps (Scheme 27).¹¹⁸

One-step APEX is based on the reaction between the K-region of an unactivated PAH and arylsilanes or diiodo derivatives, catalyzed by palladium (II) (Scheme 23, left). This APEX reaction most likely proceeds through the next steps: i) transmetalation of the arylsilane reagent to an

¹¹⁵ K. Xu, J. I. Urgel, K. Eimre, M. Di Giovannantonio, A. Keerthi, H. Komber, S. Wang, A. Narita, R. Berger, P. Ruffieux, C. A. Pignedoli, J. Liu, K. Müllen, R. Fasel, X. Feng, *J. Am. Chem. Soc.* **2019**, *141*, 7726-7730.

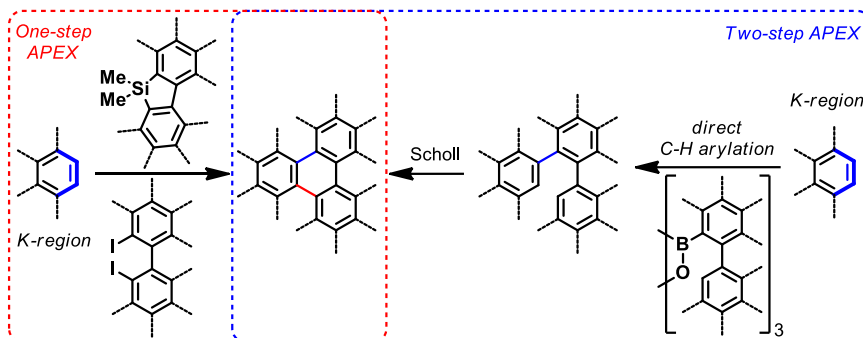
¹¹⁶ R. Zuzak, I. Pozo, M. Engelund, A. Garcia-Lekue, M. Vilas-Varela, J. M. Alonso, M. Szymonski, E. Guitián, D. Pérez, S. Godlewski, D. Peña, *Chem. Sci.* **2019**, *10*, 10143-10148.

¹¹⁷ C. Moreno, M. Vilas-Varela, B. Kretz, A. Garcia-Lekue, M. V. Costache, M. Paradinas, M. Panighel, G. Ceballos, S. O. Valenzuela, D. Peña, A. Mugarza, *Science* **2018**, *360*, 199-203.

¹¹⁸ a) H. Ito, K. Ozaki, K. Itami, *Angew. Chem. Int. Ed.* **2017**, *56*, 11144-11164; b) H. Ito, Y. Segawa, K. Murakami, K. Itami, *J. Am. Chem. Soc.* **2019**, *141*, 3-10.

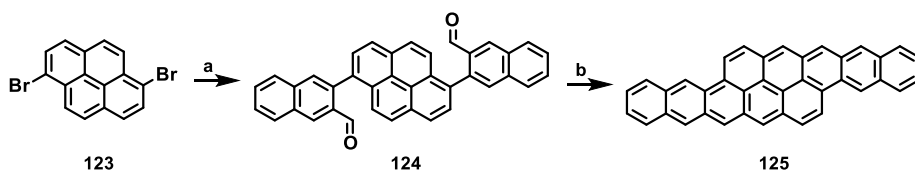
1. Background

arylpalladium species, ii) the K-region selective π -coordination of arylpalladium and iii) carbopalladation followed by β -hydrogen elimination.¹¹⁹ On the other hand, two-step APEX is based on a sequential C-H arylation with boron derivatives and Scholl reaction.¹²⁰



Scheme 27. Schematic representation of one- and two-step APEX methodologies reported by K. Itami and co-workers.

In analogy to APEX methodology, the dehydrative π -extension (DPEX) has been recently reported as an efficient methodology for the preparation of zig-zag edged nanographenes such as DBATT (**125**, Scheme 28).¹⁸ This strategy is based on an acid-promoted reductive intramolecular cyclization of aromatic aldehydes. The key step on the reported synthetic pathway is carried out in presence of SnCl_2 and H_2SO_4 and exhibited good yields. Remarkably, a wide variety of zigzag edged nanographenes are reported.



Scheme 28. DPEX methodology toward compound **125**; a) Suzuki coupling, b) DPEX.

¹¹⁹ a) K. Ozaki, K. Kawasumi, M. Shibata, H. Ito, K. Itami, *Nat. Commun.* **2015**, *6*, 6251; b) W. Matsuoka, H. Ito, K. Itami, *Angew. Chem. Int. Ed.* **2017**, *56*, 12224-12224.

¹²⁰ K. Mochida, K. Kawasumi, Y. Segawa, K. Itami, *J. Am. Chem. Soc.* **2011**, *133*, 10716-10719.

Summary

The development of new methodologies for the preparation of well-defined nanographenes remains a hot topic among the scientific community. The novel reported methodologies have shown to be complementary to the conventional pathways, providing access to new precursors and geometries completely unaffordable a few decades before. Despite the breakthrough on the preparation of large PAHs by alternative strategies, the solubility of the final compounds is a nuisance for researchers, who struggle for a proper characterization and evaluation of the properties of the prepared compounds.

Recently, new graphene-like structures have arisen as a result of a symbiosis between solution chemistry and on-surface synthesis.¹²¹ Thus, novel precursors have been prepared through organic synthesis, providing candidates for the last reactions over the metal surface. However, the preparation of nanographenes on metal surfaces limits subsequent handling over the prepared compounds. Therefore, the novel graphene molecules are forced to overcome the solubility problem in order to improve their handling and to understand and tune their properties in solution.

1.3.2. Helicene-containing nanographenes

Helicenes are a family of organic compounds consisting on *ortho*-fused PAHs in which all rings are angularly arranged. The helical structure of helicenes is a consequence of the repulsive steric interaction between terminal aromatic rings. They are classified according to the length of the helical structure, thus, helicenes can be named as [*n*]helicenes, where *n* is the number of the *ortho*-fused rings that constitute the helix. Although heteroaromatic rings are usually present on helicene-like molecules, carbohelicenes or helicenes formed only by carbon atoms are of special interest regarding the actual relevance of carbon based materials. Remarkably, when looking at graphene edges, the presence of carbohelicenes is easily recognizable. For instance, cove-type edges are masked carbo[4]helicenes, while fjord regions are directly related with carbo[5]helicenes.¹²²

¹²¹ M. Kolmer, R. Zuzak, A. K. Steiner, L. Zajac, M. Englund, S. Godlewski, M. Szymonski, K. Amsharov, *Science* **2019**, *363*, 57-60.

¹²² M. Gringas, *Chem. Soc. Rev.* **2013**, *42*, 968-1006.

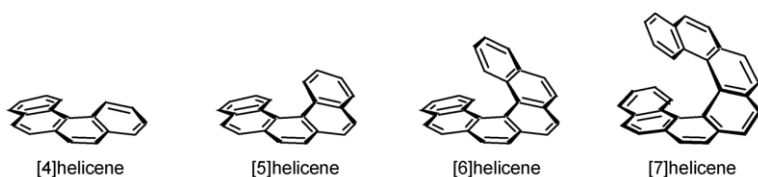


Figure 21. All carbon, ortho-fused benzene rings called “carbohelicenes”.¹²²

The steric congestion at the inner rim of helicenes led to an out-of-plane arrangement of the carbon atoms. This structural feature introduces a new dimensionality on carbon-based compounds, which would affect their properties, having in mind the strong structure-properties relationship of this kind of molecules.

Regarding nanographenes, the introduction of one or more tridimensional helicene moieties would disrupt the π -electron system. This fact would result on an interesting tool to enhance their solubility since the strong π - π stacking present on flat nanographenes might be avoided on their helicene containing derivatives due to the mismatching of the aromatic surfaces.

Furthermore, helicenes bring interesting structural features along, such as chirality. The introduction of chirality on carbon materials is a hot topic nowadays and is being extensively studied for further applications. In this sense, chiral derivatives of fullerenes,^{5c} carbon nanodots¹²³ or graphene quantum dots¹²⁴ based on the attachment of chiral subunits have been recently prepared. Along with chirality, chiroptical properties arise, thus, optical rotation, circular dichroism or even circularly polarized luminescence may be launched by the introduction of helicene moieties in the structure of nanographenes. The next section presents the main chiroptical properties

Circular Dichroism and Circularly Polarized Luminescence – key chiroptical properties

Circular Dichroism (CD) is defined as the difference between the absorption of left and right circularly polarized lights considering the chemical vision of light as a wave. In the right-circular polarized light, the associated electric and magnetic vectors describe a clockwise helix, as the wave propagates toward the observer, whereas for the left-circular polarized light the

¹²³ L. Đorđević, F. Arcudi, A. D’Urso, M. Cacioppo, N. Micali, T. Bürgi, R. Purrello, M. Prato, *Nat. Commun.* **2018**, *9*, 3442.

¹²⁴ N. Suzuki, Y. Wang, P. Elvati, Z.-B. Qu, K. Kim, S. Jiang, E. Baumeister, J. Lee, B. Yeom, J. H. Bahng, J. Lee, A. Violi, N. A. Kotov, *ACS Nano* **2016**, *10*, 1744-1755.

propagation of these vectors describes an anticlockwise helix. Therefore, circular polarization confers chiral character to a beam of light owing to the helical chirality associated to the corresponding propagation. Thus, their interactions with any chiral compound result in two chiral physical entities of diastereomeric type. Accordingly, the CD is defined as the difference:

$$CD = A^L - A^R \quad (1)$$

where A^L and A^R are the absorbances of left and right circularly polarized light, respectively. The output of CD instruments is usually measured as ellipticity (θ , in mdeg). However, it can be expressed as difference of molar absorptivities, in analogy to the Lambert-Beer law:

$$\Delta\varepsilon = \varepsilon^L - \varepsilon^R = \frac{CD}{c \cdot b} \quad (2)$$

which is independent of the concentration c (expressed in mol·L⁻¹) and of the pathlength b (expressed in cm).

The definition of equation (1) directly reveals that CD can be measured only in correspondence to absorption bands. Thus, CD is a signed quantity, because ε^L can be smaller or larger than ε^R (and consequently A^L and A^R) and therefore, for each absorption band, the CD spectra of two enantiomers are always exactly mirror images of opposite sign.

A useful derived quantity is the g -factor (g_{abs}), sometimes also called anisotropy or dissymmetry factor, defined as:

$$g_{abs} = \frac{\Delta\varepsilon}{\varepsilon} = \frac{\varepsilon^L - \varepsilon^R}{\frac{1}{2}(\varepsilon^L + \varepsilon^R)} = \frac{A^L - A^R}{A} \quad (3)$$

where A represents the conventional absorbance of non-polarized light. It should be stressed that g is independent of the concentration and of the pathlength (as long as the CD and absorbance measurements are performed on the same sample), which do not need to be known or measured.

Regarding transitions, it is useful to remark that for each electronic transition, an electric and a magnetic transition dipole can be defined where the intensity of an absorption band is directly related to the oscillator strength f . By analogy with absorbance, the integral of a CD band is directly proportional to the scalar product of these vectors and is defined as rotational strength,

1. Background

R_{ij} . Finally, it is useful to mention a general rule of CD spectroscopy: *the integral below the CD spectrum over the whole electromagnetic spectrum is zero* or, in other words, the sumatory of all rotatory strengths is zero.¹²⁵

The experimental CD spectrum provides information on the overall molecular stereochemistry of chiral structures at their ground states. Therefore, it is useful for structural determination and is commonly displayed together with any other experimental spectrum or with less sophisticated calculated theoretical curve by TD-DFT methods.

The **Circularly Polarized Luminescence (CPL)** is the emission analogue of CD. It could be defined as the difference on the emission of right- and left-circularly polarized light by chiral enantiopure luminescent systems. The difference in the luminescence intensity (ΔI) is defined by the expression:

$$\Delta I = I^L - I^R \quad (4)$$

where I^L and I^R are the luminescence intensity of left- and right-circularly polarized light, respectively.

Because of the difficulty in measuring absolute emission intensities, it is common to report the degree of CPL in terms of the luminescence dissymmetry factor, g_{lum} , which represents the ratio of the difference in left and right intensities divided by the average total luminescence intensity:

$$g_{lum} = \frac{\Delta I}{\frac{1}{2}I} = \frac{I^L - I^R}{\frac{1}{2}(I^L + I^R)} \quad (5)$$

The extra factor of $\frac{1}{2}$ in this equation is included to make the definition of g_{lum} consistent with the definition of the related quantity in CD and it is known as the Kuhn dissymmetry ratio (equation 3). In this sense, the values of g_{lum} are found between -2 and +2 (completely right- or left-polarized emission, respectively). Moreover, it was demonstrated that the g_{lum} value for a specific emission transition can be also defined as:

$$g_{lum} = 4Re \left[\frac{\mu^{gn} \cdot m^{gn}}{|\mu^{gn}|^2 + |m^{gn}|^2} \right] \quad (6)$$

¹²⁵ N. Berova, L. Di Bari, G. Pescitelli, *Chem. Soc. Rev.* **2007**, *36*, 914-931.

where μ^{gn} and m^{gn} refer to the electric dipole transition moment and the imaginary magnetic dipole transition moment. Thus, measurements of large g_{lum} values are possible when the electronic transitions involved are electric dipole forbidden, but magnetic dipole allowed. Since the magnetic dipole is usually much lower than the electric dipole, the denominator is governed by the term $|\mu|^2$. This is the reason why CPL has been extensively studied on lanthanide (III) complexes, for which large g_{lum} values arise from the magnetically-allowed f-f electronic transitions.¹²⁶ The problem is that these transitions usually have very low luminescence intensities and, therefore, are more difficult to measure.¹²⁷

Up to now, the highest levels of CPL have been mainly achieved from chiral lanthanide complexes, which typically exhibit g_{lum} values between 0.05 and 0.5, although an outstanding value of 1.38 has been reported for a europium (III) complex.¹²⁸ Taking advantage of these intense CPL values, new applications for lanthanide complexes are arising such as chiral emitters on CPL-OLEDs.¹²⁹ Regarding purely organic molecules, slightly smaller CPL levels than those obtained from the lanthanide complexes arise when these molecules are self-organized into helical polymers or supramolecular aggregates¹³⁰ or when taking part as dopant on achiral polymers.¹³¹

On the other hand, CPL active single organic molecules are especially valuable due to three main factors: i) good solubility in common organic solvents, reducing fluorescence quenching, ii) appropriate size for certain applications or specific material manufacturing processes and iii) absence of transition metals allowing applications for which environmental/toxicity factors are crucial.¹³²

¹²⁶ F. Zinna, L. Di Bari, *Chirality* **2015**, *27*, 1-13.

¹²⁷ a) E. M. Sánchez-Carnerero, A. R. Agarrabeitia, F. Moreno, B. L. Maroto, G. Muller, M. J. Ortiz, S. de la Moya, *Chem. Eur. J.* **2015**, *21*, 13488-13500; b) G. Longhi, E. Castiglioni, J. Koshoubu, G. Mazzeo, S. Abate, *Chirality* **2016**, *28*, 696-707.

¹²⁸ J. L. Lunkley, D. Shirovani, K. Yamanari, S. Kaizaki, G. Muller, *J. Am. Chem. Soc.* **2008**, *130*, 13814-13815.

¹²⁹ F. Zinna, U. Giovanella, L. Di Bari, *Adv. Mater.* **2015**, *27*, 1791-1795.

¹³⁰ J. Kumar, T. Nakashima, T. Kawai, *J. Phys. Chem. Lett.* **2015**, *6*, 3445-3452.

¹³¹ Y. Yang, R. C. da Costa, D.-M. Smilgies, A. J. Campbell, M. J. Fuchter, *Adv. Mater.* **2013**, *25*, 2624-2628.

¹³² M. Li, S.-H. Li, D. Zhang, M. Cai, L. Duan, M.-K. Fung, C.-F. Chen, *Angew. Chem. Int. Ed.* **2018**, *57*, 2889-2893.

Instrumentation for CPL measurements

Although spectrophotometers used for measuring the CPL signal are mainly homemade instruments, some commercial CPL instrumentation can be found in the market. Most of these optical equipments (either commercial or homemade) follow the technological approach developed by Muller (Figure 22).¹³³ This configuration does not differ from a conventional spectrofluorimeter, thus, a CPL instrument can be considered, in fact, as a sophisticated fluorimeter where some extra modules are added in order to discriminate right- and left-circularly polarized lights. As for fluorescence measurements, CPL is measured at a right-angle detection method (90° excitation mode). Following the sample compartment, a photo-elastic modulator (PEM) in combination with a linear polarized are located in order to transform both non-circular and circular polarized light into linear polarized light which will be detected at the photon counter.

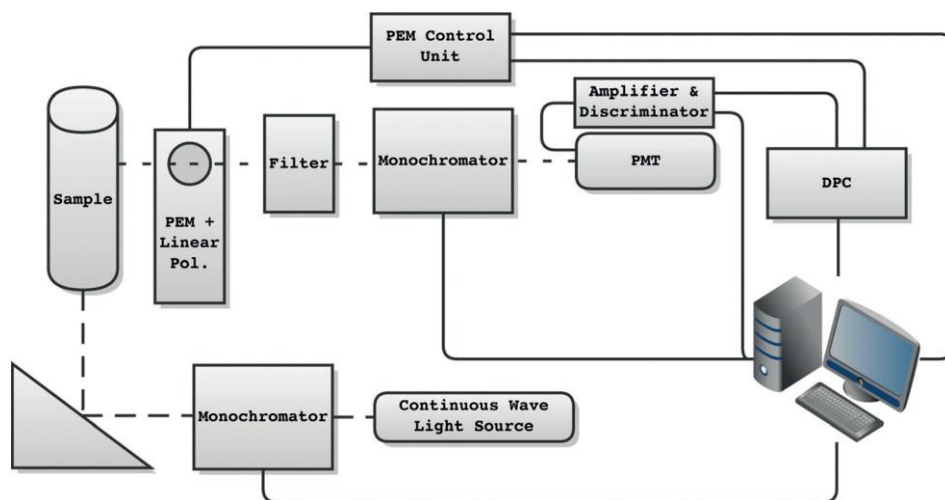


Figure 22. Schematic diagram for instrumentation used on CPL measurements.^{127a}

Indeed, it has been assumed for a long time that the main source of artifacts in the measurement of CPL is the linear polarization in the luminescence beam. This phenomenon is originated from the passing of this linearly polarized light through the very slightly birefringent PEM. Therefore, it is extremely important when performing CPL experiments to check for linear polarization in the

¹³³ G. Muller in *Luminescence of Lanthanide Ions in Coordination Compounds and Nanomaterials* (Ed.: A. de Bettencourt-Dias), Wiley, Hoboken 2014, pp. 77–124.

emission by looking at the signal at a frequency of $2 \times$ the frequency of the PEM acting as an oscillating quarter-wave plate.¹³⁴

1.3.2.1. CPL-active helical- and helicene-based compounds

Helicenes are structures that can be prepared as enantiomerically pure compounds or as racemic mixtures. If the interconversion barrier is high enough to avoid the racemization process, both enantiomers could be separated and their chiroptical properties studied separately. Thus, the preparation of enantiomerically pure helicene-compounds exhibiting CPL has been extensively reported during the last years, such as metalated helicenes, heteroatom-containing helicenes and carbohelicenes.¹³⁵ Helicene-based compounds with chiroptical properties have been also implemented on luminescent devices such as CPL-OLEDs.¹³¹

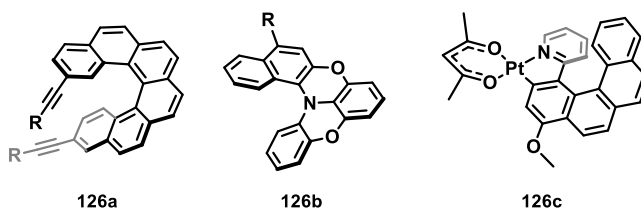


Figure 23. Selected examples of CPL-active helicene-containing compounds.

Despite of the wide variety on helicene-based organic molecules exhibiting CPL, the chiroptical properties studied on helicene-containing nanographenes and π -extended helicenes are reduced to the evaluation of their optical rotation, optical rotatory dispersion or circular dichroism. Thus, the introduction of CPL in graphene-related materials would afford new candidates of great potential for applications in the area of organic electronic materials, including circularly polarized ellipsometry-based tomography, optical computing and information processing.

On the other hand, binaphthyl derivatives and helical organic molecules have been reported as efficient structures with high levels of CPL. Binaphthyls are chiral and usually flexible compounds that can experience changes on their conformation due to external stimuli. When a particular chiral binaphthyl has intrinsic fluorescence and, therefore, chiral emission, these changes on the

¹³⁴ a) H. P. J. M. Dekkers, P. F. Moraal, J. M. Timper, J. P. Riehl, *Appl. Spectrosc.* **1985**, *39*, 818-821; b) J. P. Riehl, F. S. Richardson, *Chem. Rev.* **1986**, *86*, 1-16.

¹³⁵ W.-L. Zhao, M. Li, H.-Y. Lu, C.-F. Chen, *Chem. Commun.* **2019**, DOI: 10.1039/c9cc06861a.

molecular geometry will affect the chiroptical properties. Thus, binaphthyl derivatives have been reported as ON/OFF molecular switches showing CPL or not depending on the pH.¹³⁶ Similar acid/base switchings has been observed also in organic and organometallic helicenes.¹³⁷

This kind of chiroptical switching is not only reserved for acid/base conditions, coordinating compounds may tune their CPL response in presence or not of charged species such as anions or metal species. Thus, BINOL-boron derivatives have been reported as anion responsive compounds with controllable CPL.¹³⁸ On the other hand, it has been found that *o*-OPEs (*ortho*-Oligo(phenylene)ethynyls) are able to bind metal cations, which induce a helical arrangement of the molecular backbone thanks to chiral and promoting CPL response acting as CPL switches.¹³⁹

1.3.2.2. Laterally-extended helicenes as contorted nanographenes

The growing interest on helicenes in combination with the gold rush on nanographene chemistry has triggered the emergence of large PAHs and nanographenes arranged in a helical shape or embedding helicenes. Depending on how the aromatic rings are fused around a helicene moiety, it is mandatory to adopt a standard nomenclature for this new family of helicenes. Thus, classical helicenes are described as angularly fused aromatic rings (Figure 24A). Accordingly with the definition coined by T. Don Tilley and co-workers in 2017, increasing the size of a helicene by alternation of linear and angular ring fusion leads to “expanded helicenes” (Figure 24B). If the addition of extra rings takes place on the lateral extension of the π -system, we would talk about “laterally-extended helicenes” (Figure 24C). Finally, if the resulting structure possesses both

¹³⁶ K. Takaishi, M. Yasui T. Ema, *J. Am. Chem. Soc.* **2018**, *140*, 5334-5338.

¹³⁷ N. Saleh, B. Moore, M. Srebro, N. Vanthuyne, L. Toupet, J. A. G. Williams, C. Roussel, K. K. Deol, G. Muller, J. Autschbach, J. Crassous, *Chem. Eur. J.* **2015**, *21*, 1673-1681.

¹³⁸ H. Maeda, Y. Bando, K. Shimomura, I. Yamada, M. Naito, K. Nobusawa, H. Tsumatori, T. Kawai, *J. Am. Chem. Soc.* **2011**, *133*, 9266-9269.

¹³⁹ a) S. P. Morcillo, D. Miguel, L. Alvarez de Cienfuegos, J. Justicia, S. Abbate, E. Castiglioni, C. Bour, M. Ribagorda, D. J. Cárdenas, J. M. Paredes, L. Crovetto, D. Choquesillo-Lazarte, A. J. Mota, M. C. Carreno, G. Longhi, J. M. Cuerva, *Chem. Sci.* **2016**, *7*, 5663-5670; b) S. Resa, D. Miguel, S. Guisán-Ceinos, G. Mazzeo, D. Choquesillo-Lazarte, S. Abbate, L. Crovetto, D. J. Cárdenas, M. C. Carreño, M. Ribagorda, G. Longhi, A. J. Mota, L. Álvarez de Cienfuegos, J. M. Cuerva, *Chem. Eur. J.* **2018**, *24*, 2653-2662; c) P. Reiné, A. M. Ortuño, S. Resa, L. Álvarez de Cienfuegos, V. Blanco, M. J. Ruedas-Rama, G. Mazzeo, S. Abbate, A. Lucotti, M. Tommasini, S. Guisán-Ceinos, M. Ribagorda, A. G. Campaña, A. Mota, G. Longhi, D. Miguel, J. M. Cuerva, *Chem. Commun.* **2018**, *54*, 13985-13988.

structural features, we may describe these compounds as “laterally-extended expanded helicenes” (Figure 24D).¹⁴⁰

Due to the large number of reported organic molecules based on helicenes, this thesis will be focused on laterally-extended carbohelicenes, moreover, enantiopure examples will be highlighted. In this sense, purely hexagonal laterally-extended mono-helicenes will be described in the first instance and finishing with multihelicene-containing nanographenes.

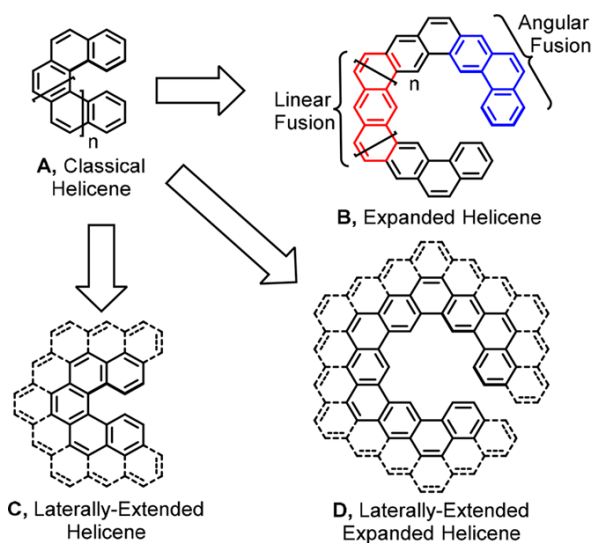


Figure 24. Classification of larger helicenes.¹⁴⁰

As a simple example of enantiopure laterally- π -extended [n]helicenes, I. Starý, I. G. Stará and co-workers reported the preparation of dibenzo[n]helicenes by [2+2+2]cycloisomerization of aromatic triynes (**127**, Figure 25).¹⁴¹ Lately, the same authors reported the preparation of an extended analogue to **127** using an alkyne cyclotrimerization reaction as the final step. The authors measured and compared the ECD spectra and the optical rotation of [7]helicene, **127** and **129** finding that the optical rotation on **129** was much higher than that on **127** and similar to that of parent [7]helicene (Figure 25).¹⁴² In 2018, K. Tanaka and co-workers reported the enantioselective preparation of dibenzo[7]helicene derivatives by rhodium-catalyzed [2+2+2]

¹⁴⁰ G. R. Kiel, S. C. Patel, P. W. Smith, D. S. Levine, T. Don Tilley, *J. Am. Chem. Soc.* **2017**, *139*, 18456-18459.

¹⁴¹ A. Jančařík, J. Rybaček, K. Cocq, J. V. Chocholoušová, J. Vacek, R. Pohl, L. Bednářová, P. Fiedler, I. Čiśařová, I. G. Stará, I. Starý, *Angew. Chem. Int. Ed.* **2013**, *52*, 9970-9975.

¹⁴² M. Buchta, J. Rybaček, A. Jančařík, A. A. Kudale, M. Buděšínský, J. V. Chocholoušová, J. Vacek, L. Bednářová, I. Čiśařová, G. J. Bodwell, I. Starý, I. G. Stará, *Chem. Eur. J.* **2015**, *21*, 8910-8917.

cycloaddition reactions (**127**, Figure 25).¹⁴³ They also reported the CPL spectra of the prepared compound with a g_{lum} value of -2.2×10^{-3} at 494 nm. Remarkably, a change in the signal is observed, since the less energetic band on the CD spectra does not show the same sign to the CPL band.

Recently, K. Matsuda and co-workers reported the preparation of hexa-*peri*-hexabenz[7]helicene **128**, which can be considered as a helical analogue to HBC. The authors reported an elegant synthetic route starting from simple molecules and the final enantiomers were separated by chiral stationary phase HPLC (CSP-HPLC) and their CD spectra evaluated.¹⁴⁴

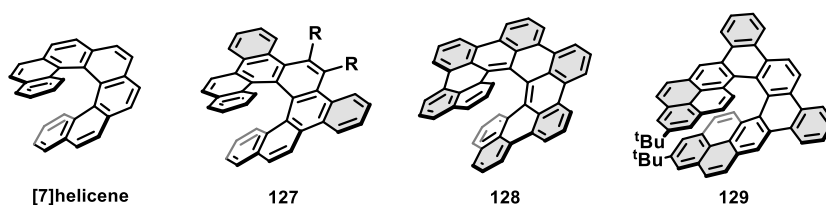


Figure 25. [7]helicene and selected laterally-extended [7]helicenes.

Recently, N. Jux and co-workers have coined a novel terminology for a new group of compounds, named “superhelicenes”. This newborn family consists of extended PAHs, such as HBC units, arranged in a helical shape. Superhelicenes are a perfect model for the study of graphene helicoids such as graphene nanosprings or nanosolenoids, which could exhibit superior properties than multilayer graphene of similar size in terms of controlling thermal conductivity,¹⁴⁵ tensile¹⁴⁶ or magnetic properties.¹⁴⁷

The first compound coined as superhelicene was reported in 2018,¹⁴⁸ which consisted of two HBC units linked through an oxa[7]superhelicene (**132**, Scheme 29). The authors reported a synthetic pathway starting from diphenyl ether that was transformed into **130** after aromatic bromination and double Sonogashira reaction with *p*-*tert*-butylphenylacetylene. The backbone of **130** was extended by a two-fold Diels-Alder reaction and the final Scholl reaction was achieved

¹⁴³ R. Yamano, Y. Shibata, K. Tanaka, *Chem. Eur. J.* **2018**, *24*, 6364-6370.

¹⁴⁴ Y. Nakakuki, T. Hirose, H. Sotome, H. Miyasaka, K. Matsuda, *J. Am. Chem. Soc.* **2018**, *140*, 4317-4326.

¹⁴⁵ H. Zhan, G. Zhang, C. Yang, Y. Gu, *J. Phys. Chem. C* **2018**, *122*, 7605-7612.

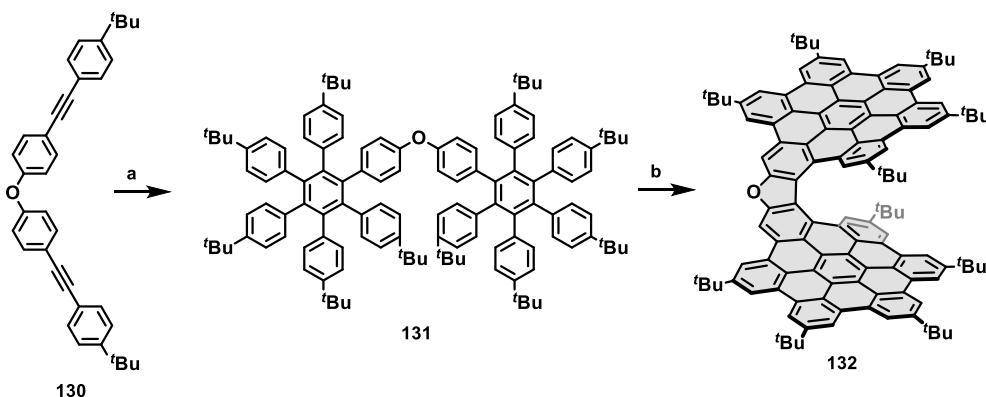
¹⁴⁶ H. Zhan, Y. Zhang, C. Yang, G. Zhang, Y. Gu, *Carbon* **2017**, *120*, 258-264.

¹⁴⁷ F. Xu, H. Yu, A. Sadrzadeh, B. I. Yakobson, *Nano Lett.* **2016**, *16*, 34-39.

¹⁴⁸ D. Reger, P. Haines, F. W. Heinemann, D. M. Guldi, N. Jux, *Angew. Chem. Int. Ed.* **2018**, *57*, 5938-5942.

by using a combination of 2,3-dichloro-5,6-dicyano-1,4-benzoquinone (DDQ) and triflic acid. The authors highlighted that such ring closure to form a furan moiety was unprecedented.

The authors were able to obtain ^1H and ^{13}C NMR spectra of several derivatives, confirming that helical nanographenes exhibit higher solubility than those that are completely planar. Photophysical analysis by means of UV-Vis and fluorescence spectra showed a red-shifted absorbance in comparison with related planar HBC derivatives, which is in concordance with a delocalization of the electron density between the HBC units. Moreover, the fluorescence quantum yield ranged an extraordinary 80 – 85%. On the other hand, the electrochemical band gap was evaluated as 2.4 eV in concordance with that derived from the absorption and fluorescence spectra (2.4 eV) and lower than that of HBC derivatives. Unfortunately, no racemic resolution was reported and, therefore, their chiroptical properties were not studied.



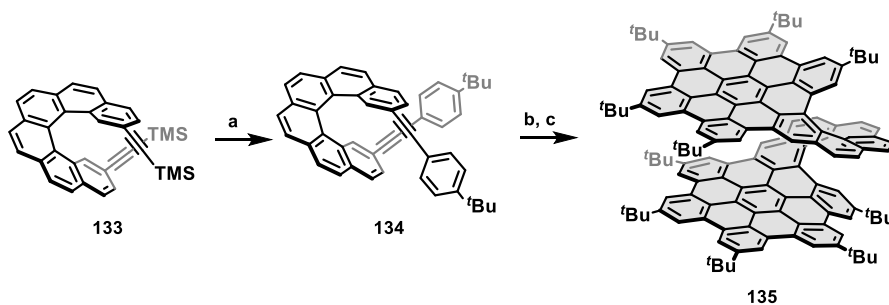
Scheme 29. Last steps on the reported preparation of oxa[7]superhelicene **132**; a) Diels-Alder reaction; b) DDQ, TfOH.

The same year, almost simultaneously, N. Martín and co-workers reported the first helical bilayer nanographene, consisting of two HBC units linked by a carbo[10]helicene (**135**).¹⁴⁹ The authors reported a straightforward synthesis starting from enantiopure *M*-**133** (Scheme 30), which was deprotected and subjected to Sonogashira coupling with *p*-tert-butyl iodobenzene. Then two-fold Diels-Alder reaction over the alkynes with *tetrakis*-(*p*-tert-butylphenyl)-cyclopentadienone

¹⁴⁹ P. J. Evans, J. Ouyang, L. Favereau, J. Crassous, I. Fernández, J. Perles, N. Martín, *Angew. Chem. Int. Ed.* **2018**, *57*, 6774-6779.

1. Background

afforded the oligophenylene precursor that was finally transformed in **135** by using FeCl_3 (Scheme 30). The *tert*-butyl groups provide enough solubility to the compound, thus, the corresponding ^1H and ^{13}C NMR spectra of **135** was reported. Moreover, the X-ray structure was included unequivocally confirming its structure and providing information about the disposition of the HBC units. Remarkably, both HBCs are disposed almost in a parallel disposition with the carbon atoms aligned over each other as in an AA-stacked graphite.



Scheme 30. Synthesis of helical bilayer nanographene **135**.

Despite being an extended conjugated system, the bilayer graphene **135** shows a UV-Vis absorption maxima centered at the same range of wavelengths in comparison with hexa-*tert*-butylhexa-*peri*-hexabenzocoronene (tBu-HBC). The authors reported the CD spectrum of the *M* enantiomer where two Cotton effects could be identified at low concentrations. Remarkably, when increasing the concentration, the CD signal evolves to a single negative Cotton effect shifted to lower energies, suggesting that the formation of aggregates at higher concentrations takes place in a chiral fashion (Figure 26).

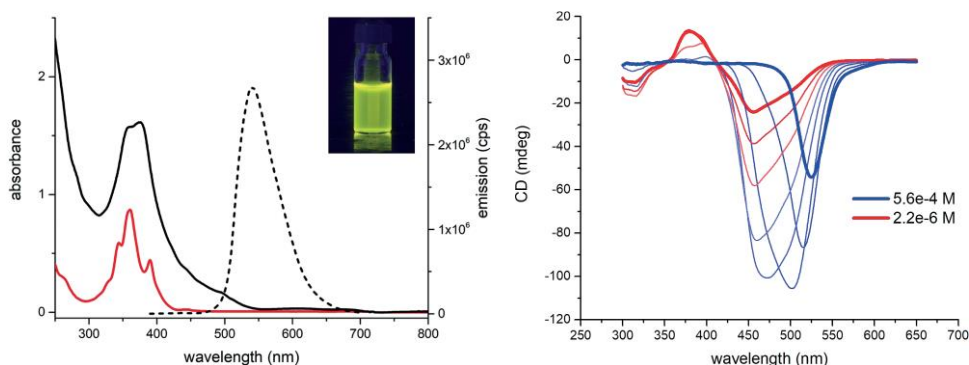
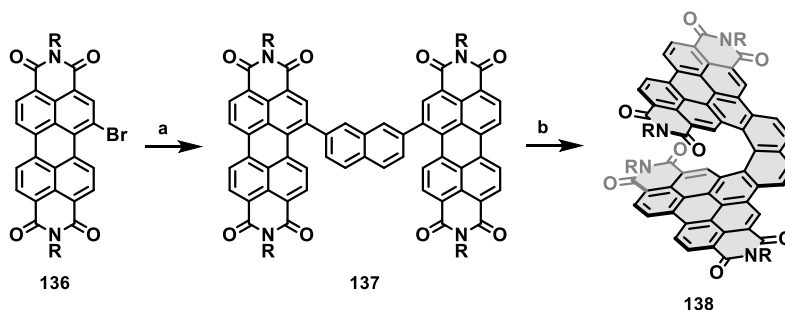


Figure 26. Left: UV-Vis and fluorescence spectra of **135** (black) and UV-Vis spectrum of *t*BuHBC (red); Right: CD spectrum of *M*-**135**.¹⁴⁹

Structurally related π -extended helicenes were prepared by C. Nuckolls and co-workers, who reported the preparation and characterization of superhelicenes based on perylene-diimides (Scheme 31).¹⁵⁰ The enantiopure compounds show extremely intense Cotton effects at their CD spectra. Despite the extraordinary (chir)optical properties exhibited by this kind of compounds, with red-shifted absorbance and fluorescence maxima along with high luminescence quantum yields, no CPL spectra were reported.



Scheme 31. Synthesis of PDI-based superhelicenes **CXXIX**. a) Suzuki coupling; b) $h\nu$, I_2 .

It has been probed that the introduction of a tridimensional moiety such helicenes into graphene molecules results in an enhancement of their solubility and, therefore, allowing a unequivocal characterization of its structure in solution along with the evaluation of their optical and chiroptical properties. The recently created family of superhelicenes attempts to understand the properties of helical graphene. Despite of the outstanding reported molecules, new approaches to fully laterally-extended helicenes are yet to be explored.¹⁵¹

1.3.2.3. Multiple helicenes as contorted nanographenes

In addition to simple helical π -conjugated systems, nanographenes showing multihelicity have gained considerable attention in recent years.¹⁵² Multihelicity provides plural electronic states and molecular dynamics, and π -extension often causes a dramatic change of electronic structure.

¹⁵⁰ a) N. J. Schuster, D. W. Paley, S. Jockusch, F. Ng, M. L. Steigerwald, C. Nuckolls, *Angew. Chem. Int. Ed.* **2016**, *55*, 13519-13523; b) N. J. Schuster, R. H. Sánchez, D. Bukharina, N. A. Kotov, N. Berova, F. Ng, M. L. Steigerwald, C. Nuckolls, *J. Am. Chem. Soc.* **2018**, *140*, 6235-6239; c) M. Milton, N. J. Schuster, D. W. Paley, R. H. Sánchez, F. Ng, M. L. Steigerwald, C. Nuckolls, *Chem. Sci.* **2019**, *10*, 1029-1034.

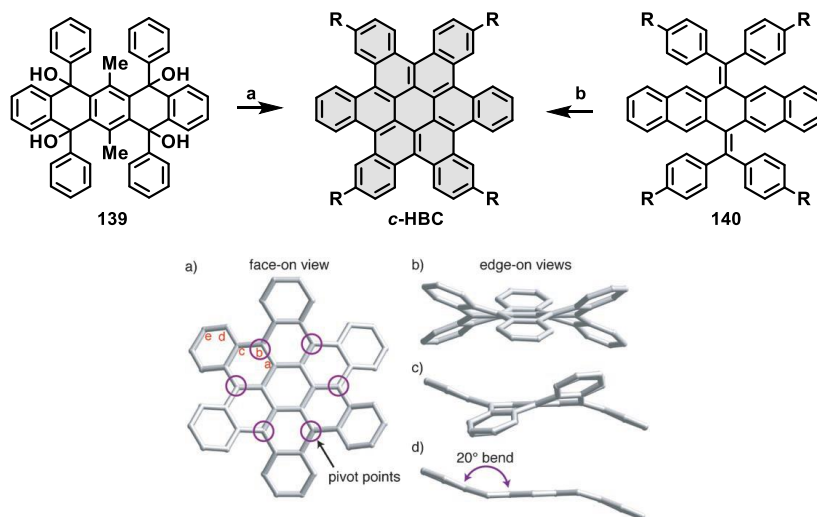
¹⁵¹ M. Daigle, D. Miao, A. Lucotti, M. Tommasini, J.-F. Morin, *Angew. Chem. Int. Ed.* **2017**, *56*, 6213-6217.

¹⁵² C. Li, Y. Yang, Q. Miao, *Chem. Asian J.* **2018**, *13*, 884-894.

1. Background

Both of them also define three dimensional molecular shape and molecular packing in crystalline state. These characteristics of multihelical and extended π -systems expand the applicability of helicenes toward crystal engineering, supramolecular organization or chiral sensing.

According to the classification made by K. Müllen and co-workers (Figure 13),⁴⁵ where the term nanographene is only applied for PAHs with a size of more than 1 nm, HBC can be considered as the smallest nanographene. In this sense, the smallest multihelical nanographene would be its structural isomer, the hexa-*cata*-hexabenzocoronene (*c*-HBC). The contortion on *c*-HBC is due to the six embedded [4]carbohelicenes that form the aromatic structure. The first synthesis of *c*-HBC dates back to 1965, where Clar and co-workers reported its preparation under harsh conditions.¹⁵³ More recently, C. Nuckolls and co-workers have reported a novel methodology for the preparation of substituted *c*-HBC and the evaluation of their electronic properties as active layer in field-effect transistors. This new strategy not only increased the yield on the final compound, but also allowed the introduction of long chains that enhanced its solubility.¹⁵⁴



Scheme 32. Top: First reported synthesis of *c*-HBC and methodology followed by C. Nuckolls and co-workers. a) Cu, 400°C, 2%; b) I₂, hv, 83-87% (R=OC₁₂H₂₅). Bottom: Crystal structure of *c*-HBC.¹⁵⁴

¹⁵³ E. Clar, J. F. Stephen, *Tetrahedron* **1965**, *21*, 467-470.

¹⁵⁴ S. Xiao, M. Myers, Q. Miao, S. Sanaur, Keliang Pang, Michael L. Steigerwald, C. Nuckolls, *Angew. Chem. Int. Ed.* **2005**, *44*, 7390-7394.

Double-helicene-containing nanographenes

The configuration instability of parent carbo[4]helicene restrain its isolation in an enantioenriched form at room temperature, unless substituents are placed to increase its configurational stability. On the other hand, carbo[5]helicenes can be resolved into enantiomers, but the enantioenriched samples fully racemize over several days under ambient conditions. Configurational stability of helicenes with $n < 6$ can be improved by installment of substituents at various positions.¹⁵⁵

Remarkably, the isomerization barriers on compounds with more than one helicene in the structure are known to be higher than those formed by monohelicene substructures. This fact could be observed on a series of PAHs bearing two or three carbo[5]helicenes when compared to parent carbo[5]helicene (24.1 kcal·mol⁻¹). It is mandatory to remark that the presence of more than one chiral entity originates different diastereomers with different interconversion energies between them. Therefore, special attention is given to the interconversion energy from the more stable conformation to that of higher energy. Thus, the interconversion barrier for parent hexabenzoperylene (HBP, **141a**, Figure 27) was reported to be 27.4 kcal·mol⁻¹,¹⁵⁶ slightly lower than its derivative bearing long chains (**141b**) that was estimated to be 28.7 kcal·mol⁻¹.¹⁵⁷ Since the direct fusion of two carbo[5]helicenes would lead to an unstable diradicaloid structure,¹⁵⁸ HBP would be the simplest analogue to a double carbo[5]helicene sharing the central ring. Remarkably, when four extra benzene rings are attached to the HBP skeleton, four [4]helicenes could be formed (**142**). In that case, the isomerization barrier is increased up to 30.9, suggesting that the presence of these new [4]helicenes plays a key role.¹⁵⁹

On the other hand, the fusion of two carbo[5]helicenes without sharing any benzene ring (**143**, Figure 27) leads to a structure with an isomerization barrier of 31.8 kcal·mol⁻¹, meaning 4.4 kcal·mol⁻¹ more than that reported for the parent carbo[5]helicene.¹⁶⁰ The isomerization barrier

¹⁵⁵ P. Ravat, R. Hinkelmann, D. Steinebrunner, A. Prescimone, I. Bodoky, M. Juriček, *Org. Lett.* **2017**, *19*, 3707-3710.

¹⁵⁶ H. Marom, S. Pogodin, I. Agranat, *Polycyclic Aromat. Compd.* **2007**, *27*, 295-310.

¹⁵⁷ J. Luo, X. Xu, R. Mao, Q. Miao, *J. Am. Chem. Soc.* **2012**, *134*, 13796-13803.

¹⁵⁸ J. Liu, R. Berger, K. Müllen, X. Feng in *From Polyphenylenes to Nanographenes and Graphene Nanoribbons*. *Advances in Polymer Science* (Ed.: K. Müllen, X. Feng), Springer, Cham 2017, pp. 1–32.

¹⁵⁹ Y. Yang, L. Yuan, B. Shan, Z. Liu, Q. Miao, *Chem. Eur. J.* **2016**, *22*, 18620-18627.

¹⁶⁰ H. Kashiwara, T. Asada, K. Kamikawa, *Chem. Eur. J.* **2015**, *21*, 6523-6527.

1. Background

of an extended analogue to **143** was reported by K. Müllen and co-workers.¹⁶¹ This extended terrylene (**144**) showed an isomerization barrier of 29.0 kcal·mol⁻¹, slightly lower than **143**. However, this isomerization barrier was calculated just by observing a decrease on the CD signal decay after heating **144** at 80°C for 6h, therefore, a proper estimation of the isomerization barrier is lacking. Furthermore, note that for **143** two additional carbo[4]helicene units are formed on the structure which may have an effect on the isomerization barrier as seen for compound **142**. Therefore, this decreasing on the isomerization barrier could not be associated to the extended structure as, in fact, it is expected to be higher due to the increased rigidity on extended analogues. Unfortunately, no isomerization barrier was reported for compound **145**,¹⁶² which would be directly comparable to that of **143** to quantify if the extension would affect the isomerization barrier.

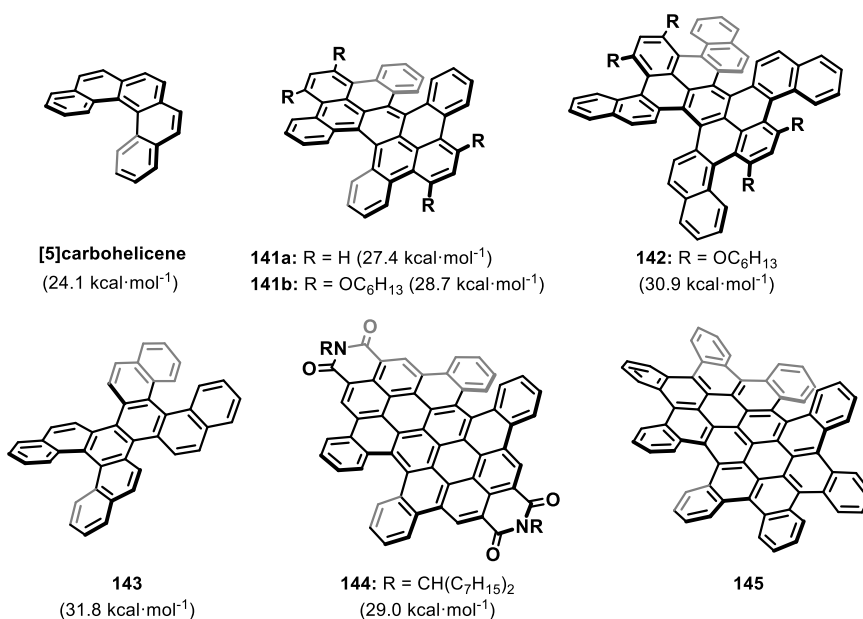


Figure 27. Carbo[5]helicene and selected double[5]carbohelicenes. Their isomerization barriers are shown in brackets.

¹⁶¹ C. L. Eversloh, Z. Liu, B. Müller, M. Stangl, C. Li, K. Müllen, *Org. Lett.* **2011**, *13*, 5528-5531.

¹⁶² S. Xiao, S. J. Kang, Y. Wu, S. Ahn, J. B. Kim, Y.-L. Loo, T. Siegrist, M. L. Steigerwald, H. Li, C. Nuckolls, *Chem. Sci.* **2013**, *4*, 2018-2023.

This tendency is also observed on carbo[6] and [7]helicene when compared with their respective double helicenes. The double carbo[6]helicene reported by K. Itami and co-workers (**146**, Figure 28) exhibits a calculated interconversion barrier of $43.5 \text{ kcal}\cdot\text{mol}^{-1}$.¹⁶³ On the other hand, for the double carbo[7]helicene reported by K. Müllen and co-workers (**147**, Figure 28) it was established as $46.0 \text{ kcal}\cdot\text{mol}^{-1}$ by DFT methods, while its extended version (**148**, Figure 28) shows a interconversion barrier of $46.4 \text{ kcal}\cdot\text{mol}^{-1}$ suggesting that the laterally π -extension may increase the interconversion barrier of multiple helicenes.¹⁶⁴ These values are higher than those of their respective monohelicenes (36.2 and $41.7 \text{ kcal}\cdot\text{mol}^{-1}$ for carbo[6] and [7]helicene respectively).¹⁶⁵

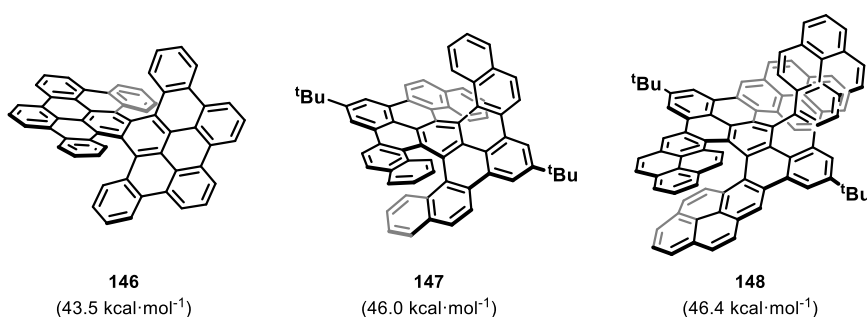


Figure 28. Selected double [6] and carbo[7]helicenes. Their theoretical isomerization barriers are shown in brackets.

Triple helicene-containing nanographenes

The arrangement of three carbo[5]helicenes into a single PAH would lead to different propeller shapes depending on the shared rings. Hexabenzotriphenylene (HBT, **149**, Figure 29) was the first reported triple carbo[5]helicene,¹⁶⁶ where each helicene shares three benzene units with the other two. A conformational study on **149** afforded a detailed energy profile analysis of the different diastereomers. Thus, the interconversion free energy was experimentally calculated by measuring the rate constant at different temperatures by using the Eyring-Polanyi methodology

¹⁶³ T. Fujikawa, Y. Segawa, K. Itami, *J. Am. Chem. Soc.* **2015**, *137*, 7763-7768.

¹⁶⁴ a) Y. Hu, X.-Y. Wang, P.-X. Peng, X.-C. Wang, X.-Y. Cao, X. Feng, K. Müllen, A. Narita, *Angew. Chem. Int. Ed.* **2017**, *56*, 3374-3378; b) Y. Hu, G. M. Paternò, X.-Y. Wang, X.-C. Wang, M. Guizzardi, Q. Chen, D. Schollmeyer, X.-Y. Cao, G. Cerullo, F. Scotognella, K. Müllen, A. Narita, *J. Am. Chem. Soc.* **2019**, *141*, 12797-12803.

¹⁶⁵ R. H. Janke, G. Haufe, E.-U. Würthwein, J. H. Borkent, *J. Am. Chem. Soc.* **1996**, *118*, 6031-6035.

¹⁶⁶ a) D. Peña, D. Pérez, E. Guitián, L. Castedo, *Org. Lett.* **1999**, *1*, 1555-1557; b) D. Peña, A. Cobas, D. Pérez, E. Guitián, L. Castedo, *Org. Lett.* **2000**, *2*, 1629-1632.

and finding a free energy barrier, from the C_2 - to the D_3 -symmetric diastereomer, of 26.2 kcal·mol⁻¹.

In 2017, S. Watanabe and co-workers reported a propeller triple helicene in which the three carbo[5]helicenes share two benzene rings with his neighbor (trinaphtotriphenylene, TNT, **150**, Figure 29).¹⁶⁷ The conformational study, underpinned by NMR, confirmed that in the most stable geometry all helicenes possess the same configuration, hence, *PPP* (or *MMM*). The experimental value of the isomerization barrier (from *PPP* to *PPM*) was established as 27.4 kcal·mol⁻¹, slightly higher than that reported for **149**. Furthermore, T. Mori and co-workers compared the theoretical and experimental CD and CPL spectra of single carbo[5]helicene and **149**, although no CPL spectra was obtained for **150** (Figure 30).¹⁶⁸

When six extra benzene rings are fused to the bay regions of **149**, three extra carbo[5]helicene moieties arise. The synthesis of **151** was simultaneously and independently firstly reported by M. Gingras and K. Kamikawa. The former used a synthetic procedure based on a Yamamoto-type cyclotrimerization reaction,¹⁶⁹ while the later took advantage of the well-known aryne chemistry to form triphenylene derivatives.¹⁷⁰ The presence of six carbohelicenes lead to a wide variety of conformers where the most stable ones are those with the same configuration on the inner helicenes and the opposite on the outer ones. Additionally, one year later, the group of D. Peña reported the on-surface assisted preparation of an extended nanographene starting from **151**, which was prepared by aryne chemistry, followed by cyclodehydrogenative reaction of the six carbohelicenes.¹⁷¹ Recently, an analogue to **151** bearing carbo[7]helicenes on the outer part instead of [5]carbohelicenes has been reported by P. Rabat and co-workers.¹⁷²

¹⁶⁷ H. Saito, A. Uchida, S. Watanabe, *J. Org. Chem.* **2017**, *82*, 5663-5668.

¹⁶⁸ H. Tanaka, Y. Kato, M. Fujiki, Y. Inoue, T. Mori, *J. Phys. Chem. A* **2018**, *122*, 7378-7384.

¹⁶⁹ V. Berezhaia, M. Roy, N. Vanthuyne, M. Villa, J.-V. Naubron, J. Rodriguez, Y. Coquerel, M. Gingras, *J. Am. Chem. Soc.* **2017**, *139*, 18508-18511

¹⁷⁰ T. Hosokawa, Y. Takahashi, T. Matsushima, S. Watanabe, S. Kikkawa, I. Azumaya, A. Tsurusaki, K. Kamikawa, *J. Am. Chem. Soc.* **2017**, *139*, 18512-18521.

¹⁷¹ R. Zuzak, J. Castro-Esteban, P. Brandimarte, M. Engelund, A. Cobas, P. Piątkowski, M. Kolmer, D. Pérez, E. Guitián, M. Szymonski, D. Sánchez-Portal, S. Godlewski D. Peña, *Chem. Commun.* **2018**, *54*, 10256-10259.

¹⁷² F. Zhang, E. Michail, F. Saal, A.-M. Krause, P. Ravat, **2019**, *25*, 16241-16245.

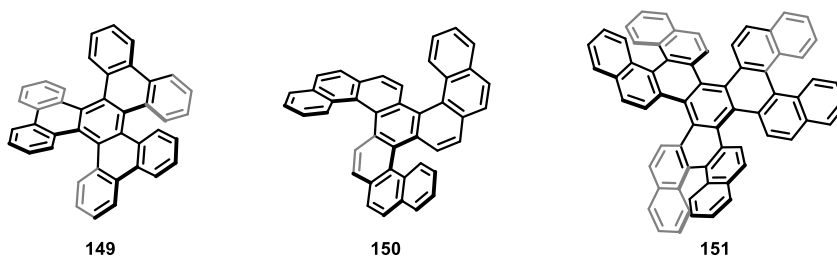


Figure 29. Selected propeller-shaped triple carbo[5]helicenes.

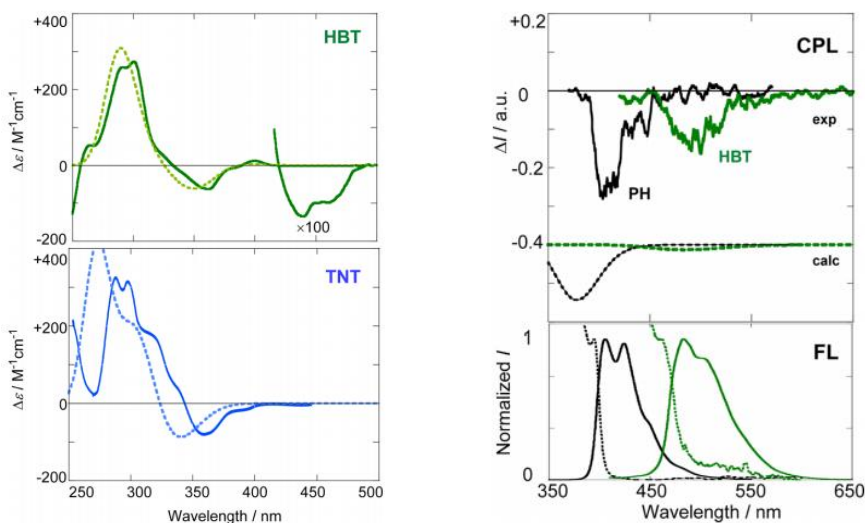


Figure 30. Left: Experimental (solid lines) and calculated (dotted lines) CD spectra of **149** (HBT, green) and **150** (TNT, blue). Right: Experimental (solid lines) and calculated (dotted lines) fluorescence and CPL spectra of carbo[5]helicene (PH, black) and **149** (green).¹⁶⁸

Extended nanographenes containing multiple helicene

Purely hexagonal PAHs containing multiple helicenes are reduced to examples where the helicene moiety is vaguely surrounded by aromatic rings, hence, laterally extension is missing. Recently, large nanographenes molecules containing laterally extended helicenes are gaining interest among chemists. Recently, the group of K. Müllen reported the preparation of a series of *c*-HBC derivatives containing four laterally extended carbo[5]helicenes (**152**, Figure 31).¹⁷³

¹⁷³ Y. Chen, T. Marszalek, T. Fritz, M. Baumgartner, M. Wagner, W. Pisula, L. Chen, K. Müllen, *Chem. Commun.* **2017**, 53, 8474-8477.

These contorted derivatives are stronger donor materials compared to conventional flat coronenes or HBCs.

Furthermore, during the last year, the group of J. Wang has carried out an outstanding work in this field reporting a series of multihelicene-containing nanographenes based on HBCs. The first reported example was an hexapole[7]helicene, which is based on a central HBC unit surrounded by six carbo[7]helicene units (**153**, Figure 31). The final compound was characterized by NMR, MS, STM and SCXRD. Its optical and chiroptical properties were evaluated (except for CPL) and the cyclic voltammetry showed up to six reversible oxidation waves.¹⁷⁴ Moreover, they reported its N-doped analogue, which shows lower band gap and increased CD signal.¹⁷⁵

Following the same methodology, consisting in the cyclotrimerization of extended diphenylacetylenes, the authors prepared the extended version, a hexapole [9]helicene. In this case, no enantiopure samples were measured due to problems related with the separation on chiral HPLC. Nevertheless, an outstanding optical band gap value of 1.55 eV ($\lambda = 800$ nm) was measured and underpinned by DFT calculations (1.66 eV).¹⁷⁶

Finally, their flagship compound was the nanographene propeller containing 258 conjugated carbon atoms, which represents the largest three-dimensional conjugated polycyclic aromatic hydrocarbon ever prepared using scalable solution chemistry (**154**, Figure 31).¹⁷⁷ The nanographene molecule consists on seven fused HBC units where the crowdedness lead to six carbo[7]helicenes. The authors followed a synthetic route based on that reported by K. Müllen for the preparation of the graphite disk containing 222 carbon atoms.¹⁰⁵

The structure of the reported compound was confirmed by means of NMR, MS, and SCXRD despite of its size (3.50 nm width and 1.25 height). The compound showed an absorption spectrum ranging from 300 to 800 nm with more than half of the spectral range exhibiting an extinction coefficient larger than $100,000 \text{ M}^{-1}\cdot\text{cm}^{-1}$. Although the fluorescence quantum yield was low (0.016), the compound exhibits an emission spectra ranging from 750 to 1200 nm.

¹⁷⁴ Y. Zhu, Z. Xia, Z. Cai, Z. Yuan, N. Jiang, T. Li, Y. Wang, X. Guo, Z. Li, S. Ma, D. Zhong, Y. Li, J. Wang, *J. Am. Chem. Soc.* **2018**, *140*, 4222-4226.

¹⁷⁵ X. Guo, Z. Yuan, Y. Zhu, Z. Li, R. Huang, Z. Xia, W. Zhang, Y. Li, J. Wang, *Angew. Chem. Int. Ed.* **2019**, *58*, 2-9.

¹⁷⁶ Y. Wang, Z. Yin, Y. Zhu, J. Gu, Y. Li, J. Wang, *Angew. Chem. Int. Ed.* **2019**, *58*, 587-591.

¹⁷⁷ Y. Zhu, X. Guo, Y. Li, J. Wang, *J. Am. Chem. Soc.* **2019**, *141*, 5511-5517.

Remarkably, the CD spectra of both enantiomers *PPPPPP/MMMMMM* showed a record-high Cotton effect in the visible spectrum with $|\Delta\epsilon|$ values of 1182 and 1090 $\text{M}^{-1}\cdot\text{cm}^{-1}$ at 374 and 405 nm, respectively.

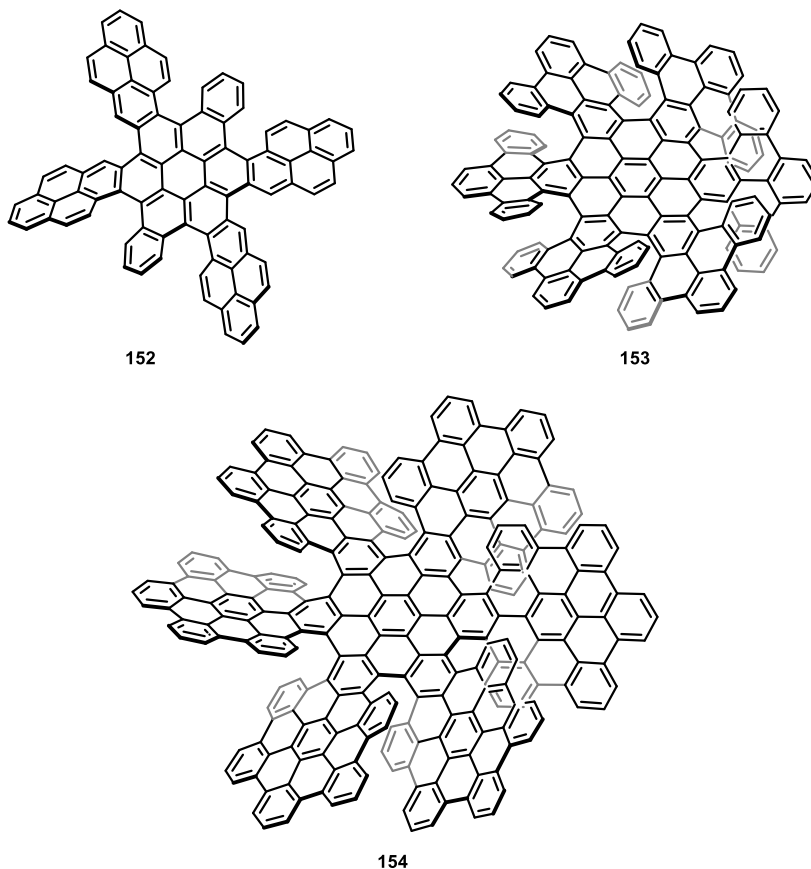


Figure 31. *c*-HBC-based nanographene containing four [5]carbohelicenes (left), hexapole[7]helicene (right) and HBCs-based hexapole[7]helicene (bottom).

1.3.3. Nanographenes containing non-hexagonal rings

As introduced in section 1.1.2., during the preparation of graphene different defects may arise. The presence of these defects is directly related with a modification of the properties of pristine graphene. Most common defects are mainly composed by the introduction non-hexagonal rings into the hexagonal lattice, breaking the planarity in some cases.

Nanographenes can be defined as molecular models for the study of graphene-related materials. In this sense, purely hexagonal nanographenes have been extensively studied by K. Müllen's group and many others as reported on previous sections. Regarding the introduction of curvatures on π -systems, carbohelicenes have been pointed as versatile moieties, which not only enhance solubility on PAHs, but also introduce chirality. Helicenes and cyclophanes are described as exoskeletal approaches for the introduction of distortion in nanographenes.¹⁶³

On the other hand, endoskeletal approaches are based on the introduction of non-hexagonal rings into the aromatic backbone. These structural motifs are then directly related to defective graphene and therefore nanographenes bearing this feature may serve as models for the study of the influence of defects on the geometry and properties of pristine graphene.

Furthermore, the introduction of non-hexagonal rings into a hexagonal lattice of sp^2 carbon atoms is mandatory in order to reproduce the 3D structure of curved nanocarbons.¹⁷⁸ This family of carbon allotropes is a relatively unexplored group of materials, predicted to exhibit interesting properties. In 1991, A. L. Mackay and H. Terrones proposed a 3D arrangement of sp^2 carbon atoms known as Mackay crystal or Schwarzite, since all carbons are placed on the Schwarz minimal P surface (Figure 32).¹⁷⁹ This first 3D nanocarbon solely consists of a combination of six- and eight-membered rings, however, in 1992, a negatively curved carbon crystal with six- and seven-membered rings was also identified as a class of Mackay crystal.¹⁸⁰

In addition to Schwarzites, various other exotic nanocarbons with negative curvatures can be constructed by incorporating seven- or/and eight-membered rings.¹⁸¹ Representative examples are shown on Figure 28, where the inclusion of heptagons are basic on the formation of fullerene dimers,¹⁸² as joint of CNTs with different diameters,¹⁸³ for the junction of several CNTs,¹⁸⁴ and on

¹⁷⁸ Y. Segawa, H. Ito, K. Itami, *Nat. Rev. Mater.* **2016**, *1*, 1-14.

¹⁷⁹ A. L. Mackay, H. Terrones, *Nature* **1991**, *352*, 762.

¹⁸⁰ T. Lenosky, X. Gonze, M. Teter, V. Elser, *Nature* **1992**, *355*, 333-335.

¹⁸¹ E. Ōsawa, M. Yoshida, M. Fujita, *MRS Bull.* **1994**, *19*, 33-38.

¹⁸² a) N. Kaur, K. Dharamvir, V. K. Jindal, *Chem. Phys.* **2008**, *344*, 176-184; b) A. Takashima, T. Nishii, J. Onoe, *J. Phys. D: Appl. Phys.* **2012**, *45*, 485302.

¹⁸³ D. N. Weldon, W. J. Blau, H. W. Zandbergen, *Chem. Phys. Lett.* **1995**, *241*, 365-372.

¹⁸⁴ D. Wei, Y. Liu, *Adv. Mater.* **2008**, *20*, 2815-2841.

negatively curved graphene sheet.¹⁸⁵ All the above mentioned examples agree to the presence of [7] or [8]circulene/s as the inductive moiety for saddle topology.

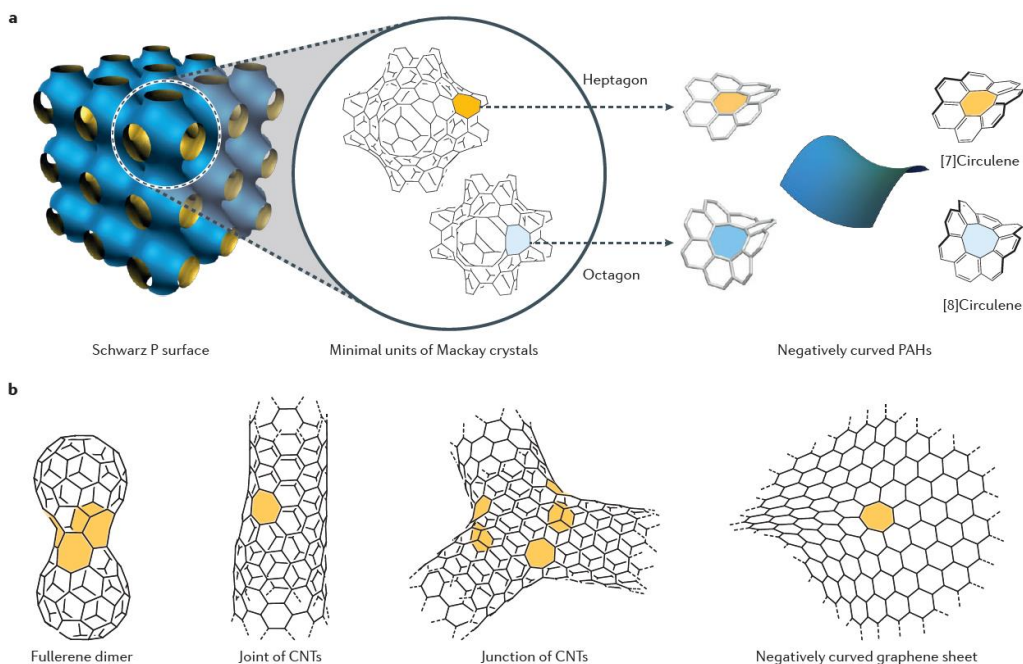


Figure 32. Examples of 3D nanocarbons containing embedded heptagons and octagons.¹⁷⁸

1.3.3.1. [*n*]circulenes

The presence of non-hexagonal rings into a hexagonal network has its illustrative example on [*n*]circulenes. This family of PAHs are characterized for featuring a central *n*-sided ring fully surrounded by fused six-membered benzenoid rings. Four types of [*n*]circulenes can be identified: positively curved ($n = 3 - 5$), planar ($n = 6$), negatively curved ($n = 7 - 16$) and helical ($n > 16$).¹⁸⁶

In positively curved circulenes, the internal ring exhibits angles smaller than 120° , thus, the polygon causes a distortion of the surrounding benzenoid rings and creates strain that forces the planar form to adopt a bowl-shaped geometry. In case of the central ring formed by a six membered ring, no distortion would be observed since the angles would match with those of the

¹⁸⁵ S. Iijima, T. Ichihashi, Y. Ando, *Nature* **1992**, 356, 776-778.

¹⁸⁶ M. Rickhaus, M. Mayor, M. Juriček, *Chem. Soc. Rev.* **2017**, 46, 1643-1660.

1. Background

surrounding rings (120°), therefore, [6]circulene (coronene) will show a planar geometry. In negatively curved circulenes, the values of the internal angles are larger than 120° . As a result, an internal ring with $n = 7 - 16$ induces ring strain that forces the planar form to adopt a saddle-shaped geometry. According to calculations, when the number of ring sides are higher than sixteen, circulenes start to adopt unique helical geometries.¹⁸⁷

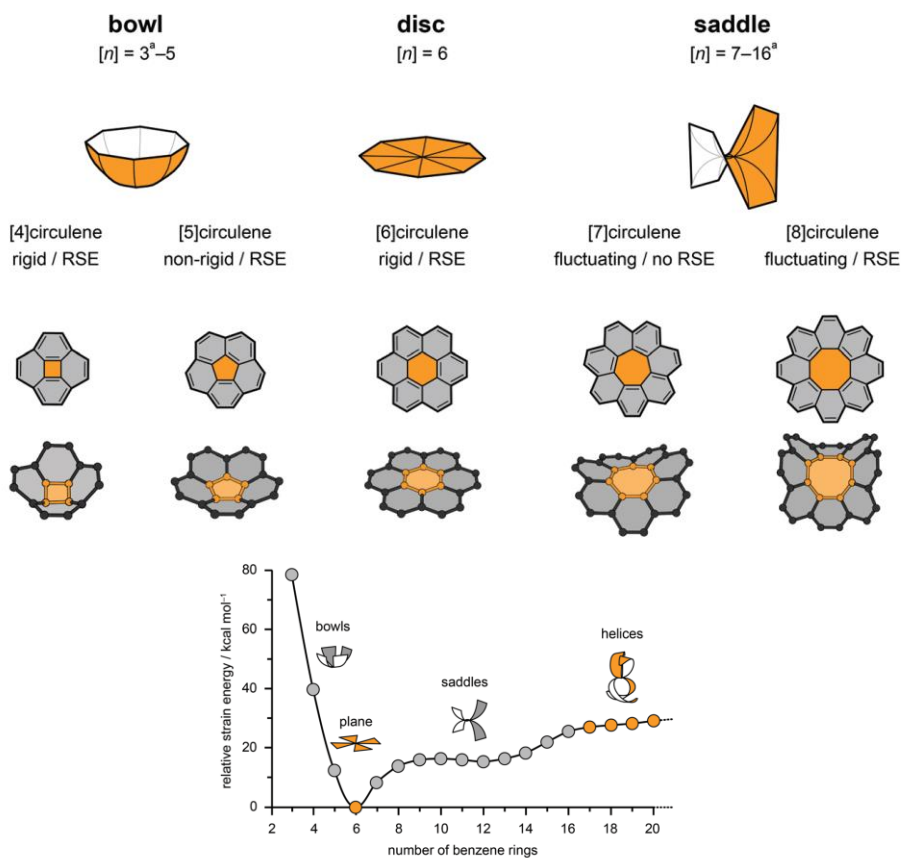


Figure 33. Top: structure of [n]circulenes and their tridimensional arrangement; Bottom: relative strain energy of different [n]circulenes. RSE = relative strain energy.¹⁸⁶

Positively curved circulenes, such as corannulene ([5]circulene), can be envisioned as molecular bowls. Structurally, corannulene is identified as a section of fullerenes or as endcaps on CNTs. Although the first reported synthesis of corannulene dates back to 1966,¹⁸⁸ its chemistry

¹⁸⁷ H. Christoph, J. Grunenberg, H. Hopf, I. Dix, P. G. Jones, M. Scholtissek, G. Maier, *Chem. Eur. J.* **2008**, *14*, 5604-5616.

¹⁸⁸ W. E. Barth, R. G. Lawton, *J. Am. Chem. Soc.* **1966**, *88*, 380-381.

experimented an extensively study since the discovery of fullerenes in 1985.¹ In this sense, a wide variety of nanographenes based on corannulene has been prepared and their properties studied as reported on the comprehensive reviews by the pioneers on the field J. S. Siegel and L. T. Scott.¹⁸⁹ More recently, M. C. Stuparu and co-workers have gathered relevant examples on corannulene-based nanographenes reported since 2006.¹⁹⁰ Therefore, the chemistry of corannulene and nanographenes containing five-membered rings has been extremely exploited during the last decades.

Despite the importance of negative curvature in exotic nanocarbon structures, nanographenes containing seven-membered rings are scarce and known to be difficult to form because of their relative ring strain (Figure 33).

1.3.3.2. Synthetic strategies towards heptagon-containing nanographenes

Within the bottom-up approaches based on organic synthesis for the preparation of well-defined distorted saddle-shaped nanographenes, three main strategies have been used to create the key heptagonal carbocycle (Figure 34).¹⁹¹ Firstly, the direct use of a functionalized seven-membered ring as starting material and subsequent creation of the surrounding aromatic backbone in consecutive steps. A second approach that has been quite extensively used consists on the generation of the heptagon by means of an intramolecular closing reaction mainly by a final oxidative cyclodehydrogenation, although Friedel-Crafts reaction and Pd-catalyzed C-H arylation have also been used. Recently, an alternative approach has been reported in which a ring expansion reaction of cyclohexanone moieties gives rise to the central heptagon in the hexagonal lattice.

¹⁸⁹ a) Y.-T. Wu, J. S. Siegel, *Chem. Rev.* **2006**, *106*, 4843-4867; b) V. M. Tsefrikas, L. Scott, *Chem. Rev.* **2006**, *106*, 4868-4884.

¹⁹⁰ E. M. Muzammil, D. Halilovic, M. C. Stuparu, *Commun. Chem.* **2019**, *2*, 58.

¹⁹¹ I. R. Márquez, S. Castro-Fernández, A. Millán, A. G. Campaña, *Chem. Commun.* **2018**, *54*, 6705-6718.

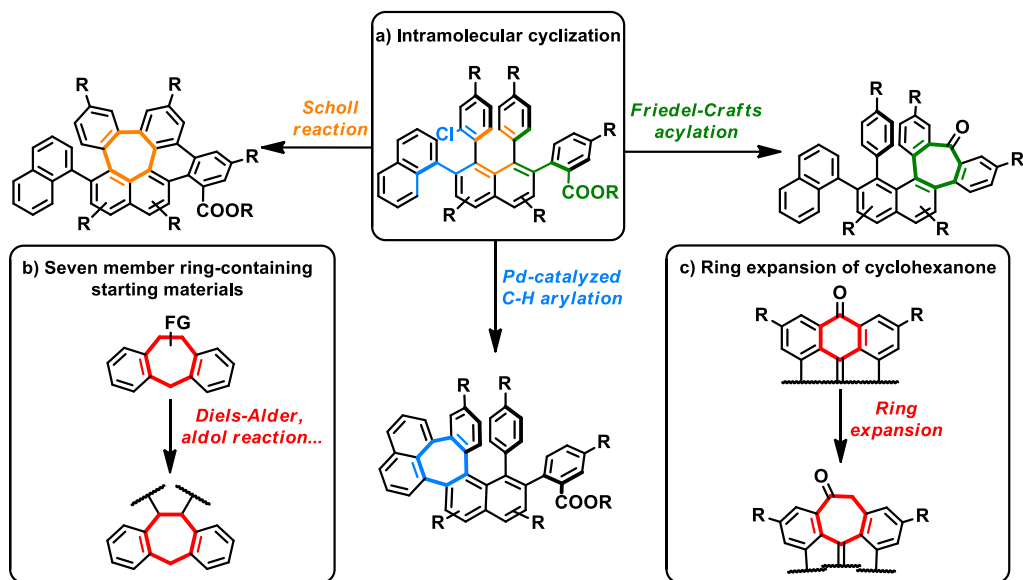


Figure 34. General approaches for the synthesis of PAHs containing heptagons.

Recently, our research group has reported a novel synthetic methodology toward functionalized HBC-like nanographenes containing a seven-membered ring. The preparation of the distorted nanographenes is based on an intermolecular Co(0)-catalyzed alkyne cyclotrimerization followed by a cyclodehydrogenation reaction, similar sequence reported by Müllen (section 1.3.1.1).¹⁹²

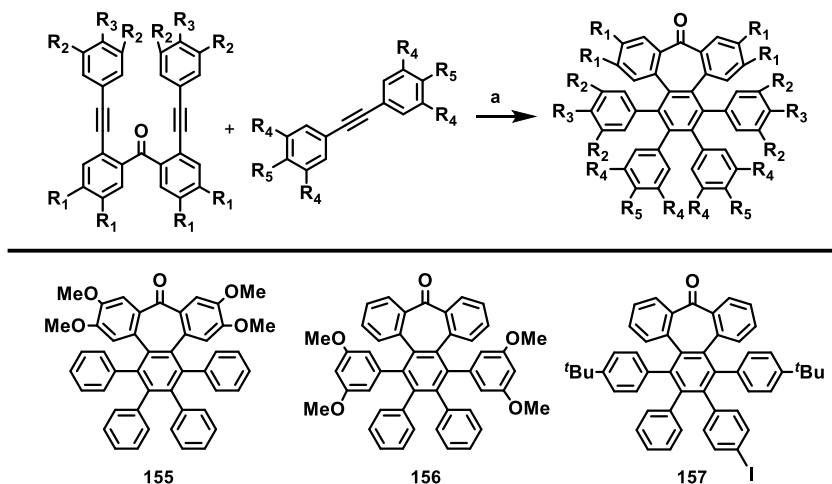
The key coupling partners on the cyclotrimerization step are a dialkyne (easily prepared from 2,2'-dibromobenzophenone by Sonogashira-Hagihara coupling) and differently functionalized diphenylacetylenes (Scheme 33). The presence of the carbonyl group, hindered the formation of undesired 9,10-dihydroanthracenes¹⁹³ while allowing for subsequent functionalization approaches.

Noteworthy, the alkyne cyclotrimerization reaction tolerates substitution in both coupling partners. Substitution at the benzophenone moiety affords compounds such as **155** (Scheme 33). Dialkynes can also incorporate *meta*- or *para*-substituted ethynylbenzenes affording the corresponding functionalized products **156** or **157**. *Meta*- and *para*-substituted

¹⁹² I. R. Márquez, N. Fuentes, C. M. Cruz, V. Puente-Muñoz, L. Sotorrios, M. L. Marcos, D. Choquesillo-Lazarte, B. Biel, L. Crovetto, E. Gómez-Bengoña, M. T. González, R. Martín, J. M. Cuerva, A. G. Campaña, *Chem. Sci.* **2017**, *8*, 1068-1074.

¹⁹³ W. Baidossi, H. Schumann, J. Blum, *Tetrahedron* **1996**, *52*, 8349-8364.

diphenylacetylenes are also allowed as in compounds **157**. Thus, a wide variety of heptagon-containing oligophenylenes were prepared.



Scheme 33. Synthetic methodology toward heptagon-containing functionalized nanographenes developed at our research group; a) $\text{Co}_2(\text{CO})_8$, 1,4-dioxane, 100°C , 16 h. ($\text{R}_1 = \text{H}, \text{OMe}$; $\text{R}_2 = \text{H}, \text{OMe}, \text{F}$; $\text{R}_3 = \text{H}, \text{tBu}, \text{OMe}$; $\text{R}_4 = \text{H}, \text{OMe}, \text{Me}$; $\text{R}_5 = \text{H}, \text{Br}, \text{I}, \text{Me}, \text{OMe}$).

The final distorted-PAHs could be prepared by oxidative cyclodehydrogenation, thus accessing to the heptagon-containing nanographenes. The presence of methoxy groups allowed controlling the regioselectivity in the oxidative aromatic coupling when using DDQ as an oxidant in acidic media (MeSO_3H). Remarkably, incomplete cyclodehydrogenation led to doubly distorted compounds, incorporating both the heptagon and [5]helicene motifs at different positions of the aromatic backbone. In contrast to the presence of methoxy groups, less activated *tert*-butylated compound resulted unaltered under similar conditions. In this case, however, the combination DDQ/TfOH was required and fully cyclodehydrogenated compound was isolated in good yield while forming five new carbon-carbon bonds in a single step, leading to a heptagon-containing HBC analogue (*hept*-HBC).

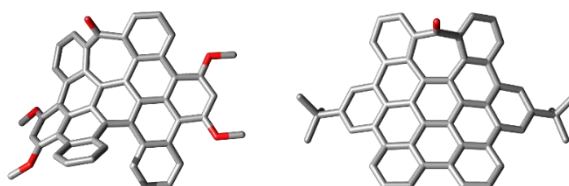
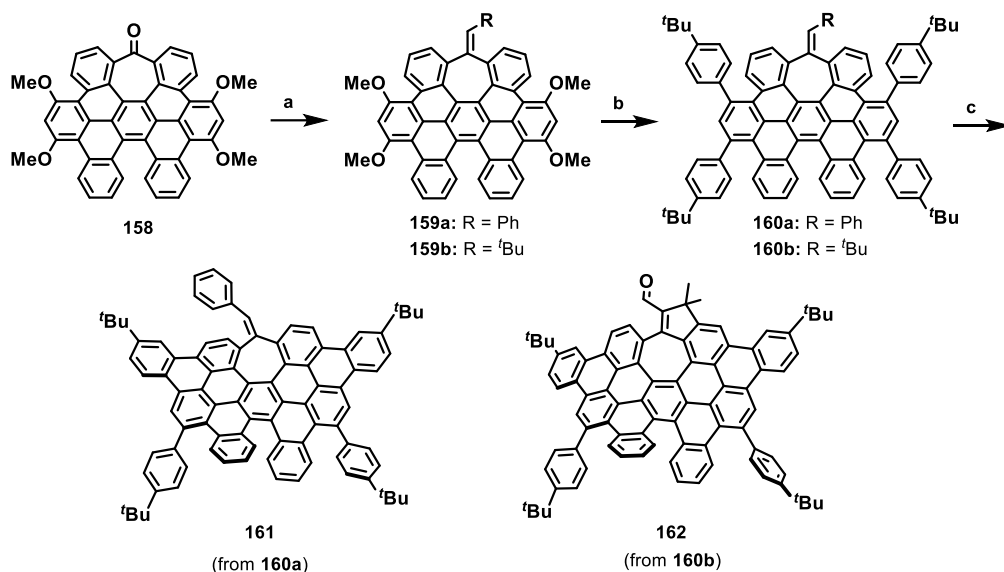


Figure 35. Left: X-Ray structure of saddle-helix hybrid nanographene; Right: DFT optimized structure of fully cyclodehydrogenated distorted nanographene (*hept*-HBC).

1. Background

The functional groups existing on the final aromatic structures may serve as tools for a further extension of the aromatic structure. In this sense, it was found that the carbonyl group participated in addition reactions by treatment with Grignard reagents (**159**). On the other hand, the necessary methoxy groups for the Scholl reaction can act as electrophiles via C–OMe cleavage. Thus, compounds **159** were found to be competent in Kumada-Tamao-Corriu reactions via C–OMe bond-cleavage, rapidly furnishing **160a** and **160b** in good yields. Subsequent Scholl reaction conditions with DDQ/Me₃SO₃H in CH₂Cl₂ afforded compounds **161** and **162** (Scheme 34).

Remarkably, the X-Ray structure of **CLIV** revealed that the π -backbone adopts a curved shape caused by the pentagon-heptagon unit and the chiral twisted conformation caused by the [5]helicene moiety. Theoretical calculations predicted the formation of the five-membered ring, where the protonation of the exocyclic double bond produces a barrierless intramolecular attack of the nearest benzenoid ring and a migration of the methyl group, which introduces a new allylic position subsequently oxidized by DDQ.¹⁹⁴ The partially cyclodehydrogenation products were also foreseen since the calculated energy barriers for the formed bonds are lower (7.9 kcal·mol⁻¹) than those that are not formed (11.4 kcal·mol⁻¹).



Scheme 34. Expansion route from doubly distorted nanographene **162**. a) PhCH₂MgCl or ^tBuCH₂MgCl, then SOCl₂; b) *p*-^tBuPhMgBr, Ni(cod)₂; c) DDQ, MeSO₃OH.

¹⁹⁴ H. Lee, R. G. Harvey, *J. Org. Chem.* **1983**, *48*, 749-751.

1.3.3.3. Reported heptagon-containing nanographenes

The first example of saddle-shaped polycyclic arenes embedding a seven-membered ring is the [7]circulene. Its synthesis was first reported by K. Yamamoto and co-workers in 1983.¹⁹⁵ Subsequently, the same authors reported further synthetic routes toward [7]circulene and even for the double[7]circulene during the following decades (Figure 36).¹⁹⁶ Although the preparation of PAHs containing seven-membered rings has been considered for a long time, it has been at the beginning of this decade when extended PAHs containing seven-membered rings have received major attraction among the chemists, due to their improved properties compared to their flat analogues.

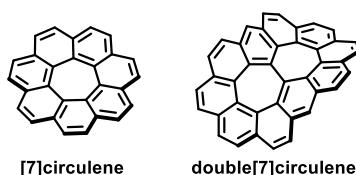


Figure 36. [7]circulene and double[7]circulene reported by Yamamoto and co-workers.

In this sense, the group of D. Kuck reported one of the first examples of extended nanographenes embedding heptagons by merging a tribenzotriquinacene (TBTQ) unit with a HBC unit (**163**, Figure 37).¹⁹⁷ The resulting compound also showed three pentagonal rings coming from the TBTQ. Two years later, the same group reported an attempt to prepare the trefoil-shaped analogue of **164** where the structural characterization of the oligophenylene precursor is described, but not achieving the desired proposed compound due to problems on the final cyclodehydrogenation reaction.¹⁹⁸ Additionally, in 2016, they reported the attempt for the preparation of a fenestrindane-linked double HBC containing two heptagonal rings where the final Scholl reaction only afforded the formation of the HBC units and not the seven-membered rings (Figure 37).¹⁹⁹

¹⁹⁵ K. Yamamoto, T. Harada, M. Nakazaki, *J. Am. Chem. Soc.* **1983**, *105*, 7171-7172.

¹⁹⁶ a) K. Yamamoto, T. Harada, Y. Okamoto, H. Chikamatsu, M. Nakazaki, Y. Kai, T. Nakao, M. Tanaka, S. Harada, N. Kasai, *J. Am. Chem. Soc.* **1988**, *110*, 3578-3584; b) K. Yamamoto, H. Sonobe, H. Matsubara, M. Sato, S. Okamoto, K. Kitaura, *Angew. Chem. Int. Ed. Engl.* **1996**, *35*, 69-70; c) K. Yamamoto, Y. Saitho, D. Iwaki, T. Ooka, *Angew. Chem. Int. Ed. Engl.* **1991**, *30*, 1173-1174.

¹⁹⁷ E. U. Mughal, D. Kuck, *Chem. Commun.* **2012**, *48*, 8880-8882.

¹⁹⁸ E. U. Mughal, B. Neumann, H.-G. Stammer, D. Kuck, *Eur. J. Org. Chem.* **2014**, *2014*, 7469-7480.

¹⁹⁹ P. An, H.-F. Chow, D. Kuck, *Synlett* **2016**, *27*, 1255-1261.

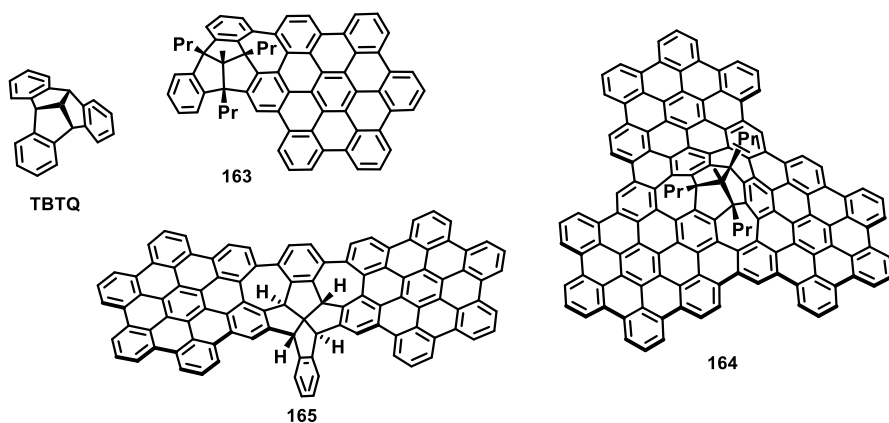


Figure 37. Prepared heptagon-containing nanographene **163** and attempted structures (**164** and **165**) by the Kuck's group.

Finally, in 2016 the same group prepared a trefoil shaped PAHs containing three heptagons and three pentagons (**166**, Figure 38) as a reduced analogue of **164**.²⁰⁰ The work was accompanied with a comprehensive study on the cyclodehydrogenation step.²⁰¹ More recently, they reported the tetrafoil downsized analogue of **166** by using the fenestrindane skeleton as the main building block.²⁰²

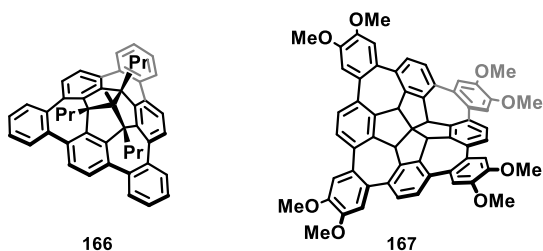


Figure 38. Prepared heptagon-containing nanographenes **166** and **167**.

Noteworthy, the group of Q. Miao has done an outstanding work on the preparation of negatively curved extended nanographenes during the last years.²⁰³ Thus, in 2012, they reported the synthesis of a HBC analogue containing one seven-membered ring (**168**, Figure 39). In this case, the authors started from a heptagon-containing compound and the aromatic backbone was

²⁰⁰ H.-W. Ip, C.-F. Ng, H.-F. Chow, D. Kuck, *J. Am. Chem. Soc.* **2016**, *138*, 13778-13781.

²⁰¹ H.-W. Ip, H.-F. Chow, D. Kuck, *Org. Chem. Front.* **2017**, *4*, 817-822.

²⁰² W.-S. Wong, C.-F. Ng, D. Kuck, H.-F. Chow, *Angew. Chem. Int. Ed.* **2017**, *56*, 12356-12360.

²⁰³ a) Q. Miao, *Chem. Rec.* **2015**, *15*, 1156-1159; b) S. H. Pun, Q. Miao, *Acc. Chem. Res.* **2018**, *51*, 1630-1642.

introduced through Diels-Alder reaction and Final Scholl reaction. However, after treatment with FeCl_3 , hence, chlorinated and partially cyclodehydrogenated were also obtained as side products. Remarkably, the non-formed bond was the same in all cases and it is directly related to the $-\text{OC}_6\text{H}_{13}$ substituents, which (apparently) are *ortho*- and *para*-directing groups on the Scholl reaction.¹⁵⁷

More recently, in 2015, Miao's group reported two related nanographenes, one containing two heptagons and other with a combination of two heptagons and two pentagons (**169**, Figure 39). These distorted graphene molecules were prepared starting from a heptagon-containing building block, while the second heptagon was introduced after a Friedel-Crafts acylation. The prepared compounds exhibit negative curvature and were tested as organic field-effect transistors.²⁰⁴

The latest structure prepared by this research group was a saddle nanographene containing two heptagons and consisting on 86 aromatic carbon atoms, which can be envisioned as two units of **168** linked by the apical carbons (**170**, Figure 39). The synthesis of **170** started from bisanthrenequinone where a ring expansion with $\text{Me}_3\text{SiCHN}_2$ led to the formation of two seven-membered rings. Further Diels-Alder and Scholl reactions afforded the desired product.²⁰⁵

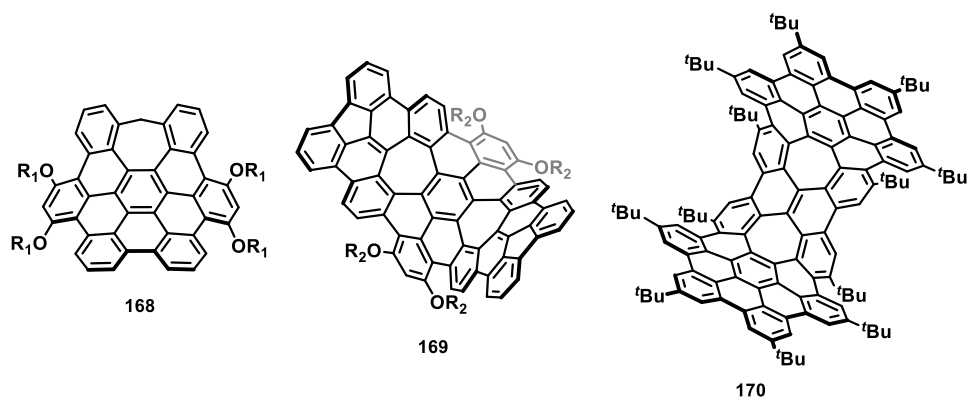


Figure 39. Prepared nanographenes **168**, **169** and **170** ($\text{R}_1=\text{C}_6\text{H}_{13}$; $\text{R}_2=\text{C}_6\text{H}_{13}$ or C_8H_{17}).

Apart from nanographenes with multiple odd-membered rings the Miao's group also reported extended analogues to [7] and [8]circulene (Figure 40). Thus, in 2017, the authors reported the preparation of tetrabenzo[7]circulene starting from simple building blocks and forming the

²⁰⁴ K. Y. Cheung, X. Xu, Q. Miao, *J. Am. Chem. Soc.* **2015**, *137*, 3910-3914.

²⁰⁵ S. H. Pun, C. K. Chan, J. Lu, Z. Liu, Q. Miao, *Angew. Chem. Int. Ed.* **2018**, *57*, 1581-1586.

seven-membered ring after a Friedel-Crafts acylation.²⁰⁶ On the other hand, an outstanding extended [8]circulene consisting of 96 aromatic carbon atoms was prepared,²⁰⁷ where the eight membered ring is constructed on the last step via Scholl reaction. Compound **172** exhibited a flexible conformation where the saddle geometry is 4.1 kcal·mol⁻¹ higher in energy than the twisted framework with an interconversion barrier of 6.2 kcal·mol⁻¹. Regarding its optical properties, the authors reported that **172** exhibits aggregation induced emission from the aggregates formed after the addition of water into a THF solution.

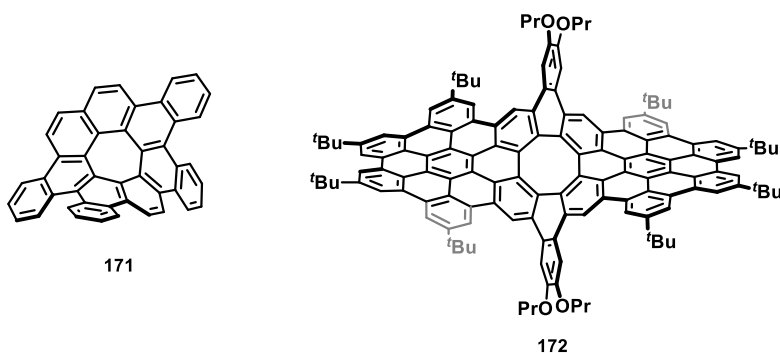


Figure 40. Extended [7] and [8]circulenes reported by the Miao's group.

In 2012 K. Itami and L. T. Scott also reported an remarkable example, which was prepared through a straightforward synthesis starting from coronene. The authors prepared a grossly warped nanographene containing multiple odd-membered-rings, combining a central pentagon with five surrounding heptagons, which were introduced in a late stage via Scholl reaction.²⁰⁸ The synthesis was carried out by following three different approaches based on C–H arylation. Remarkably, the authors previously reported one of these three approaches for the preparation of the precursor,²⁰⁹ as a technique for planarize corannulene units by introducing aryl substituents. Noteworthy, this approach has been widely used for an opposite aim, such as for twisting acenes.²¹⁰

²⁰⁶ X. Gu, H. Li, B. Shan, Z. Liu, Q. Miao, *Org. Lett.* **2017**, *19*, 2246-2249.

²⁰⁷ K. Y. Cheung, C. K. Chan, Z. Liu, Q. Miao, *Angew. Chem. Int. Ed.* **2017**, *56*, 9003-9007.

²⁰⁸ K. Kawasumi, Q. Zhang, Y. Segawa, L. T. Scott, K. Itami, *Nat. Chem.* **2013**, *5*, 739-744.

²⁰⁹ Q. Zhang, K. Kawasumi, Y. Segawa, K. Itami, L.T. Scott, *J. Am. Chem. Soc.* **2012**, *134*, 15664-15667.

²¹⁰ Y. Xiao, J. T. Mague, R. H. Schmehl, F. M. Haque, R. A. Pascal Jr., *Angew. Chem. Int. Ed.* **2019**, *58*, 2831-2833.

Regarding the cyclodehydrogenation step on the formation of **173**, the authors have reported a comprehensive study on the mechanism of the Scholl reaction, proposing a cascade mechanism based on the formation of aryl cations.²¹¹ Compound **173** could be subsequently functionalized with BPin groups for further Suzuki coupling reactions. If the coupled units bear tetraethyleneglicol substituents, the resulting distorted nanographene exhibits good solubility in polar solvents such as water, allowing its use in bioapplications.²¹² Recently, **173** was characterized by means of STM at submolecular resolution upon adsorption on several metallic substrates where different self-assembly processes were observed. The supramolecular networks exhibited regular homochiral domains, constituting an interesting pathway for the design of functional chiral nanostructures.²¹³ The possibility of having direct imaging of curved nanostructures on surfaced is a remarkable breakthrough since non-planar systems are elusive to adsorption on metal surfaces as the interaction is favored on planar compounds.

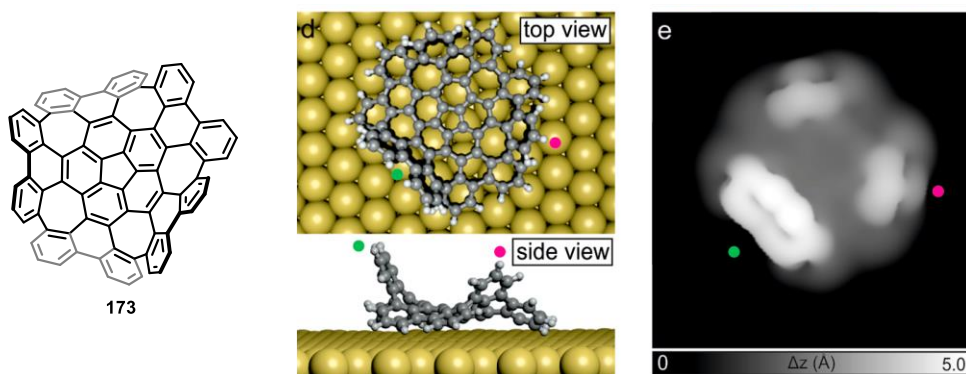


Figure 41. Grossly warped nanographene **173** and DFT-simulated geometry and STM image of the molecule.²¹³

The group has also reported a propeller-shaped PAH containing three seven-membered rings and three [4]helicenes (**174**, Figure 42). Compound **174** is a triphenylene derivative where the heptagonal rings were formed through palladium-catalyzed C-H arylations. Remarkably, the closure of the non-hexagonal ring is favored rather than the formation of a hexagonal ring that would lead to an analogue of **149**.²¹⁴ Similar unexpected generation of heptagons was reported

²¹¹ K. Kato, Y. Segawa, L. T. Scott, K. Itami, *Chem. Asian J.* **2015**, *10*, 1635-1639.

²¹² H.-A. Lin, Y. Sato, Y. Segawa, T. Nishihara, N. Sugimoto, L. T. Scott, T. Higashiyama, K. Itami, *Angew. Chem. Int. Ed.* **2018**, *57*, 2874-2878.

²¹³ J. I. Urgel, M. Di Giovannantonio, Y. Segawa, P. Ruffieux, L. T. Scott, C. A. Pignedoli, K. Itami, R. Fasel, *J. Am. Chem. Soc.* **2019**, *141*, 13158-13164.

²¹⁴ K. Kawai, K. Kato, L. Peng, Y. Segawa, L. T. Scott, K. Itami, *Org. Lett.* **2018**, *20*, 1932-1935.

by F. Durola and co-workers, where they isolated a highly distorted PAHs containing a hexabenzoc[7]circulene in combination with a [5]helicene when trying to obtain an analogue to **149**.²¹⁵

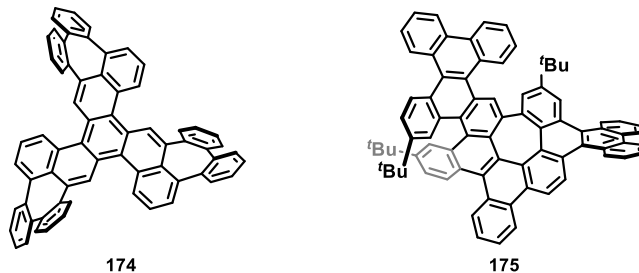


Figure 42. PAHs containing seven membered rings found after unexpected Scholl reaction.

Last but not least, the group of N. Martín has recently synthesized an exotic nanographene that combines both positive and negative curvatures. The synthetic pathway is based on the bromination and subsequent Sonogashira coupling over pristine corannulene. The resulting alkyne is subjected to a Diels-Alder reaction, originating the HBC backbone. The final Scholl reaction is decisive, whereas employing FeCl_3 at low temperatures affords a nanographene combining a five membered ring and a [6]helicene (**176**), the use of DDQ/TfOH at 0°C give rise to the desired nanographene containing two odd-membered rings (**177**, Figure 43).

The cyclodehydrogenation step was studied by DFT calculations to shed light on the followed mechanism. Thus, arenium cation and radical cation were compared in terms of activation and final products free energies. Moreover the photophysical properties of the prepared compounds were evaluated and the electrochemical analysis suggested a decrease of the band gap in comparison with HBC.

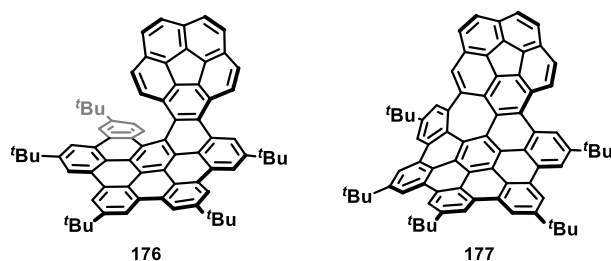


Figure 43. Novel nanographenes combining pentagons and helicenes (**176**) and combining positive and negative curvatures (**177**).

²¹⁵ A. Pradham, P. Dechambenoit, H. Bock, F. Durola, *J. Org. Chem.* **2013**, *78*, 2266-2274.

The most recent example of heptagon-containing nanographene is that reported by F. Würthner and co-workers in 2019.²¹⁶ The authors reported a new PAHs that may be envisioned as a fragment of Schwarzite 6-1-2-p. The structure of **180** contains 11 aromatic rings and was prepared through a newly developed strategy based on the transformation of unfunctionalized precursors into borinic acids that underwent a double Suzuki coupling mediated by Pd catalysts (Figure 44).

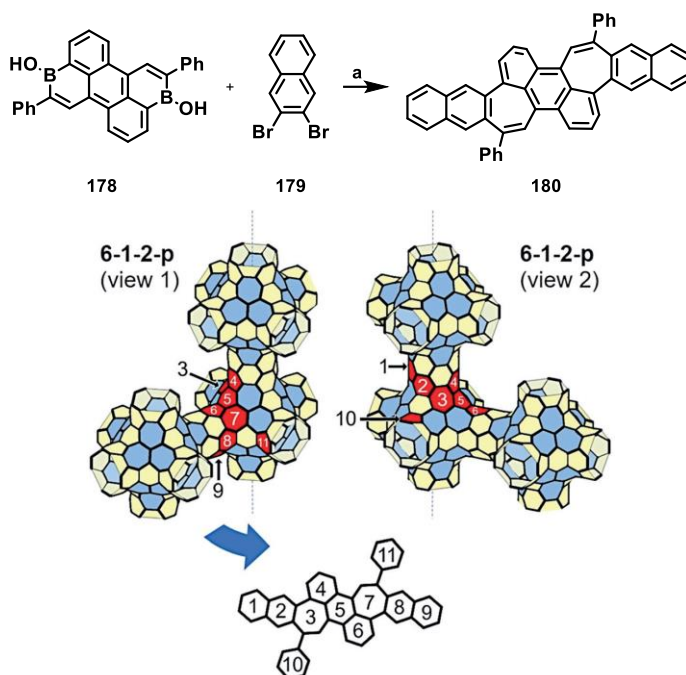


Figure 44. Synthesis of the last reported heptagon-containing nanographene (**180**). a) Suzuki coupling. Structure of **180** as part of Schwarzite 6-1-2-p.

²¹⁶ J. M. Farrel, V. Grande, D. Schmidt, F. Würthner, *Angew. Chem. Int. Ed.* **2019**, *58*, 16504-16507.

2. OBJECTIVES

According to the information gathered in the background section, where the state-of-the-art on the synthetic nanographenes field is reported, and taking advantage of the previous results made by our research group, we postulate the next general objectives for this thesis:

- To **prove the versatility** of the methodology developed by our research group for the preparation of functionalized heptagon-containing nanographenes. We aim to prepare a new family of distorted nanographenes containing heptagon/s and helicene/s based on HBC units.
- The prepared curved aromatic compounds might be, presumably, high soluble in contrast to most of the previously reported extended planar nanographenes. Therefore, we aim to carry out a proper **structural characterization**, assigning unequivocally the structure of each prepared compound.
- The optical properties of large nanographenes molecules are not usually reported due to their low solubility. Thus, a **complete optical characterization** will be carried out, finding a relationship between their structure and their optical properties.
- The nonlinear optical properties on nanographenes are so far evaluated on HBC derivatives. Thus, we aim to study the nonlinear optical properties such as **two-photon absorption** in the prepared distorted nanographenes absorption in order to understand the influence of the π -extension in this property. Moreover, we aim to evaluate if the two-photon absorption response is improved by the inclusion of heptagons into the aromatic structure.
- The evaluation of the **chiroptical properties** in nanographene molecules is so far reduced to circular dichroism. Thus, to introduce new chiroptical properties into nanographenes, we aim to evaluate the **Circularly Polarized Luminescence** (as well as their Circular Dichroism) of the saddle-helix hybrid nanographenes prepared and try to improve it by modifying the aromatic structure.
- The HOMO-LUMO gap is a crucial value on the preparation of transistors based on organic compounds (OFETs). Therefore, the bandgap of the prepared compounds will be evaluated by means of **electrochemical measurements** such as Cyclic Voltammetry and Square Wave Voltammetry.

3. RESULTS AND DISCUSSION

Regarding the outlined objectives, this section describes the obtained results and their discussion. The synthesis, purification and structural characterization of the designed compounds will be described as well as the evaluation of the physical properties in terms of linear and non-linear optical properties, electrochemical and spectroelectrochemical properties, chiroptical properties and even surface or/and X-Ray analysis in those suitable cases. The results will be compared and contextualized in the field of highly curved nanocarbon materials.

3.1. Ribbon-shaped nanographene combining TPA-UC and CPL

Although the wide variety on the preparation of purely hexagonal nanographenes, helicene-containing, and non-hexagonal rings containing PAHs, the combination of these three structural characteristics into one single molecule remained unexplored to date. Thus, a preliminary example was reported by K. Itami and co-workers,²¹⁷ where the authors prepared a series of laterally extended dithia[6]helicenes and coined the term “Saddle-Helix Hybrid Molecules”. However, the helicene moiety is consisted of both benzenoid and thiophene rings, thus carbon-based analogues containing carbohelicenes remain unexplored.

Therefore, the controlled introduction of these defective moieties in nanographenes can implement interesting new combinations of optical properties, such as TPA-based upconversion and Circularly Polarized Luminescence. Remarkably, the combination of both responses in a single organic molecules has never been addressed although it would represent the foundation for the development of TPA-based UC-CPL.

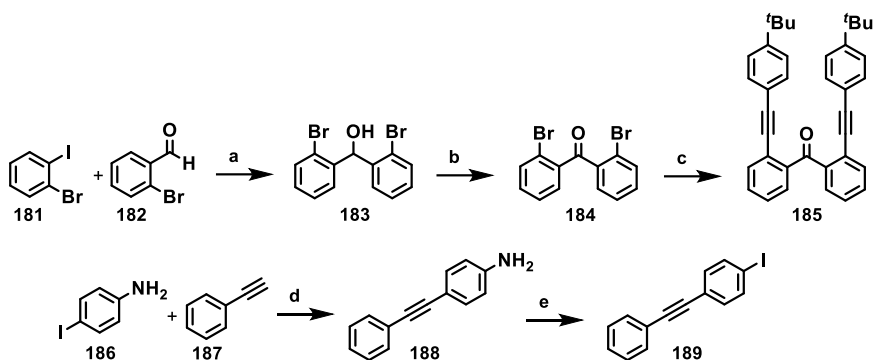
In this sense, large π -conjugated linkers between donor-acceptor moieties are basic structural features required for two-photon absorbing chromophores. On the other hand, chiral molecules able to produce circularly polarized luminescence are of increasing interest due to their promising applications in optical devices and biosensors. Nevertheless, the CPL of an enantiopure nanographene remains still unexplored.

²¹⁷ T. Fujikawa, Y. Segawa, K. Itami, *J. Org. Chem.* **2017**, *82*, 7745-7749.

3.1.1. Synthesis and structural characterization

Based on the straightforward synthetic route toward functionalized heptagon-containing PAHs developed by our research group, we used it to create an aromatic backbone incorporating a π -extended helical moiety in the structure. Thus, starting from 2-bromoiodobenzene (**181**) and after the iodine/magnesium exchange by addition of "Turbo Grignard", the nucleophilic attack of the *in situ* formed Grignard reagent over 2-bromobenzaldehyde (**182**) was carried out.²¹⁸ Subsequent oxidation of the obtained secondary alcohol (**183**) with Dess-Martin periodinane afforded the resulting 2,2'-dibromobenzophenone (**184**).

Subsequently, a two-fold Sonogashira coupling over the dibromo derivative **184** gave rise to the dialkyne **185**, containing two of the three required alkynes for the cyclotrimerization reaction. The third alkyne (**189**) would contain an aromatic iodine for a further expansion of the aromatic surface *via* Sonogashira coupling. Therefore, the corresponding diphenylacetylene was prepared by Sonogashira coupling between 4-iodoaniline (**186**) and phenylacetylene (**187**). The outcoming aniline was transformed into the corresponding iodine derivative by means of Sandmeyer reaction with potassium iodide (Scheme 35).

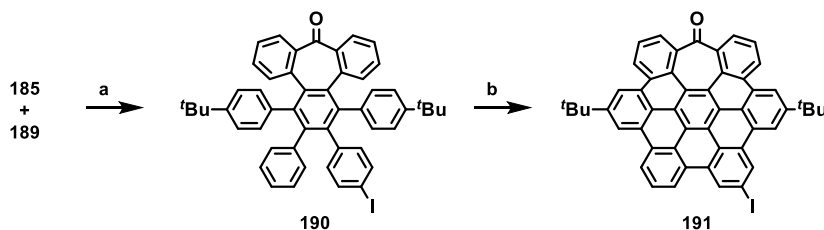


Scheme 35. Synthesis of compounds **185** and **189**. Reagents and conditions: a) i -PrMgCl-LiCl, THF, -78°C to r.t., 16 h, 83%; b) DMP, CH_2Cl_2 , r.t., 16 h, 75%; c) *p*-*tert*-butylphenylacetylene, $\text{PdCl}_2(\text{CH}_3\text{CN})_2$, $\text{P}(\text{tBu})_3\cdot\text{BF}_4$, CuI, i -Pr₂NH, THF, r.t., 16 h, 99%; d) $\text{PdCl}_2(\text{PPh}_3)_2$, CuI, Et₃N, THF, r.t., 16 h, 91%; e) NaNO_2 , KI, H_2SO_4 , H_2O , THF, 0°C , 3 h, 67%.

The [2+2+2] alkyne cyclotrimerization reaction between **185** and **189** was promoted by the addition of one equivalent of $\text{Co}_2(\text{CO})_8$. Firstly, the dialkyne **185** was stirred in the presence of the

²¹⁸ A. Krasovskiy, P. Knochel, *Angew. Chem. Int. Ed.* **2004**, *43*, 3333-3336.

cobalt catalyst to presumably form a metallacycle intermediate, which reacts with the alkyne **189** to form a new benzene ring and, therefore, the seven-membered ring. The resulting heptagon-containing oligophenylene **190** was subjected to Scholl reaction by the combination of DDQ and TfOH affording the distorted PAH **191** in an extraordinary 86% yield (Scheme 36).

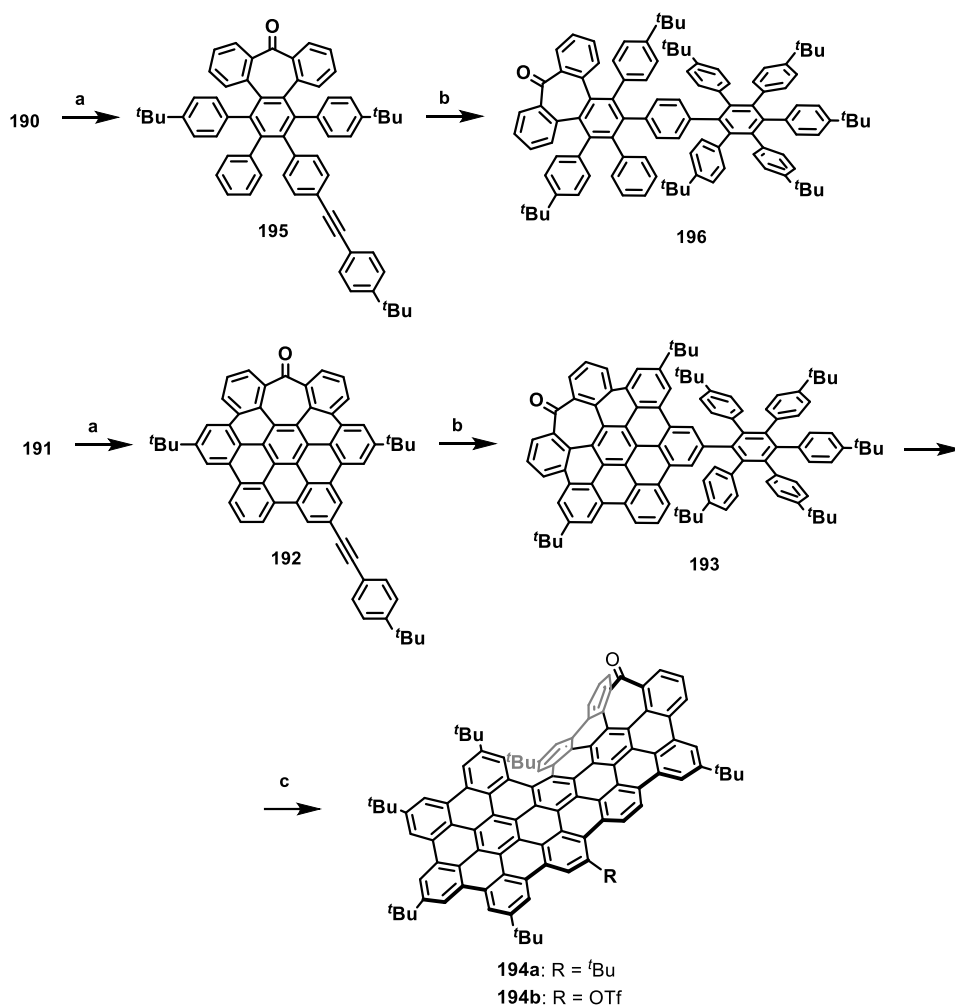


Scheme 36. Reagents and conditions: a) $\text{Co}_2(\text{CO})_8$, 1,4-dioxane, 100°C , 16 h, 45%; b) DDQ, $\text{CF}_3\text{SO}_3\text{H}$, CH_2Cl_2 , 0°C , 10 min, 87%.

The easy functionalization of the aromatic core allowed the expansion of the structure. Taking advantage of the halogenated position, a Sonogashira coupling with *p*-*tert*-butylphenylacetylene was carried out obtaining an alkyne suitable for [4+2] cycloadditions. Thus, a subsequent Diels-Alder reaction with 2,3,4,5-tetrakis-(*p*-*tert*-butylphenyl)-cyclopentadienone gave rise to the corresponding oligophenylene **193**. Finally, a cyclodehydrogenation promoted by DDQ in acid media afforded the desired compound **194a** as a major product (46%) with orange color in solution. Remarkably, after the final step, we isolated a small amount of the triflate derivative **194b** (5%), obtained by the exchange of a *tert*-butyl group.

Alternatively, a second synthetic pathway was tested, in this case compound **190** was directly subjected to Sonogashira coupling with 4-*tert*-butylphenylacetylene to obtain the alkyne **195**, analogue to **192**. Diels-Alder reaction with the corresponding cyclopentadienone over **195** afforded the oligophenylene **196**. A final Scholl reaction was tested over the precursor **196**, where only traces of an orange product were detected by TLC. No enough quantity was isolated after flash column chromatography for a proper structural characterization. Therefore, the first route was chosen as the efficient methodology for the preparation of **194** at milligram scale.

Compound **194a** was firstly characterized by MALDI-TOF mass spectrometry, finding one dominant peak in the mass spectrum at 1385.6. Moreover, an additional peak at $m/z = 2771.2$ was found corresponding to the mass of two molecules of **194a** and can be evaluated as a dimer of the compound.



Scheme 37. Final steps on the route to **194**. a) *p*-*tert*-butylphenylacetylene, PdCl₂(PPh₃)₂, CuI, Et₃N, THF, r.t., 16 h, 99% (**192**), 99% (**195**); b) 2,3,4,5-*tetrakis*-(*p*-*tert*-butylphenyl)-cyclopentadienone, Ph₂O, reflux, 8 h, 33% (**193**), 40% (**196**); c) DDQ, CF₃SO₃H, 0°C, 10 min, 46% (**194a**), 5% (**194b**) (from **193**).

When looking at the high resolution mass spectrum, the isotopic distribution pattern of the dominant peak is in good agreement with the calculated pattern (Figure 40). The mass spectra suggest that all the possible intramolecular carbon-carbon bonds were constructed during the last step with exception of that located at the fjord region of the newly created [5]carbohelicene.

The good solubility of **194a** in organic solvents (CHCl₃, CH₂Cl₂, dichloroethane, tetrachloroethane, acetone, THF, and to some extent even in hexane) allowed us to undertake its structure determination also by means of NMR spectroscopy. Remarkably, the ¹H-NMR spectrum obtained

at room temperature was clear enough for the correct interpretation of the multiplicity on each signal (Figure 45), in contrast to that reported for the similar non-distorted nanographene **84** (Page 58),⁷⁰ where a broadening on the obtained signals was observed even heating, directly related to π - π stacking. This strong aggregation tendency observed on compound **84** prevented to report a ^{13}C -NMR spectrum, thus, the distortion created on compound **194a** breaks this tendency and allowed the measurement of a ^{13}C -NMR spectrum. On the other hand, the incorporation of a triflate residue into the structure of compound **194b** was confirmed by means of ^{19}F -NMR, where a single signal at -75.19 ppm was found.

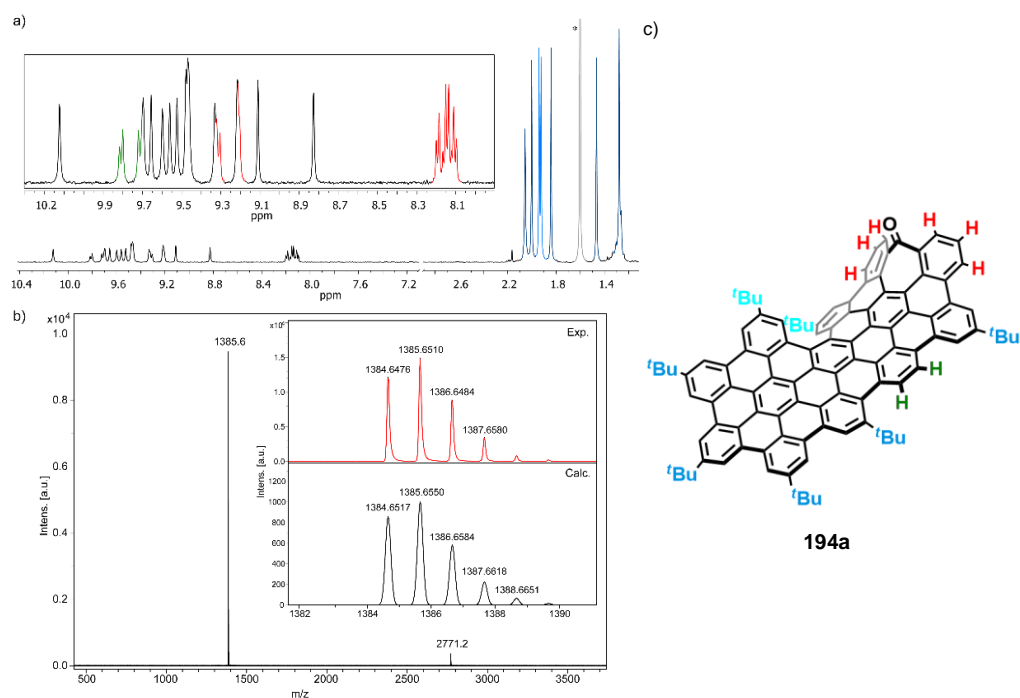


Figure 45. a) Partial ^1H -NMR spectrum (500 MHz, $\text{C}_2\text{D}_2\text{Cl}_4$, 293K) of **194a**; b) MS and HR-MS (MALDI-TOF) of **194a**.

Additionally, slow methanol vapor diffusion into a chlorobenzene solution of racemic **194a**, whilst the slow evaporation of a solution of compound **194b** in a CH_2Cl_2 /hexane mixture, allowed the growing of diffraction-quality single crystals. X-ray crystallography revealed the structure of **194a** with a distorted conformation of the aromatic backbone (Figure 46 shows the *P* enantiomer). As expected, the inclusion of the heptagon causes a saddle-shaped curvature in the hexagonal network, that is 10.8 Å wide and 1.4 Å deep (Figure 46a), similar to that obtained for

the triflate derivative and reaching deviation from planarity with angles of up to 24° between the mean plane of the aromatic ring next to the heptagon and the mean plane of the hexagonal planar region (Table 1). The molecular packing shows the presence of π -stacking of **194a** to form groups of two stacked molecules with a π - π distance of *ca.* 3.4-3.5 Å.

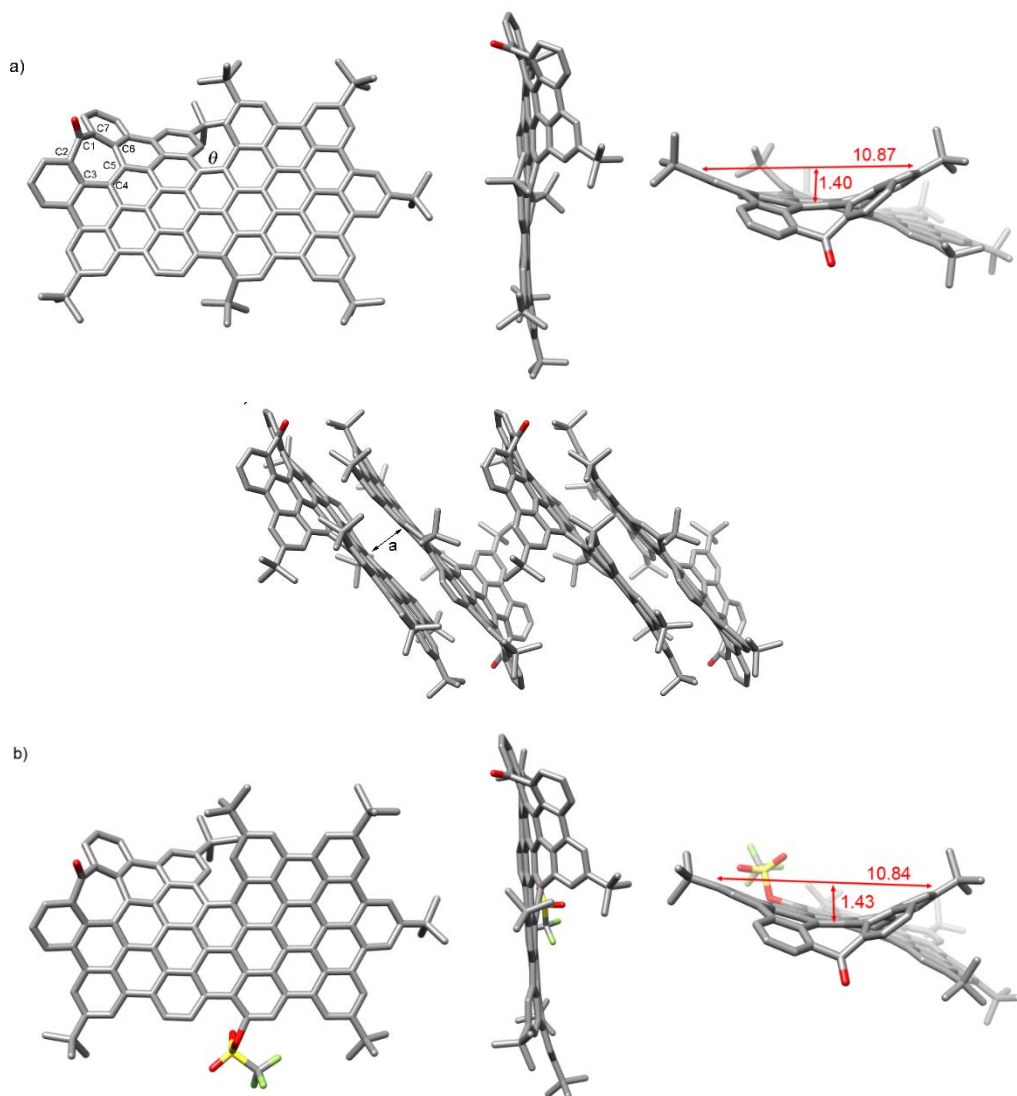
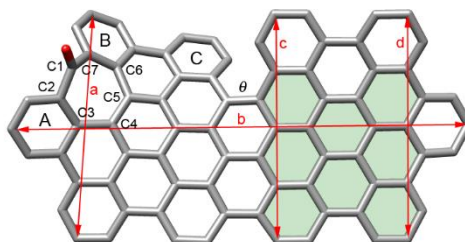


Figure 46. a) X-ray crystal structure of **194a**; b) X-ray crystal structure of **194b**. Top-left: top view, selected bond lengths (Å): C1–C2, 1.466; C2–C3, 1.422; C3–C4, 1.482; C4–C5, 1.432; C5–C6, 1.486; C6–C7, 1.407; C1–C7, 1.464; top- and bottom-right: front view showing the dimensions (in Å) of the aromatic saddle-shaped region; middle: molecular packing, π - π distance (a): *ca.* 3.4–3.5 Å; Hydrogen atoms and solvent molecules have been omitted for clarity.

Table 1. Relevant distances and angles in the X-ray structure of **194a** and **194b**.

| | 194a | 194b |
|--|-------------------|-------------|
| Distance a [Å] ^a | 9.83 | 9.90 |
| Distance b [Å] ^a | 19.83 | 19.78 |
| Distance c [Å] ^a | 9.81 | 9.75 |
| Distance d [Å] ^a | 9.82 | 9.77 |
| Bond Distance C1–C2 [Å] ^b | 1.466(6) | 1.471(6) |
| Bond Distance C2–C3 [Å] ^b | 1.422(6) | 1.421(6) |
| Bond Distance C3–C4 [Å] ^b | 1.482(5) | 1.482(6) |
| Bond Distance C4–C5 [Å] ^b | 1.432(5) | 1.434(6) |
| Bond Distance C5–C6 [Å] ^b | 1.486(5) | 1.477(6) |
| Bond Distance C6–C7 [Å] ^b | 1.407(5) | 1.409(6) |
| Bond Distance C1–C7 [Å] ^b | 1.464(6) | 1.469(6) |
| Angle θ [°] ^c | 29.8 | 33.2 |
| Angle A-planar region [°] ^d | 24.1 ^e | 20.4 |
| Angle B-planar region [°] ^d | 48.6 ^e | 48.6 |
| Angle C-planar region [°] ^d | 40.1 ^e | 45.6 |

^aC–C distance, measured with the CCDC Mercury software.^{S10} ^bFrom the .cif file. ^cTorsional angle. ^dAngle between the mean plane of the labeled aromatic ring and the mean plane of the planar region (colored in green). ^eIn this case one of the edge atoms of the planar region was not considered for calculating the mean plane due to a distortion induced by the presence of a *t*-butyl group.

These dimers do not establish π - π interactions among them and are separated by layers of disordered solvent molecules. Within each pair, the molecules are arranged antiparallely, interacting mainly through the planar regions on the non-defective side. The [5]helicene moieties are located outside the interaction region. The carbon-carbon bond lengths observed in the seven-membered ring indicate localization of π -bonds corresponding to a 2,4,6-cycloheptatrien-

1-one or tropone unit with carbon-carbon single bonds between sp^2 - sp^2 carbons, similarly to previously reported aromatic saddles.¹⁹⁷

It is noteworthy that the twisted conformation caused by the [5]helicene moiety difunctionalized with *tert*-butyl groups originates a torsion angle (θ) of *ca.* 30°, the highest ever reported to date for a [5]helicene.¹⁴⁹ This distortion from planarity enhances solubility avoiding strong π , π -interactions between molecules. Thus, despite the large π -surface constituted by 25 aromatic rings, with a length of *ca.* 1.98 nm and width of *ca.* 0.98 nm, **194a** showed a solubility of up to 16 mg·mL⁻¹ in CH₂Cl₂.

3.1.2. Optical properties

The optical properties of **194a** were determined by one-photon absorption and two-photon absorption spectroscopy in the UV-vis and NIR regions and emission spectroscopy with linear and non-linear excitation. The UV-vis spectrum of **194a** in the 300-800 nm region revealed a structured absorption band between 400 and 500 nm with a maximum at 444 nm. The corresponding molar absorptivity was estimated to be of 6.6×10^4 M⁻¹·cm⁻¹. Based on TD-DFT calculations, this structured band is composed of three different transitions predicted at 507, 464 and 449 nm in good agreement with the observed peaks at 493, 475 and 444 nm, respectively.

Additional contribution from the typical vibronic progression of rigid aromatic systems to the band structure cannot be completely ruled out. The lowest energy $S_0 \rightarrow S_1$ transition, calculated at 527 nm, is observed as a very weak band at 555 nm in agreement with its predicted weak oscillator strength. This band is only clearly observed in more concentrated solutions (10^{-5} M). The assignment of this band to the monomer is also supported by its observation on the photoluminescence excitation spectrum collected at 600 nm.

The emission spectrum of **194a** (one-photon excitation, OPE) (Fig. 47b, black line) consists of three major vibronic bands at 560, 601 and 649 nm with decreasing intensities as the wavelength increases. The vibronically resolved emission spectrum is typical of rigid aromatic fluorophore.²¹⁹ The difference between consecutive bands in the progression is consistent with the coupling of the electronic transition with ring breathing modes observed in the 1250 cm⁻¹ region of the IR

²¹⁹ W. E. Acree, A. I. Zvaigzne, J. C. Fetzer, *Appl. Spectrosc.* **1990**, *44*, 1193-1195.

spectrum. The fluorescence quantum yield (ϕ_f) is 13%. The excitation independent emission and an overlapping between the absorption and excitation spectra indicate that the sample is homogeneous and has neither impurities nor aggregates. The optical band gap estimated from the curve crossing of the normalized absorption and emission spectra is 2.22 eV. The emission lifetime was measured at two different wavelengths, at the maximum and the red edge of the emission band, showing a very small wavelength dependence. Emission lifetime is multiexponential (25.6, 18.1 and 3.5 ns) with the major contribution (68%) coming from the longest time-constant.

The different lifetimes might be due to the relaxation pathways involving the two different saddle-to-saddle diastereoisomers that are rapidly interchanging at the fluorescence timescale. The average fluorescence lifetime is $\tau = 21.5$ ns, significantly longer than that of related fluorescent dyes, such as perylene bisimides.²²⁰

As anticipated based on its push-pull geometry with an extended aromatic network connecting the electron acceptor heptagon unit to the electron donating *tert*-butyl groups and the calculated dipole moment of 4.64 D, **194a** behaved as a nonlinear fluorophore with a clear upconverted fluorescence upon two-photon absorption. Excitation in the 700-950 nm region with a femtosecond laser with a high excitation power density (1 MW cm^{-2}) causes the simultaneous absorption of two NIR-photons leading to emission at higher energies (500-700 nm, Figure 47a). The emission spectrum induced by excitation with two-photons of 770 nm (TPE in Figure 47b, red dashed line) is exactly coincident with the one induced by a single photon of 353 nm (OPE in Figure 42b). The TPA maximum appears at *ca.* 760 nm with a cross-section (σ_2) of 130 GM resulting in a two-photon brightness ($\sigma_2\phi$) of 17 GM (Figure 47a, red line). Although moderate, the TPA value is remarkable considering the distortion from planarity, required for inducing chiroptical properties, of **194a** and the lack of electronic coupling effects observed in branched push-pull structures.²²¹ Importantly, no net absorption above 600 nm was observed in the linear absorption spectrum. Moreover, TPE was recorded with different incident power, confirming the quadratic dependence of the upconverted emission on the excitation power (Figure 47c). It is

²²⁰ F. Wurthner, *Chem. Commun.* **2004**, 1564-1579.

²²¹ a) Z. Zeng, Z. Guan, Q.-H. Xu, J. Wu, *Chem. Eur. J.* **2011**, *17*, 3837-3841; b) S. de Reguardati, J. Pahapill, A. Mikhailov, Y. Stepanenko, A. Rebane, *Opt. Express* **2015**, *24*, 9053-9066.

3. Results and discussion

noteworthy that the TPA maximum appears shifted to higher energy transitions when compared with the OPA maximum.

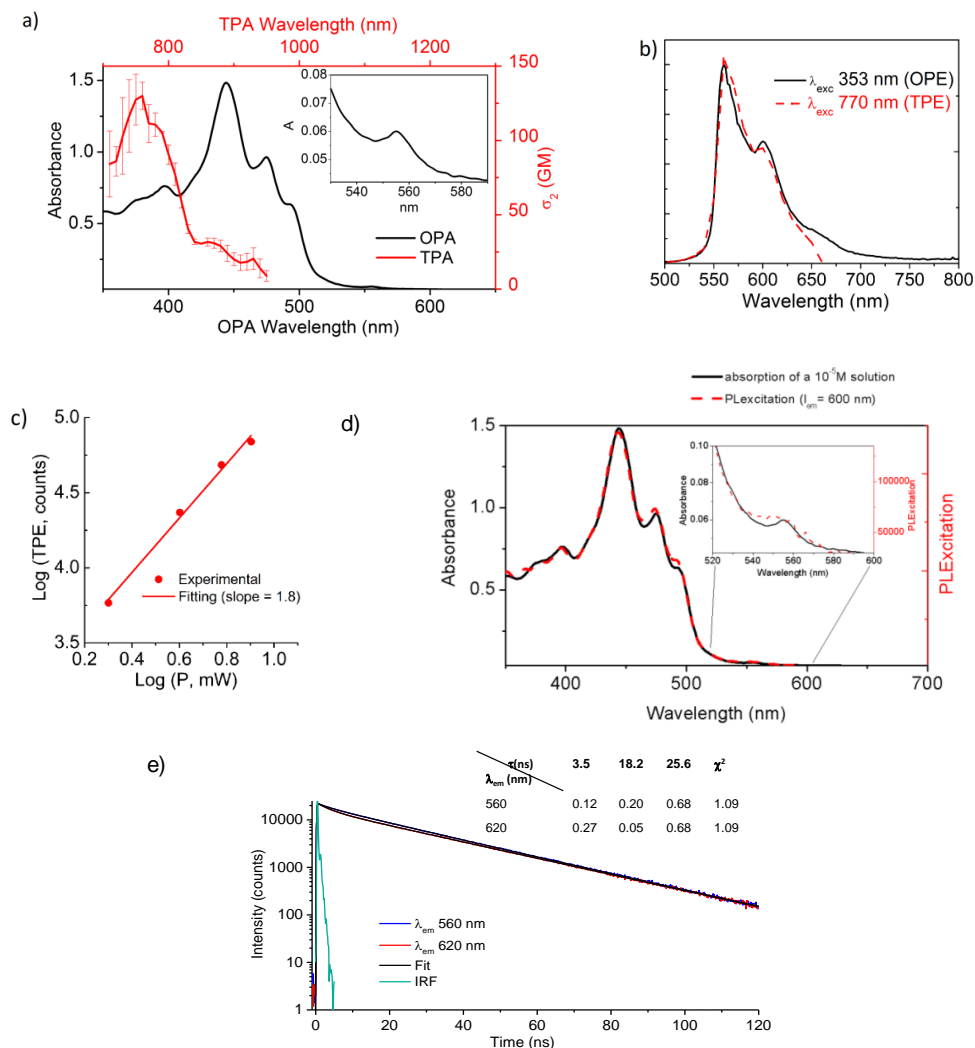


Figure 47. a) Two-photon and one-photon absorption (TPA and OPA) of **194a** in CH_2Cl_2 (inset: OPA of **194a** in the 530-590 nm region at 10^{-5} M in CH_2Cl_2); b) two-photon induced emission (TPE) upon excitation at 770 nm and one-photon induced emission (OPE) upon excitation at 353 nm; c) log-log plot showing quadratic dependence; d) absorption and excitation spectra overlapping; e) Fluorescence emission decays of compound **194a** in CH_2Cl_2 collected at 560 nm (in blue) and 620 nm (in red) and corresponding multiexponential fitting. The instrumental response function (IRF) is shown in green.

Theoretical calculations show that the four lowest energy transitions are all described by a redistribution of the electron density within the sp^2 core with a minor charge transfer to the helicene (Figure 48). On the other hand, the strongest charge transfer occurs for higher energy

transitions increasing the TPA probability. Namely, the transitions predicted at 380 and 397 nm that involve charge transfer between the helicene and the heptagon and the 385 nm transition involving an electron density transfer from the sp^2 core to the heptagon.

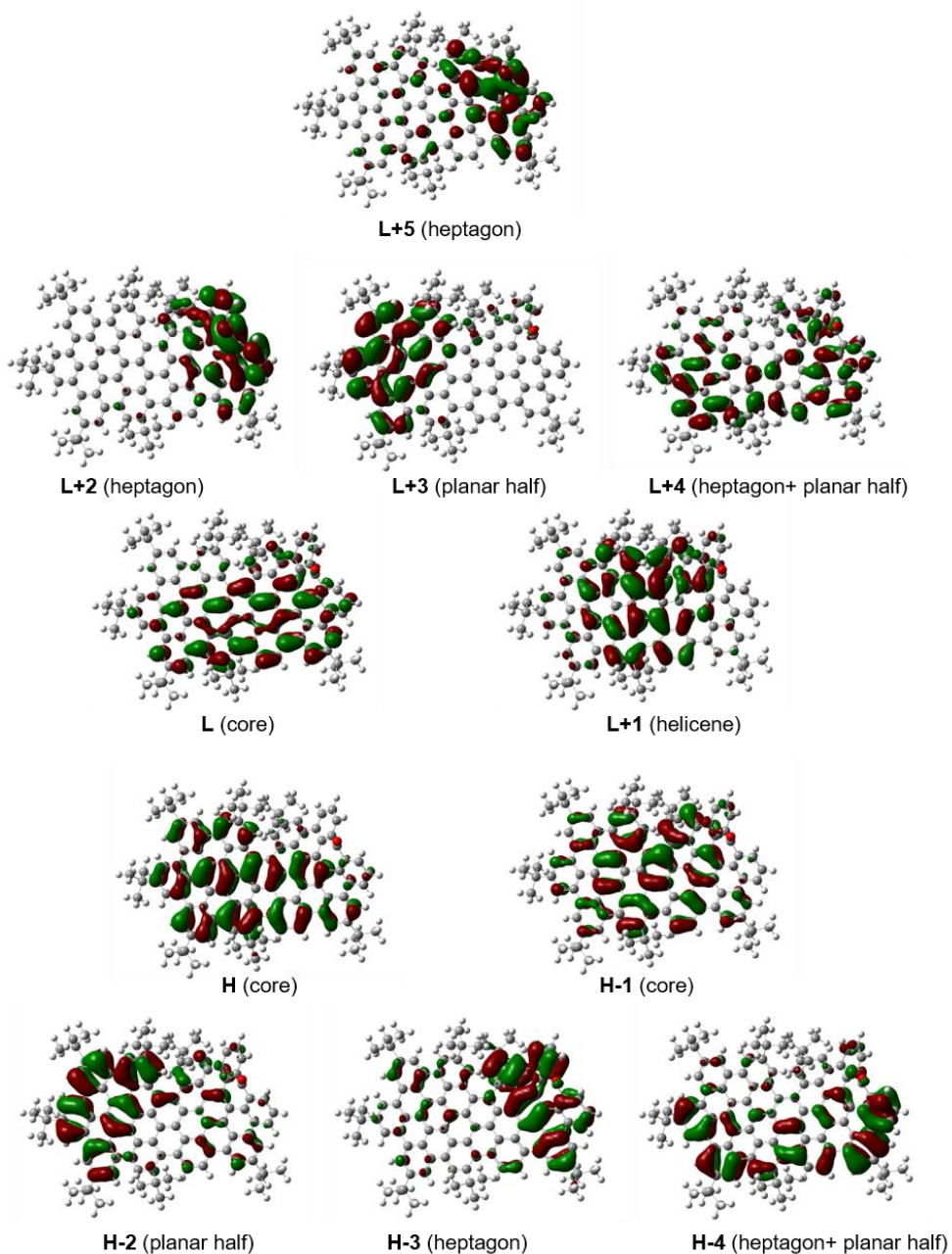


Figure 48. Isodensity surface for the frontier orbitals of *M-194a* involved in the lowest energy transitions.

3. Results and discussion

Table 2. Molecular orbitals involved in the lower energy electronic transitions (>300 nm) predicted by TD-DFT at the B3LYP/6-31g(d,p) level for *M-194a* in vacuum: orbitals involved (H, HOMO and L, LUMO), percentage contribution of each excitation to the CI expansion (%), wavelength of the transition (nm), oscillator strength (*f*) and rotatory strength velocity form (R_{vel} , 10^{-40} cgs)

| | Exp. | | Calc. | | | | <i>f</i> | R_{vel} |
|-----------------|----------------------|-----------------------|---------|------|----|-------|----------|-----------|
| | λ^{exp} (nm) | λ^{calc} (nm) | H-n→L+m | | CI | | | |
| S ₁ | 555 | 527 | H-1 | L | 22 | 0.003 | -0.1 | |
| | | | H | L+1 | 19 | | | |
| S ₂ | 493 | 507 | H | L | 29 | 0.12 | -11.5 | |
| | | | H-1 | L+1 | 12 | | | |
| S ₃ | 475 | 464 | H-1 | L+1 | 31 | 1.13 | 83.4 | |
| | | | H | L | 13 | | | |
| S ₄ | 444 | 449 | H | L+1 | 19 | 0.42 | -57.5 | |
| | | | H-1 | L | 18 | | | |
| S ₅ | | 446 | H | L+2 | 16 | 0.02 | -11.3 | |
| | | | H-2 | L | 11 | | | |
| S ₆ | | 430 | H | L+3 | 12 | 0.04 | 35.8 | |
| | | | H | L+2 | 11 | | | |
| | | | H-2 | L | 10 | | | |
| S ₇ | | 427 | H-1 | L+2 | 23 | 0.05 | -15.4 | |
| | | | H | L+2 | 17 | | | |
| S ₉ | 397 | 409 | H | L+3 | 15 | 0.15 | -66.2 | |
| | | | H-3 | L | 14 | | | |
| S ₁₀ | | 407 | H-1 | L+3 | 29 | 0.17 | 59.0 | |
| S ₁₁ | | 401 | H-2 | L+1 | 15 | 0.05 | 46.7 | |
| S ₁₂ | | 397 | H-3 | L+1 | 31 | 0.08 | 105.7 | |
| S ₁₃ | 384 | 385 | H | L+4 | 24 | 0.16 | -12.4 | |
| S ₁₄ | 375 | 380 | H-1 | L+4 | 24 | 0.05 | 12.6 | |
| S ₁₈ | | 367 | H | L+6 | 20 | 0.02 | -24.0 | |
| | | | H-3 | L+2 | 12 | | | |
| S ₁₉ | | 365 | H-2 | L+2 | 32 | 0.08 | -5.8 | |
| S ₂₀ | | 361 | H-1 | L+5 | 10 | 0.04 | 5.0 | |
| S ₂₁ | | 359 | H-1 | L+6 | 22 | 0.04 | 0.0 | |
| S ₂₂ | | 357 | H-5 | L | 19 | 0.01 | 35.1 | |
| S ₂₃ | | 356 | H-5 | L | 13 | 0.06 | 78.0 | |
| S ₂₄ | 351 | 351 | H-4 | L+3 | 29 | 0.14 | -100.3 | |
| S ₂₅ | | 345 | H | L+7 | 26 | 0.03 | 54.8 | |
| S ₂₆ | | 343 | H-3 | L+3 | 15 | 0.01 | 0.1 | |
| S ₂₇ | | 342 | H-5 | L+1 | 15 | 0.02 | 26.1 | |
| | | | H-1 | L+7 | 14 | | | |
| S ₃₁ | | 333 | H-2 | L+4 | 19 | 0.09 | -39.4 | |
| S ₃₂ | | 332 | H-4 | L+2 | 20 | 0.06 | -25.3 | |
| S ₃₄ | 312 | 327 | H-2 | L+5 | 17 | 0.13 | 65.9 | |
| S ₃₅ | | 326 | H-1 | L+7 | 10 | 0.02 | -18.0 | |
| S ₃₆ | | 325 | H-3 | L+5 | 22 | 0.01 | -41.2 | |
| S ₃₇ | | 324 | H-6 | L+2 | 21 | 0.07 | 41.2 | |
| S ₃₉ | | 323 | H-7 | L+1 | 11 | 0.02 | 5.6 | |
| S ₄₁ | | 320 | H-4 | L+3 | 20 | 0.01 | -29.5 | |
| S ₄₂ | | 318 | H-8 | L | 10 | 0.03 | -9.3 | |
| | | | H-4 | L+1 | 10 | | | |
| S ₄₄ | | 317 | H-8 | L | 13 | 0.03 | 33.9 | |
| S ₄₅ | | 316 | H-6 | L+1 | 14 | 0.06 | -7.5 | |
| S ₄₆ | | 315 | H-1 | L+9 | 11 | 0.06 | -4.1 | |
| S ₄₇ | | 315 | H-9 | L | 14 | 0.04 | -32.4 | |
| S ₄₉ | | 313 | H | L+10 | 11 | 0.04 | -9.5 | |
| S ₅₀ | | 312 | H-9 | L+1 | 12 | 0.03 | 6.6 | |

^a Only contributions higher than 10% were included. With the exception of the lowest energy transition, only transitions with oscillator strength higher than 0.01 are listed.

3.1.3. Chiroptical properties

Encouraged by the good optical properties of **194a**, we aimed to study its chiroptical properties. To this end, **194a** bears bulky *tert*-butyl groups at the [5]helicene region to allow chiral resolution of each enantiomer *M*-**194a** and *P*-**194a**. Both enantiomers were separated and isolated either by analytical or semipreparative chiral HPLC (Figure 49). We determined the Gibbs activation energy (ΔG^\ddagger (T)) for the racemization process by following the decay of the enantiomeric excess by chiral HPLC over time at three different temperatures (140, 160 and 180°C). From this first measure, the rate constant of racemization at each temperature was obtained from the slope (Equation 7, Figure 50).

$$\ln(ee) = -k \cdot t \quad (7)$$

$$\ln\left(\frac{k}{T}\right) = \frac{-\Delta H^\ddagger}{R} \cdot \frac{1}{T} + \ln\frac{k_B}{h} + \frac{\Delta S^\ddagger}{R} \quad (8)$$

Thus, applying the Eyring-Polanyi equation, the enthalpy, entropy and Gibbs activation energy were calculated, resulting in ΔG^\ddagger (298 K) = 33.0 kcal·mol⁻¹·K⁻¹ (ΔH^\ddagger = 32.1 kcal·mol⁻¹, ΔS^\ddagger = -3 cal·mol⁻¹), in the range of values recently reported by Juríček for [5]helicenes difunctionalized in the fjord region, and ensuring stability toward racemization at room temperature.¹⁵⁶

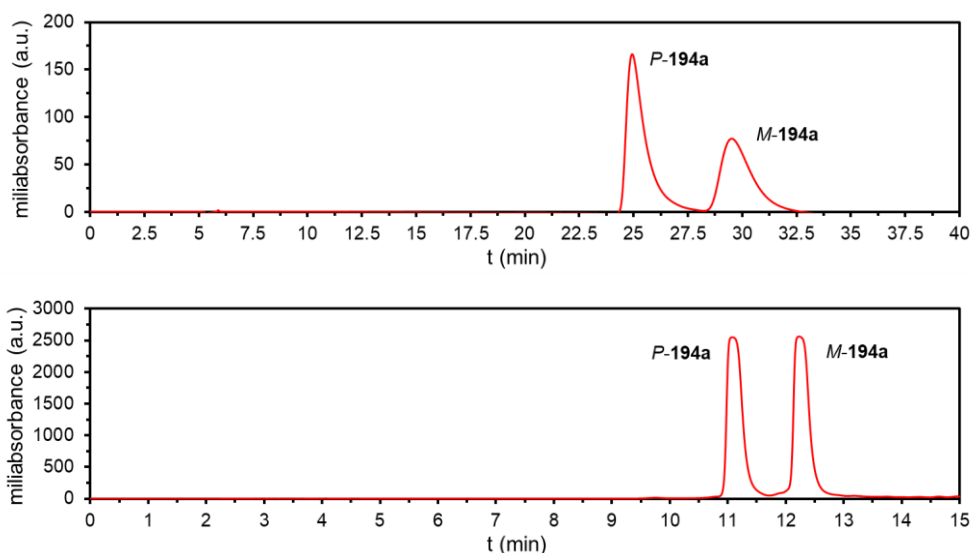


Figure 49. Chromatograms corresponding to the separation of *M*-**194a** and *P*-**194a** after the analytical run (top) and the semipreparative run (bottom).

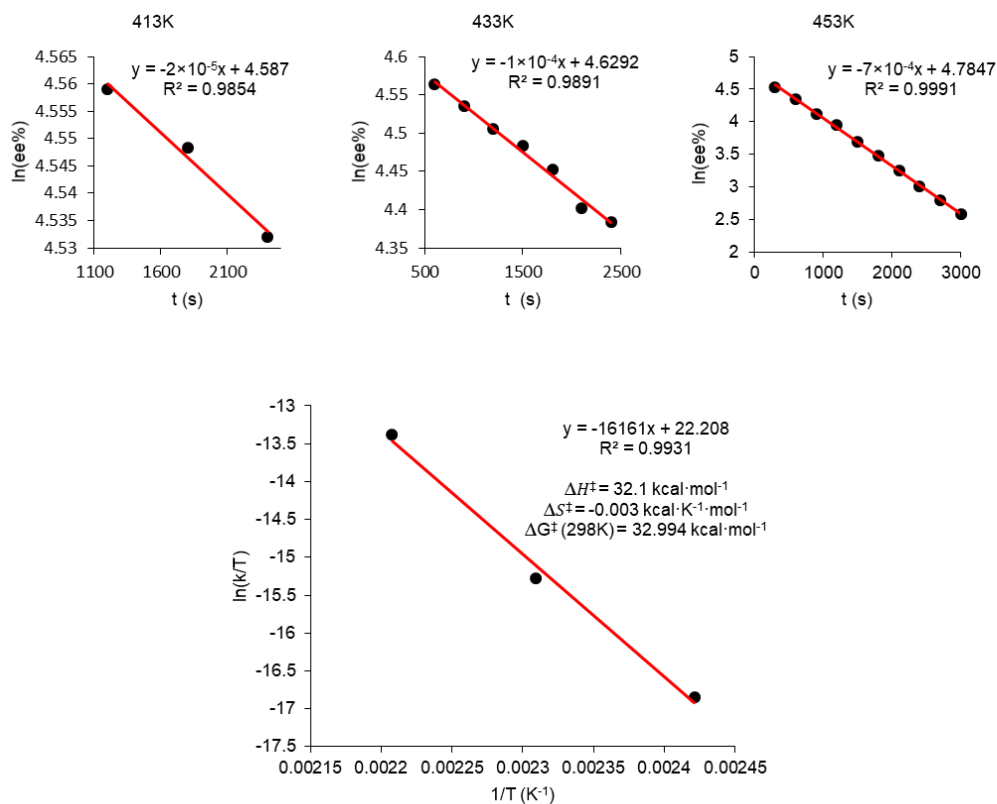


Figure 50. Plots of $\ln(\text{ee}\%)$ vs time at three different temperatures (top) and Eyring-Polanyi plot (bottom).

Firstly, an enantiopure sample of *M*-**194a** was dissolved in CH_2Cl_2 in order to evaluate its optical rotation. The $[\alpha]_{\text{D}}^{25}$ obtained after the measurement over a c 0.037 solution revealed a value of -186.12° , expected sign for a *M*-helicene and one order of magnitude less than pristine [5]carbohelicene.

The circular dichroism (CD) spectra of both enantiomers are depicted in Figure 46. We based our stereochemical assignment on TD-DFT calculations on the geometry of both enantiomers *M* and *P*-**194a**. In agreement with the calculations, we correlate the main features of the CD spectrum observed as positive bands at 370, 385 and 475 nm and negative CD band at 498 nm with the *P*-**194a** enantiomer (Figure 51c). The absolute configuration of simple [*n*]helicenes has been usually

related with the sign of the first intense band at the longest wavelength of the CD spectra.²²² Nevertheless, CD bands corresponding to minor absorption bands due to the presence of substituents show shapes and signs strongly dependent of the global structure. Moreover, vibronic contributions can also determine the sign of the observed bands.²²³ It is worth noting that the sign of the longest wavelength CD band determines the sign of the CPL spectra despite its intensity. Taking into account the presence of a very weak band at 555 nm, we increased the concentration up to 10^{-3} M, thus being able to observe the corresponding CD band (Figure 51a, inset). The dissymmetry value g_{abs} of **194a** in CH_2Cl_2 ranged from 2.7×10^{-3} at 370 nm to 5.3×10^{-4} at 555 nm. The major contribution to the electronic transition of *M*-**194a** observed at 475 nm was calculated as the H-1 to the L+1 (Figure 48). This band is predicted by the calculations at 464 nm and shows a significant contribution from the chiral moiety (the L+1 orbital is clearly centered at the helicene). In general, the CD spectrum computed in the 300-550 nm is well predicted by the calculations. The strongest features in the CD spectrum are calculated at 397 and 380 nm and experimentally observed as a structured band in the 350-400 nm region (Figure 51c). Both transitions involve the charge transfer between the helicene and the heptagon units (Table 2 and Figure 48).

Interestingly, these are also the transitions that appear to be more active in the two-photon absorption spectrum. Therefore, the presence of the heptagon unit and the possibility of having a charge transfer between the chiral moiety and the heptagon favour both the CD response and the two-photon absorption.

We also recorded the circularly polarized luminescence (CPL) spectra of *M*-**194a** and *P*-**194a** (Figure 51b) at 10^{-5} M in CH_2Cl_2 , thus discarding the formation of aggregates that would lead to artifact signals due to photoselection.²²⁴ As expected, the CPL spectrum showed an emission maxima at 560 nm upon irradiation with UV light ($\lambda_{exc} = 372$ nm) whose sign correlates with the lowest energy CD sign (band at 555 nm). Remarkably, CPL emission maxima matches the same energy transition observed for the upconverted emission upon two-photon absorption ($\lambda_{exc} = 770$

²²² F. Furche, R. Ahlrichs, C. Wachsmann, E. Weber, A. Sobanski, F. Vögtle, S. Grimme, *J. Am. Chem. Soc.* **2000**, *122*, 1717-1724.

²²³ S. Abbate, G. Longhi, F. Lebon, E. Castiglioni, S. Superchi, L. Pisani, F. Fontana, F. Torricelli, T. Caronna, C. Villani, R. Sabia, M. Tommasini, A. Lucotti, D. Mendola, A. Mele, D. A. Lightner, *J. Phys. Chem. C* **2014**, *118*, 1682-1695.

²²⁴ H. Tanaka, Y. Inoue, T. Mori, *ChemPhotoChem* **2018**, *2*, 386-402.

nm), which would represent an unprecedented process of TPA-based upconverted CPL. We evaluated the g_{lum} value as 2.3×10^{-4} for **194a**, which, to the best of our knowledge, represents the first reported circularly polarized emission for an enantiopure nanographene. Unfortunately the comparison between the optical properties of **194a** with those of a model heptagon-free compound was not possible as, in our hands, the synthesis of a purely hexagonal model compound with similar length and width incorporating a [5]helicene subunit led to a complex mixture of compounds which could not be purified and characterized properly. In this case, the distortion caused by the [5]helicene subunit and the presence of the *tert*-butyl groups are not sufficient to confer the necessary processability and solubility to the model compound. The dipole moment created by the tropone moiety seems to be mandatory for the processability of the model compound that has a lower estimated dipole moment (1.02 D) when compared with compound **194a**.

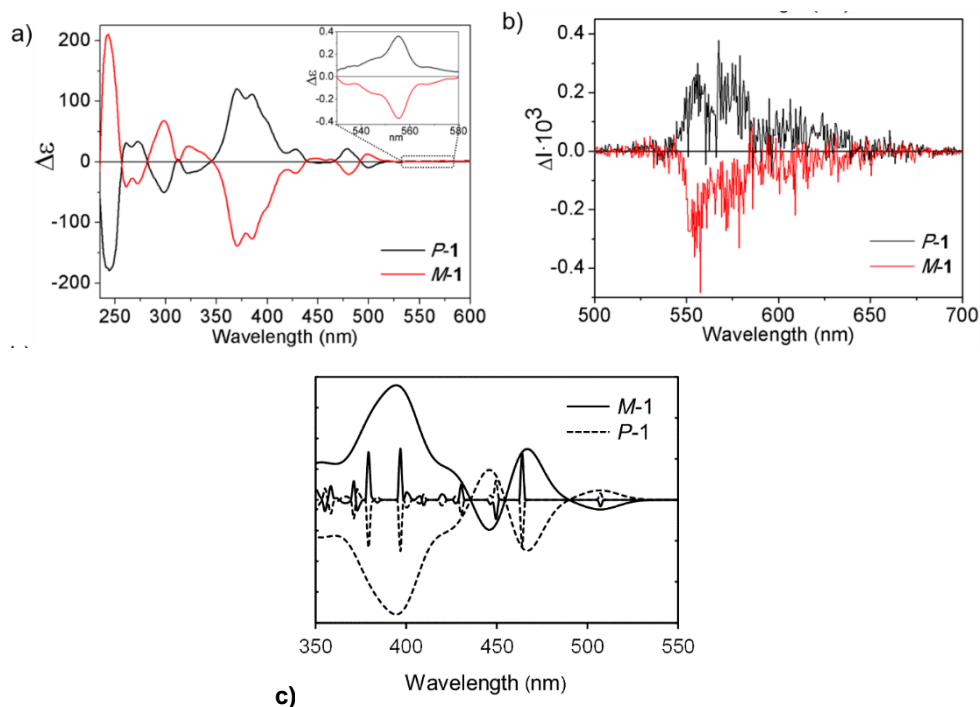


Figure 51. a) CD spectra of *M*-**194a** and *P*-**194a** at 10^{-5} M in CH_2Cl_2 . Inset: CD spectra of *M*-**194a** and *P*-**194a** in the 530-580 nm region at 10^{-3} M in CH_2Cl_2 ; b) CPL spectra of *M*-**194a** and *P*-**194a** at 10^{-5} M in CH_2Cl_2 upon excitation at 372 nm; c) TD-DFT predicted transitions and simulated CD spectra of *M*-**194a** and *P*-**194a**.

3.1.4. Electrochemical properties

The good solubility of **194a** in organic solvents allowed us to also evaluate its electrochemical behaviour. Cyclic voltammetry (CV) (1 mM, $n\text{Bu}_4\text{NPF}_6$, in THF) showed reversible reduction peaks at -2.06 and -2.37 V and reversible oxidation peaks at 0.60 and 0.90 V versus Fc/Fc^+ (Figure 52) (THF was used as solvent due to its large electrochemical window on the reduction process). Hence, the HOMO-LUMO energy gaps based on the first half-wave oxidation and reduction potentials resulted in 2.66 eV. In situ spectroelectrochemical measurements showed the spectroscopic response of **194a** during its oxidation/reduction. During a potential sweep, the new species generated exhibited significantly red-shifted absorption maxima at 710 and 680 nm upon oxidation and reduction, respectively, drastically diminishing the optical band gaps down to 1.74 eV upon oxidation and to 1.82 eV upon reduction (Figure 52b).

Moreover, the oxidized specie was relatively stable as we could generate it chemically by addition of arylammonium salt tris(4-bromophenyl)ammonium hexachloroantimonate (commonly known as "magic blue")²²⁵ showing also the red-shifted absorption maxima. The $^1\text{H-NMR}$ of a solution of **194a** upon addition of "magic blue" (1 equiv.) showed a peak broadening as expected for the formation of radical species. The NIR absorption maxima together with their chiroptical properties and stability would make these oxidized species promising materials for optoelectronic devices.

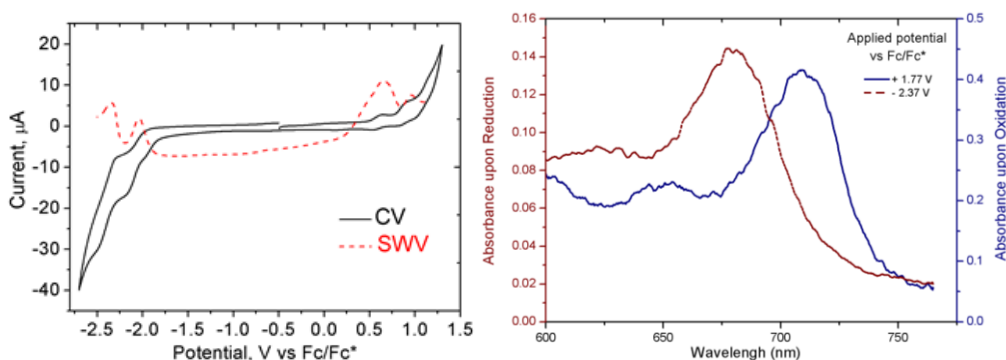


Figure 52. Left: cyclic (CV) and square wave (SWV) voltammograms of **194a** (1 mM) in THF (internal standard Fc/Fc^+ , $\nu = 0.1 \text{ V s}^{-1}$). Right: UV-vis absorbance spectra at two selected applied potential showing the absorption maxima of the new oxidized and reduced species generated.

²²⁵ N. G. Connelly, W. E. Geiger, *Chem. Rev.* **1996**, *96*, 877-910.

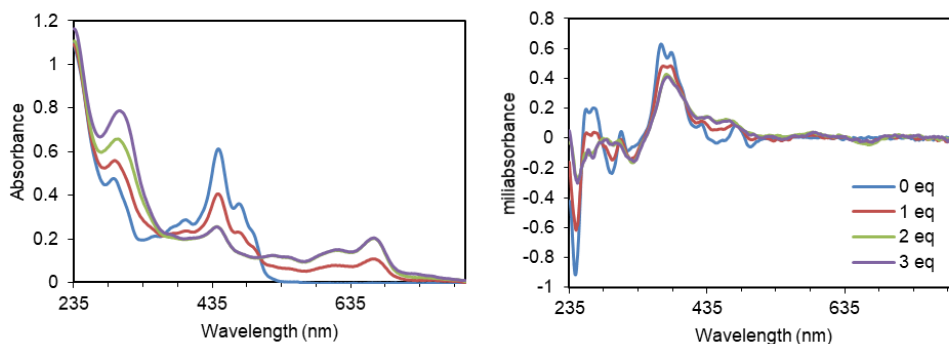


Figure 53. Left: absorbance spectra of **194a** upon addition of increasing equivalents of “Magic Blue”. Right: CD spectra of *M-194a* upon addition of increasing equivalents of “Magic Blue”.

3.1.5. On-surface study

In order to study the behaviour of this nanographene on a substrate, we carried out preliminary experiments to test the feasibility to deposit this large molecule on a single crystal surface under high or ultra-high vacuum (HV/UHV) conditions. Thermal in-vacuum sublimation of **194a** is a challenge due to its high molecular weight, which prevents their evaporation before partial or total decomposition. However, we succeeded in depositing submonolayer coverage of **194a** on Cu(111) by means of a pulsed-injection device.²²⁶ This novel deposition method is based on the injection inside the UHV system of microdroplets of a solution containing the molecule of interest by means of a fast pulsed valve. This system allows for the deposition of soluble molecules and macro-molecules without decomposition and a minimum solvent contamination.

Room temperature scanning tunneling microscopy (RT–STM) images of the Cu(111) surface before (Figure 54a) and after deposition of **194a** (Figure 54c) clearly show that the Cu surface is covered by homogeneously distributed features with elongated shape and approximate dimensions of 2.3 nm and 1.3 nm along both in-plane axis, and 1.8 Å of apparent height. The good agreement between the dimensions obtained from STM and those extracted from X-ray crystallography, together with the control experiments presented in Figure 49c, allow us to assign these features to the nanographene molecule **194a** (Figure 54d). Higher resolution STM images revealing the distorted geometry of **194a** were impossible to obtain given the diffusion of both

²²⁶ J. M. Sobrado, J. A. Martín-Gago, *J. Appl. Phys.* **2016**, *120*, 145307.

solvent and **194a** at RT when trying to approach the tip, as evidenced by the appearance of horizontal spikes in the STM images. It is worthy to note the weak surface-molecule interaction, dominated by van der Waals forces between the π -electrons of **194a** and the electron gas of Cu(111). This interaction is weakened by the presence of the *tert*-butyl groups which further separate the molecular plane from the surface. Although LT-STM images are required to obtain high-resolution images of **194a**, this preliminary study shows the feasibility of depositing **194a** under ultra-clean conditions on a single crystal surface, opening a door towards in-depth atomic characterization of its electronic, optoelectronic, and chiral properties.

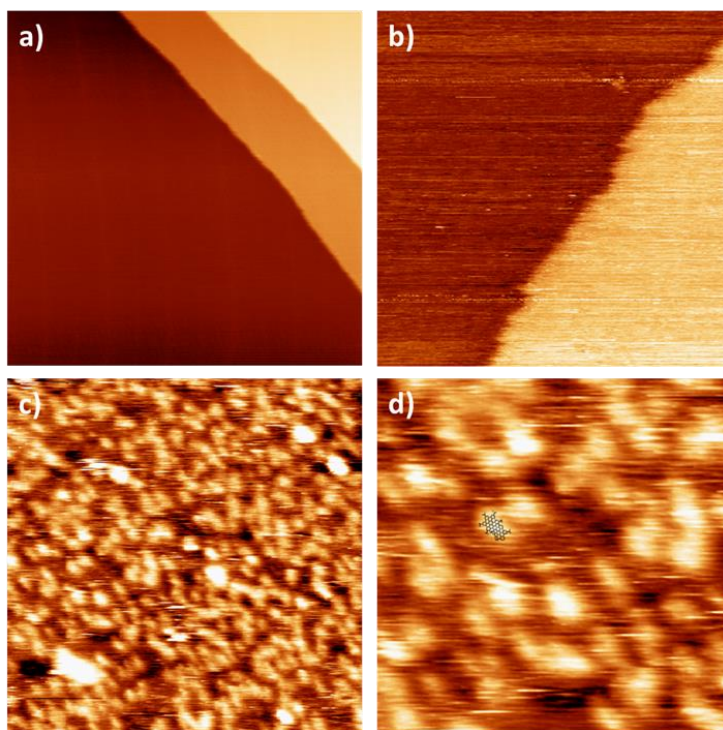


Figure 54. a) STM images of the clean Cu(111) surface; b) after CH_2Cl_2 deposition; c) and d) and after deposition of submonolayer coverage of **194a** under HV conditions. a) Size: 100 nm x 100nm, $I = 16$ pA, $V = 1.6$ V; b) Size: 50 nm x 50 nm, $I = 25$ pA, $V = -1.0$ V; c) Size: 50 nm x 50 nm, $I = 25$ pA, $V = 1.0$ V; d) Size: 20 nm x 20 nm, $I = 25$ pA, $V = 1.0$ V.

3.2. Extended ribbon-shaped saddle-helix hybrid nanographene

Regarding the outstanding (chir)optical properties coming from the previously prepared ribbon-shaped nanographene, we wondered if the presence of the seven-membered ring may affect the TPA response when embedded into a hexagonal lattice. The idea arose when looking at the high TPA levels observed on graphene quantum dots (GQD), which possess a non-defined structure. Remarkably, defects have been postulated as cause of their high fluorescence quantum yield and, moreover, TPA responses on doped GQDs are outstanding in comparison with that of their all-carbon analogues.

Therefore, the preparation of a new series of nanographenes presenting and not a seven-membered ring into their structure, and the corresponding study of their non-linear optical properties would shed light on the influence of defects in the non-linear optical response of GQDs. This relationship was not able to be studied on the previously commented system since the preparation of a hexagonal analogue to compound **194a** was not possible, whose preparation led to a complex mixture of compounds and could not be purified and characterized properly.

Having all the requirements in mind, we designed a new synthetic strategy leading to a series of novel nanographenes consisting of three HBC units. This new family of nanographenes differs between them on the presence and not of a heptagon into their structure. Thus, the different TPA values would be directly related to the presence of defects into the hexagonal structure. Moreover, the tropone-containing nanographene could be derivatized into its all-carbon analogue, exploring the influence of the carbonyl group into the TPA response.

3.2.1. Synthesis and structural characterization

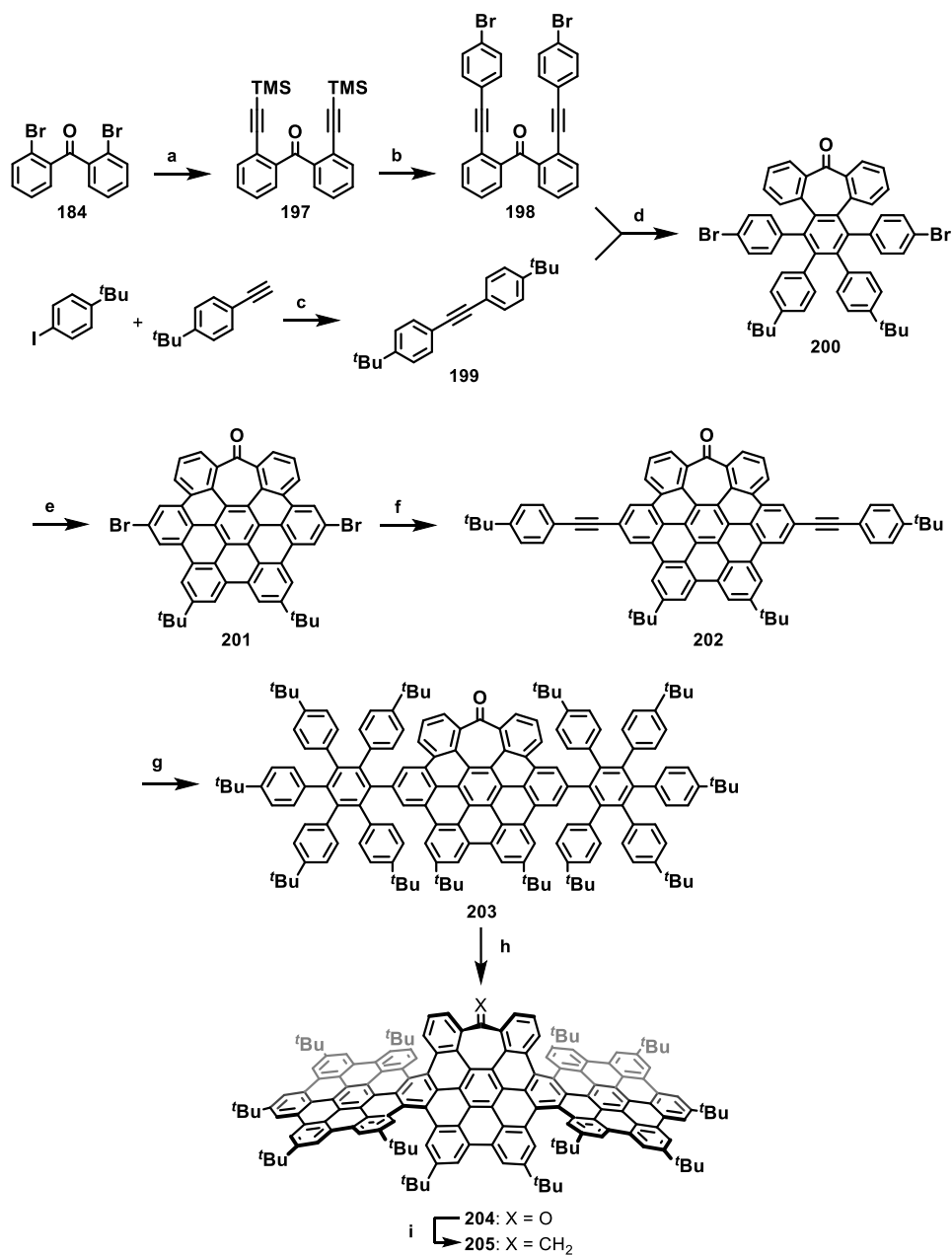
The preparation of the different analogues (presenting and not the seven-membered ring) was carried out following two different methodologies. Regarding the synthesis of the heptagon-containing analogues, we take advantage of our recently developed methodology for the preparation of functionalized distorted HBC-like compounds. Respecting to the purely hexagonal analogue, a classic synthetic strategy based on the combination of Sonogashira cross coupling and Diels-Alder reactions was followed to prepare the corresponding oligophenylenes that were finally subjected to Scholl reaction.

Thus, starting from compound **184**, and after a two-fold Sonogashira coupling with TMSA, the dialkyne derivative **197** was easily prepared. This protected dialkyne was deprotected and coupled with 1-bromo-4-iodobenzene in one step affording the dibromo derivative **198**. On the other hand, the diphenylacetylene derivative **199** was obtained as product of the Sonogashira coupling between 4-*tert*-butyliodobenzene and 4-*tert*-butylphenylacetylene. Compounds **198** and **199** were subjected to cobalt-catalyzed [2+2+2] alkyne cyclotrimerization reaction giving rise to the tropone-containing oligophenylene **200** (Scheme 38).

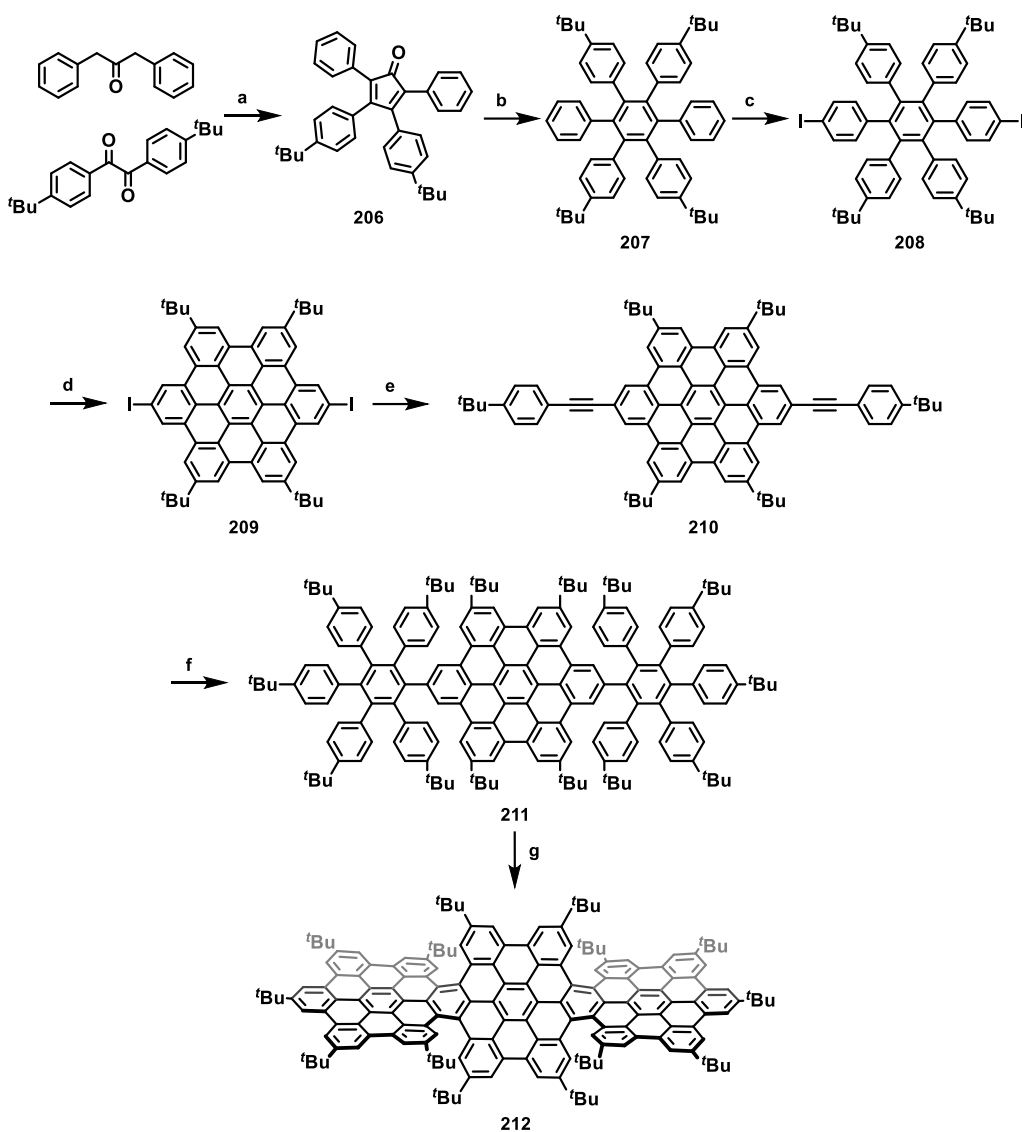
Subsequently, Scholl reaction promoted by the oxidant/acid combination of DDQ and trifluoromethanesulfonic acid created the distorted HBC-like nanographene **201** bearing two aryl bromides, which can be used for a further Sonogashira coupling with 4-*tert*-butylphenylacetylene. The resulting dialkyne was subjected to a double Diels-Alder reaction by heating up to 258°C in presence of two equivalents of the corresponding cyclopentadienone to create the precursor **203**. Finally, cyclodehydrogenation reaction over **203** creates twelve new aryl-aryl bonds, giving rise to the carbonyl-containing compound **204**, consisting of three HBC units (with a tropone unit at the central one) and four [5]helicene moieties. In order to compare the influence of the carbonyl group with an all-carbon analogue, compound **204** was treated with Tebbe's reagent, creating an exocyclic terminal alkene where the carbonyl group was located.

On the other hand, the preparation of the purely hexagonal analogue was achieved starting with the preparation of the cyclopentadienone **206** after aldol condensation between the starting materials depicted on Scheme 34. Diels-Alder reaction over the diene **206** with diphenylacetylene **199** gave rise to the hexaphenylbenzene derivative **207** that was subsequently iodinated on the available position *via* reaction with PIFA and iodine. The diiodo derivative **208** was subjected to cyclodehydrogenation reaction by treatment with FeCl₃, affording the hexabenzocoronene derivative **209**.

The aromatic surface was then extended along the *para* positions through Sonogashira reaction with 4-*tert*-butylphenylacetylene and subsequent Diels-Alder reaction with the corresponding cyclopentadienone. Finally, Scholl reaction promoted by the combination of DDQ and trifluoromethanesulfonic acid gave rise to the final compound consisting of three units of HBC arranged in a linear disposition where the central unit shares two benzene rings and showing four identical [5]helicene moieties (**212**, Scheme 39).



Scheme 38. Synthetic route towards distorted ribbon-shaped nanographenes **204** and **205**. Reagents and conditions: a) TMSA, PdCl₂(CH₃CN)₂, CuI, P(*t*Bu)₃H-BF₄, THF, (*i*Pr)₂NH, r.t., 16 h, 90%; b) 1-bromo-4-iodobenzene, PdCl₂(PPh₃)₂, CuI, Et₃N, DBU, THF, H₂O, 70°C, 16 h, 67%; c) PdCl₂(PPh₃)₂, CuI, Et₃N, THF, r.t., 16 h, 99%; d) Co₂(CO)₈, toluene, 110°C, 16 h, 56%; e) DDQ, CF₃SO₃H, CH₂Cl₂, 0°C, 10 min, 52%; f) 4-*tert*-butylphenylacetylene, Pd(PPh₃)₄, CuI, Et₃N, THF, 70°C, 16 h, 76%; g) 2,3,4,5-*tetrakis*-(*p-tert*-butyl)phenylcyclopentadienone, Ph₂O, 258°C, 10 h, 45%; h) DDQ, CF₃SO₃H, CH₂Cl₂, 0°C, 10 min, 33%; i) Tebbe's reagent, THF, 0°C, 3 h, 80%. *PPMM* enantiomer is shown.



Scheme 39. Synthetic route towards purely hexagonal nanographene **212**. Reagents and conditions: a) KOH, EtOH, reflux, 15 min, 85%; b) **199**, Ph₂O, reflux, 16 h, 77%; c) PIFA, I₂, CH₂Cl₂, RT, 75%; d) FeCl₃, CH₂Cl₂, CH₃NO₂, 0°C to r.t., 16 h, 58%; e) 4-*tert*-butylphenylacetylene, PdCl₂(PPh₃)₂, CuI, Et₃NEt, toluene, 60°C, 16 h, 75%; f) 2,3,4,5-tetrakis-(*p*-*tert*-butylphenyl)-cyclopentadienone, Ph₂O, reflux, 16 h, 29%; g) DDQ, CF₃SO₃H, CH₂Cl₂, 0°C to r.t., 10 min, 29%. *PPMM* enantiomer is shown.

The structure of compounds **204**, **205** and **212** were confirmed by means of mass spectrometry, where the high resolution mass spectrum (HR-ESI-TOF) showed single peaks centered at 2112.0857, 2110.1011 and 2196.2068 respectively. The calculated isotopic distribution overlaps perfectly with the obtained experimentally, confirming the structure of the final compounds.

The good solubility of the final compounds in common organic solvents allowed us to characterize their structures by dint of NMR spectroscopy. In contrast to previously reported planar analogues,²²⁷ which were only characterized by mass spectrometry due to their low solubility and high tendency to form aggregates. Conversely, the presence of the seven-membered ring and the helicene moieties increased the solubility of the resulting compound by minimizing the intermolecular π - π interactions. Thus, the ^1H -NMR confirmed the structure of compounds **204**, **205** and **212** (Figure 50). Moreover, a ^{13}C -NMR spectrum was recorded for **204**, whilst heteronuclear correlation NMR spectroscopy techniques were applied in order to list carbon signals on **205** and **212**.

The obtained ^1H -NMR spectra of **204** and **205** showed a reduced number of signals in the aromatic zone, suggesting that the obtained compounds were present as single and symmetric diastereoisomers. After injection of **204** into both normal and chiral stationary phase HPLC, a single chromatographic peak was obtained, thereby confirming the generation of a single *meso* diastereoisomer. On the other hand, the ^1H -NMR of compound **212** exhibited a more complex set of signals at the aromatic zone. When injected into normal phase HPLC, **212** was resolved into two peaks that were collected independently. The summed ^1H -NMR spectra of each collected peak was found to be equal to that obtained before the HPLC run, confirming that the obtained mixture was composed by two diastereoisomers in a 1.3:1.0 ratio (**212a:212b**) (Figure 55).

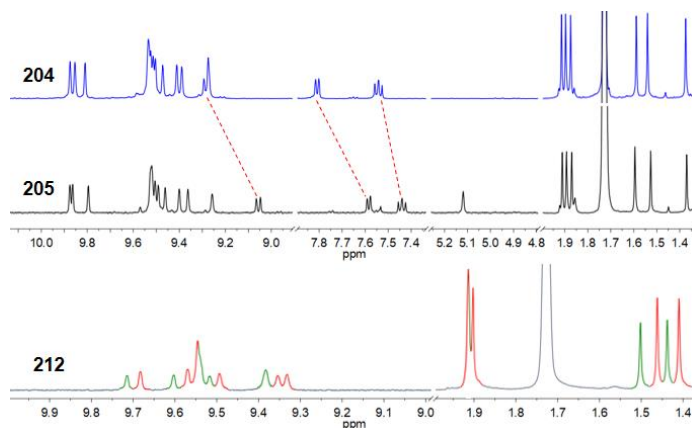


Figure 55. Stack plot of partial ^1H -NMR spectra of compounds **24**, **25** and **32** (500 MHz, $\text{C}_4\text{D}_8\text{O}$). Aromatic signals have a magnification factor of 6 \times .

²²⁷ J. Wu, L. Gherghel, M. D. Watson, J. Li, Z. Wang, C. D. Simpson, U. Kolb, K. Müllen, *Macromolecules* **2003**, *36*, 7082-7089.

Unfortunately, crystals with enough quality for X-ray diffraction were not grown by using different crystallization techniques. Therefore, DFT calculations were performed in order to carry out a deep study on the structure of the final compounds. Considering that the central HBC unit creates four [5]carbohelicene moieties when is connected to the two lateral HBCs and that the obtained diastereoisomer showed a *meso* configuration, two possible configurations arise from the structure of **204**, *PPMM-204* and *PMPM-204* according to the proposed nomenclature.

The geometries of both *PPMM-* and *PMPM-204* were optimized at CAMB3LYP/6-31G(d,p) density functional level (Figure 51). Comparison of the relative energies of *PPMM-* and *PMPM-204* indicated the former to be *ca.* 5 kcal·mol⁻¹ more stable than the latter. Considering that the absence of *tert*-butyl groups at the edges of the carbo[5]helicenes created around the tropone moiety, should result in an easily surmountable isomerization barrier that would lead to the more stable diastereoisomer and, thereby, suggesting that the observed ¹H-NMR spectrum corresponds to the *PPMM* diastereoisomer of **204**. Furthermore, DFT simulated ¹H-NMR shifts for *PPMM-204* are also in good agreement with those found at the experimental spectrum.

On the other hand, suitable crystals of precursor **203** for X-ray diffraction were grown from slow evaporation of a CH₂Cl₂/MeOH solution. The obtained structure is also in agreement with the formation of the *PPMM* diastereoisomer of **204** since the hexaphenylbenzene units are oriented in a perpendicular fashion to the central distorted HBC unit.

When looking at the ¹H-NMR spectrum of **205**, a similar signal pattern is observed with exception of the signals closer to the carbonyl group, which are upfield shifted in comparison to that of compound **204**. Moreover, a new signal centered at 5.12 ppm appeared, corresponding to the exocyclic double bond (Figure 50). As expected, the spectrum of compound **205** is not composed by a mixture of diastereoisomers, suggesting that the conformation is retained after the final synthetic step.

Regarding compound **212**, the presence of *tert*-butyl groups at the four carbo[5]helicenes is directly related to an increase of the isomerization barrier, hindering the convergence to the most stable diastereoisomer. This fact, would explain the attainment of **212** as a mixture of stable and separable diastereoisomers. Remarkably, the obtained diastereoisomers are expected to be highly symmetric since the number of signals are reduced.

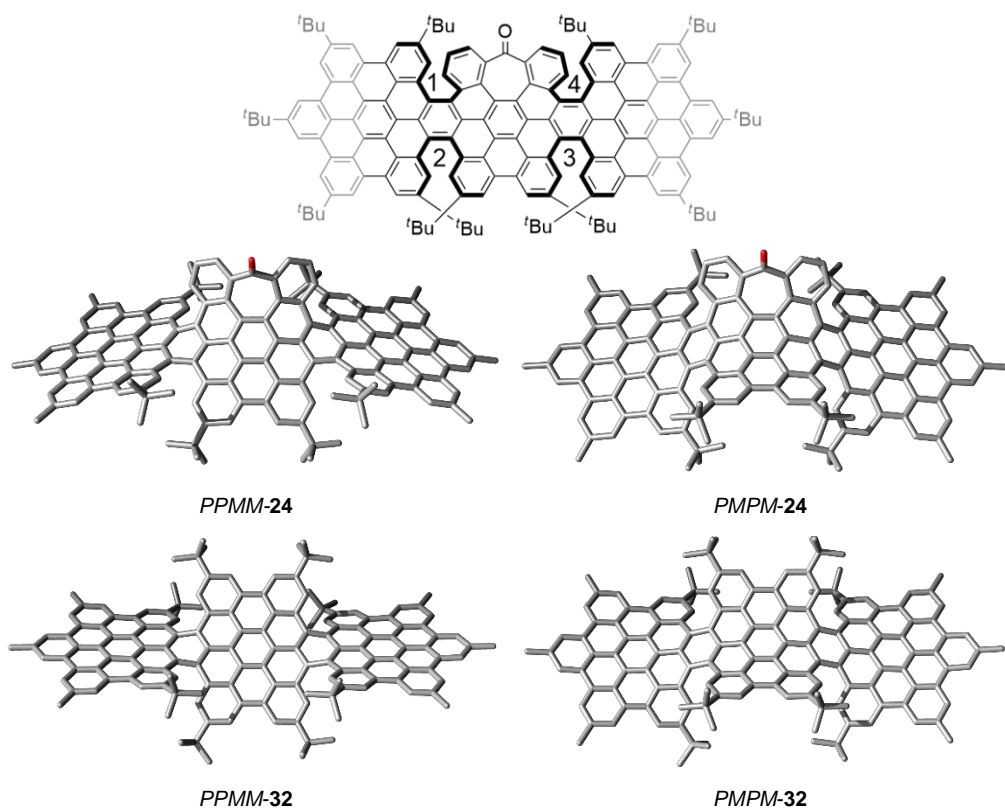


Figure 56. Top: proposed numeration for the helicenes present on compound **204**. Bottom: DFT-CAMB3LYP/6-31G(d,p) optimized structures of **PPMM-204** (left) and **PMPM-204** (right). Hydrogen atoms were omitted for clarity and tBu groups were substituted by Me for a lower computational cost.

3.2.2. Optical properties

The optical properties of the prepared compounds were evaluated by means of one-photon, two-photon absorption and fluorescence spectroscopy. The OPA spectra of compounds **204**, **205** and **212** were recorded in the range of 300 to 700 nm at a concentration of *ca.* 10^{-6} M in CH_2Cl_2 . The three compounds exhibited a similar spectrum, where the profile drawn a more intense band at high energy wavelengths (300-450 nm) and a relative less intense band between 500-625 nm.

Compounds **204** and **205** gave more intense OPA signals, with maximum epsilon values of $7.0 \times 10^4 \text{ M}^{-1}\cdot\text{cm}^{-1}$ at 434 nm and $8.3 \times 10^4 \text{ M}^{-1}\cdot\text{cm}^{-1}$ at 433 nm respectively. Conversely, compound **212** presented considerable less intense OPA, being the maximum epsilon value evaluated as $4.0 \times 10^4 \text{ M}^{-1}\cdot\text{cm}^{-1}$ at 443 nm that is approximately half of that of the seven-membered ring containing analogues. The red-shifted band present in the three spectra exhibit a maximum centered at 578

nm ($3.9 \times 10^4 \text{ M}^{-1}\cdot\text{cm}^{-1}$), 577 nm ($4.7 \times 10^4 \text{ M}^{-1}\cdot\text{cm}^{-1}$) and 575 nm ($1.9 \times 10^4 \text{ M}^{-1}\cdot\text{cm}^{-1}$) for **204**, **205** and **212** respectively. These obtained data are in good agreement with those resulted from TD-DFT calculations where the lowest energy transition was found at 563 nm for *PPMM-204*, in contrast to that for the *PMPM* conformation, which was centered at 490 nm, suggesting *PPMM* as the most stable conformation.

The theoretical simulation of the transitions involved in the absorption spectrum of *PPMM-204* showed that the lowest energy transition centered at 563 nm involves charge transfers from the HOMO-1 and HOMO to the LUMO+1 and LUMO respectively. Remarkably, the electron density in the HOMO and LUMO molecular orbitals are mainly centered at the central distorted HBC unit, whilst in the HOMO-1 and LUMO+1 are mainly located at the helicenes (Figure 53).

The three compounds presented intense fluorescence after one-photon excitation with a similar emission profile, the emission spectra consists of two major vibronic bands with decreasing intensities at 599 and 645 nm for **204**, 597 and 640 nm for **205**, and 592 and 643 nm for **212**. The Stokes shifts were found to be low and similar for the three analogues (*ca.* 20 nm). Regarding fluorescence quantum yield (ϕ_F), it was found to be slightly higher values in the case of the seven-membered ring containing nanoribbons and was evaluated as 71% for **204**, 76% for **205** and 69% for **212**. The overlapping between the absorption and the excitation spectra is almost perfect on the three compounds indicating that the samples are homogeneous and do not present either impurities or aggregates. The optical bandgap was estimated from the curve crossing of the normalized absorption and emission spectra and was found to be *ca.* 2.15 eV for the three studied compounds.

Regarding the non-linear optical responses, compounds **204**, **205** and **212** showed two-photon absorption upconversion when irradiated with a Ti:sapphire femtosecond laser in the 730-930 nm region. As reported for carbon dots,²²⁸ TPA spectra (TPA, red line on Figure 52) showed their maximum value at the lowest energy wavelength (730 nm) with a cross-section (σ_2) of 287, 286 and 128 GM for **204**, **205** and **212** respectively. The emission spectra recorded after excitation with two photons of 800 nm overlap perfectly with those obtained by a single photon excitation

²²⁸ C. I. M. Santos, I. F. A. Mariz, S. N. Pinto, G. Gonçalves, I. Bdkin, P. A. A. P. Marques, M. G. P. M. S. Neves, J. M. G. Martinho, E. M. S. Maçôas, *Nanoscale* **2018**, *10*, 12505-12514.

3. Results and discussion

of 500 nm (OPE, black dashed line on Figure 52) and the two-photon brightness ($\sigma_2\phi$) was estimated as 203, 218 and 88 GM for **204**, **205** and **212** respectively. Importantly, no net OPA was observed above 700 nm. Furthermore, TPE was recorded with different incident power, confirming the quadratic dependence of the upconverted emission on the excitation power (Figure 52).

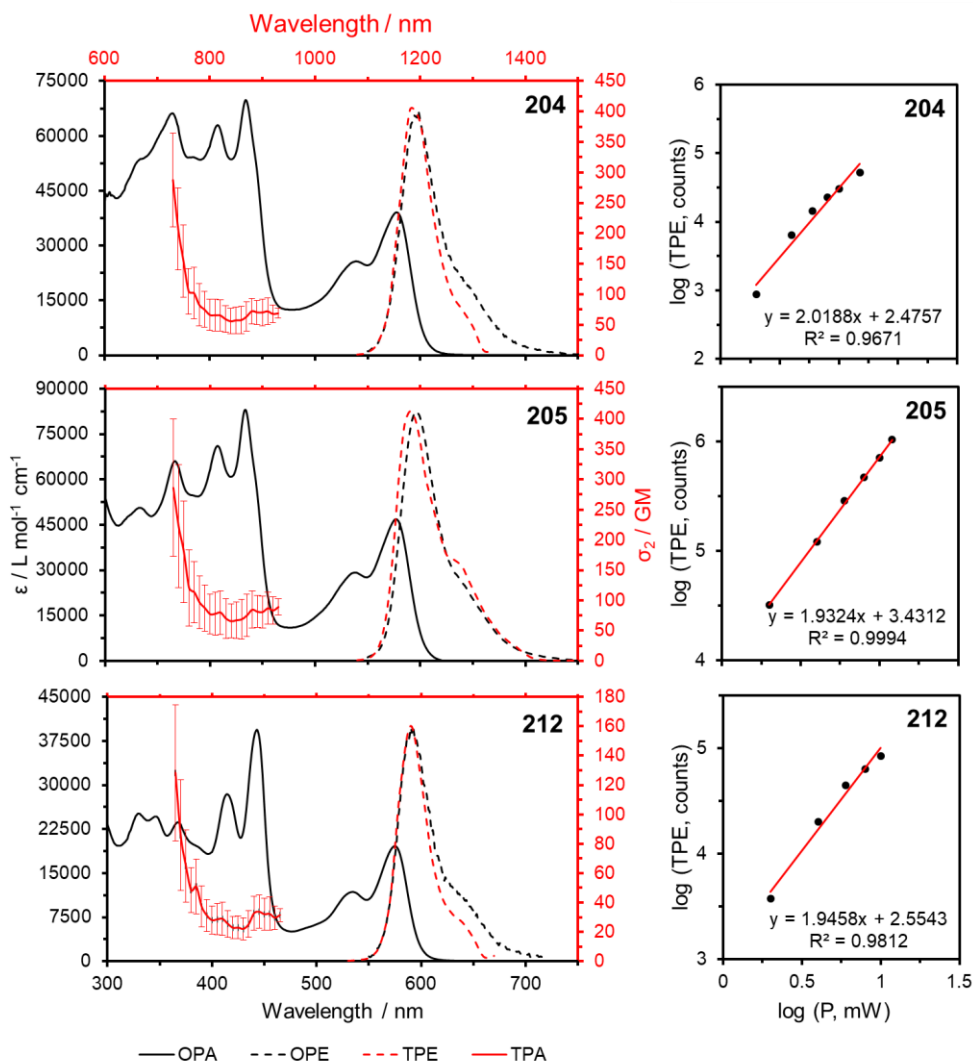


Figure 57. One-photon absorption (OPA), two-photon absorption (TPA), one-photon excitation emission (OPE) and two-photon excitation emission (TPE) spectra of compounds **204** ($\lambda_{\text{exc}} = 500 \text{ nm}$), **205** ($\lambda_{\text{exc}} = 548 \text{ nm}$) and **212** ($\lambda_{\text{exc}} = 500 \text{ nm}$) measured at $\text{ca. } 10^{-6} \text{ M}$. log-log plot of the two-photon excited emission intensity (TPE) as a function of the excitation power (P).

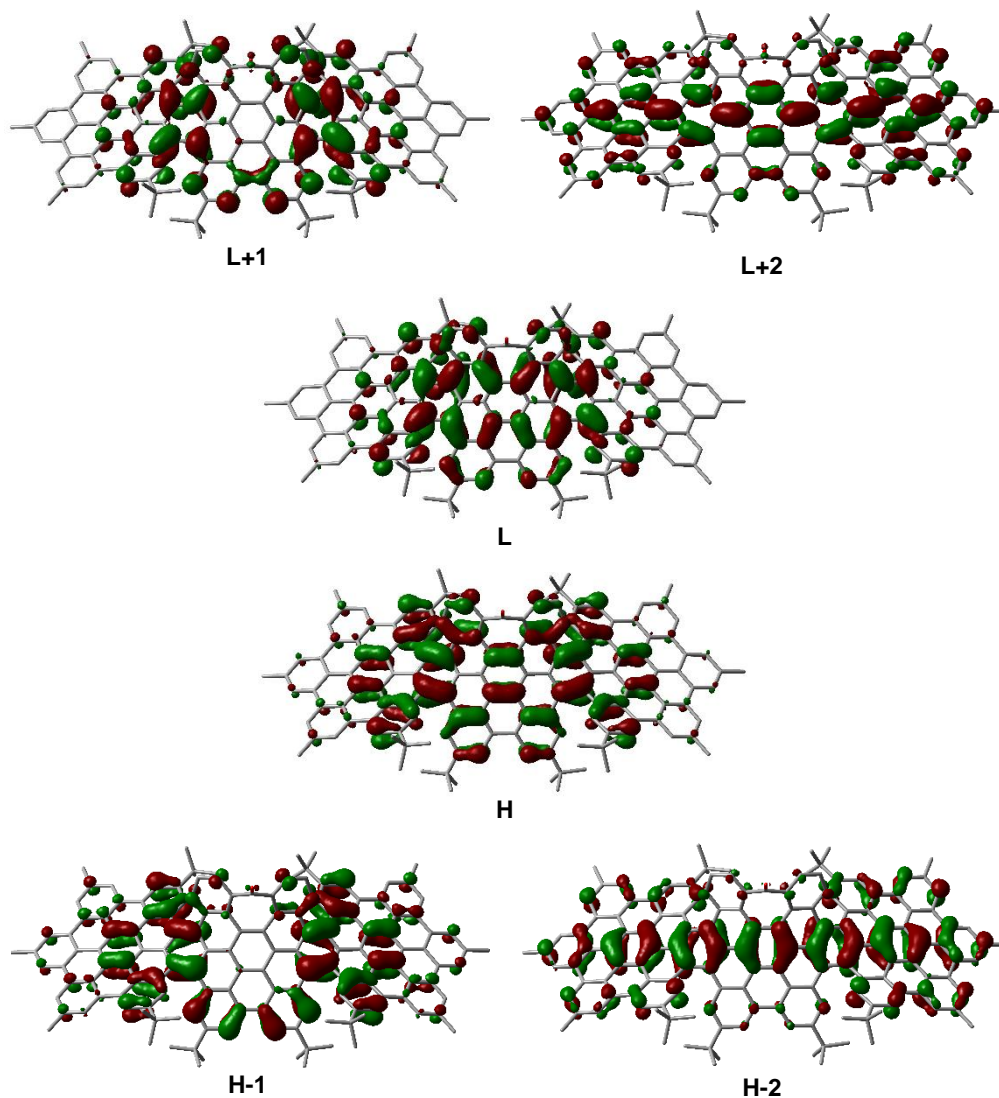


Figure 58. Isodensity (isoval = 0.02) surface for the frontier orbitals of *PPMM-204* involved in the lowest energy transitions.

It was expected that the presence of the carbonyl group increased the TPA response of **204** respect to **205**, since its electron withdrawing character would interfere in the charge mobility. However, all-carbon analogue **205**, with an exocyclic double bond, showed a TPA cross section of practically the same value of **204**, which in both cases is twice of that for compound **212**. The slight difference between **204** and **205**, can be understood considering the relationship between the size of the reported molecules and the electron withdrawing power of a single carbonyl group

at the center of the structure. On the other hand, the fact that the presence of functionalization at the seven-membered ring does not affect significantly the TPA response, points to these structural defect as responsible of the two-fold increase in the TPA when comparing with compound **212**.

Thus, the experimental results suggest that the saddle-shaped curvature created by the presence of a seven-membered ring definitively affects the TPA capability of these family of ribbon shaped nanographenes.

3.2.3. Electrochemical properties

The electrochemical behavior of the prepared analogues was also evaluated in terms of cyclic voltammetry (CV) and Square Wave Voltammetry (SWV). The electrochemical measurements were carried out by dissolving the samples in a 0.1 M solution of $n\text{Bu}_4\text{N}^+\text{PF}_6^-$ in THF and scanning in a range from -3.5 to 1.0 V. Three reversible oxidation waves were found for **204**, while for **205** and **212** only two were observed. Remarkably, the first observed oxidation is shifted to higher potential when the carbonyl group is present (0.54 V), whilst the value remains similar for the all-carbon analogues (0.46 and 0.47 V for **205** and **212** respectively), this fact is in concordance to the presence of the ketone moiety which may increase the oxidation potential. In addition, up to five reduction waves were found after scanning in the negative potentials region, where the first reduction wave is shifted to less negative potentials in the case of saddle-helix hybrid nanographenes **204** and **205**.

Therefore, the electrochemical HOMO-LUMO energy gap based on the first half-wave oxidation and reduction potentials resulted in 2.27, 2.31 and 2.56 eV for **204**, **205** and **212** respectively. Noteworthy, the seven-membered ring containing analogues exhibit a lower bandgap value when compared to their fully hexagonal analogue. The slight difference between **204** and **205** could be related to the presence of the ketone moiety, which typically shows a lower energy LUMO. On the other hand, compound **212** presents larger HOMO-LUMO gap (2.56 eV) compared with those saddle-helix hybrid nanographenes. These results indicate that saddle-shaped curvature has also a clear effect on the energy gap of these family of nanographenes, decreasing its HOMO-LUMO gap in *ca.* 10%.

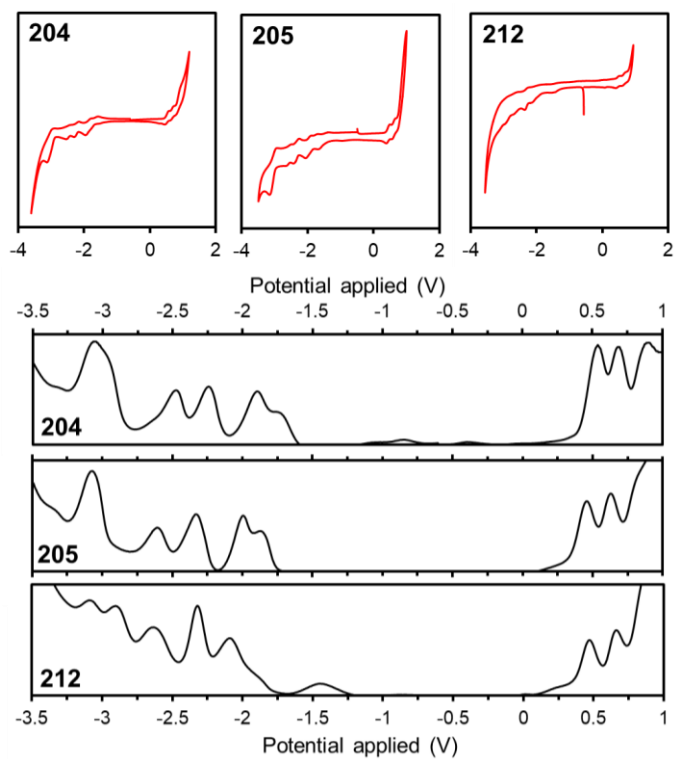


Figure 59. Top: Cyclic Voltammograms of **204**, **205** and **212** (1 mM) in THF; Bottom: Square Wave Voltammograms of **204**, **205** and **212** (1 mM) in THF (internal standard Fc/Fc⁺, $\nu = 0.1 \text{ V}\cdot\text{s}^{-1}$).

3.3. Undecabenzo[7]superhelicene

Theoretical and experimental studies have demonstrated that folding graphene induces changes in its original characteristics, tuning the electronic transport²²⁹ and the thermal properties.²³⁰ Recent works also show that graphene helicoids (GH), like nanosprings or nanosolenoids, could exhibit superior properties than multilayer graphene (MLG) of similar size in terms of controlling thermal conductivity,²³¹ tensile²³² or magnetic properties.²³³

In this sense, helical twisted nanographenes are promising candidates also in the field of chiral electronics and very relevant recent examples have been presented on chiral enantiopure nanographenes showing inherent chiroptical properties and electronic responses of interest in a variety of applications.

This section describes the synthesis, characterization and (chir)optical properties of the first fully π -extended [7]carbohelicene as a constituent of a chiral nanographene. In the final molecule, a [7]carbohelicene is fully surrounding by fused benzene rings leading to the first undecabenzo[7]helicene. The prepared compound is a HBC-based helicene, a new member of the recently coined family of “superhelicenes” and the first one constituted by three HBC-like units: two heptagon containing saddle-shaped HBCs at the edges and one central planar HBC unit. This super[7]helicene constitutes a nanographene helicoid that is a primary substructure of a graphenic Riemann surface¹⁴¹ with remarkable non-linear and chiroptical properties.

3.3.1. Synthesis and structural characterization

Based on our described methodology for the preparation of heptagon-containing functionalized hexaphenylbenzenes, a straightforward synthetic route to the proposed superhelicene is planned. Thus, starting from compound **190**, whose synthesis was described on section 3.1., a protected alkyne could be introduced into the core structure through a Sonogashira reaction with trimethylsilylacetylene. Subsequent one-pot deprotection and Sonogashira coupling with a

²²⁹ K. Kim, Z. Lee, B. D. Malone, K. T. Chan, B. Alemán, W. Regan, W. Gannett, M. F. Crommie, M. L. Cohen, A. Zettl, *Phys. Rev. B* **2011**, *83*, 245433.

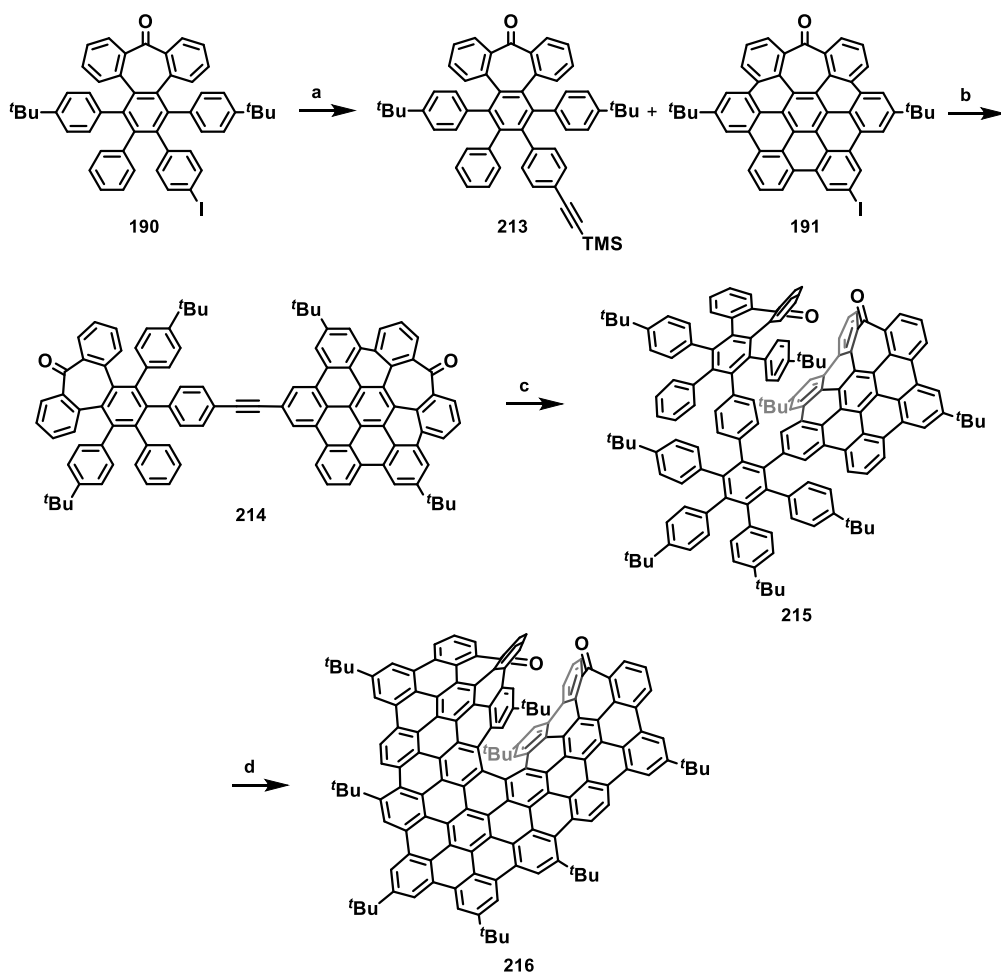
²³⁰ N. Yang, X. Ni, J.-W. Jiang, B. Li, *Appl. Phys. Lett.* **2012**, *100*, 093107.

²³¹ H. Zhan, G. Zhang, C. Yang, Y. Gu, *J. Phys. Chem. C* **2018**, *122*, 7605-7612.

²³² H. Zhan, Y. Zhang, C. Yang, G. Zhang, Y. Gu, *Carbon* **2017**, *120*, 258-264.

²³³ F. Xu, H. Yu, A. Sadrzadeh, B. I. Yakobson, *Nano Lett.* **2016**, *16*, 34-39.

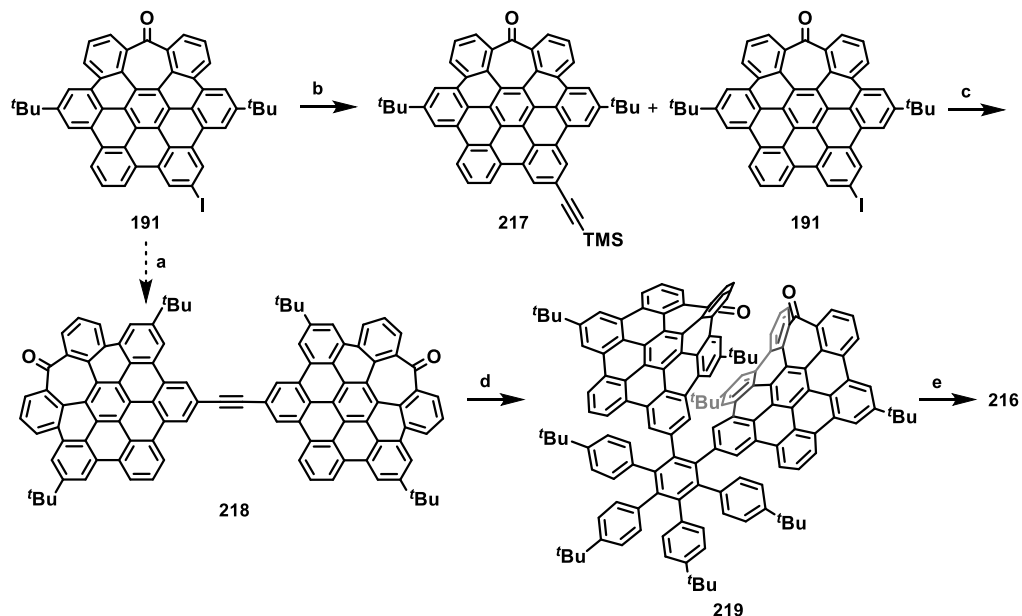
heptagon containing distorted HBC **191** gave rise to the substituted alkyne **214**, which contains the substructures of the two distorted HBC units. The third unit of hexaphenylbenzene was created in the next step via Diels-Alder reaction with 2,3,4,5-tetrakis-(*p*-*tert*-butyl-phenyl)-cyclopentadienone. Final oxidative cyclodehydrogenation reaction created the two new units of HBCs in a single step and creating 13 new aryl-aryl bonds. Remarkably, the helical nanographene strip **216** was obtained as major product (Scheme 40), where the rest of fractions belonged to mixtures of partially dehydrogenated compounds as it was observed by mass spectrometry.



Scheme 40. Synthetic route yielding **216**. Reagents and conditions: a) trimethylsilylacetylene, PdCl₂(PPh₃)₂, CuI, Et₃N, THF, r.t., 16 h, 99%; b) PdCl₂(PPh₃)₂, CuI, Et₃N, DBU, THF, H₂O, reflux, 24 h, 84%; c) 2,3,4,5-tetrakis-(*p*-*tert*-butyl-phenyl)-cyclopentadienone, Ph₂O, reflux, 10 h, 75%; d) DDQ, CF₃SO₃H, CH₂Cl₂, 0°C, 10 min, 7%.

3. Results and discussion

On the other hand, an alternative synthetic route was designed and tested. Unfortunately, first attempts on the one-pot preparation of the symmetric compound **218** from the iodine derivative **191** following the conditions reported on literature²³⁴ led to mixtures of Glaser byproducts (Scheme 41). In addition, treatment of **214** with a mixture of DDQ and trifluoromethanesulfonic acid did not afford the expected product **218**.



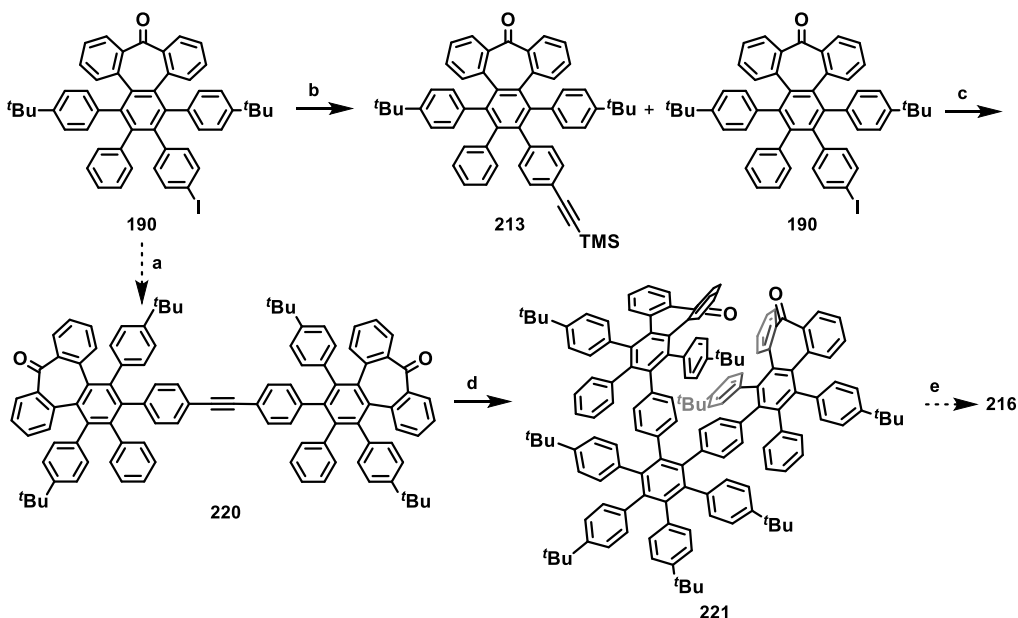
Scheme 41. Alternative synthetic route yielding **216**. Reagents and conditions: a) trimethylsilylacetylene, PdCl₂(PPh₃)₂, CuI, Et₃N, DBU, THF, H₂O, 60°C, 18 h; b) trimethylsilylacetylene, PdCl₂(PPh₃)₂, CuI, Et₃N, THF, r.t., 16 h, 99%; c) PdCl₂(PPh₃)₂, CuI, Et₃N, DBU, THF, H₂O, reflux, 24 h; d) 2,3,4,5-tetrakis-(p-tert-butyl-phenyl)-cyclopentadienone, Ph₂O, reflux, 10 h; e) DDQ, CF₃SO₃H, CH₂Cl₂, 0°C, 10 min, 2% (3 steps).

Finally, starting from the distorted iodine derivative **191**, a similar derivative to **213** was prepared by Sonogashira reaction with trimethylsilylacetylene (**217**). When coupled with a second unit of heptagon-containing HBC (**191**) the preparation of compound **218** was achieved, which was used without further purification in the next reaction since its low solubility did not allow a proper processability and, hence, structural characterization. Thus, compound **219** was obtained after Diels-Alder reaction between **218** and 2,3,4,5-tetrakis-(p-tert-butyl-phenyl)-cyclopentadienone. The final Scholl reaction over **219** afforded the desired compound with an overall yield of 2% in

²³⁴ M. J. Mio, L. C. Kopel, J. B. Braun, T. L. Gadzikwa, K. L. Hull, R. G. Brisbois, C. J. Markworth, P. A. Grieco, *Org. Lett.* **2002**, *4*, 3199-3202.

the last three steps (Scheme 41). Remarkably, by following this alternative route a less amount of partially dehydrogenated compounds was obtained, thus facilitating the purification of the final compound.

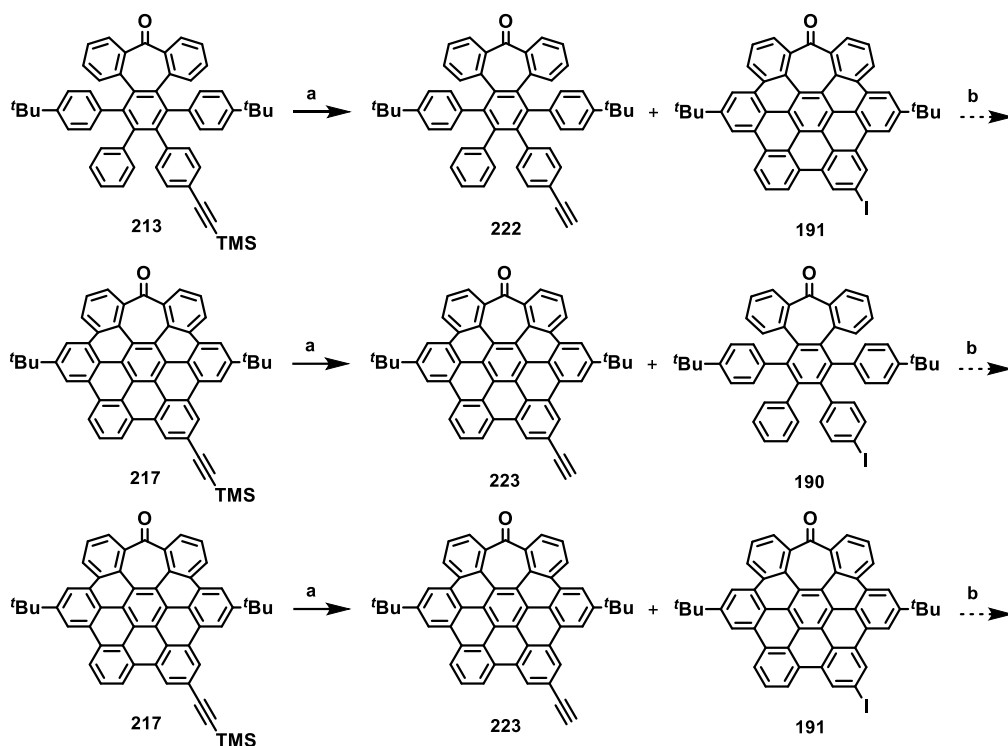
A third synthetic route was also tested, where the creation of all the necessary aryl-aryl bonds were intended to be formed in the last step. As for the synthetic route depicted on Scheme 41, the preparation of the symmetric alkyne **220** through one-pot Sonogashira coupling of two units of **190** was firstly tried, unfortunately the Sonogashira product was not detected. Thus, the strategy of *in situ* deprotection and Sonogashira coupling was used successfully, coupling the protected alkyne **213** and the iodine derivative **190**. Diels-Alder reaction with the corresponding cyclopentadienone over the alkyne bridged doubly distorted hexaphenylbenzene **220** afforded the oligophenylene precursor **221**. Last Scholl reaction over the precursor **221** gave rise to a small amount of compound **216** that was detected by TLC, unfortunately no enough amount was obtained for a proper characterization (Scheme 42).



Scheme 42. Synthetic route yielding **216**. Reagents and conditions: a) trimethylsilylacetylene, PdCl₂(PPh₃)₂, CuI, Et₃N, DBU, THF, H₂O, 60°C, 18 h; b) trimethylsilylacetylene, PdCl₂(PPh₃)₂, CuI, Et₃N, THF, r.t., 16 h, 99%; c) PdCl₂(PPh₃)₂, CuI, Et₃N, DBU, THF, H₂O, reflux, 24 h, 23%; d) 2,3,4,5-tetrakis-(*p*-tert-butyl-phenyl)-cyclopentadienone, Ph₂O, reflux, 10 h, 25%; e) DDQ, CF₃SO₃H, CH₂Cl₂, 0°C, 10 min.

Regarding the straightforward character and the higher yields obtained, the decision was to follow the synthetic methodology depicted on Scheme 40. Moreover, the structure of the intermediates used in this route was also easier to characterize than those depicted on Scheme 41 since their solubility was not higher enough to obtain a proper ^1H and ^{13}C -NMR spectrum. On the other hand, the conversion of **221** into the final helical nanographene **216** involves the formation of 18 new aryl-aryl bonds, increasing the probability to obtain mixtures of partial cyclodehydrogenated byproducts.

Noteworthy, the synthesis of **214** through the preparation of a terminal alkyne by deprotection of the TMS group on **213** and further Sonogashira reaction with **191** mainly afforded Glaser byproducts and the recovery of unreacted **191**. Moreover, deprotection of **217** and subsequent Sonogashira coupling with **191** did not give rise to the desired compound. Therefore, the *in situ* deprotection and Sonogashira one-pot coupling between **213** and **191** was found as an effective step that also shortened the synthetic route. Indeed, the reaction conditions used for this two-step reaction were taken from those used for the one-pot synthesis of diphenylacetylenes.²³⁴



Scheme 43. Attempted synthesis of compounds **214** (top), **218** (middle) and **218** (bottom). Reagents and conditions: a) TBAF, THF, reflux, 2 h; b) $\text{PdCl}_2(\text{PPh}_3)_2$, CuI, Et_3N , THF, r.t., 16 h.

The structural characterization of the final helical nanographene **216** was addressed by means of ^1H -NMR, ^{13}C -NMR, 2D-NMR (HSQC, COSY) and 1D-ROESY. Besides, either MS or HRMS measurements by MALDI-TOF showed only one peak with the mass and the isotopic distribution pattern in good agreement with the calculated one for **216**.

Up to 15 signals were found at the ^1H -NMR spectrum spread from 7.8 to 10.4 ppm as expected for extended nanographenes where the chemical shifts values are shifted to downfield due to the strong internal induced magnetic field. Conversely, as a result of its helical structure, some signals are upfield shifted since their corresponding protons are placed facing the aromatic π -electron cloud. This fact and the multiplicity on the observed signals allowed to distinguish between the green and blue set of signal depicted on Figure 60.

Taking advantage of the 2D-NMR techniques, it could be easy to confirm again the protons belonging to the blue and green set of signals from the ^1H - ^1H COSY analysis. Remarkably, this technique also permitted to identify and link singlets with long-range W coupling, such as protons depicted in pink, orange or the ones in black on Figure 60. Moreover, the chemical shift of the orange singlets are in concordance to their position, facing the aromatic π -electron cloud of the other end of the helical nanographene. As expected, purple protons were also easy to identify at the ^1H - ^1H COSY spectrum.

Even though the unequivocal assignment to each proton was not possible in all cases. This relationship was only possible for pink signals, where a signal coming from H_1 was found after irradiation of the signal at 10.40 in a ^1H - ^1H ROESY experiment. Moreover a second signal was identified after irradiation of the same proton (depicted in red on Figure 60), centered at 2.22 ppm and assigned to the *tert*-butyl group depicted in blue. Thus, the *tert*-butyl group found at 0.01 ppm was directly pointed as the one depicted in red due to its shielded character. No distinction between black *tert*-butyls were possible since no signals coming from them at the ^1H - ^1H ROESY experiment were found.

Finally, ^{13}C -NMR spectrum in combination with ^{13}C -DEPT-135 and ^1H - ^{13}C -HSQC allowed to identify both the chemically equivalent carbonyl carbons and the majority of sp^2 C-H signals along with the *tert*-butyl $-\text{CH}_3$ carbons. Unfortunately, the assignment of the quaternary carbons was not possible due to the overlapping observed.

3. Results and discussion

On the other hand, the $^1\text{H-NMR}$ spectrum obtained from compound **215** was quite complex, this fact was pointed to a mixture of conformers since the *tert*-butyl signals found were the integrates by the double of the expected value and a single peak was observed in the HR-MS spectrum. In order to obtain a clear $^1\text{H-NMR}$ spectrum, a variable temperature experiment was performed, recording different spectra while heating up to 100°C . When analyzing the resulting spectra, a broadening on the aromatic signals was observed, while the signals related to the *tert*-butyl groups did not coalesce. The evaluation of the temperature dependence on the $^1\text{H-NMR}$ spectrum suggest that the interconversion barrier would be higher than 100°C and the observed shifting on the signals may be related to intermolecular interactions.

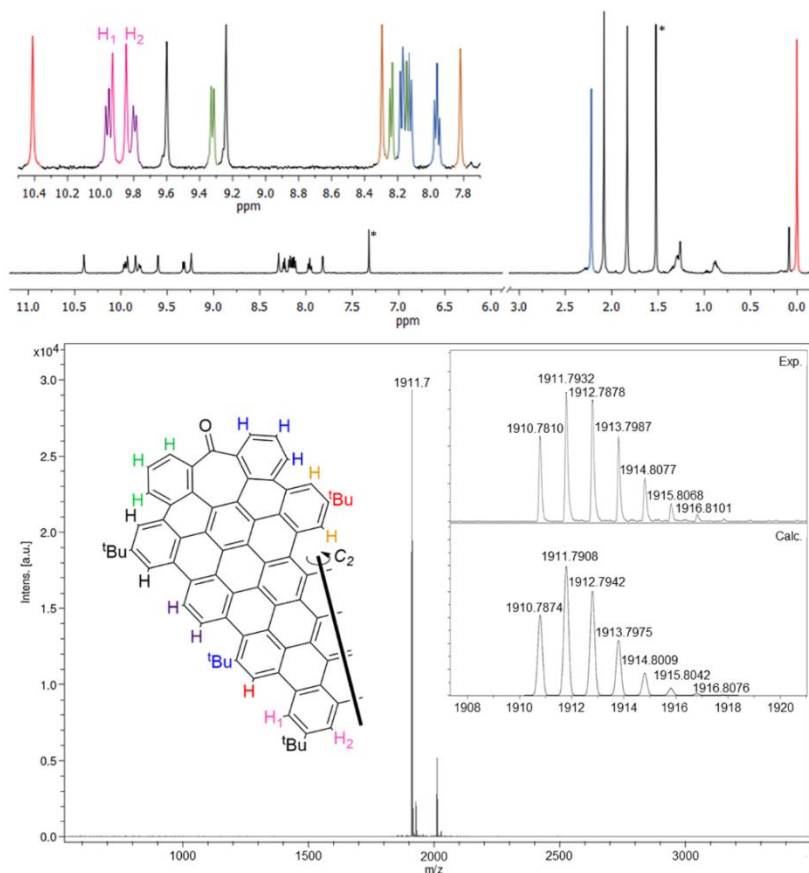


Figure 60. Top: Partial $^1\text{H-NMR}$ spectrum of **216** (500 MHz, CD_2Cl_2 , 293K), *residual solvent peak. Bottom: color code for protons assigned to the signals at the $^1\text{H-NMR}$ spectrum, MS spectrum and isotopic distribution HR-MS (MALDI-TOF) of **216**.

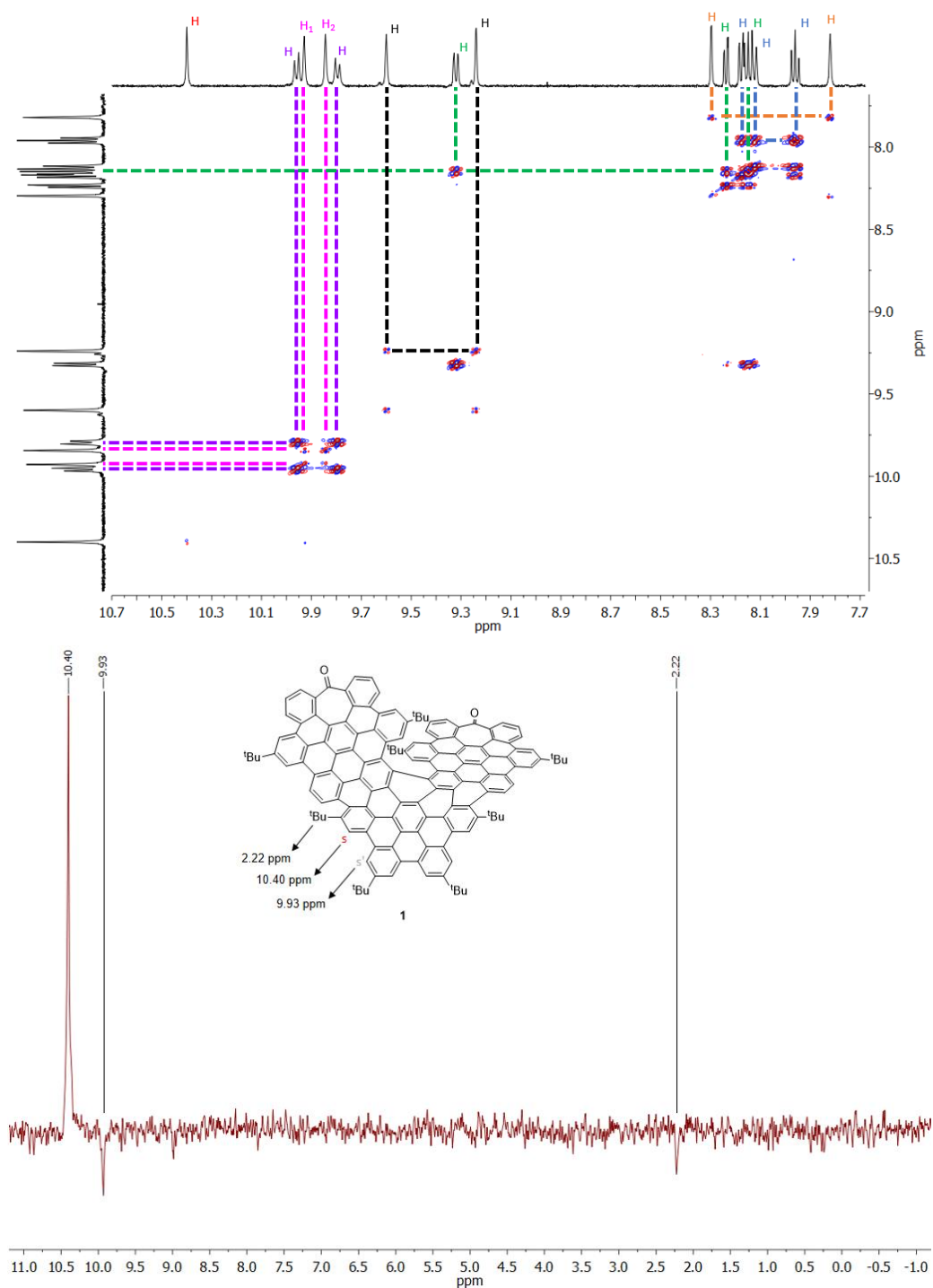


Figure 61. Top: Partial ^1H - ^1H COSY spectrum of **216** (500 MHz, CD_2Cl_2 , 293K). Bottom: ^1H - ^1H 1D ROESY (500 MHz, CD_2Cl_2 , 293K) spectrum of compound **216** after irradiating the singlet at 10.40 ppm.

Single crystals of **216** were grown from methanol/chloroform mixtures. Unfortunately, X-ray diffraction measurements even with a synchrotron radiation source did not afford any useful results due to the small size of the crystals obtained. Therefore, DFT calculations at the CAMB3LYP/6-31G(d,p) level of theory were performed in order to study the conformational disposition of **216**.

According to the theoretical calculations, the 39-ring π -surface of **216** forms a ribbon of around 3 nm length and 1 nm width, fully arranged in a spiral shape around a central [7]carbohelicene where the two ends of the helical ribbon present a saddle-curvature derived from the inclusion of seven-membered rings (Figure 62).

As mention on the previous sections, the tropone unit is not a static system since it shows a dynamic character being possible to flip, converting one saddle conformation into its mirror image. Thus, three different conformations arise on the structure of **216** depending on the conformation of the tropone unit, named endo-endo, endo-exo and exo-exo. Endo-endo describes the conformation adopted when the two carbonyl groups are pointing inwards the helix, exo-exo would correspond to that conformation where the carbonyl groups are pointing outwards the helix and endo-exo if the two tropones were oriented to the same direction, one inwards and other outwards the helix.

Energetically, the most stable conformation was found to be the endo-endo conformer, after analysis of the Boltzmann distribution it was found that almost every molecule of **216** would be adopting these conformation (Table 3). Thus, the two ketones face each other pointing inwards giving a good packing of the curved π -surfaces accommodating the seven-membered rings. The carbon-carbon distances of the seven-membered ring measured on the optimized structure are the typical for a cyclohepta-2,4,6-trienone and similar to those obtained from the X-ray structure of compound **194a**.

In the most stable geometry of *M*-**216** the helix completes a whole turn over itself as the first and last [7]helicene rings are placed over each other. The *tert*-butyl groups at the ends of the [7]helicene stand over the π -surface of the opposite curved-HBC areas, which is reflected on their very low $^1\text{H-NMR}$ chemical shift, as commented above. The angle between the two planes of the terminal rings is 25.3° , shorter than that of the single [7]helicene (32.8°) and the torsion angles

along helical inner rim are $\theta = 30.0, 29.0, 21.7, 27.9$ and 30.2° with a mean value of 27.8° , which is larger than that of the [7]helicene (22°) and stands out from the family of extended [7]helicenes (Table 5).²³⁵

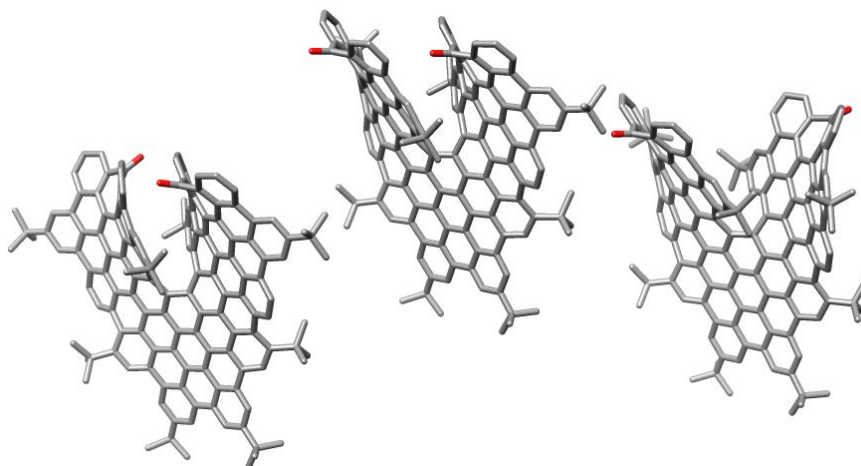


Figure 62. DFT (CAMB3LYP/6-31G (d,p)) optimized structure of endo-endo-*M*-**216** (left), endo-exo-*M*-**216** (middle) and exo-exo-*M*-**216** (right). Hydrogen atoms were omitted for clarity.

Table 3. Relative energies and Boltzmann distribution on the conformers of compound **216** at 298K.

| Conformer | Relative energy (kcal·mol ⁻¹) | Boltzmann population (%) |
|-----------|---|--------------------------|
| Endo-Endo | 0.00 | 99.9948 |
| Endo-Exo | 5.83 | 0.0052 |
| Exo-Exo | 11.77 | 2.4756×10^{-7} |

3.3.2. Optical properties

Noteworthy, **216** presents good solubility in common organic solvents such as chloroform, dichloromethane or hexane (up to $8.33 \text{ mg}\cdot\text{mL}^{-1}$ in CHCl_3). Helical nanographene **216** shows orange color in dichloromethane solution. Thus, its UV-vis spectrum recorded in the 300-800 nm region presents a broad absorption band centered at 472 nm, with a maxima also at 510 nm. The longest wavelength absorption band is centered at 580 nm extending up to 600 nm (Figure 63).

²³⁵ M. Joly, N. Defay, R. H. Martin, J. P. Declercq, G. Germain, B. Soubrier-Payen, M. V. Meerssche, *Helv. Chim. Acta* **1977**, *60*, 537-560.

According to TD-DFT calculations, this band is dominated by the transitions from the HOMO-1 and HOMO to the LUMO and LUMO+1, with the HOMO and LUMO involving mostly the central planar HBC and the [7]helicene moiety and the HOMO-1 and LUMO+1 extending over the distorted HBCs at the two edges (Figure 64). The molar absorptivity coefficient was estimated as $1.6 \times 10^5 \text{ M}^{-1}\cdot\text{cm}^{-1}$ at 472 nm. The vibronic progression might also contribute to the absorption band, as it is typical in aromatic systems.

Compound **216** exhibited notably intense orange-red fluorescence when irradiated with UV light, with a maximum centered at 610 nm. The fluorescence quantum yield (ϕ_f) is 9.8% in CH_2Cl_2 which is among the highest described for π -extended [7]helicenes and represents a notably 4.7-fold increase in comparison with the one described for heptahelicene ($\phi_f = 2.1\%$).²³⁶ The excitation independent emission and the overlapping between the absorption and excitation spectra confirmed the purity of the sample and the absence of aggregates up to 10^{-5} M concentration. The average emission lifetime is $\tau = 18.0 \pm 2$ ns, with a shorter component of 5.0 ± 0.3 ns and a major contribution of a longer component of 23 ± 2 ns. The different lifetimes might be due to the presence of a flexible conformational system at the excited state.^{128b} as it is the case of the different saddle-to-saddle conformers of **216** at the ground state. No emission from triplet excited state could be observed up to 1650 nm even at low temperature (77K) (Figure 65).

Furthermore, the extended aromatic network of **216** favours the nonlinear absorption by simultaneous interaction with two photons in the NIR region. Excitation with a pair of degenerated photon in the 700-900 nm region using a femtosecond laser results in emission at higher energies (TPE at 550-700 nm in Figure 58). The upconverted emission overlaps with the one-photon induced emission spectrum. The two-photon absorption (TPA) cross-section (σ_2) was calculated using the two-photon induced emission method.^{221b} A maximum σ_2 of 870 GM was estimated at *ca.* 800 nm corresponding to an overall transition energy of 400 nm. This value represents a 6.7-fold increase in comparison with the one reported for compound **194a** and a 3-fold increase with those obtained for compounds **204** and **205**. The quadratic dependence of the TPE on the excitation power was confirmed by using different incident power (Figure 63, right), and no net linear absorption was observed above 600 nm.

²³⁶ E. V. Donckt, J. Nasielski, *Chem. Phys Lett.* **1968**, *2*, 409-410.

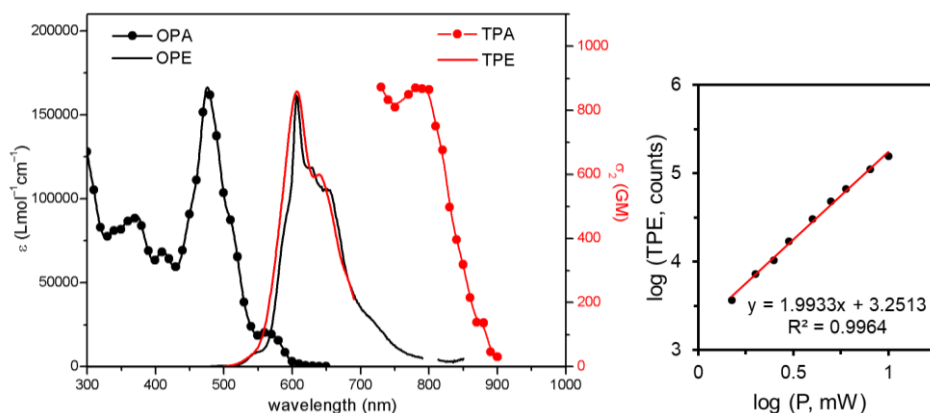


Figure 63. Left: One- and two-photon absorption (OPA, black circles and TPA, red circles) and one and two-photon induced emission (OPE, black line, $\lambda_{\text{exc}} = 490$ nm and TPE, red line, $\lambda_{\text{exc}} = 800$ nm) of **216** in CH₂Cl₂ at *ca.* 1×10^{-6} M. Right: log-log plot of the two-photon excited emission intensity (TPE) as a function of the excitation power (P).

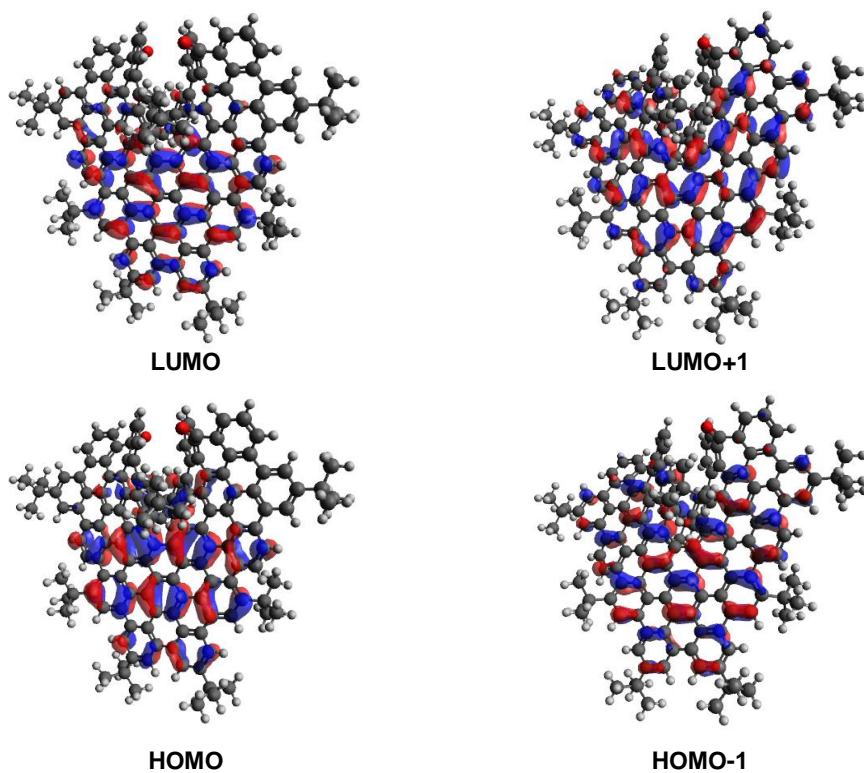


Figure 64. Isodensity (isoval = 0.02) surface for the frontier orbitals of *M-216* involved in the lowest energy transitions.

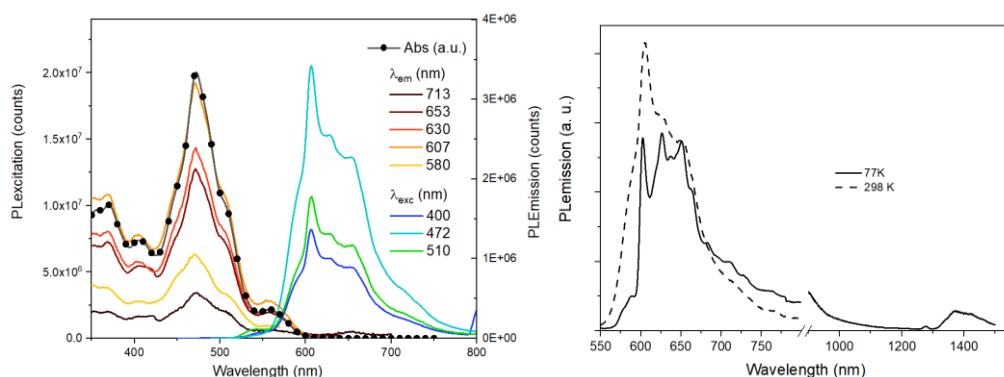


Figure 65. Left: Photoluminescence excitation spectra (PLExcitation) collected at different emission wavelengths (λ_{em}) and photoluminescence emission spectra (PLEmission) excited at different wavelength (λ_{exc}) of **216** in CH_2Cl_2 . The absorption spectra in arbitrary units is also shown to highlight the overlap between the PLExcitation and absorption spectra. Right: Emission spectra at low temperature (77K) compared with the emission at room temperature recorded for **216** in CH_2Cl_2 . No triplet emission was observed. The signal at 1400 nm is leaking 2nd order reflection of the strong fluorescence emission at 600-750 nm.

The helicene moiety does not usually exhibit good nonlinearity, however, remarkably TPA cross-section of **216** resulted two orders of magnitude higher than that reported for carbo[6]helicene.²³⁷ Thus, the expansion of the electronic delocalization beyond the helicene core improved the nonlinear optical responses as it has been reported for the case of hexa and heptahelicene derivatives.²³⁸

3.3.3. Chiroptical properties

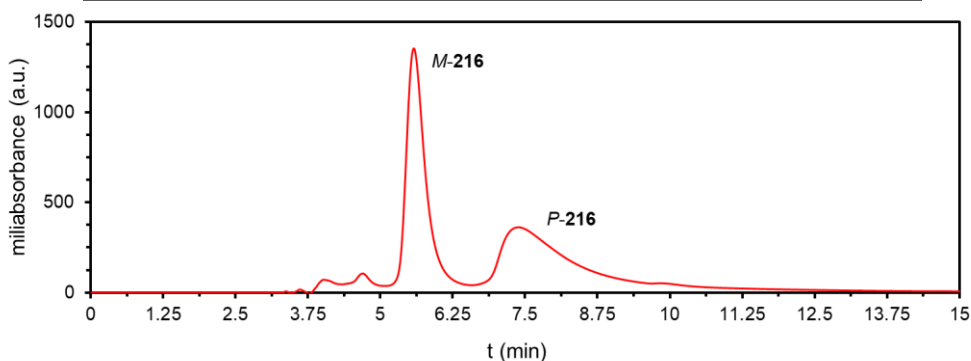
Chiral resolution of **216** was achieved by chiral HPLC using the optimized mobile phase gradient summarized on Table 4. These mixtures of solvents allowed to accomplish an effective separation of the two enantiomers in a short time, being possible to fully separate *M*- and *P*-**216** in 10 min. The obtained chromatogram is showed in Figure 61, where two main peaks centered at $t_R = 5.5$ min and $t_R = 7.5$ min were found that were assigned to the *M* and *P* enantiomers of **216** respectively. Remarkably, other diastereoisomers were not observed in HPLC traces during the enantiomeric resolution of **216**, indeed, small peaks observed in the range of 4 to 5 min. corresponded to partially dehydrogenated byproducts as obtained after their HR-MS analysis.

²³⁷ Y. Vesga, C. Diaz, J. Crassous, F. E. Hernandez, *J. Phys. Chem. A*. **2018**, *122*, 3365-3373.

²³⁸ C. Diaz, Y. Vesga, L. Echevarria, I. G. Stará, I. Starý, E. Anger, C. Sen, M. El Sayed Moussa, N. Vanthuyne, J. Crassous, A. Rizzo, F. E. Hernandez, *RSC Adv.* **2015**, *5*, 17429-17437.

Table 4. Mobile phase gradient used for the racemic resolution of compound **216**.

| Time (min) | Hexane (%) | CH ₂ Cl ₂ (%) |
|------------|------------|-------------------------------------|
| 0.00 | 20.00 | 80.00 |
| 5.00 | 18.00 | 82.00 |
| 8.00 | 10.00 | 90.00 |
| 9.00 | 10.00 | 90.00 |
| 10.00 | 20.00 | 80.00 |

**Figure 66.** Chromatogram obtained after the racemic resolution of compound **216**.

Enantiopure **216** resulted configurationally stable showing a great stability to racemization as expected from the [7]pitch difunctionalized in the fjord region with bulky *tert*-butyl groups. Thus, neither racemization nor decomposition were observed by chiral HPLC after heating a hexadecane solution of enantiopure **216** at 180°C for 24 h and then additional 4 h at 200°C, which is in agreement with the described barrier of racemization of heptahelicene.²³⁹

Optical rotation of the *M* enantiomer of **216** was evaluated in a CH₂Cl₂ solution at c 1.72 × 10⁻³ concentration and 25°C, obtaining an outstanding value of -5695°. This result is in concordance with that obtained for pristine *P*-[7]helicene (5900°) and notably higher to that measured for the previously reported extended [7]helicenes (Table 5).

Electronic circular dichroism (ECD) spectra of both enantiomers were measured in CH₂Cl₂ solutions and are presented in Figure 67. Enantiopure **36** shows several Cotton effects along the

²³⁹ a) R. H. Martin, M. J. Marchant, *Tetrahedron* **1974**, *30*, 347-349; b) R. H. Janke, G. Haufe, E.-U. Würthwein, J. H. Borkent, *J. Am. Chem. Soc.* **1996**, *118*, 6031-6035.

UV-vis range, two main bisignated signals centered at 375 nm and 500 nm and a broad absorption band centered at 580 nm. The first HPLC fraction showed negative Cotton effect at 400 nm ($|\Delta\epsilon|$ of $112 \text{ M}^{-1}\cdot\text{cm}^{-1}$, $g_{abs} = 2 \times 10^{-3}$) and at the lowest energy transition at 580 nm ($|\Delta\epsilon|$ of $43 \text{ M}^{-1}\cdot\text{cm}^{-1}$, $g_{abs} = 2.5 \times 10^{-3}$). The second eluted enantiomer demonstrate a clear mirror image with positive Cotton effect at the longest wavelengths above 500 nm.

TD-DFT methods were applied in order to simulate the ECD spectra of both enantiomers of compound **216**. By comparing the calculated and the experimental spectra, it would be easy to assign the correct configuration to each chromatographic peak. Thus, according with the simulated ECD spectra of *M*-**216** (Figure 67), the first HPLC fraction corresponds with this enantiomer while the second one is assigned to the *P*-enantiomer. Hence, the sign of the ECD signal at the longest wavelength is consistent with that described for carbo[n]helicenes by R. Ahlrichs and co-workers, who observed that the CD spectra of *M*-helicenes are characterized by transitions with negative rotatory strengths at low energy wavelengths.²²²

As shown in Figure 62, CPL spectra were recorded for both enantiomers at $5 \times 10^{-6} \text{ M}$ in CH_2Cl_2 , thus avoiding any photoselection originated from the presence of aggregates. Upon irradiation with a green light ($\lambda_{exc} = 490 \text{ nm}$) mirror-shaped CPL spectra centered at 610 nm were obtained for both enantiomeric forms as expected from a pure circularly polarized luminescence without any optical artifacts. In addition, the CPL signal was also confirmed by looking at the signal at a frequency of $2 \times$ the frequency of the PEM acting as an oscillating quarter-wave plate.¹²⁸

The emission dissymmetry factor, g_{lum} , reached a value of 2×10^{-3} which represents a significant one order of magnitude increase in comparison with the CPL emitter nanographene reported on section 3.1. (**194a**). The dissymmetry factors relationship (g_{lum}/g_{abs}) at 580 nm is 0.8 suggesting that the dissymmetry of **216** is mainly kept at the excited state, and that the $\pi\text{-}\pi^*$ electronic transition does not involve any important structural changes, as it is inherent to extended aromatics.²⁴⁰

²⁴⁰ H. Tanaka, Y. Inoue, T. Mori, *ChemPhotoChem* **2018**, *2*, 386-402.

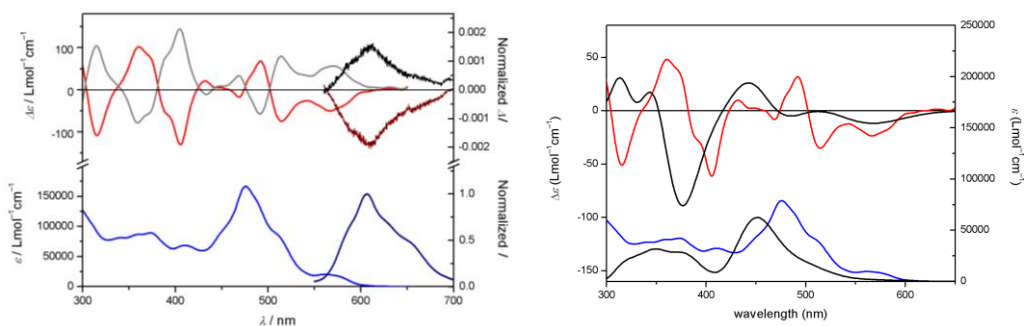
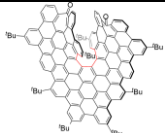


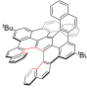
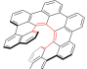
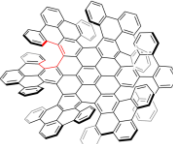


Figure 67. Left: Experimental ECD and CPL ($\lambda_{\text{exc}} = 490$ nm) of *M*- (red and wine) and *P*- (gray and black) enantiomers of **216** in CH₂Cl₂ at ca. 5×10^{-6} M; Experimental UV-vis (blue) and normalized fluorescence (navy, $\lambda_{\text{exc}} = 490$ nm) spectra of **216** in CH₂Cl₂ at ca. 5×10^{-6} M. Right: Comparison between experimental and simulated ECD spectra of *M*-**216**; Comparison between experimental and simulated UV-vis spectra of **216**.

Table 5. Main photophysical properties of **216**, [7]helicene, and structurally related π -extended [7]carbohelicenes.

| |  Undecabenzobenzene [7]helicene (216) |  [7]helicene |  Dibenzobenzene [7]helicene ^a |  Double dibenzobenzene [7]helicene |  Hexabenzobenzene [7]helicene |  Hexapole [7]helicene |
|---------------------------------------|--|--|---|---|--|--|
| θ^b | 27.8° | 22.0° | 22.8° | 23.6°, 21.8° | 27° | 23.8°—25.3° |
| ϵ (λ_{abs}) | 160,000 (472 nm) | 85,114 (268 nm) | ~70,000 (324 nm) | n.r. | 40,000 (459 nm) 4,700 (675 nm) | 92,000 (618 nm) |
| λ_{em} | 606 nm | 454 nm | 494 nm | 565 nm | - ^c | - |
| ϕ_F | 0.098 | 0.021 | 0.060 | 0.340 | - | - |
| τ | 18.0 ± 2 ns 2.0×10^{-3} (400 nm) | 13.8 ns | n.r. ^d | n.r. | - | - |
| $g_{\text{abs}}(\lambda)$ | 2.5×10^{-3} (580 nm) | $\sim 5.0 \times 10^{-3}$ (268 nm) | 1.2×10^{-3} (400 nm) | n.r. | 5.0×10^{-3} (459 nm) 1.6×10^{-2} (680 nm) | n.r. |
| $g_{\text{lum}}(\lambda)$ | 2.0×10^{-3} (610 nm) | n.r. | 2.2×10^{-3} (494 nm) | n.r. | - | - |
| $[\alpha]_D$ | -5695 ^e | +5900 ^{ef} | +1773 ^{ef} | n.r. | n.r. | +500 ^{ef} |

^a Data refer to R = 4-tol

^b Mean torsion angle in degrees along the helical inner rim (highlighted in red), measured from either the X-ray structures published by the Cambridge Crystallographic Data Centre or from the DFT-optimized structure (compound **216**).

^c Nonfluorescent

^d n.r. = not reported

^e *M*-enantiomer

^f *P*-enantiomer

3.3.4. Electrochemical properties

Cyclic voltammetry (CV) and Squared Wave Voltammetry (SWV) of **216** were measured in a THF solution at 1 mM concentration. CV of **216** shows two reversible oxidation and nine quasi-reversible reduction waves from -3.5 to +1.3 V (Figure 68). Squared-wave voltammetry (SWV) suggests the single-electron character of each redox process since all the observed waves possess a similar intensity and/or area. This good electron accepting capability might find application as n-type materials in organic electronics or photovoltaic applications.²⁴¹ The electrochemical HOMO-LUMO gap, calculated from the first half-wave oxidation and reduction potentials resulted 2.33 eV, in the range of the optical band gap obtained from the curve crossing of the normalized absorption and emission spectra (2.20 eV) and also in good concordance with the DFT obtained value (2.60 eV).²⁴²

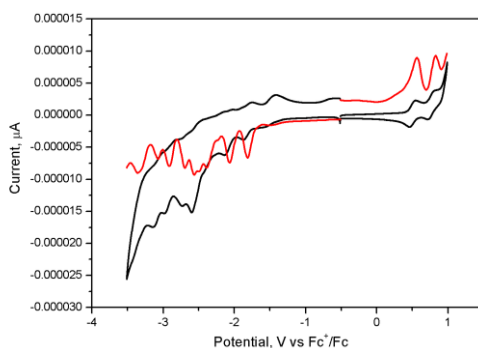


Figure 68. Cyclic (black line) and square wave (red line) voltammograms of **216** (1 mM) in THF (internal standard: Fc/Fc^+ , $\nu = 0.05$ V/s).

²⁴¹ a) B. C. Thompson, J. M. Fréchet, *Angew. Chem. Int. Ed.* **2008**, *47*, 58-77; b) J. L. Delgado, P.-A. Bouit, S. Filippone, M. A. Herranz, N. Martín, *Chem. Commun.* **2010**, *46*, 4853-4865; c) J. E. Anthony, A. Facchetti, M. Heeney, S. R. Marder, X. Zhan, *Adv. Mater.* **2010**, *22*, 3876-3892.

²⁴² G. Zhang, C. B. Musgrave, *J. Phys. Chem. A* **2007**, *111*, 1554-1561.

3.4. Multiple helicene distorted saddle-helix hybrid nanographene

Regarding the outstanding non-linear optical and chiroptical properties arisen from the polyaromatic structure of the Undecabenz[7]superhelicene, we wondered about the possibility of tune this properties. The introduction of multiple helicenes has been a widely used strategy toward the modification of the electronic structure of PAHs. In addition, we would like to evaluate if the chiroptical properties could be enhanced if extra helicenes are added to the same structure of the previously cited superhelicenes. On the other hand, the position of the seven membered ring could be modified in order to induce changes in the dipole moment of the molecule and, therefore, into its non-linear response. In this sense, we have designed and synthesized a new saddle-helix hybrid nanographene consisting of a combination of different sized carbohelicenes.

3.4.1. Synthesis and structural characterization

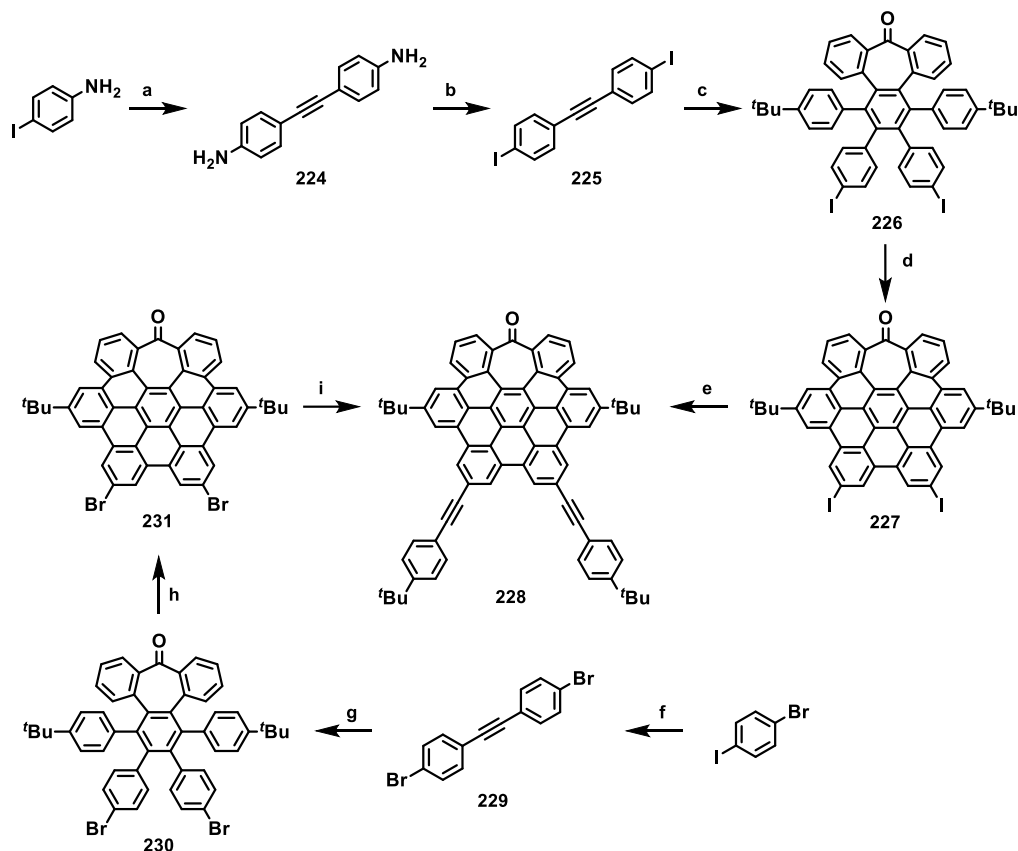
The synthetic methodology developed by our research group not only allows to introduce functionalization at the rings coming from the dialkyne fragment. As shown in section 3.1. the introduction of functionalization at the diphenylacetylene unit allowed the possibility of a further extension of the aromatic surface. In this case a symmetric dihalogenated diphenylacetylene could be used in order to extend the aromatic backbone in two directions at the same time.

Firstly, an approach using a diiodinated diphenyl acetylene was tested. Thus, compound **224** was prepared from 4-iodoaniline in one step by using the one-pot Sonogashira coupling reported by R. G. Brisbois, P. A. Grieco and co-workers.²³⁴ Double Sandmeyer reaction over the diamine **224** gave rise to the diiodinated diphenylacetylene **225**, which was reacted with dialkyne **185** in presence of $\text{Co}_2(\text{CO})_8$ to afford the [2+2+2] alkyne cyclotrimerization product **226**. The creation of five new aryl-aryl bonds and, therefore, a diiodinated distorted HBC-like nanographene was promoted by Scholl reaction by using a mixture of DDQ and trifluoromethanesulfonic acid. Despite the good yields obtained in the next two-fold Sonogashira coupling, we were forced to redraw a new synthetic route to **228** since Scholl reaction over **226** started to afford very low yields (Scheme 44).

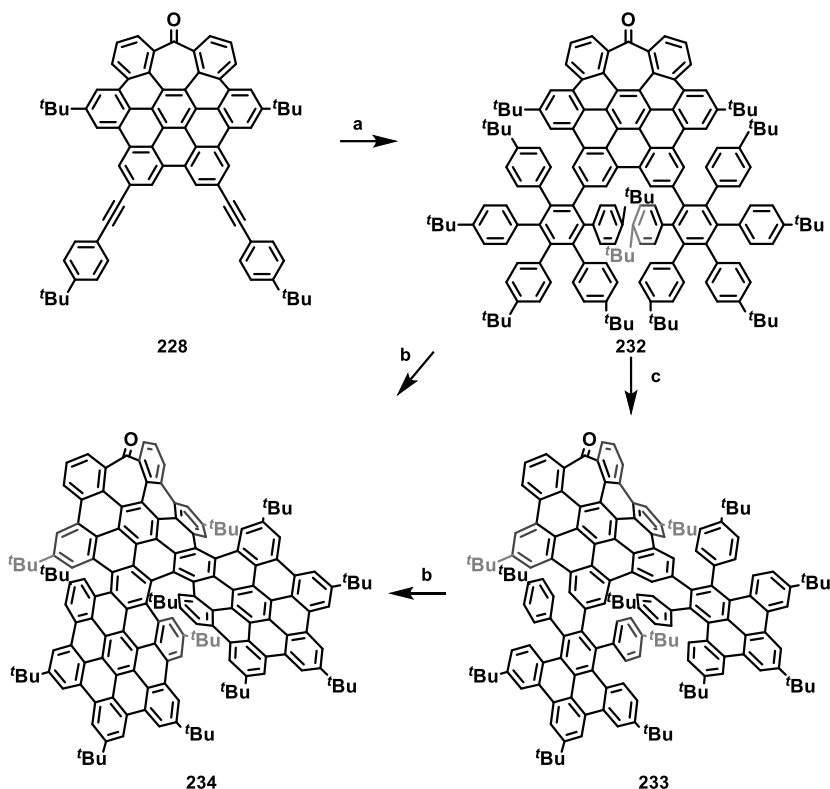
Thus, a second synthetic route was then proposed, where the preparation of a dibrominated analogue to **225** was required. The new pathway starts from 1-bromo-4-iodobenzene that, after

a one-pot double Sonogashira coupling, is transformed into the diphenylacetylene derivative **229**. The alkyne cyclotrimerization between **229** and **185** afforded the heptagon—containing hexaphenylbenzene **230**, which was converted into its corresponding distorted HBC-like nanographene **231**. The two brominated positions in compound **231** are subjected to Sonogashira coupling with 4-*tert*-butylphenylacetylene affording **228** in good yields (Scheme 44).

Compound **228** was then directly subjected to a double Diels-Alder reaction with two equivalents of 2,3,4,5-*tetrakis*-(4-*tert*-butylphenyl)cyclopentadienone. The oligophenylene **229** consisting of 115 carbon atoms was placed subsequently placed under Scholl conditions giving rise to the final compound **234** (Scheme 45).



Scheme 44. Synthetic routes toward intermediate **228**. Reagents and conditions: a) TMSA, PdCl₂(PPh₃)₂, CuI, DBU, MeCN, H₂O, 70°C, 16 h, 46%; b) NaNO₂, KI, H₂O, H₂SO₄, THF, 0°C, 2 h, 95%; c) **185**, Co₂(CO)₈, dioxane, 100°C, 16 h, 29%; d) DDQ, CF₃SO₃H, CH₂Cl₂, 0°C, 10 min, 60%; e) 4-*tert*-butylphenylacetylene, PdCl₂(PPh₃)₂, CuI, Et₃N, THF, r.t., 16 h; f) TMSA, PdCl₂(PPh₃)₂, CuI, DBU, MeCN, H₂O, reflux, 24 h; g) **185**, Co₂(CO)₈, toluene, 110°C, 16 h, 20%; h) DDQ, CF₃SO₃H, CH₂Cl₂, 0°C, 10 min, 83%; i) 4-*tert*-butylphenylacetylene, PdCl₂(PPh₃)₂, CuI, Et₃N, THF, r.t., 16 h.



Scheme 45. Synthetic routes toward compound **234**. Reagents and conditions: a) 2,3,4,5-tetrakis-(4-tert-butylphenyl)cyclopentadienone, Ph_2O , 259°C , 23%; b) DDQ, $\text{CF}_3\text{SO}_3\text{H}$, CH_2Cl_2 , 0°C , 10 min; c) FeCl_3 , $(\text{CHCl}_2)_2$, MeNO_2 , 70°C , 16 h. *MMP-234* enantiomer is shown.

Remarkably, attempted Scholl conditions over **232** by using FeCl_3 rather than the mixture of DDQ and acid afforded the partially cyclodehydrogenated product (**233**) with 16 hydrogens more than the expected product as inferred from the HR-MS spectrum obtained. Conversely, the obtained $^1\text{H-NMR}$ spectrum was not possible to be assigned to any structure with high accuracy. When compound **233** was subjected to Scholl reaction under the combination of DDQ and triflic acid the final compound was isolated. ESI-TOF HR-MS showed a single peak of $m/z = 2111.0776$, suggesting the formation of the expected nanographene containing two [5]helicenes and a central [7]helicene. This experience also suggest that the first tested conditions were more efficient on the ring formation of the distorted system, whereas FeCl_3 give the impression of being less favorable for such non-planar nanographenes.

The recorded $^1\text{H-NMR}$ spectrum of compound **234** was quite complex, suggesting that the obtained compound was obtained as a mixture of diastereoisomers, whose separation was not possible by flash column chromatography, nor preparative TLC. Considering all the possible configurations at the helicene moieties and their combinations, three possible diastereoisomers could be formed during the cyclodehydrogenation reaction. Therefore, according to the suggested nomenclature, the three diastereoisomers would be named *MMM-*, *MMP-* and *PMP-***234** (and their corresponding enantiomers). The structure of the three diastereoisomers was optimized by means of DFT calculations at the CAM-B3LYP 6-31G(d,p) level of theory (Figure 69). Bearing symmetry aspects in mind along with the troponone flipping, configurations *MMM* and *PMP* would possess C_2 symmetry whilst diastereoisomer *MMP-234* would show C_1 symmetry.

First attempted diastereomeric resolution of the resulted configurations by normal phase HPLC did not afford any separation, obtaining a chromatogram showing a single peak. Therefore, chiral phase HPLC was directly used in order to perform the racemic resolution simultaneously.

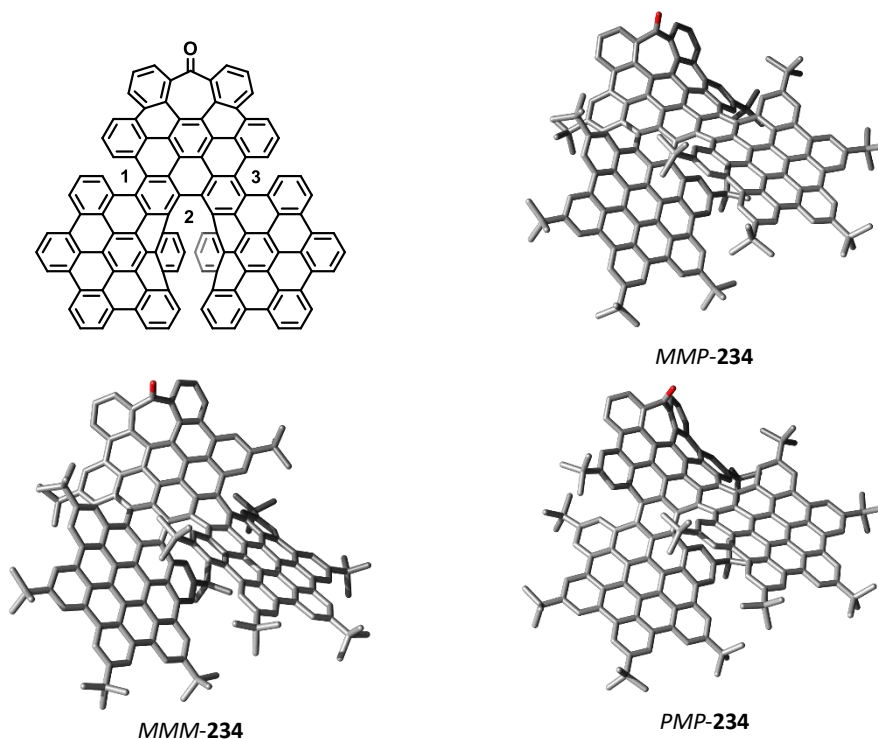


Figure 69. Suggested nomenclature of the helicenes present at compound **234** and DFT optimized geometries of the three possible diastereoisomers of compound **234**.

A good separation was obtained by using an isocratic flow composed of hexane/CH₂Cl₂ (8:2), the chromatogram obtained is depicted in Figure 70. Four main peaks were found when fixing the detector wavelength at 620 nm (A to D in Figure 70), whereas two minor peaks centered at $t_R = 9.5$ and 14.5. Remarkably, peaks A and C showed identical UV spectrum as well as for peaks B and D, suggesting that A-C and B-D are two enantiomeric pairs. On the other hand, the minor peaks exhibited similar UV profile than the major ones, and were presumably assigned to the third enantiomeric pair.

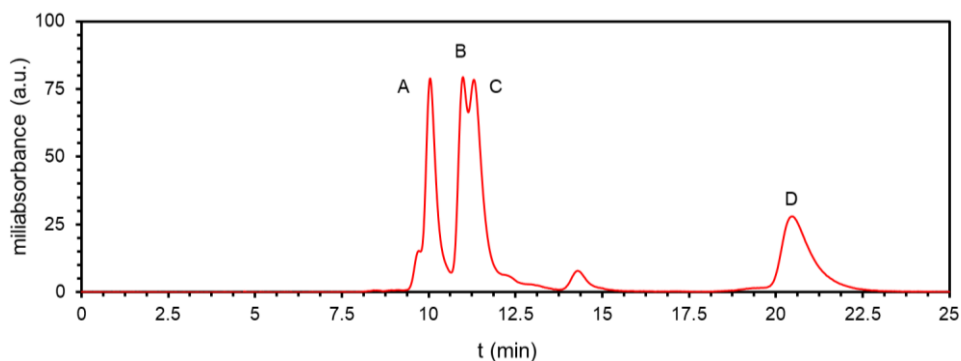


Figure 70. Obtained chromatogram after injection of **234** into chiral HPLC.

Noteworthy, when a toluene solution of **234** is refluxed overnight and then injected into a chiral phase HPLC, a more understandable chromatographic profile is obtained (Figure 71). In this case, two major peaks corresponding to peaks A and C in Figure 70 were observed, moreover, the UV profiles matched perfectly with those obtained for peaks A and C. Conversely, the minor peaks are still observed. Apparently peaks B and D are converted into A and C when heating, suggesting that the interconversion barrier between the pair A-C and B-D is easily surmountable at *ca.* 110°C.

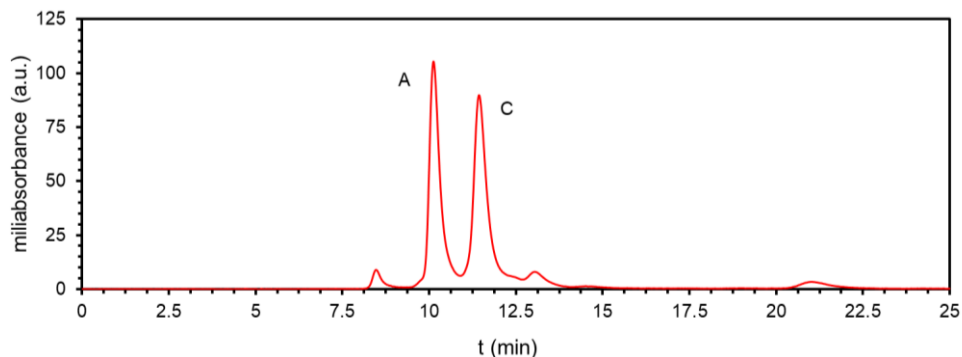


Figure 71. Obtained chromatogram after heating **234** at *ca.* 110°C during 16 h.

3. Results and discussion

Both separations were achieved at semipreparative scale, thus, enough amount of each peak was collected, being possible to obtain clear ^1H -NMR spectra. The ^1H -NMR spectra obtained for fractions A, C and D are depicted in Figure 72, remarkably, the spectrum obtained for fractions A and C was much more complex to that obtained for fraction D which, in fact, only showed six singlets at the *tert*-butyl zone confirming that fractions B and D would belong to the symmetric pairs *MMM/PPP* or *PMP/MPM*-**234**. On the other hand, up to twelve *tert*-butyl signal (one overlapping with the H_2O singlet) were observed in the spectrum of fraction A and C, suggesting a non-symmetric system. Thus, fractions A and C were assigned to the thermodynamic more stable pair *MMP/PPM*-**234**. Unfortunately, no enough amount coming from the minor peaks was collected to obtain a proper ^1H -NMR spectrum, which would belong to one of the symmetric pairs.

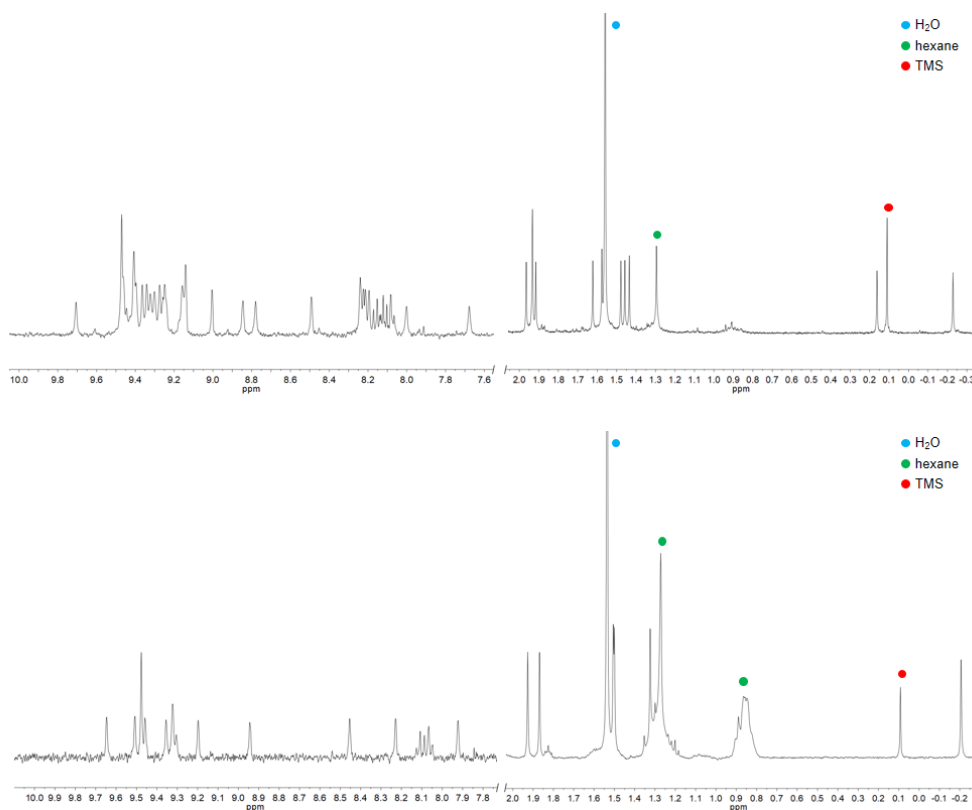


Figure 72. Partial ^1H -NMR spectra of fractions A and C (top) and D (bottom) (400 MHz, CD_2Cl_2 , 293K). Signals arising from secondary solvents or internal standards are indicated with colored dots. Aromatic signals have a magnification factor of 10 \times .

When looking at the optimized structures of compound **234**, it is easy to observe that the saddle curvature induced by the inclusion of the seven-membered ring is well accommodated in the geometry of the pair *MMP/PPM-234*, while, for the other diastereoisomers, the combination of the [5]helicenes causes a partial planarization of the distorted HBC unit. This fact would mean an increase on the relative energies for the symmetric diastereoisomers and, therefore, an answer for the interconversion toward the non-symmetric one when heating (theoretical calculations are currently ongoing in order to confirm this hypothesis).

3.4.2. Optical properties

Compound **234** exhibited good solubility in common organic solvents, presenting dark green color in low concentrated solutions (*ca.* 10^{-6} M) that turns nearly black in high concentrated solutions (*ca.* 10^{-3} M). The UV-vis spectra of *MMP/PPM-234* and the symmetric fraction are depicted in Figure 73. *MMP/PPM-234* showed an absorption spectrum ranging from 250 to 700 nm with defined maxima centered at 365 nm ($\epsilon = 1.45 \times 10^5 \text{ M}^{-1}\cdot\text{cm}^{-1}$), 505 nm ($\epsilon = 6.00 \times 10^4 \text{ M}^{-1}\cdot\text{cm}^{-1}$) and a red shifted broad band extending up to 700 nm. On the other hand, fraction D showed a similar absorption profile with lower ϵ values such as $6.00 \times 10^4 \text{ M}^{-1}\cdot\text{cm}^{-1}$ at 360 nm or $2.36 \times 10^4 \text{ M}^{-1}\cdot\text{cm}^{-1}$ at 523 nm. Remarkably, the lowest energy band is well resolved into two broad bands that extend up to 750 nm for the symmetric fraction in comparison to that obtained for *MMP/PPM-234*. This red-shifted absorbance wavelengths are comparable to those reported for the green nanographene propeller by J. Wang and co-workers (**154**).¹⁷⁸

The emission spectra of both diastereoisomers were obtained after irradiation of the samples with UV light of 360 nm. The fluorescence spectrum is extended along the 600-850 nm range for both diastereoisomers, with maxima centered at 697 and 715 nm for *MMP/PPM-234* and fraction D respectively. Remarkably, fraction D showed a more resolved emission spectrum in comparison to that obtained for *MMP/PPM-234*, where two well-defined bands could be observed as part of a vibronic structure, as expected for rigid extended PAHs. The Stokes shift is quite short for the two studied diastereoisomers not exceeding 50 nm, furthermore, the optical HOMO-LUMO gap taken from the crossing point between the absorbance and emission spectra was evaluated as 1.95 and 1.89 eV for *MMP/PPM-234* and fraction D respectively. The emission LQY (ϕ_f) was evaluated as 43% for the nonsymmetric diastereoisomers and 30% for the fraction D. These

values are, to the best of our knowledge, the highest values for a NIR nanographene emitter. Moreover, the overlapping between the excitation and the absorption spectra confirmed the purity of the samples and prove the absence of aggregates.

When both diastereoisomers were excited with a 900 nm wavelength by using a femtosecond laser caused the simultaneous absorption of two NIR-photons leading to emission at higher energies. The emission spectra after excitation with two photons are depicted in figure 73 (TPE), both spectra exhibited a similar maxima when compared with their one-photon excitation spectra suggesting that the reached excited states after one- and two-photon excitations are equivalent. Furthermore, preliminary two-photon absorption spectra (TPA in Figure 73) showed a maxima at higher energies with TPA cross-sections of *ca.* 300 and 100 GM at 770 nm.

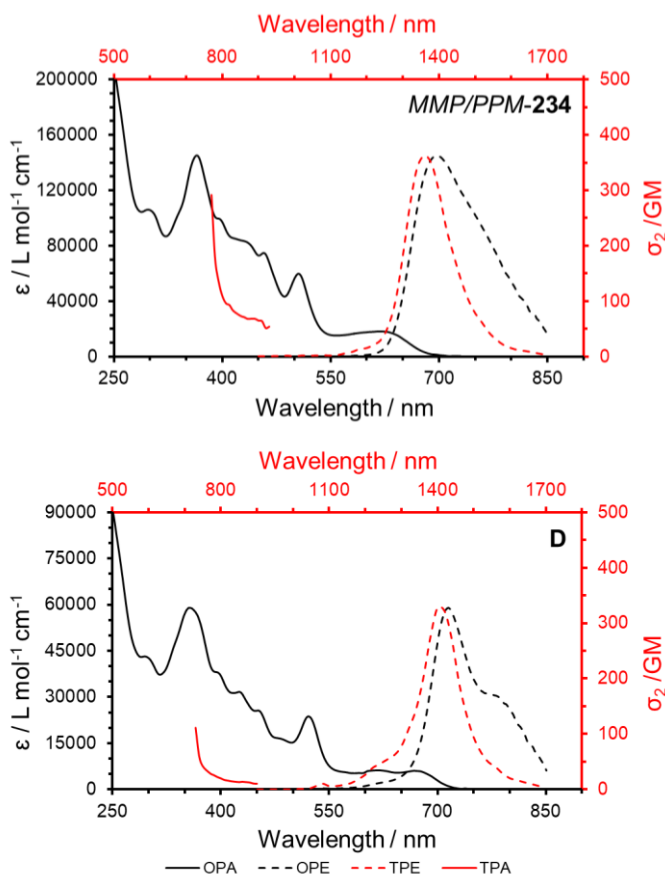


Figure 73. One-photon absorption (OPA), two-photon absorption (TPA), one-photon excitation emission (OPE) and two-photon excitation emission (TPE) spectra of compounds *MMP/PPM-234* and fraction D ($\lambda_{\text{exc}} = 360$ or 900 nm) measured in CHCl_3 solutions at *ca.* 10^{-6} M.

The TPA detection range permitted by the Ti:sapphire laser is found between 730 to 900 nm. Thus, the log/log plot does not show a quadratic dependence in the range of 730 to 770 nm between the emission and the power applied. This, fact is explained because of the red-shifted OPA exhibited by the two diastereoisomers that show minimal absorbance in the 730-770 range. On the other hand, the TPA values are usually referred to an average of multiple measurements that would afford a reliable value with errors intervals. The reproducibility is being carried out in collaboration with Dr. Ermelinda Maçôas from the University of Lisbon.

3.4.3. Chiroptical properties

Since the separation of the different diastereoisomers was only achieved after chiral HPLC, it is supposed that each isolated peak would correspond to a single enantiomer. Thus, CD and CPL measurements were carried out over solutions of fractions A and D in chloroform at 10^{-6} M concentrations, the obtained spectra are depicted in Figure 74.

Fraction A showed an intense CD spectrum with a bisignated signal at 385 nm and a broad positive Cotton effect that extends up to 700 nm ($g_{abs} = 2.5 \times 10^{-3}$), on the other hand, fraction D exhibited less intense CD signals with negative Cotton effects both at 400 nm and at the lowest energy band ($g_{abs} = 2.0 \times 10^{-3}$). It is easy to recognize that both spectra are not mirror images, suggesting that the separated fractions do not belong to a couple of enantiomers and confirming the guess arisen from the $^1\text{H-NMR}$ spectra, where each fraction was assigned to a different diastereoisomer.

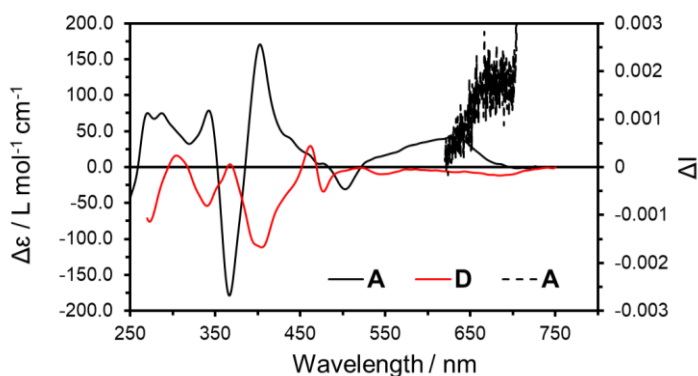


Figure 74. Experimental ECD spectrum of fraction A (black) and fraction D (red) CHCl_3 at $ca. 10^{-6}$ M. Experimental CPL spectrum of fraction A (black dotted, $\lambda_{exc} = 370$ nm) CHCl_3 at $ca. 10^{-6}$ M.

Regarding CPL measurements, it was only possible to obtain a clear NMR spectrum from fraction A up to date (Figure 75). Thus, the sign of the CPL spectra and that of the lowest energy band at the CD spectrum are in concordance and the g_{lum}/g_{abs} ratio is calculated as 0.8, similar value to that obtained for undecabenz[7]superhelicenes (**216**). A less intense CPL spectrum is expected for fraction D since the CD band at 700 nm showed a lower g_{abs} value, in case of a similar g_{lum}/g_{abs} ratio.

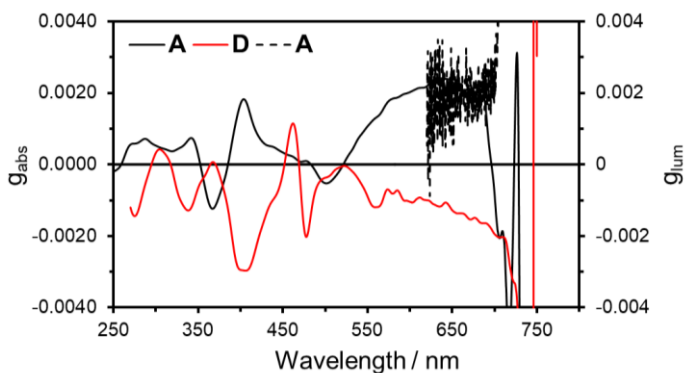


Figure 75. g_{abs} values of fraction A (black) and fraction D (red) and g_{lum} values of fraction A.

Moreover, TD-DFT calculations are currently ongoing in order to compare and assign each fraction with each diastereoisomer. On the other hand, our guess is that the enantiomeric pairs would be assigned to fractions B/D and fractions A/C according to their UV-vis spectra. As for the already measured fractions, after a proper HPLC separation the CD and CPL spectra would confirm this assignation. Finally, electrochemical and spectroelectrochemical measurements would complete the evaluation of their physical properties and a possible functionalization/extension of the aromatic surface will be tested taking advantage of the carbonyl group.

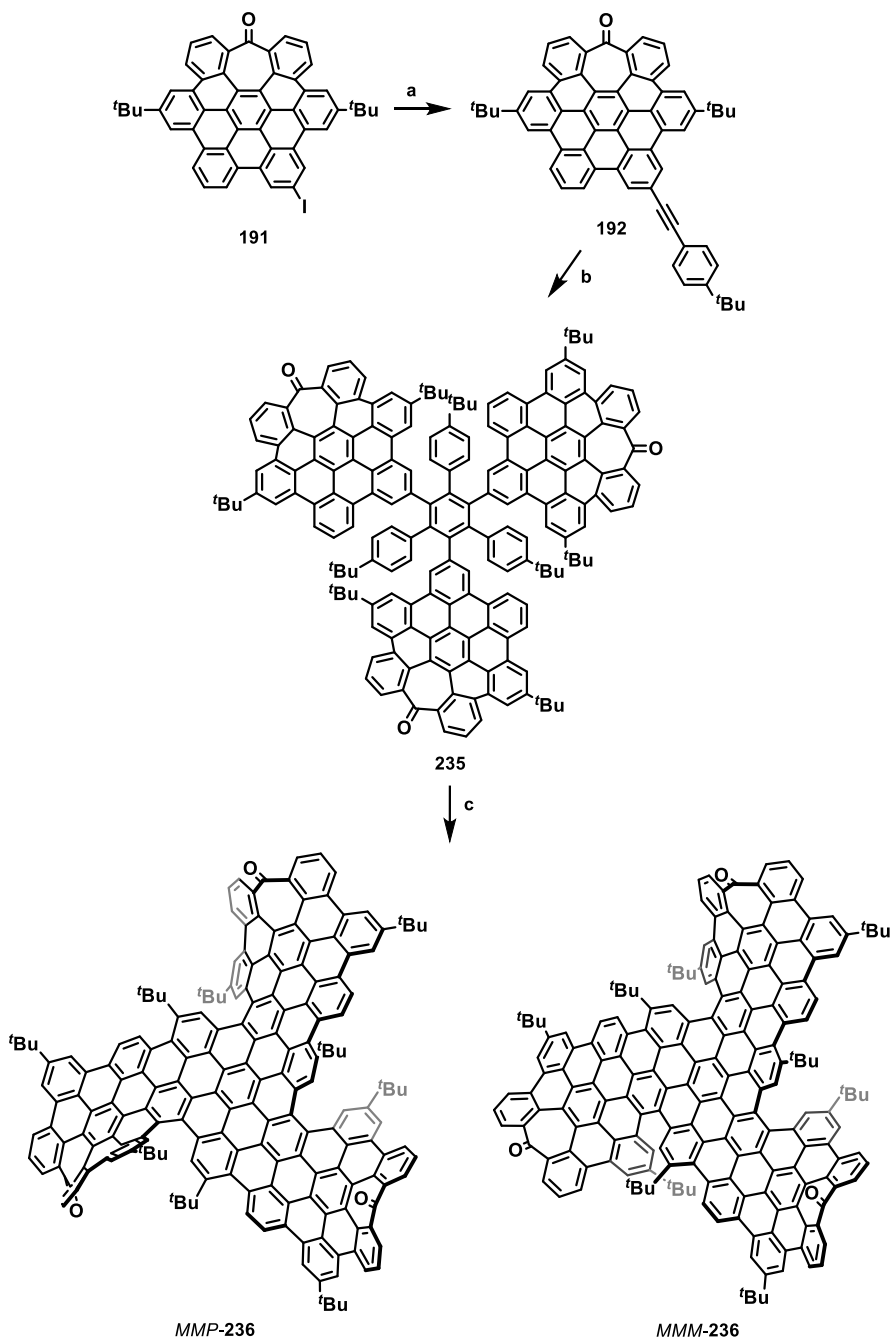
3.5. Triskelion-shaped saddle-helix hybrid nanographene

This section describes the synthesis of an edge-distorted nanographene constituted by four HBC-type units, combining three heptagon-containing HBCs fused to a central planar hexagonal HBC leads to a Y-shaped aromatic surface that could remind the basic scaffold of the Y-shaped multiterminal intramolecular junction of carbon nanotubes. The large aromatic surface of the prepared compound, constituted by 153 conjugated carbon atoms leading to 52 fused rings arranged in a triangular shape of *ca.* 2.5 nm side. The prepared nanographene can be considered as analogue to compound **94**, described at the background section, which was impossible to characterize in a proper way due to its low solubility. Thus, we aimed to not only improve the solubility of such larger nanographene but also introduce new features such as chiroptical properties.

3.5.1. Synthesis and structural characterization

The synthesis of the target compound started with the preparation of the previously reported distorted heptagon-containing HBC analogue bearing functional groups, namely a ketone and an aryl iodide moieties, for further expansion of the aromatic surface. Taking advantage of the incorporated aryl iodide, a Sonogashira cross-coupling reaction with *p-tert*-butylphenylacetylene was carried out giving rise to compound **192** as reported in section 3.1.

In a similar fashion to that tested by Müllen and co-workers for the preparation of compound **94**,¹⁰³ three units of **192** were firstly linked *via* $\text{Co}_2(\text{CO})_8$ mediated alkyne cyclotrimerization reaction generating a branched oligophenylene derivative. Conversely, the propeller-like polyphenylene was obtained as a unique regioisomer where the three bulky distorted HBC units are located as alternate 1,3,5-substituents of the central benzene ring, in contrast to that reported by Müllen and co-workers, where the [2+2+2] alkyne cyclotrimerization afforded a mixture of regioisomers. Still, compound **235** was obtained as a mixture of atropisomers coming from the different spatial disposition of **192** around the cobalt center during the cyclotrimerization reaction (Figure 79, top). Subjecting this mixture to a final Scholl-type oxidative cyclodehydrogenation with the combination of trifluoromethanesulfonic acid and DDQ as oxidant created the central HBC unit leading to nanographene **236** (Scheme 46).



Scheme 46. Synthetic route toward compound **236**. Reagents and conditions: a) *p*-tert-butylphenylacetylene, $\text{PdCl}_2(\text{PPh}_3)_2$, CuI , Et_3N , THF, r.t., 16 h, 99%; b) $\text{Co}_2(\text{CO})_8$, toluene, 110°C, 16 h, 69%; c) DDQ, $\text{CF}_3\text{SO}_3\text{H}$, 0°C, 10 min, 22% (PPM/MMP-236), 2% (PPP/MMM-236). MMP- and MMM-236 enantiomers are depicted.

Mass analysis of the final compound by MALDI-TOF confirmed the isolation of a single compound with $m/z = 2437.9$. The molecular composition of **326** ($C_{189}H_{120}O_3$) is also in a perfect agreement with the isotopic distribution pattern of the high-resolution mass peak obtained ($m/z = 2436.9218$).

In the final synthetic step, three [5]carbohelicenes moieties are created due to the steric hindrance caused by the presence of bulky *tert*-butyl substituents. Therefore, compound **236** was obtained as a mixture of the two possible diastereoisomers, *i.e.* C_3 -symmetric *PPP/MMM-56* and non-symmetric *PPM/MMP-236* pairs. Each formed pair are pointed as arisen products from each of the two atropisomers of precursor **235** (Figure 79, top).

Compound **236** exhibited a good solubility in common organic solvents (CH_2Cl_2 , $CHCl_3$, THF and to some extent in hexane), this fact allowed its characterization by means of 1H -NMR spectroscopy finding two set of signals in a 1 to 10 ratio. Both diastereoisomers were separated by HPLC, obtaining two well resolved chromatogram peaks with subtle differences in the corresponding UV-vis traces. Mass analysis of each HPLC fraction also indicated the isolation of the diastereoisomeric forms of **236**.

Subsequently, we separated both diastereoisomers of **236** by HPLC, obtaining two well resolved chromatogram peaks, in agreement with the 1H -NMR analysis, and with subtle differences in the corresponding UV-Vis traces. Mass analysis of each HPLC fraction also indicated the isolation of the diastereoisomeric forms of **236**. Both isomers were very soluble in organic solvents which allowed us to carry out their unequivocal characterization by NMR analysis. Thus, 1H -NMR spectrum of the minor compound corresponding to the first HPLC fraction ($t_R = 4.6$ min) shows only three different signals corresponding to non-equivalent *tert*-butyl groups and thirteen aromatic protons (Figure 76, bottom), which is in agreement with the symmetric structure of *PPP/MMM* pair of enantiomers, **236a**. Major compound **236b** ($t_R = 5.5$ min) could then be attributed to the non-symmetrical *PPM/MMP* pair of enantiomers as derived from its 1H -NMR analysis (Figure 76, bottom, blue). Unambiguous assignment of the structures of both diastereoisomers **236a** and **236b** was also complemented by 2D-NMR analysis.

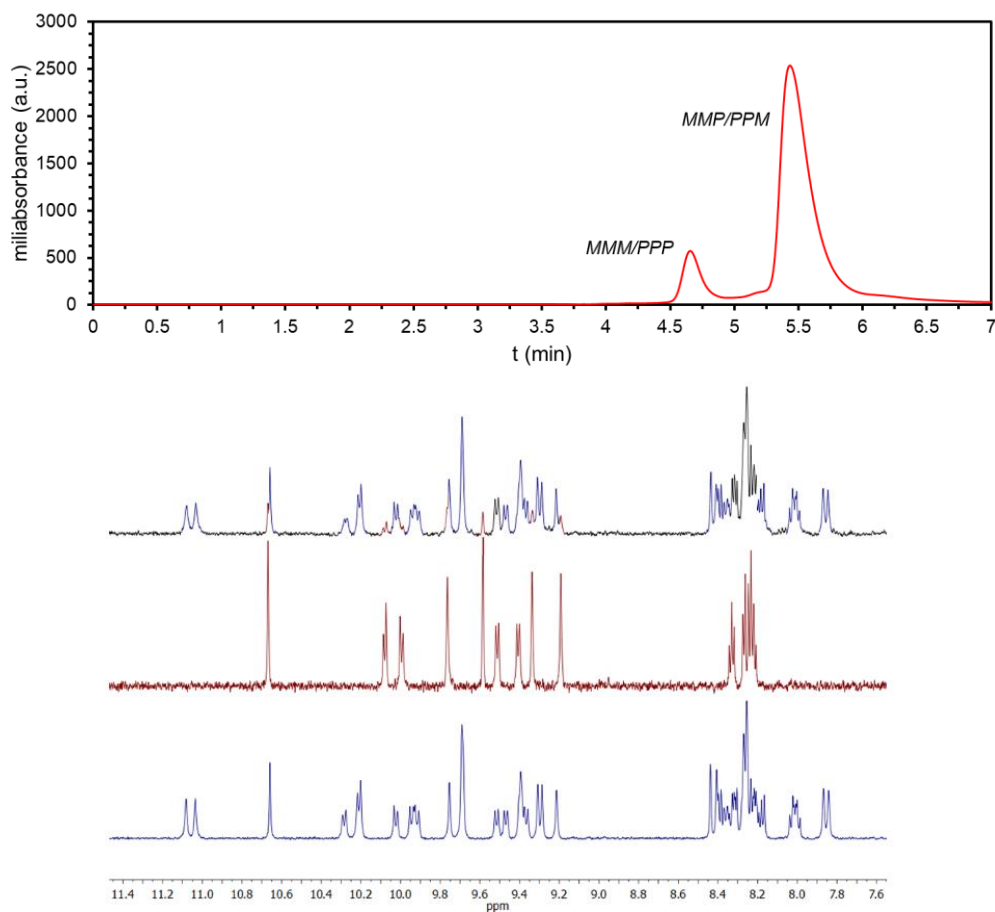


Figure 76. Top: Chromatogram obtained after separation on semipreparative normal phase HPLC. Bottom: ¹H-NMR spectrum of the mixture of diastereoisomers (black), *MMM/PPP-236* pair (red), *MMP/PPM-236* pair (blue).

Theoretically optimized structures (DFT-CAMB3LYP/6-31G (d, p)) show compound **236a** as a warped distorted C_3 -symmetry nanographene of 24.6 Å side-length (measured from one carbonyl group to the contiguous one), centered on a planar [6]circulene which spreads giving a slightly edge-distorted HBC fused with three intensively distorted hept-HBCs at the edges (Figure 77). Each *hept*-HBC unit shows a distance of 10.5 Å between the *tert*-butyl groups due to the saddle curvature caused by the presence of the seven-membered rings (Figure 78).

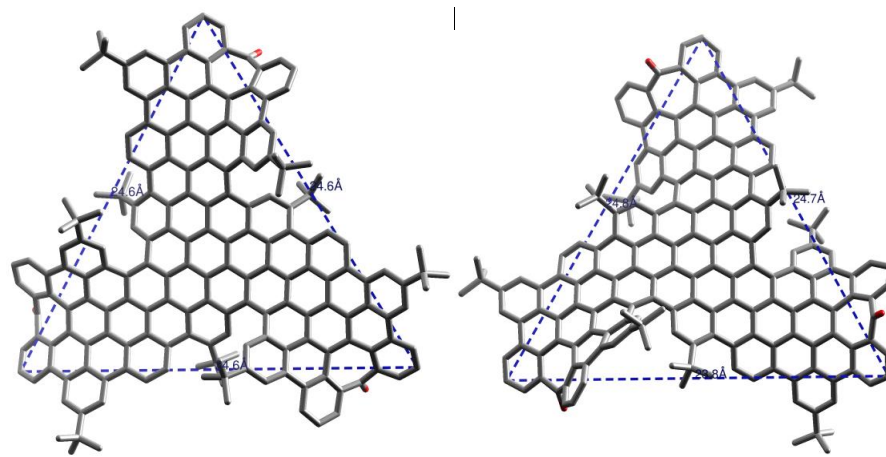


Figure 77. Left: 3D top view of the DFT optimized **236a** structure showing the size of the triangular shape. Right: 3D top view of the DFT optimized **236b** structure showing the size of the triangular shape.

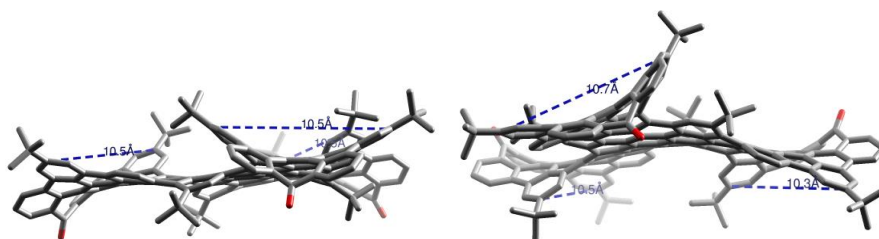


Figure 78. Top: 3D frontal view of the DFT optimized **236a** structure showing the distortion of the *hept*-HBCs. Bottom: 3D frontal view of the DFT optimized **236b** structure showing the distortion of the *hept*-HBCs.

The three [5]helicene moieties separating those HBCs, show mean dihedral angles (θ) of 26.3° , slightly higher than the one reported for a single carbo[5]helicene.²⁴³ In the case of **236b** the length of the unequal helicene side is slightly shorter than the other two sides (23.8 versus 24.8 Å) (Figure 79, bottom, right). On the other hand, despite the mean torsion angles of the three [5]helicenes are similar between each other (25.6°) only in the case of the unequal helicene this mean torsion angle comes from such different torsion angles as 32.8 , 35.1 and 8.8° , while in the other cases those values were much more similar (20.9 , 28.2 and 27.1°). These data highlights how this unequal [5]helicene presents a non-homogeneous curvature, in contrast to the other ones, starting with a subtle curvature from the central quasi-planar π -surface of the molecule

²⁴³ a) R. Kuroda, *J. Chem. Soc., Perkin Trans. 2* **1982**, 789-794; b) C. F. Chen, C. Y. Shen. In *Helicene Chemistry, From Synthesis to Applications*; Springer: Berlin, **2017**, 21-21.

and acquiring a deep distortion at the two last benzene rings, due to the simultaneous presence of the defects, namely heptagons and carbo[5]helicenes (Figure 79).

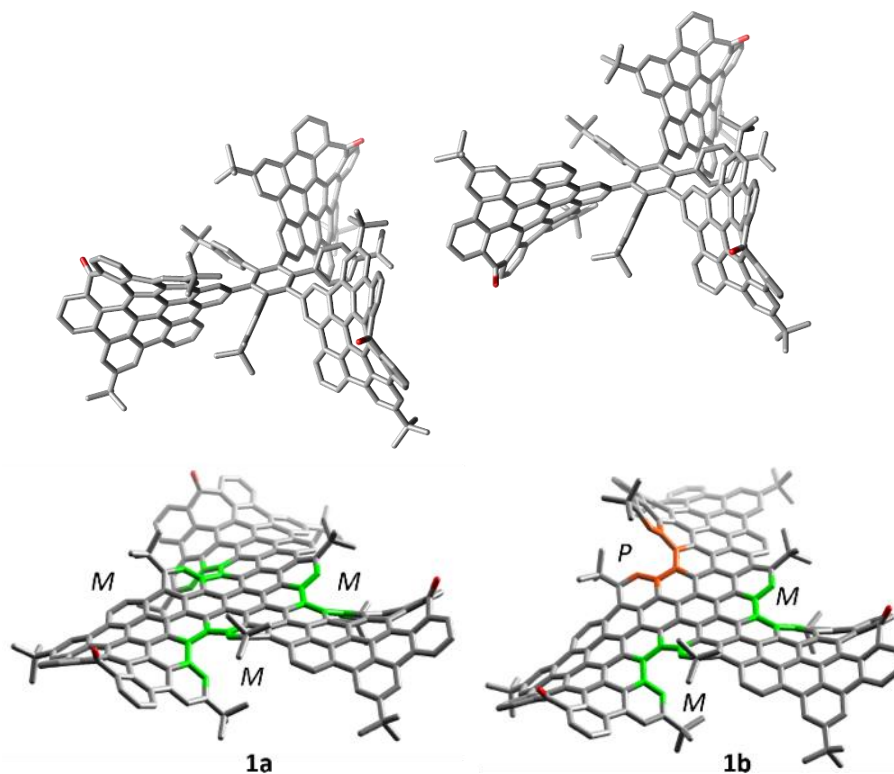


Figure 79. Top: DFT (CAMB3LYP/6-31G(d,p)) optimized structures of the atropisomers of **55**. Left: precursor of the *MMM*/*PPP*-**56** pair. Right: precursor of the *MMP*/*PPM*-**56** pair. Bottom: Left: DFT calculated structure of compound *MMM*-**56**. Right: DFT calculated structure of compound *MMP*-**56**. *M*-helicenes are highlighted in green, *P*-helicene is highlighted in orange.

The relative stability of both diastereoisomers **236a**/**236b** found by means of theoretical calculations (DFT-CAMB3LYP/6-31G(d,p)) was opposite to the experimentally observed 1/10 ratio of **236a**/**236b** suggesting symmetric diastereoisomer **236a** to be more stable than non-symmetric **236b**. On the other side, study of the precursor **235** atropisomers (Figure 79, top), shows inverse theoretical relative energies compared with those of the final products, being **235b** more stable than **235a** (Table 6). This supports the idea of each diastereoisomer of **236** to come from the corresponding atropisomer of **235** and agrees with the assignment of both of them according to the symmetry of the observed $^1\text{H-NMR}$ spectra. Epimerization was not observed after heating a tetrachloroethane solution of **236** at 100°C for 24 h.

Table 6. Relative DFT energies for compounds **236** and **235**.

| Compound | Relative energy (kcal·mol ⁻¹) | Boltzmann population (%) |
|----------------|---|--------------------------|
| MMM-236 | 0.00 | 99.999973 |
| MMP-236 | 8.96 | 0.000027 |
| 235 (Pro-236a) | 2.49 | 1.48 |
| 235 (Pro-236b) | 0.00 | 98.52 |

3.5.2. Optical properties

As commented above, the great distortion from planarity showed in the optimized structures resulted in a significant good solubility. Although side *tert*-butyl groups visibly help with solubility problems, in this case, it is the simultaneous presence of defects (*i.e.* helicenes and saddle-shaped heptagons) that increased solubility. This becomes clear when comparing with other reported purely hexagonal PAHs of similar shape and size that present very poor solubility even with the presence of side *tert*-butyl groups or long alkyl branched chains, hindering any NMR characterization.^{99,100,103,104} The enhanced solubility allows us to ensure a high degree of purity, and an unequivocal structural characterization which are unavoidable to rigorously evaluate photophysical properties and obtain reliable structure-property relationships, avoiding any minor impurity that could lead to false results. Therefore, we proceeded to the photophysical evaluation of each diastereoisomer **236a** (symmetric, minor compound) and **236b** (non-symmetric, major compound) separately.

Both diastereoisomers presented magenta color when dissolved in CH₂Cl₂. After recording their UV-vis absorption spectra in the range of 300-700 nm a clear vibronic structure could be observed (Figure 80). On the recorded spectra stand out two main maximum absorption bands with high molar absorptivity coefficients at 549 ($\epsilon = 2.27 \times 10^5 \text{ M}^{-1}\cdot\text{cm}^{-1}$) and 517 nm ($\epsilon = 2.97 \times 10^5 \text{ M}^{-1}\cdot\text{cm}^{-1}$) for **56a** and slightly red-shifted at 556 ($\epsilon = 3.17 \times 10^5 \text{ M}^{-1}\cdot\text{cm}^{-1}$) and 522 nm ($\epsilon = 4.12 \times 10^5 \text{ M}^{-1}\cdot\text{cm}^{-1}$) for **56b**. Remarkably, this last value is one order of magnitude higher than common dyes such as perilene diimides (PDI)²²⁰ and represent a considerable 4-fold and 2.7-fold increase in

comparison with recently described multiple-PDI based nanoribbons^{151a} and nanographenes,²⁴⁴ respectively. Curiously, **236b** exhibits a more intense absorptivity coefficient (1.4 fold) when compared with the symmetric **236a**. The origin of the electronic transitions involves a complex contribution of several “HOMO-*n*→LUMO+*n*” orbitals which extends over the aromatic surface without focusing on specific structural motifs (Figures 81 and 82).

The fluorescence spectra of both diastereoisomers (Figure 80, dashed lines) were measured in a range from 550 to 800 nm with an intense maximum centered at 643 nm for **236a** ($\lambda_{\text{exc}} = 510$ nm) and 650 nm for **236b** ($\lambda_{\text{exc}} = 510$ nm) and extended to 750 nm with high luminescence quantum yield (LQY, ϕ_f) value of 27.6% in CH_2Cl_2 for both diastereoisomers. This LQY is almost seven times higher than for [5]helicene (*ca.* 4%).³¹ The emission lifetime is multiexponential with average values in the range of 5-6 ns. The optical HOMO-LUMO gaps estimated from edge of the absorption spectra resulted 2.01 eV and 2.06 eV for **236a** and **236b**, respectively, in the range predicted by TD-DFT calculations (2.4 and 2.5 eV for **236a** and **236b** respectively). Cyclic voltammetry measurements in tetrahydrofuran (THF) shows a reversible reduction wave at -2.36 V (vs Fc/Fc+, see SI, Fig. S30) but no clear oxidation potentials were observed.

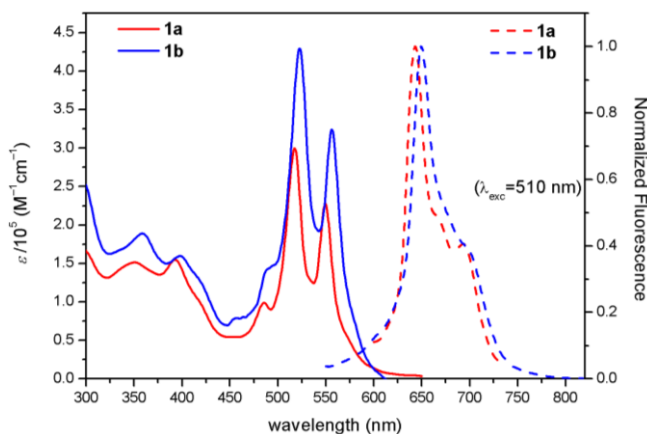


Figure 80. UV-vis absorption (solid lines) and normalized fluorescence (dashed lines) ($\lambda_{\text{exc}} = 510$ nm) spectra of **56a** and **56b** in CH_2Cl_2 at *ca.* 10^{-6} M.

Comparison of the optical properties of compound **236** and **194a** shows that absorption and emission are red-shifted by nearly 100 nm in the case of **236** as expected for the larger aromatic

²⁴⁴ G. Liu, T. Koch, Y. Li, N. L. Doltsinis, Z. Wang, *Angew. Chem. Int. Ed.* **2019**, *58*, 178-183.

surface (twice as large). LQY (ϕ_F) has also doubled in **236** and the brightness ($\epsilon \times \phi_F$) has increased by more than one order of magnitude (13 fold) going from $8.58 \times 10^3 \text{ M}^{-1}\cdot\text{cm}^{-1}$ for **194a** to $1.13 \times 10^5 \text{ M}^{-1}\cdot\text{cm}^{-1}$ for this *triskelion*-shaped nanographene (**236b**). To the best of our knowledge, both compounds constitute the only reported examples of PAHs containing a fully laterally π -extended [5]helicenes. In this sense, comparison with other fluorescence PAHs containing three units of [5]helicene shows that emission is red-shifted up to 180 nm again in the case of **236** with a LQY one order of magnitude higher, suggesting the great influence of the laterally π -extended helicenes.¹⁴¹

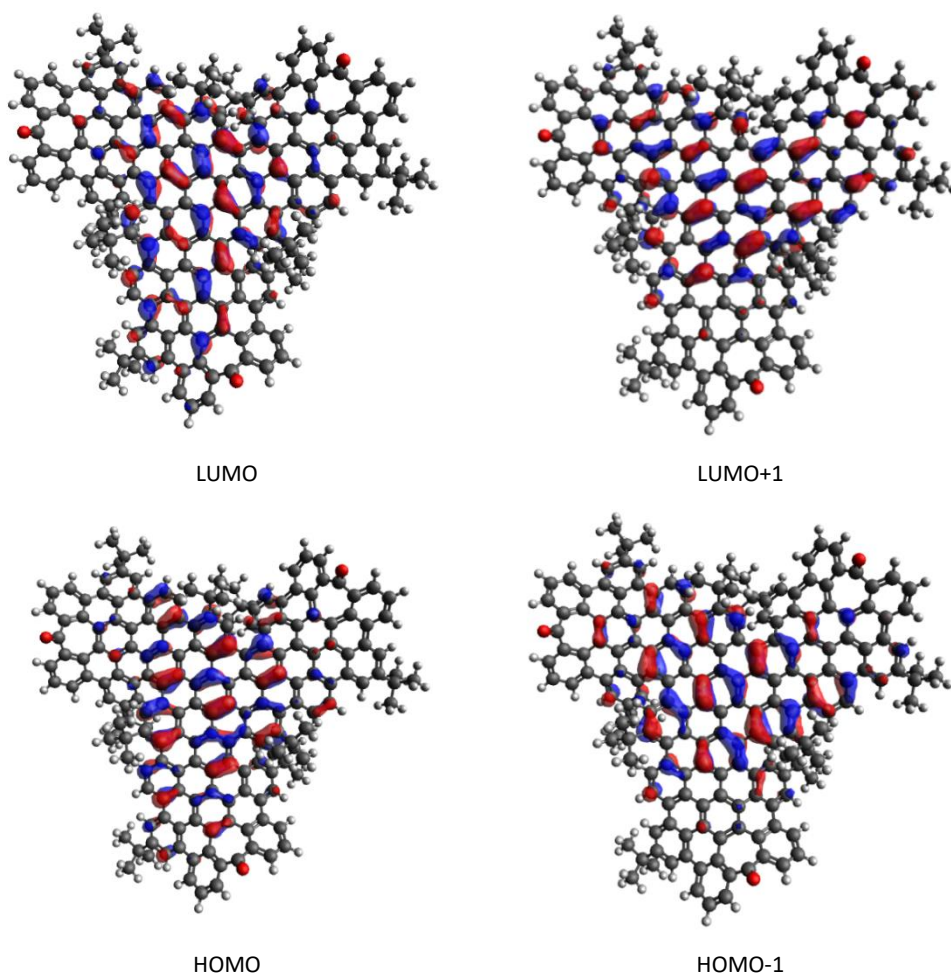


Figure 81. DFT calculated main HOMO and LUMO orbitals contributing to the lowest energy electronic transitions of (*M,M,M*)-**236**.

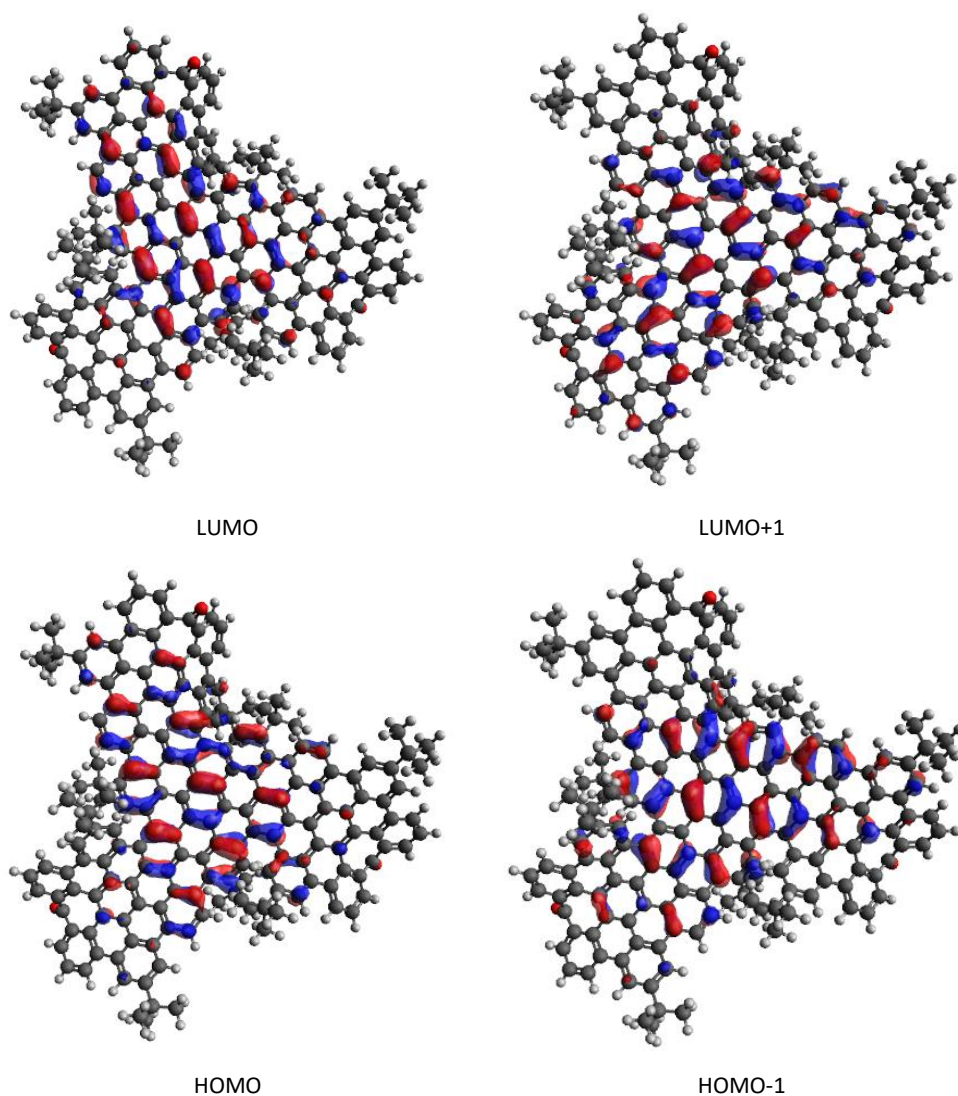


Figure 82. DFT calculated main HOMO and LUMO orbitals contributing to the lowest energy electronic transitions of (*M,M,P*)-**236**.

This improved emission response of **236** can be attributed to the larger π -surface of **236** and the distortion from planarity in comparison with previous multiple carbo[5]helicenes. In this sense, it is noteworthy that luminescence properties in solution have not been reported for previously synthesized hexagonal triangular nanographenes of similar size (Page 61 to 64) and only a related monodisperse nanographene reported by Li and co-workers (**98**) showed a LQY of 2% in

solution.²⁴⁵ This suggests the great influence of the incorporation of curvature in the photoluminescence responses of PAHs. Furthermore, LQY of **236** is in the range or even better than reported values for generally used graphene-based luminescence material such as graphene quantum dots, (GQDs, usually ranging from 2 to 23%)²⁴⁶ with the additional advantage of presenting a well-defined structure, especially in terms of size and shape that are known to strongly modulate properties of GQDs.

Regarding to the nonlinear optical properties, the two-photon absorption (TPA) cross-sections of both diastereoisomers seem to be in agreement with the observed one photon absorption, with **236a** presenting a TPA cross-section (σ_2) of 146 GM at *ca.* 860 nm while **236b** presents higher σ_2 of 224 GM at similar wavelength. Excitation with two photons in the near infrared (750-920 nm) results in up-converted emission at 600-750 nm overlapping the one-photon-induced emission spectrum ($\lambda_{\text{exc}} = 490$ nm) (Figure 83). The TPA cross-section is in the range of previously reported ribbon-shaped nanographene or carbon nanodots.²²⁸ The two-photon brightness ($\sigma_2 \times \phi_F$) is 40 GM and 62 GM for **236a** and **236b**, respectively. This represents a significant 3.6 fold increase in comparison with the previously reported distorted ribbon-shaped nanographene commented above (**194a**).

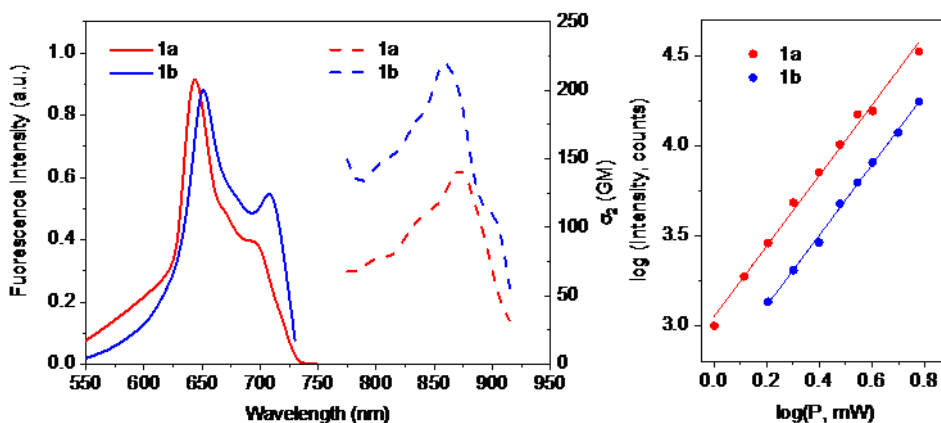


Figure 83. Two-photon absorption (TPA, ---) and two-photon induced emission (TPE, -) spectra of **236a** (red) and **236b** (blue) (left panel) and the log-log plot of the emission intensity as a function of the excitation power at 830 nm (right panel). A slope of 1.95 confirms the participation of two-photons in the absorption process.

²⁴⁵ M. L. Mueller, X. Yan, J. A. McGuire, L. S. Li, *Nano Lett.* **2012**, *10*, 2679-2682.

²⁴⁶ L. Li, G. Wu, G. Yang, J. Peng, J. Zhao, J. J. Zhu, *Nanoscale* **2013**, *5*, 4015-1039.

3.5.3. Chiroptical properties

Subsequently, each racemic diastereoisomer **236a** and **236b** was resolved into their enantiomers by chiral HPLC using a cellulose-based stationary phase and CH₂Cl₂/THF (98.5:1.5) as eluent (Figure 84). Chiral HPLC analysis shows no racemization after heating a tetrachloroethane solution of **236b** at 100°C for 24 h.

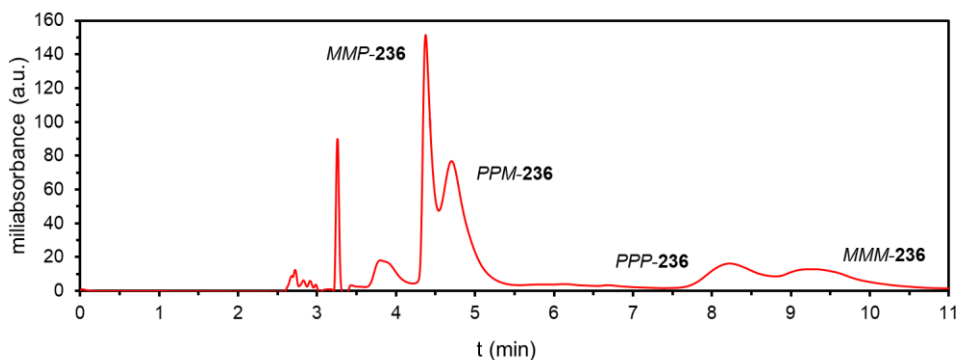


Figure 84. Chromatogram obtained after injection of **236** into CSP-HPLC.

The minor compound assigned to the more symmetric diastereoisomer **236a** was resolved into two peaks whose ECD spectra measured in CH₂Cl₂ showed a clear mirror image with several Cotton effects along the UV-visible range (Figure 85, left). It can be observed a bisignated signal centered at 370 nm, an intense absorption band centered at 446 nm and two consecutive less intense bands at the longest wavelengths (517 and 550 nm). The first eluted fraction ($t_R = 8$ min) presented a positive Cotton effect at 446 nm ($|\Delta\epsilon| = 252 \text{ M}^{-1}\cdot\text{cm}^{-1}$, $g_{abs} = 8.2 \times 10^{-3}$) and two consecutive negative Cotton effect at both 517 ($|\Delta\epsilon| = 103 \text{ M}^{-1}\cdot\text{cm}^{-1}$, $g_{abs} = 3.5 \times 10^{-4}$) and 550 nm ($|\Delta\epsilon| = 58 \text{ M}^{-1}\cdot\text{cm}^{-1}$, $g_{abs} = 2.5 \times 10^{-4}$) (Figure 85, left, red). The second eluted enantiomer of minor compound **236a** ($t_R = 9$ min) exhibited the corresponding mirror image (Figure 85, left, green) with positive Cotton effect at the longest wavelengths above 500 nm that correspond to the main maximum absorption bands at the UV-vis spectrum (Figure 80, red).

In respect to the major diastereoisomer **236b**, the two isolated peaks showed a quite complex ECD spectra in CH₂Cl₂ with up to nine Cotton effects (Figure 85, right); from a bisignated signal centered at 350 nm, to intense absorption bands at 425, 495, 526, and 557 nm and a minor band at the longest wavelength (590 nm). In this case, the first eluted peak ($t_R = 4.5$ min) showed

positive cotton effect both at the most intense band 425 nm ($|\Delta\epsilon| = 106 \text{ M}^{-1}\cdot\text{cm}^{-1}$, $g_{abs} = 8.8 \times 10^{-4}$) and at the longest wavelength, 590 nm ($|\Delta\epsilon| = 8 \text{ M}^{-1}\cdot\text{cm}^{-1}$, $g_{abs} = 2.0 \times 10^{-4}$) (Figure 85, right, red) opposite to what it is shown for second eluted HPLC fraction (Figure 85, right, in green).

From those results, it is clearly shown that the enantiomeric forms of symmetric diastereoisomer **236a** (*MMM-236* and *PPP-236*) presents considerable higher chiroptical responses in terms of the dissymmetry factor (g_{abs}) corresponding to non-symmetric **236b** enantiomers (*MMP-236* and *PPM-236*).

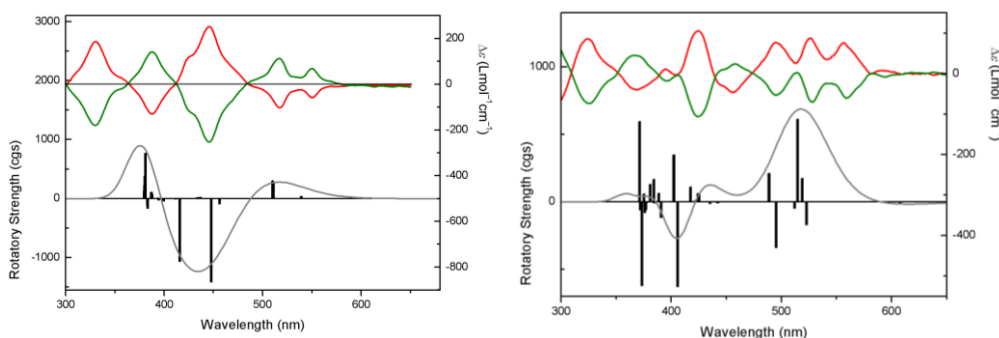


Figure 85. Left: Top: Experimental ECD of **236a** enantiomers: *MMM-* and *PPP-236* (green and black, respectively) in CH_2Cl_2 at *ca.* $5 \times 10^{-6} \text{ M}$; Bottom: calculated ECD spectrum for *MMM-236* (UV-correction - 0.6 eV). Right: Top: Experimental ECD of **236b** enantiomers: *MMP-* and *PPM-236* (red and green, respectively) in CH_2Cl_2 at *ca.* $2 \times 10^{-6} \text{ M}$; Bottom: calculated ECD spectrum for *MMP-236* (UV-correction - 0.6 eV).

The assignment of each of the four enantiomers chirality was done by comparison of the experimental ECD described above with the TD-DFT simulated ECD spectra (Figure 85). According to these results, the first HPLC fractions of both racemic resolutions correspond with *PPP-236* and *MMP-236* enantiomers, respectively (Figure 85). Curiously, the first Cotton effect of *PPP-236* is negative (550 nm), in opposition to what it is generally described for *P*-carbo[n]helicenes.²²² Also for *MMP-236*, the first Cotton effect is positive (at 590 nm), despite the presence of two *M*-carbo[5]helicenes versus an unique *P*-carbo[5]helicene motif in the structure. Although the complexity of the orbitals contribution to the electronic transitions makes difficult to elucidate the contribution of each helicene moiety to the resulting ECD bands, the good agreement between calculated and experimental ECD spectra shapes let no doubt about the chiral assignment. In any case, those results highlight the importance of the relative distribution of the chiral motifs in the structure, whose contribution can sum or subtract giving place to

unpredictable profiles and intensities of the ECD spectra. Thus, the assignment of chirality based exclusively on the chirality of the carbo[n]helicene scaffolds can be mistaken and the use of theoretical simulation of those ECD spectra is a useful tool to understand the origin of the electronic transitions causing each Cotton effect.²⁴⁷ On the other hand, the sign of the measured $[\alpha]_D^{20}$ value of the first HPLC fraction of **236b** was positive (+3843 °), in agreement with the sign of the first Cotton effect of its ECD spectrum and also with the sign of the theoretically computed value (+1189 °) for *MMP-236b*. The specific optical rotation values of **236a** and **236b** were theoretically obtained by calculation of the frequency-dependent electric dipole-magnetic dipole polarizability tensor, $\beta_{\alpha\beta}(\nu)$, using ab initio DFT at B3LYP/6-311g(2d,2p) level of theory at the sodium D line frequency (589.3 nm) and converted to sodium D line specific rotations $[\alpha]_D$ using:

$$[\alpha]_D = \frac{28800\pi^2 N_A \nu^2}{c^2 M} \gamma_s \beta$$

therefore, supporting again the ECD-based assignment done by comparison between experimental and calculated ECD spectra.

Finally, as expected from a chiral and emissive compound, **236** resulted active in CPL. Thus, the CPL of the four enantiomers was measured and the enantiomeric forms of each diastereoisomer gave CPL of opposite signs as expected for pure CPL. Likewise, the sign of the CPL spectra are in both cases in good correlation with the sign of the longest wavelength ECD band. Regarding to symmetric **236a** (Figure 86, in wine and black), the CPL spectra of both enantiomers show a maximum centered at 643 nm upon irradiation with UV light ($\lambda_{exc} = 490$ nm) with a similar profile to the corresponding fluorescence spectrum (Figure 80, in red) and a g_{lum} value estimated as 3×10^{-4} similar to the previously reported for a heptabenz[5]helicene containing nanographene (**194a**). In the case of the enantiomeric forms of mayor compound **236b**, a CPL signal was found between 600 and 700 nm with a maximum centered at 656 nm (Figure 85, in wine and black) coinciding with that of their fluorescence spectra (Figure 80, in blue). A g_{lum} value of 2×10^{-4} was found, less intense when compared with the symmetric counterpart **236a**. Therefore, as in the case of ECD response, the enantiomers of symmetric **236a** exhibit a more intense CPL signal in comparison with their respective non-symmetric ones (**236b**). The presence of a helicene of

²⁴⁷ a) I. Warnke, F. Furché, *WIREs Comput. Mol. Sci.* **2012**, *2*, 150-166; b) C. Adamo, D. Jacquemin, *Chem. Soc. Rev.* **2013**, *42*, 845-856.

opposite chirality might be the responsible of this attenuation in the chiroptical responses both in the absorption (ECD) and the emission (CPL).

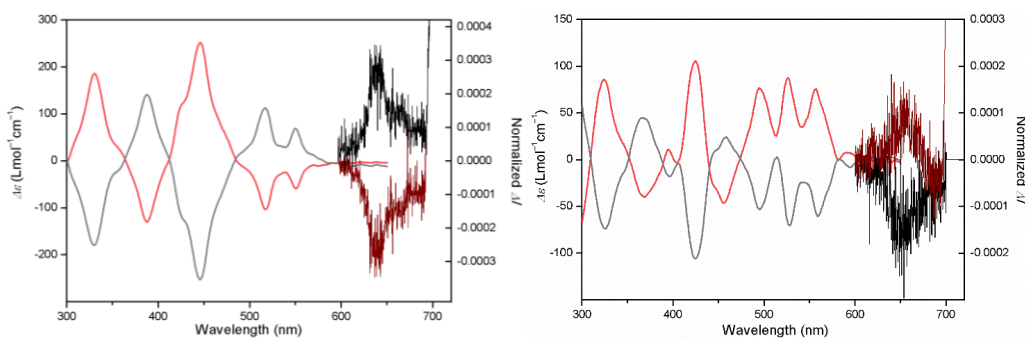


Figure 86. Left: Experimental ECD and CPL ($\lambda_{\text{exc}} = 490 \text{ nm}$) of **236a** enantiomers: *MMM-236* (gray and black, respectively) and *PPP-236* (red and wine, respectively) in CH_2Cl_2 at *ca.* $5 \times 10^{-6} \text{ M}$. Right: Experimental ECD and CPL ($\lambda_{\text{exc}} = 490 \text{ nm}$) of **236b** enantiomers: *MMP-236* (red and wine, respectively) and *PPM-236* (gray and black, respectively) in CH_2Cl_2 at *ca.* $2 \times 10^{-6} \text{ M}$.

4. EXPERIMENTAL SECTION

This section describes relevant information about how most of the experimental work was carried out. Reporting everyday life procedures and experiments, from the glassware used to set up a reaction through the monitoring and purification of the desired compound and up to general information about characterization and evaluation of the physical properties of the prepared compounds. Following by the description of the synthetic procedures, characterization of each compound and ending with information about the X-Ray diffraction structures and a copy of the representative NMR spectra of the prepared compounds.

4.1. General information

- **Glassware:** glassware used in the different reactions, both anhydrous and non-anhydrous required conditions, was previously washed and properly dried into an oven at 100°C overnight.

- **Reagents and solvents:** unless otherwise stated, all reagents and solvents were purchased from commercial sources. Non-anhydrous solvents such as CH₂Cl₂, hexane, EtOAc or THF were used without further purification and purchased from VWR, Scharlau, VWR and Honeywell respectively. Anhydrous solvents were used without further purification with the exception of anhydrous THF which was freshly distilled over Na/benzophenone and cooled down to room temperature under inert atmosphere.

- **Thin layer chromatography:** reactions were monitored by TLC, carried out on aluminum sheets coated with silica gel with fluorescent indicator UV₂₅₄ (purchased from Alugram SIL G/UV₂₅₄, Mackerey-Nagel, Germany or from Sigma-Aldrich) and observed under UV light (254 or 365 nm) and/or stained with phosphomolybdic acid (5% ethanol solution).

- **Purification of reaction mixtures:** flash column chromatographies were carried out using silica gel 60 (230-400 mesh, Scharlab, Spain) or silica gel 40-63 μm (230-400 mesh, SILICYCLE, Canada).

- **Nuclear magnetic resonance spectroscopy:** all ¹H and ¹³C spectra were recorded on *Varian 300* or *400 MHz*, *Bruker Nanobay Avance III HD 400 MHz*, *Bruker Avance NEO 400 MHz*, *Varian Direct Drive 500 MHz*, *Bruker Avance NEO 500 MHz* or *Varian Direct Drive 600 MHz* spectrometers, at a constant temperature of 298 K. Chemical shifts are reported in ppm and referred to residual solvent peak. Coupling constants (*J*) are reported in Hertz (Hz). Assignment of the ¹³C NMR signals were accomplished by DEPT-135, HSQC and HMBC techniques.

- **Mass spectrometry:** high resolution mass spectrometry measurements were performed on a Bruker ULTRAFLEX III spectrometer equipped with a matrix-assisted laser desorption ionization source coupled with a time of flight spectrometer as detection system (MALDI-TOF) or on a Waters XEVO GL-XS QTof mass spectrometer equipped with an electrospray ionization source coupled with a time of flight spectrometer as detection system (ESI-TOF).

- **Infrared spectroscopy:** the spectra were recorded on a Perkin Elmer Spectrum Two IR spectrometer using attenuated total reflection (ATR) of the solid compound. The spectral range was 4000-450 cm^{-1} .

- **Melting point:** evaluated for solid compounds after placing them into a capillary tube and measured on a Stuart SMP3 melting point apparatus up to 300°C.

- **High performance liquid chromatography:** isolations, diastereomeric and racemic resolutions were performed on an Agilent 1260 Series equipped with the following modules: quaternary pump (G7111B 1260 Quat Pump), automatic sample injector (G2258A 1260 DL ALS), column thermostat (G1316A 1260 TCC), DAD detector (G7115A 1260 DADWR) and an automatic sample collector (G1364C 1260 FC-AS).

For isolations and diastereomeric resolutions at analytical scale, Merck LiChroCART® (4 × 250 mm) packed with porous silica (Si 60, 5 μm) was used as column. For semi-preparative scale, the selected column was an Agilent Zorbax Rx-SIL (9.4 × 250 mm) packed with porous silica (5 μm). In both cases, the column temperature was set at 25°C and the flow was constant during operation.

In case of racemic resolutions at analytical scale, CHIRALPAK® IC analytical column (4.6 × 250 mm) packed with cellulose tris-(3,5-dichlorophenylcarbamate) immobilized on silica gel (5 μm) was used as column. Whilst for racemic resolutions at semi-preparative scale, CHIRALPAK® IA semi-preparative column (10 × 250 mm) packed with amylose tris-(3,5-dimethylphenylcarbamate) immobilized on silica gel (5 μm) was used as column. In all cases the column temperature was set at 25°C and the flow was constant during operation.

- **Electrochemistry:** cyclic voltammograms and square wave voltammograms were recorded on a PGSTAT204 potentiostat/galvanostat (Metrohm Autolab B. V.) in a conventional three electrode

cell under inert atmosphere at 25°C. A platinum wire as counterelectrode, a silver wire quasireference electrode and a glassy carbon disk working electrode were used. Potential values were referred to the ferrocenium/ferrocene ($\text{FeCp}_2^+/\text{FeCp}_2$) system, ferrocene was added as an internal reference after each measurement.

- **Spectroelectrochemistry:** UV-vis spectra at different potentials were measured on a *PGSTAT204* potentiostat/galvanostat with an *Autolab Spectrophotometer UB* module (*Metrohm Autolab B. V.*) on a three electrode cuvette (0.10 cm pathlength) under Ar atmosphere at 25°C. A Pt-wire counterelectrode, an Ag-wire quasireference electrode and a Pt-mesh working electrode were used. Scan rate was 0.10 V/s and the spectra recorded every 50 mV.

- **Linear optical and chiroptical properties:** absorbance, electronic circular dichroism (ECD), fluorescence and circularly polarized luminescence (CPL) measurements were performed on an *Olis DSM172* spectrophotometer equipped with a *Hamamatsu* 150 W xenon arc lamp or a fixed wavelength LED as light source, a *Hamamatsu* photomultiplier tube (PMT) as detector for absorbance and ECD and a *Hamamatsu* photon counting detector for fluorescence and CPL measurements. Different settings and data processing were selected and carried out using the *Olis GlobalWorks* software. A fixed slitwidth of 1.0 mm and an integration time of 0.01 s were selected for both absorbance and fluorescence measurements. For ECD measurements a fixed slitwidth of 1.00 mm and an integration time of 0.10 s was set, whilst for CPL experiments was 1.00 s.

Emission lifetimes were measured by the Single-Photon Timing technique in a home-built setup using a linear excitation source operating at 330 nm with a 4 MHz repetition rate (second harmonic of a Coherent Radiation Dye laser 700 series, 560-610 nm, 130 mW, 5 ps, 4 MHz), an *Hamamatsu R2809U-01* MCP-PMT (290-700 nm) as the detector and a *SPC-160* photon counting board from *Becker & Hickl GmbH*.

- **Non-linear optical properties:** the two-photon absorption (TPA) spectra were measured by two-photon induced fluorescence (TPF) using the same standard to account for the collection efficiency and excitation pulse characteristics. The TPA cross-section of the reference was taken

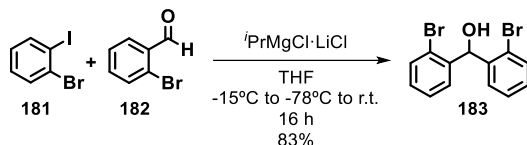
4. Experimental section

from bibliography.²⁴⁸ The excitation source was a Ti:sapphire laser (*Tsunami BB, Spectra-Physics*, 710-990 nm, 107 w, 100 fs, 82 MHz).

The two-photon emission was measured within a narrow wavelength bandwidth centered at the maximum selected by the *H20Vis Jobin Yvon* monochromator placed at the entrance of a PMC-100-4 photomultiplier tube (*Becker and Hickl GmbH*). The integrated intensity over the entire emission band was extrapolated using the emission spectra corrected by the detector sensitivity.

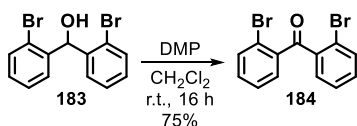
4.2. Synthesis and characterization of the prepared compounds

- Compound 183



Procedure modified from literature.²⁴⁹ To a stirring solution of 2-bromoiodobenzene (3.67 mL, 29.27 mmol) in THF (80 mL) placed into an acetone bath at -15°C was added $i\text{PrMgCl}\cdot\text{LiCl}$ (1.3 M in THF, 25 mL, 32.5 mmol) and stirred for 30 min at -15°C . The reaction was cooled to -78°C and 2-bromobenzaldehyde (4.17 mL, 36 mmol) was added dropwise. The cold bath was left in place and the reaction was allowed to warm to room temperature overnight. The reaction mixture was quenched with HCl 2M (2 mL), diluted with water (100 mL) and extracted twice with CH_2Cl_2 ($2 \times 100\text{mL}$). The combined organic phases were dried with anhydrous Na_2SO_4 , filtered and concentrated under reduced pressure. The crude material was purified by flash column chromatography (SiO_2 , hexane/ CH_2Cl_2 , 4:1) affording compound **183** (8.31 g, 83%) as a colorless oil. ^1H NMR (300 MHz, CDCl_3): δ = 7.58 (d, $J=7.9$, 2H), 7.37 – 7.24 (m, 4H), 7.22 – 7.13 (m, 2H), 6.38 (d, $J=3.8$, 1H), 2.82 (d, $J=4.0$, 1H).

- Compound 184

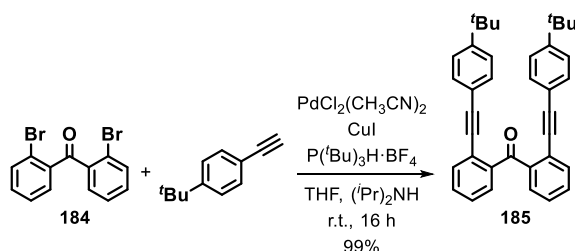


²⁴⁸ N. S. Makarov, M. Drobizhev, A. Rebane, *Opt. Express* **2008**, *16*, 4029-4047.

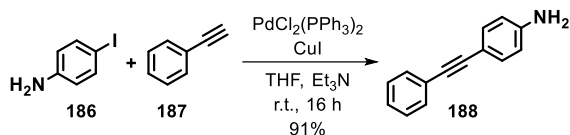
²⁴⁹ T. K. Wood, W. E. Piers, B. A. Keay, M. Parvez, *Angew. Chem. Int. Ed.* **2009**, *48*, 4009-4012.

Compound **183** (4.20 g, 12.28 mmol) was dissolved in CH₂Cl₂ (50 mL) and placed into an ice-water bath, then Dess-Martin periodinane (6.76 g, 15.93 mmol) was added slowly under vigorous stirring. The reaction mixture was allowed to warm to room temperature and stirred overnight. The reaction mixture was diluted with CH₂Cl₂ (50 mL) and washed twice with Na₂S₂O₃ and NaHCO₃ (2 × 100 mL). The organic layer was dried over anhydrous Na₂SO₄, filtered and the solvent removed under vacuum. The crude was purified by flash column chromatography (SiO₂, hexane/CH₂Cl₂, 4:1) giving rise to compound **184** (3.13 g, 75%) as a white solid. ¹H NMR (300 MHz, CDCl₃): δ = 7.69 – 7.59 (m, 2H), 7.49 – 7.42 (m, 2H), 7.42 – 7.30 (m, 4H).

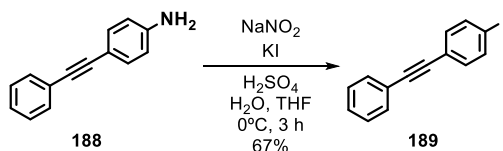
- Compound 185



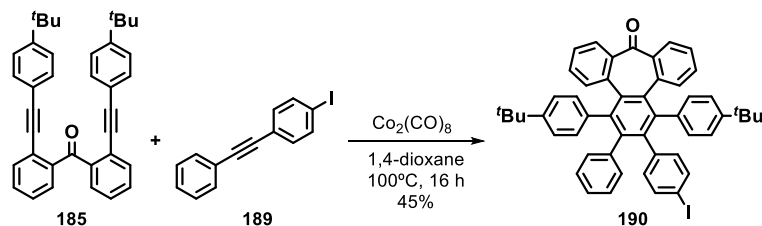
Into a properly dried and degassed flask were placed compound **184** (500 mg, 1.47 mmol), PdCl₂(CH₃CN)₂ (60 mg, 0.23 mmol), CuI (50 mg, 0.26 mmol) and *tris*-(*tert*-butyl)-phosphonium tetrafluoroborate (130 mg, 0.45 mmol). The solids were purged with Ar and then freshly distilled THF (3 mL) and (i-Pr)₂NH (6 mL) were added and bubbled with Ar. 4-*tert*-butylphenylacetylene (0.83 mL, 4.57 mmol) was added dropwise and the reaction mixture was stirred overnight at room temperature and then diluted with CH₂Cl₂ (100 mL) and washed with NH₄Cl_{sat} (2 × 100 mL). The organic layer was dried with anhydrous Na₂SO₄, filtered and the solvent removed in the rotavapor. The crude material was purified by flash column chromatography (SiO₂, hexane/CH₂Cl₂, 7:3) affording compound **185** (720 mg, 99%) as a brownish foam. ¹H NMR (500 MHz, CD₂Cl₂) δ = 7.69 (ddd, *J*=7.7, 1.5, 0.5, 2H), 7.62 (ddd, *J*=7.7, 1.3, 0.5, 2H), 7.51 (td, *J*=7.6, 1.5, 2H), 7.45 (td, *J*=7.6, 1.3, 2H), 7.29 (d, *J*=8.7, 4H), 7.13 (d, *J*=8.7, 4H), 1.29 (s, 18H). ¹³C NMR (126 MHz, CD₂Cl₂); δ = 197.18 (C), 152.36 (C), 141.59 (C), 133.68 (CH), 131.72 (CH), 131.64 (CH), 130.31 (CH), 128.53 (CH), 125.59 (CH), 123.18 (C), 120.03 (C), 95.85 (C), 87.49 (C), 35.10 (C), 31.28 (CH₃). HR-MS (EI): *m/z* calc. for C₃₇H₃₄O [M]⁺: 494.2610; found: 494.2607.

- Compound 188

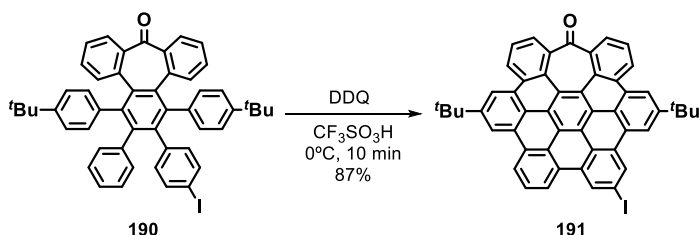
A solution of phenylacetylene (0.60 mL, 5.50 mmol) in freshly distilled THF (1 mL) was added dropwise over a suspension of 4-iodoaniline (1.00 g, 4.56 mmol), $\text{PdCl}_2(\text{PPh}_3)_2$ (35 mg, 0.05 mmol) and CuI (19 mg, 0.10 mmol) in a mixture of freshly distilled THF (3 mL) and Et_3N (10 mL) previously bubbled with Ar. The reaction mixture was stirred at room temperature overnight before being diluted with EtOAc (100 mL) and washed with $\text{NH}_4\text{Cl}_{\text{sat}}$ (2×100 mL). The organic layer was dried over anhydrous Na_2SO_4 , filtered and the solvent removed under vacuum. The residue was purified by flash column chromatography (SiO_2 , hexane/EtOAc, 3:2) giving rise to compound **188** (801 mg, 91%) as a black oil. ^1H NMR (300 MHz, CDCl_3): $\delta = 7.50$ (d, $J=7.0$, 2H), 7.38 – 7.24 (m, 5H), 6.64 (d, $J=8.3$, 2H), 3.81 (s, 2H).

- Compound 189

The amine **188** (801 mg, 4.15 mmol) was suspended in distilled water (8 mL), a solution of sulfuric acid 98% (0.7 mL) was added and the mixture was cooled to 0°C . A solution of sodium nitrite (370 mg, 5.36 mmol) in water (3 mL) was added dropwise while stirring, keeping the temperature between 0 – 4°C , during 30 min. THF (10 mL) was added to the reaction mixture and then a solution of potassium iodide (2.27 g, 13.68 mmol) in water (4 mL) was added slowly during 30 min. After 3 h the reaction mixture was diluted with EtOAc (50 mL), washed with $\text{Na}_2\text{S}_2\text{O}_3_{\text{sat}}$ (2×50 mL). The organic fraction was dried over anhydrous Na_2SO_4 and concentrated under reduced pressure. The crude material was purified by flash column chromatography (SiO_2 , hexane/EtOAc, 9:1) to give **189** (845 mg, 67%) as a white solid. ^1H NMR (300 MHz, CDCl_3): $\delta = 7.69$ (d, $J=8.4$, 2H), 7.56 – 7.48 (m, 2H), 7.39 – 7.32 (m, 3H), 7.25 (d, $J=8.4$, 2H).

- Compound 190

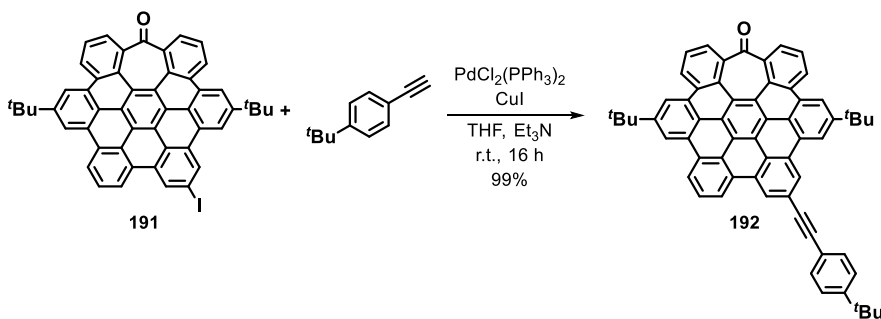
In a glovebox, **185** (300 mg, 0.60 mmol) and cobalt carbonyl (268 mg, 0.78 mmol) were placed into a 25 mL round bottom flask and capped properly. Anhydrous 1,4-dioxane (6 mL) was added and the solution stirred at 100°C during 30 min. Then a degassed solution of compound **189** (275 mg, 0.90 mmol) in anhydrous 1,4-dioxane (2 mL) was added dropwise during 30 min. The reaction was stirred 16 h under inert atmosphere at 100°C. The mixture was then cooled down to room temperature and the solvent removed under reduced pressure. The residue was adsorbed on silica gel and purified by flash column chromatography (SiO₂, hexane/CH₂Cl₂, 3:2) affording **190** (215 mg, 45%) as a white solid. ¹H NMR (500 MHz, CDCl₃): δ = 7.39 (d, *J*=7.7, 2H), 7.37 – 7.29 (m, 2H), 7.10 – 7.02 (m, 4H), 7.02 – 6.96 (m, 4H), 6.96 – 6.92 (m, 3H), 6.83 (t, *J*=7.5, 1H), 6.79 – 6.74 (m, 4H), 6.69 (t, *J*=7.4, 1H), 6.39 – 6.33 (m, 3H), 6.14 (dd, *J*=8.2, 2.2, 1H), 1.16 (s, 9H), 1.13 (s, 9H). ¹³C NMR (126 MHz, CDCl₃): δ = 200.5 (C), 148.8 (C), 148.5 (C), 146.1 (C), 142.6 (C), 141.6 (C), 141.5 (C), 141.4 (C), 140.2 (C), 140.1 (C), 137.5 (C), 137.4 (C), 136.1 (CH), 136.0 (C), 135.8 (C), 135.2 (CH), 135.1 (C), 135.0 (C), 133.6 (CH), 133.2 (CH), 133.1 (CH), 132.6 (CH), 132.3 (CH), 131.6 (CH), 130.4 (CH), 130.3 (CH), 130.2 (CH), 128.5 (CH), 128.4 (CH), 127.3 (CH), 127.02 (CH), 127.00 (CH), 126.3 (CH), 125.8 (CH), 124.4 (CH), 124.32 (CH), 124.30 (CH), 124.2 (CH), 124.1 (CH), 123.7 (CH), 123.4 (CH), 91.2 (C), 34.4 (C), 34.3 (C), 31.4 (CH₃), 31.3 (CH₃). HR-MS (MALDI, DCTB): *m/z* calc. for C₅₁H₄₃IONa [M+Na]⁺ : 821.2251; found: 821.2241.

- Compound 191

4. Experimental section

To a solution of polyphenylene **190** (100 mg, 0.13 mmol) and DDQ (168 mg, 0.74 mmol) in dry CH_2Cl_2 (6 mL) placed in an ice-water bath, trifluoromethanesulfonic acid (0.15 mL) was slowly added and the reaction mixture stirred for 10 min under argon atmosphere. The mixture was then diluted with CH_2Cl_2 (10 mL) and silica gel was added. The solvent was removed in the rotavapor and the crude material purified by flash column chromatography (SiO_2 , hexane/ CH_2Cl_2 , 3:2) giving rise to **191** (89 mg, 87%) as a yellow solid. ^1H NMR (400 MHz, CDCl_3): δ = 8.76 – 8.67 (m, 4H), 8.58 (s, 2H), 8.45 (d, $J=7.7$, 2H), 8.26 (d, $J=7.8$, 1H), 8.05 (d, $J=7.9$, 1H), 7.86 – 7.80 (m, 2H), 7.75 – 7.61 (m, 2H), 7.38 (t, $J=7.8$, 1H), 1.65 (s, 9H), 1.53 (s, 9H). ^{13}C NMR (101 MHz, CDCl_3): δ = 202.6 (C), 150.2 (C), 150.0 (C), 142.6 (C), 142.5 (C), 132.1 (C), 131.6 (C), 131.4 (C), 131.3 (C), 130.4 (CH), 130.2 (CH), 130.1 (C), 129.4 (C), 128.4 (C), 128.29 (C), 128.26 (C), 128.2 (C), 127.62 (CH), 127.61 (CH), 127.4 (C), 127.35 (C), 127.26 (CH), 126.37 (CH), 126.36 (CH), 125.1 (C), 124.9 (C), 124.3 (C), 124.2 (CH), 124.1 (CH), 123.5 (C), 123.3 (C), 123.1 (C), 123.0 (C), 122.8 (C), 122.4 (CH), 121.4 (CH), 120.93 (CH), 120.87 (C), 120.6 (CH), 120.4 (C), 118.9 (CH), 118.4 (CH), 94.1 (C), 35.8 (C), 35.7 (C), 32.0 (CH_3), 31.9 (CH_3). HR-MS (MALDI, DCTB): m/z calc. for $\text{C}_{51}\text{H}_{33}\text{IO}$ $[\text{M}]^+$: 788.1571; found: 788.1565.

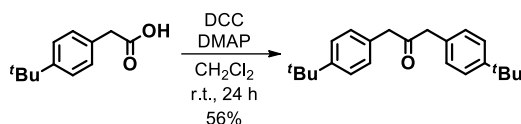
- Compound 192



p-tert-Butylphenylacetylene (70 μL , 0.38 mmol) was added dropwise to a degassed suspension of **191** (100 mg, 0.13 mmol), $\text{PdCl}_2(\text{PPh}_3)_2$ (20 mg, 0.03 mmol), CuI (5 mg, 0.03 mmol) in a mixture of $\text{THF}/\text{Et}_3\text{N}$ (1:2, 9 mL). The reaction was stirred at r.t. for 16 h. The mixture was diluted with CH_2Cl_2 (50 mL) and washed with $\text{NH}_4\text{Cl}_{\text{sat}}$ (2×50 mL) the organic layer was separated and dried over anhydrous Na_2SO_4 and the solvent was removed under reduced pressure. The crude was purified by flash column chromatography (SiO_2 , hexane/ CH_2Cl_2 3:2) affording **192** (104 mg, 99%) as a yellow solid. M. p. > 300°C; ^1H NMR (400 MHz, CD_2Cl_2): δ = 8.75 (t, $J=7.6$, 2H), 8.71 (s, 1H),

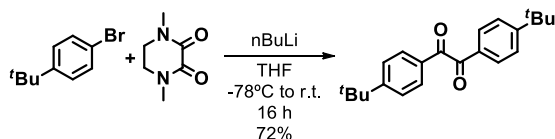
8.64 (m, 2H), 8.57 (s, 1H), 8.46 (s, 1H), 8.41 (d, $J=7.7$, 1H), 8.28 (s, 1H), 8.23 (d, $J=8.1$, 1H), 7.79 (d, $J=7.1$, 2H), 7.67 (t, $J=8.0$, 2H), 7.51 (t, $J=7.9$, 1H), 7.42 – 7.34 (m, 4H), 1.66 (s, 9H), 1.57 (s, 9H), 1.37 (s, 9H); ^{13}C NMR (101 MHz, CD_2Cl_2): δ = 202.9 (C), 152.3 (C), 150.5 (C), 150.3 (C), 142.9 (C), 142.9 (C), 131.9(CH), 131.7 (C), 131.6 (C), 130.6 (C), 130.3 (C), 129.9 (C), 129.7 (C), 129.3 (C), 129.2 (C), 128.6 (C), 128.6 (C), 127.8 (CH), 127.6 (C), 127.4 (CH), 126.6 (CH), 125.9 (CH), 125.3 (C), 125.1 (C), 124.6 (CH), 124.40 (C), 124.37 (CH), 124.3 (CH), 124.0 (C), 123.6 (C), 123.35 (C), 123.34 (C), 123.2 (C), 122.3 (CH), 122.2 (C), 121.7 (CH), 121.4 (CH), 121.3 (C), 120.9 (CH), 120.7 (C), 120.5 (C), 119.0 (CH), 118.8 (C), 90.9 (C), 89.9 (C), 36.1 (C), 36.0 (C), 35.3 (C), 32.2 (CH₃), 32.1 (CH₃), 31.6 (CH₃); HR-MS (MALDI DCTB+PPG790): m/z calc. for $\text{C}_{63}\text{H}_{46}\text{O}$ $[\text{M}]^+$: 818.3543; found: 818.3559; IR (ATR): 2953, 1679, 1610, 1578 cm^{-1} .

- 1,3-Bis-(*p*-*tert*-butyl)phenyl-2-propanone



Procedure modified from literature.²⁵⁰ To a solution of DCC (1.73 g, 8.38 mmol) and DMAP (229 mg, 1.87 mmol) in dry CH_2Cl_2 (15 mL) was added dropwise a solution of *p*-*tert*-butylphenylacetic acid (1.61 g, 8.38 mmol) in dry CH_2Cl_2 (15 mL). The reaction mixture was stirred for 24 h at room temperature under Ar atmosphere. The precipitated white solid was filtered away and the solvent removed under vacuum. The crude material was purified by flash column chromatography (SiO_2 , hexane/EtOAc, 5:1) to obtain 1,3-Bis-(*p*-*tert*-butyl)phenyl-2-propanone (756 mg, 56%) as a yellow solid. ^1H NMR (300 MHz, CDCl_3): δ = 7.35 (d, $J=8.1$, 4H), 7.11 (d, $J=8.0$, 4H), 3.70 (s, 4H), 1.33 (s, 18H).

- 1,2-Bis-(*p*-*tert*-butyl)phenylethane-1,2-dione

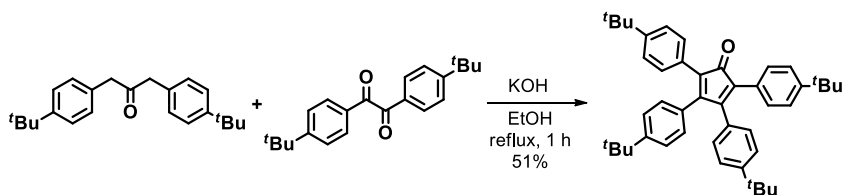


²⁵⁰ X. Geng, J. T. Mague, J. P. Donahue, R. A. Pascal, Jr, *J. Org. Chem.* **2016**, *81*, 3838-3847.

4. Experimental section

Procedure modified from literature.²⁵¹ Freshly distilled THF (7 mL) was placed in a properly dried and degassed round bottom flask. 1-Bromo-4-*tert*-butylbenzene (2.39 mL, 9.12 mmol) was added and the solution cooled down to -78°C. Then *n*-BuLi (2.5 M, 5.56 mL, 13.9 mmol) was added dropwise and the reaction mixture stirred at -78°C for 60 min. A suspension of DMPD (prepared according to literature,²⁵² 1.00 g, 7.03 mmol) in freshly distilled THF (6 mL) was added quickly, the cold bath was left in place and the reaction was allowed to warm to room temperature overnight. The reaction mixture was quenched with HCl 2M (5 mL), diluted with HCl 2M (50 mL) and extracted with CH₂Cl₂ (2 × 50 mL), the organic layers were collected, dried over anhydrous Na₂SO₄, filtered and the solvent removed in the rotavapor. The crude material was purified by flash column chromatography (SiO₂, hexane/CH₂Cl₂, 3:1) obtaining 1,2-Bis-(*p*-*tert*-butyl)phenylethane-1,2-dione (1.63 g, 72%) as a pale yellow solid. ¹H NMR (400 MHz, CDCl₃): δ = 7.91 (d, *J*=8.6, 4H), 7.52 (d, *J*=8.6, 4H), 1.34 (s, 18H).

- 2,3,4,5-Tetrakis-(*p*-*tert*-butyl)phenyl-cyclopentadienone.



Procedure modified from literature.²⁵³ In a round bottom flask were placed 1,3-Bis-(*p*-*tert*-butyl)phenyl-2-propanone (620 mg, 1.92 mmol) and 1,2-Bis-(*p*-*tert*-butyl)phenylethane-1,2-dione (620 mg, 1.92 mmol) and dissolved with EtOH absolute (15 mL). The reaction mixture was heated to reflux and then a KOH 2 M solution in EtOH absolute (6 mL) was added. The reaction mixture was allowed to cool to room temperature and then diluted with CH₂Cl₂ (50 mL) and washed with HCl 2M (2 × 50 mL). The organic layer was dried over anhydrous Na₂SO₄, filtered and the solvent removed under vacuum. The residue was purified by flash column chromatography (SiO₂, hexane/CH₂Cl₂, 4:1) affording 2,3,4,5-Tetrakis-(*p*-*tert*-butyl)phenyl-

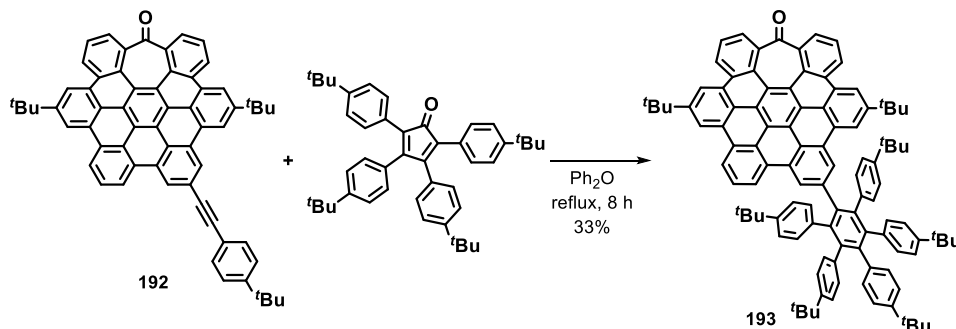
²⁵¹ D. Lungerich, J. F. Hitzengerger, M. Marcia, F. Hampel, T. Drewello, N. Jux, *Angew. Chem. Int. Ed.* **2014**, *53*, 12231-12235.

²⁵² U. T. Mueller-Westerhoff, M. Zhou, *J. Org. Chem.* **1994**, *59*, 4988-4992.

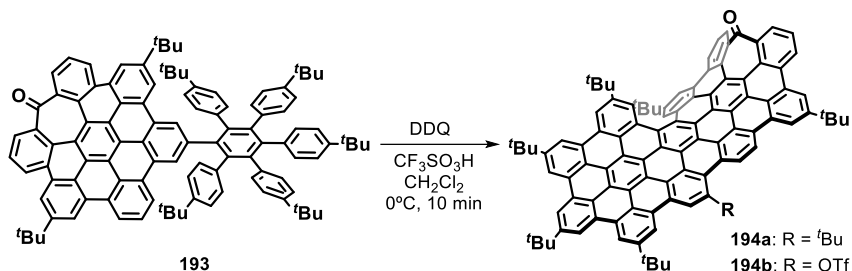
²⁵³ S. K. Sadhukhan, C. Viala, A. Gourdon, *Synthesis* **2003**, *10*, 1521-1525.

cyclopentadienone (599 mg, 51%) as a deep purple solid. ^1H NMR (300 MHz, CDCl_3): δ = 7.25 – 7.18 (m, 8H), 7.15 (d, $J=8.3$, 4H), 6.83 (d, $J=8.3$, 4H), 1.29 (s, 18H), 1.28 (s, 18H).

- Compound 193

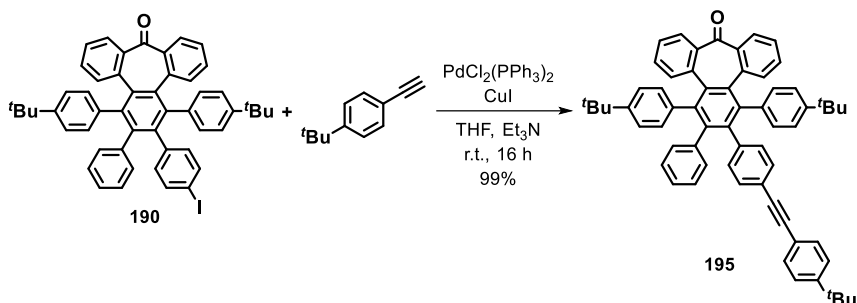


An equimolar amount of **192** (119 mg, 0.15 mmol) and 2,3,4,5-tetrakis(*p*-*tert*-butylphenyl)cyclopentadienone (89 mg, 0.15 mmol) were placed in a Schlenk tube, dissolved in diphenyl ether (1 mL) and bubbled with Ar. The reaction mixture was placed in a sand bath and refluxed over 8 h. The crude was allowed to cool to room temperature and diluted with hexane (10 mL) and purified by flash column chromatography (SiO_2 , hexane/ CH_2Cl_2 , 3:2) to afford **193** (67 mg, 33%) as a glassy yellow solid. ^1H NMR (500 MHz, CD_2Cl_2): δ = 9.04 (d, $J=8.6$, 1H), 9.01 (d, $J=8.3$, 1H), 8.90 – 8.83 (m, 4H), 8.61 – 8.57 (m, 2H), 8.50 (s, 1H), 8.43 (d, $J=1.4$, 1H), 8.07 (t, $J=7.9$, 1H), 7.90 (dt, $J=15.9$, 7.6, 2H), 7.85 (dd, $J=7.1$, 1.4, 1H), 7.82 (dd, $J=7.2$, 1.4, 1H), 7.01 (d, $J=8.1$, 2H), 6.98 – 6.91 (m, 8H), 6.90 – 6.80 (m, 8H), 6.74 (d, $J=8.2$, 2H), 1.64 (s, 9H), 1.64 (s, 9H), 1.16 (s, 9H), 1.14 (s, 18H), 0.68 (s, 18H); ^{13}C NMR (126 MHz, CD_2Cl_2): δ = 202.8 (C), 150.7 (C), 150.5 (C), 148.6 (C), 148.45 (C), 148.40 (C), 142.94 (C), 142.91 (C), 141.8 (C), 141.4 (C), 141.2 (C), 140.6 (C), 140.5 (C), 138.5 (C), 138.43 (C), 138.39 (C), 131.84 (C), 131.83 (CH), 131.7 (C), 131.51 (CH), 131.48 (CH), 131.4 (CH), 130.64, 130.58 (C), 130.10 (C), 130.07 (C), 129.2 (C), 128.9 (C), 128.6 (C), 128.5 (C), 127.9 (CH), 127.8 (C), 127.7 (C), 127.6 (CH), 127.1 (CH), 126.8 (CH), 126.6 (CH), 126.4 (CH), 125.0 (C), 124.8 (C), 124.1 (CH), 124.0 (CH), 123.96 (CH), 123.75 (C), 123.73 (CH), 123.70 (CH), 123.5 (C), 123.41 (C), 123.40 (C), 122.2 (CH), 122.15 (CH), 122.12 (C), 121.5 (C), 121.4 (CH), 121.2 (C), 121.0 (CH), 118.6 (CH), 118.4 (CH), 35.9 (C), 35.9 (C), 34.4 (C), 34.2 (C), 32.0 (CH_3), 31.9 (CH_3), 31.38 (CH_3), 31.36 (CH_3), 30.9 (CH_3). Some carbon signals could not be listed due to the overlapping observed; HR-MS (MALDI DCTB + PEGNa 1500): m/z calc. for $\text{C}_{107}\text{H}_{98}\text{O}^+$ [$\text{M}]^+$: 1398.7612; found: 1398.7594; IR (ATR): 2958, 1682, 1612, 1511 cm^{-1} .

- Compound 194

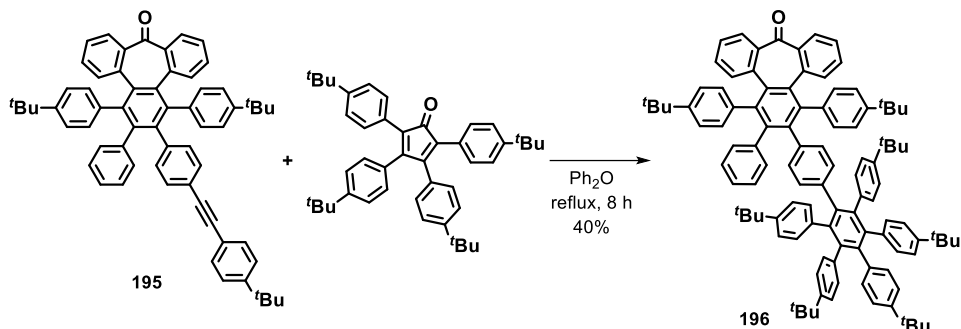
A solution of compound **193** (55 mg, 0.04 mmol) and DDQ (70 mg, 0.31 mmol) in dry CH_2Cl_2 (5 mL) was cooled to 0 – 4 °C in an ice-water bath, then trifluoroacetic acid was added (0.10 mL, 1.31 mmol) and the mixture was stirred for 10 min. The solution was diluted with CH_2Cl_2 (3 mL), then silica gel was added and the solvent removed. The crude was purified by flash column chromatography (SiO_2 , hexane/ CH_2Cl_2 1:4) to afford **194a** (25 mg, 46%) and **194b** (3 mg, 5%).

194a: M. p. > 280 °C; $[\alpha]_{\text{D}}^{25} = -186.12^\circ$ (CH_2Cl_2 , c 0.037) (*M*-**194a**); $^1\text{H NMR}$ (500 MHz, $(\text{CDCl}_2)_2$): $\delta = 10.12$ (s, 1H), 9.81 (d, $J=8.1$, 1H), 9.71 (d, $J=9.5$, 1H), 9.70 (s, 1H), 9.66 (s, 1H), 9.60 (s, 1H), 9.56 (s, 1H), 9.52 (s, 1H), 9.49 – 9.45 (m, 3H), 9.33 (s, 1H), 9.31 (d, $J=8.3$, 1H), 9.23 – 9.20 (m, 2H), 9.11 (s, 1H), 8.83 (s, 1H), 8.19 (d, $J=7.2$, 1H), 8.17 – 8.12 (m, 2H), 8.10 (d, $J=7.4$, 1H), 2.06 (s, 9H), 2.00 (s, 9H), 1.94 (s, 9H), 1.92 (s, 9H), 1.84 (s, 9H), 1.47 (s, 9H), 1.28 (s, 9H); $^{13}\text{C NMR}$ (126 MHz, CD_2Cl_2): $\delta = 202.7$ (C), 150.53 (C), 150.3 (C), 148.9 (C), 143.5 (C), 143.2 (C), 132.5 (C), 132.2 (C), 131.5 (C), 131.3 (C), 131.2 (C), 130.8 (C), 130.0 (C), 129.4 (C), 129.3 (C), 129.3 (C), 129.2 (C), 129.0 (C), 128.7 (C), 128.59 (CH), 128.55 (CH), 128.3 (C), 128.22 (CH), 128.19 (CH), 128.04 (CH), 128.02 (C), 127.99 (CH), 127.9 (C), 127.7 (C), 126.9 (CH), 126.3 (C), 126.1 (C), 125.9 (C), 125.63 (C), 125.58 (CH), 125.3 (C), 124.6 (C), 124.5 (C), 124.2 (CH), 124.1 (C), 123.93 (C), 123.87 (C), 123.8 (C), 123.5 (C), 123.3 (C), 122.3 (C), 121.5 (C), 121.43 (C), 121.2 (C), 120.9 (CH), 120.7 (C), 120.5 (C), 120.10 (C), 119.9 (CH), 119.81 (C), 119.79 (CH), 119.3 (CH), 118.7 (CH), 117.6 (CH), 39.9 (C), 36.3 (C), 36.2 (C), 35.8 (C), 35.52 (CH₃), 35.46 (C), 32.4 (CH₃), 32.3 (CH₃), 32.15 (CH₃), 32.12 (CH₃), 31.9 (CH₃), 31.6 (CH₃). Some carbon signals could not be listed due to the overlapping observed; HR-MS (MALDI DCTB+PPG1000+2000): m/z calc. for $\text{C}_{107}\text{H}_{84}\text{O}$ $[\text{M}]^+$: 1384.6517; found: 1384.6476; IR (ATR): 2953, 1668, 1606, 1462, 1362 cm^{-1} . **194b:** $^{19}\text{F NMR}$ (377 MHz, $(\text{CDCl}_2)_2$): $\delta = -75.19$; HR-MS (MALDI DCTB+PMMANa 2100 + NaI): m/z calc. for $\text{C}_{103}\text{H}_{75}\text{O}_2^+$ $[\text{M} - \text{SO}_2\text{CF}_3]^+$: 1343.5762; found: 1343.5745; IR (ATR): 2953, 1679, 1605, 1460, 1424 cm^{-1} .

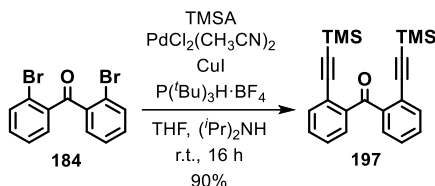
- Compound 195

In a round bottom flask, compound **190** (78 mg, 0.10 mmol), $\text{PdCl}_2(\text{PPh}_3)_2$ (2.00 mg, 3.00 μmol), CuI (1.00 mg, 5.26 μmol) were placed and purged with Ar. Then suspended with THF (5 mL) and Et_3N (5 mL) and bubbled with Ar. *p*-*tert*-Butylphenylacetylene (60 μL , 0.32 mmol) was added dropwise and the reaction mixture stirred at room temperature overnight, then diluted with CH_2Cl_2 (50 mL) and washed with $\text{NH}_4\text{Cl}_{\text{sat}}$ (2×50 mL). The organic layer was separated, dried over anhydrous Na_2SO_4 , filtered and the solvent removed under vacuum. The resulting crude material was purified by flash column chromatography (SiO_2 , hexane/ CH_2Cl_2 , 3:2) giving rise to **195** (81 mg, 99%) as a white solid. ^1H NMR (500 MHz, CD_2Cl_2): δ = 7.43 – 7.32 (m, 8H), 7.21 (dd, $J=8.0$, 1.2, 1H), 7.13 – 6.98 (m, 7H), 6.93 (dd, $J=7.7$, 5.2, 2H), 6.90 – 6.76 (m, 6H), 6.73 (t, $J=7.5$, 1H), 6.47 (d, $J=7.8$, 2H), 6.40 (td, $J=8.5$, 1.0, 2H), 1.30 (s, 9H), 1.17 (s, 9H), 1.15 (s, 9H). ^{13}C NMR (126 MHz, CD_2Cl_2): δ = 200.14 (C), 152.02 (C), 149.21 (C), 149.01 (C), 146.54 (C), 146.53 (C), 142.81 (C), 142.25 (C), 141.72 (C), 141.48 (C), 141.36 (C), 140.79 (C), 138.08 (C), 137.95 (C), 136.35 (C), 136.17 (C), 135.35 (C), 135.32 (C), 133.35 (CH), 133.34 (CH), 132.82 (CH), 132.73 (CH), 132.32 (CH), 132.23 (CH), 131.51 (CH), 131.01 (CH), 130.79 (CH), 130.62 (CH), 130.57 (CH), 130.34 (CH), 129.70 (CH), 128.71 (CH), 127.29 (CH), 127.27 (CH), 126.55 (CH), 125.97 (CH), 125.80 (CH), 124.57 (CH), 124.43 (CH), 123.85 (CH), 123.69 (CH), 120.63 (C), 120.52 (C), 89.46 (C), 89.02 (C), 35.08 (C), 34.53 (C), 34.49 (C), 31.37 (CH_3), 31.34 (CH_3), 31.30 (CH_3). HR-MS (MALDI DCTB+PMMANa600): m/z calc. for $\text{C}_{63}\text{H}_{56}\text{ONa}^+$ $[\text{M}+\text{Na}]^+$: 851.4223; found: 851.4206.

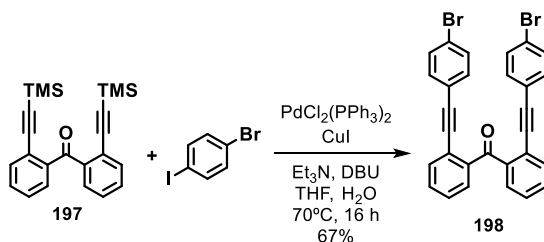
- Compound 196



An equimolar amount of **195** (115 mg, 0.14 mmol) and 2,3,4,5-tetrakis-(*p*-tert-butylphenyl)cyclopentadienone (85 mg, 0.14 mmol) were placed in a Schlenk tube, dissolved in diphenyl ether (1 mL) and bubbled with Ar. The reaction mixture was placed in a sand bath and refluxed for 8 h. The crude material was allowed to cool to room temperature and diluted with hexane (10 mL) and purified by flash column chromatography (SiO₂, hexane/CH₂Cl₂, 3:2) to afford **196** (78 mg, 40%) as a glassy colourless solid. ¹H NMR (500 MHz, CDCl₃): δ = 7.35 (td, *J*=9.1, 7.7, 0.7, 2H), 7.11 (dd, *J*=7.8, 1.1, 2H), 7.08 – 6.99 (m, 4H), 6.98 – 6.87 (m, 3H), 6.86 – 6.65 (m, 18H), 6.60 (m, 6H), 6.51 (d, *J*=7.9, 3H), 6.43 (dd, *J*=8.2, 1.4, 1H), 6.33 (d, *J*=7.9, 1H), 6.28 (d, *J*=8.4, 1H), 6.24 (d, *J*=7.4, 1H), 6.14 (s, 1H), 6.04 (dd, *J*=8.1, 1.6, 1H), 5.81 (dd, *J*=8.2, 1.8, 1H), 1.27 (s, 9H), 1.24 (s, 9H), 1.13 (s, 9H), 1.12 (s, 9H), 1.11 (s, 9H), 1.08 (s, 9H), 1.07 (s, 9H). ¹³C NMR (126 MHz, CDCl₃): δ = 200.66 (C), 148.41 (C), 148.30 (C), 147.64 (C), 147.49 (C), 147.45 (C), 147.43 (C), 147.36 (C), 146.22 (C), 146.10 (C), 142.05 (C), 141.87 (C), 140.99 (C), 140.98 (C), 140.68 (C), 140.62 (C), 140.25 (C), 140.06 (C), 138.80 (C), 138.23 (C), 138.18 (C), 138.07 (C), 137.85 (C), 137.81 (C), 136.96 (C), 136.15 (C), 135.70 (C), 135.60 (C), 135.30 (C), 135.27 (C), 133.28 (CH), 133.13 (CH), 132.67 (CH), 131.28 (CH), 131.20 (CH), 131.16 (CH), 130.87 (CH), 130.64 (CH), 130.28 (CH), 129.25 (CH), 128.34 (CH), 127.15 (CH), 126.78 (CH), 126.74 (CH), 125.52 (CH), 125.42 (CH), 125.24 (CH), 124.19 (CH), 124.16 (CH), 124.03 (CH), 123.85 (CH), 123.31 (CH), 123.21 (CH), 123.12 (CH), 123.08 (CH), 123.03 (CH), 34.42 (C), 34.35 (C), 34.27 (C), 34.24 (C), 34.18 (C), 34.17 (C), 34.13 (C), 31.61 (CH₃), 31.51 (CH₃), 31.36 (CH₃), 31.33 (CH₃). HR-MS (MALDI DCTB + PEGNa 1500): *m/z* calc. for C₁₀₇H₁₀₈ONa⁺ [M+Na]⁺: 1431.8292; found: 1431.8297.

- Compound 197

In a round bottom flask, compound **184** (500 mg, 1.47 mmol), $\text{PdCl}_2(\text{CH}_3\text{CN})_2$ (57 mg, 0.22 mmol), CuI (42 mg, 0.22 mmol) and $\text{P}(\text{tBu})_3\text{H}\cdot\text{BF}_4$ (127 mg, 0.44 mmol) were placed and purged with Ar. The solids were suspended in THF (4 mL), $(i\text{Pr})_2\text{NH}$ (10 mL) was added and the suspension bubbled with Ar. Trimethylsilylacetylene (0.61 mL, 4.41 mmol) was added dropwise and the reaction mixture was stirred at room temperature for 3h. The solvent was removed under reduced pressure, diluted with CH_2Cl_2 (100 mL) and washed with $\text{NH}_4\text{Cl}_{\text{sat}}$ (2×100 mL). The organic layer was dried over anhydrous Na_2SO_4 , filtered and the crude purified by flash column chromatography (SiO_2 , hexane/EtOAc 49:1) affording **197** (497 mg, 90%) as a yellow oil. ^1H NMR (500 MHz, CDCl_3): δ = 7.56 (dd, $J=7.6, 1.4, 2\text{H}$), 7.51 (dd, $J=7.6, 1.4, 2\text{H}$), 7.43 (td, $J=7.5, 1.6, 2\text{H}$), 7.37 (td, $J=7.5, 1.6, 2\text{H}$), 0.04 (s, 18H). ^{13}C NMR (126 MHz, CDCl_3): δ = 196.95 (C), 141.88 (C), 133.88 (CH), 131.04 (CH), 129.90 (CH), 128.38 (CH), 122.67 (C), 102.50 (C), 100.93 (C), -0.13 (CH_3). HR-MS (ESI-TOF): m/z calc. for $\text{C}_{23}\text{H}_{27}\text{OSi}_2^+$ $[\text{M}+\text{H}]^+$: 375.1600; found: 375.1604; IR (ATR): 3069, 2964, 2155, 1667, 840 cm^{-1} .

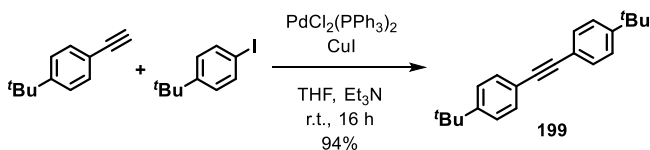
- Compound 198

197, 1-bromo-4-iodobenzene (2.51 g, 8.86 mmol), $\text{PdCl}_2(\text{PPh}_3)_2$ (141 mg, 0.20 mmol) and CuI (77 mg, 0.40 mmol) were placed in a round bottom flask and purged with Ar. Then, THF (32 mL), DBU (10 mL), Et_3N (5 mL) and H_2O (3 mL) were added, and the mixture was heated at 70°C under Ar atmosphere for 16 h. The mixture was diluted with EtOAc (120 mL) and washed with $\text{NH}_4\text{Cl}_{(\text{aq})}$ (2×40 mL) and brine (15 mL), the organic layer was separated, dried over anhydrous Na_2SO_4 and

4. Experimental section

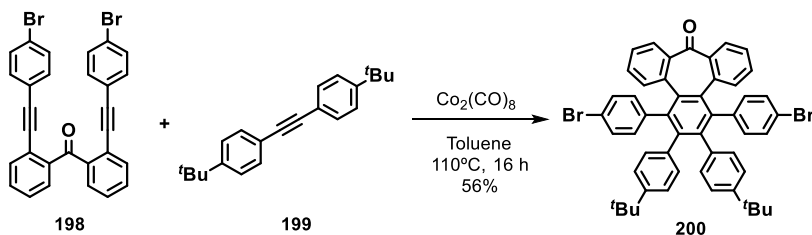
the solvent was removed in the rotavapor. The crude was purified by flash column chromatography (SiO₂, hexane/EtOAc 19:1) affording **198** (1.46 g, 67%) as an orange foam. ¹H NMR (500 MHz, CDCl₃): δ = 7.72 (d, *J*=7.1, 2H), 7.62 (d, *J*=7.1, 2H), 7.48 (m, *J*=7.6, 4H), 7.41 (d, *J*=8.0, 4H), 7.09 (d, *J*=8.0, 4H). ¹³C NMR (126 MHz, CDCl₃): δ = 196.67 (C), 141.14 (C), 133.28 (CH), 133.06 (CH), 133.06 (CH) 131.37 (CH), 131.37 (CH), 131.31 (CH), 130.05 (CH), 128.45 (CH), 122.77 (C), 122.36 (C), 121.70 (C), 94.28 (C), 88.72 (C). HR-MS (ESI-TOF): *m/z* calc. for C₂₉H₁₇OBr₂ [M+H]⁺: 538.9646; found: 538.9641; IR (ATR): 3060, 2960, 2213, 1489, 822 cm⁻¹.

- Compound 199



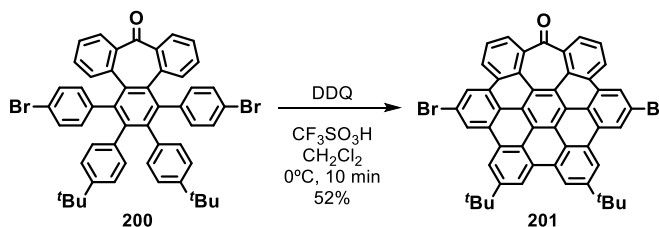
Into a properly degassed and dried round bottom flask, PdCl₂(PPh₃)₂ (40 mg, 0.06 mmol) and CuI (40 mg, 0.20 mmol) were placed and purged with Ar. The solids were suspended in a mixture 1:2 of THF and Et₃N (9 mL) and bubbled with Ar. 4-*tert*-butyl iodobenzene (0.7 mL, 3.95 mmol) was added to the reaction mixture and then 4-*tert*-butylphenylacetylene (0.9 mL, 7.55 mmol) was added dropwise. The reaction mixture was stirred at room temperature for 16 h. The mixture was diluted with CH₂Cl₂ (100 mL) and washed with NH₄Cl_(aq) (2 × 100 mL). The organic layer was separated and dried over anhydrous Na₂SO₄, filtered and the solvent removed under reduced pressure. The crude was purified by flash column chromatography (SiO₂, hexane) giving rise to **199** (1.08 g, 94%) as a white solid. ¹H NMR (300 MHz, CDCl₃): δ = 7.48 (d, *J*=8.1, 4H), 7.38 (d, *J*=8.2, 4H), 1.34 (s, 9H). ¹³C NMR (75 MHz, CD₂Cl₂): δ = 152.00 (C), 131.77 (CH), 125.95 (CH), 120.95 (C), 89.39 (C), 35.21 (C), 31.51 (CH₃).

- Compound 200



Compound **198** (375 mg, 0.70 mmol) and $\text{Co}_2(\text{CO})_8$ (308 mg, 0.90 mmol) were dissolved in dry toluene (7 mL) under Ar atmosphere. The mixture was heated at 110°C and stirred for 30 min. Then, a solution of **199** (305 mg, 1.05 mmol) in degassed dry toluene (4 mL) was added during 30 min and finally the mixture was heated at 110°C for 16 h. The solvent was removed under reduced pressure and the crude material purified by flash column chromatography (SiO_2 , hexane/ CH_2Cl_2 13:7) affording a brown solid. The solid was precipitated in hexane (200 mL) obtaining **200** (325 mg, 56%) as a white solid. ^1H NMR (500 MHz, CDCl_3): δ = 7.44 (d, $J=7.6$, 2H), 7.15 (m, 4H), 7.06 (d, $J=7.9$, 2H), 7.01 (dd, $J=8.4$, 2.1, 4H), 6.98 – 6.83 (m, 4H), 6.71 (d, $J=8.1$, 2H), 6.36 (d, $J=8.4$, 2H), 6.24 (d, $J=8.1$, 2H), 1.11 (s, 18H). ^{13}C NMR (126 MHz, CDCl_3): δ = 200.14 (C), 148.42 (C), 146.04 (C), 143.33 (C), 140.38 (C), 139.80 (C), 136.60 (C), 135.22 (C), 134.50 (C), 134.08 (CH), 133.14 (CH), 132.22 (CH), 131.18 (CH), 130.28 (CH), 129.73 (CH), 129.65 (CH), 128.89 (CH), 127.36 (CH), 124.38 (CH), 123.88 (CH), 122.82 (CH), 119.68 (C), 34.13 (C), 31.11 (CH₃). HR-MS (ESI-TOF): m/z calc. for $\text{C}_{51}\text{H}_{43}\text{Br}_2\text{O}^+$ [$\text{M}+\text{H}$] $^+$: 851.1500; found: 851.1521; IR (ATR): 3028, 2961, 1738, 758 cm^{-1} .

- Compound 201

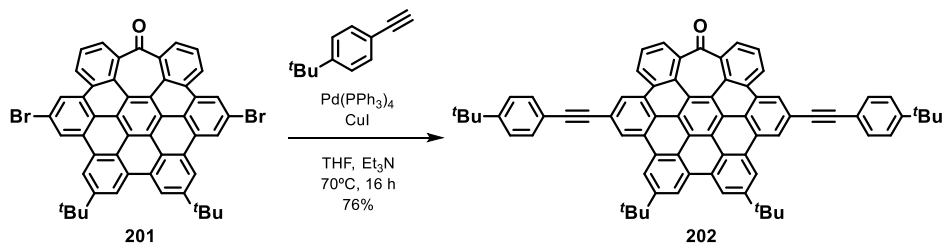


In a round bottom flask, compound **200** (115 mg, 0.14 mmol) and DDQ (173 mg, 0.76 mmol) were dissolved in dry CH_2Cl_2 (5 mL) under Ar atmosphere. The mixture was cooled down to 0°C , then trifluoromethanesulfonic acid (0.25 mL) was added and the mixture stirred at 0°C for 10 min. The mixture was then diluted with CH_2Cl_2 (10 mL) and silica gel was added. The solvent was removed in vacuo and the crude material purified by flash column chromatography (SiO_2 , CH_2Cl_2 /hexane 3:2) affording **201** (59 mg, 52%) as a yellow solid. ^1H NMR (400 MHz, CDCl_3): δ = 9.06 (s, 2H), 8.47 (d, $J=8.0$, 2H), 8.36 (s, 2H), 7.99 (t, $J=7.7$, 2H), 7.85 – 7.67 (m, 6H), 1.91 (s, 18H). ^{13}C NMR (101 MHz, CDCl_3): δ = 202.00 (C), 149.86 (C), 141.73 (C), 130.76 (C), 129.45 (C), 129.03 (C), 128.90 (C), 128.28 (C), 127.40 (CH), 126.69 (CH), 125.05 (CH), 124.33 (CH), 122.85 (C), 122.44 (CH), 122.16 (C), 121.74 (C), 121.49 (C), 121.24 (C), 120.14 (C), 118.99 (CH), 118.92 (CH), 36.05 (C), 32.25

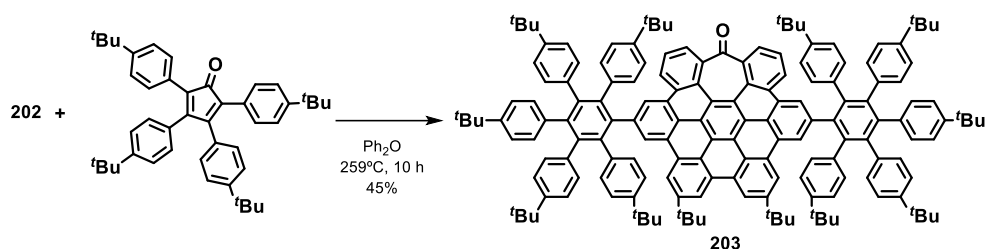
4. Experimental section

(CH₃). HR-MS (ESI-TOF): *m/z* calc. For C₅₁H₃₂Br₂ONa⁺ [M+Na]⁺: 843.0697; found: 843.0708 ; IR (ATR): 3064, 2957, 1681, 1364, 759 cm⁻¹.

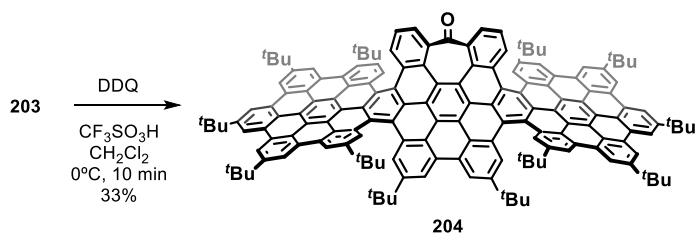
- Compound 202



Compound **201** (235 mg, 0.29 mmol), Pd(PPh₃)₄ (50 mg, 0.04 mmol) and CuI (15 mg, 0.08 mmol) were placed into a round bottom flask, capped properly and purged with Ar. The solids were suspended with a mixture of freshly distilled THF (2 mL) and Et₃N (4 mL) and bubbled with Ar. The reaction mixture was placed at 70°C and 4-*tert*-butylphenylacetylene (0.16 mL, 0.86 mmol) was added dropwise. The reaction mixture was kept at this temperature for 16 h. Once cooled to room temperature, the crude was diluted with CH₂Cl₂ (100 mL) and washed with NH₄Cl_{sat} (2 × 100 mL). The organic layer was separated, dried with anhydrous Na₂SO₄, filtered and the solvent removed at the rotavapor. The crude was purified by flash column chromatography (SiO₂, hexane/CH₂Cl₂, 1:1) affording **202** (212 mg, 76%) as a yellow solid. ¹H NMR (500 MHz, CDCl₃): δ = 9.02 (s, 1H), 8.73 (d, *J*=7.5, 1H), 8.44 (s, 1H), 8.08 (t, *J*=7.6, 1H), 8.00 - 7.86 (m, 4H), 7.81 (d, *J*=7.1, 1H), 7.62 (d, *J*=8.3, 2H), 1.94 (s, 9H), 1.48 (s, 9H). ¹³C NMR (126 MHz, CDCl₃): δ = 202.70 (C), 152.15 (C), 149.49 (C), 141.92 (C), 131.68 (CH), 130.22 (C), 129.01 (C), 128.89 (C), 128.80 (C), 127.30 (CH), 127.28 (CH), 126.91 (C), 125.95 (CH), 124.82 (CH), 124.79 (CH), 123.17 (C), 122.93 (CH), 121.52 (C), 121.46 (C), 121.36 (C), 120.56 (C), 119.85 (CH), 119.27 (C), 118.87 (CH), 91.42 (C), 90.48 (C), 36.00 (C), 35.17 (C), 32.41 (CH₃), 31.47 (CH₃). HR-MS (ESI-TOF): *m/z* calc. for C₇₅H₅₈ONa⁺ [M+Na]⁺ : 997.4385; found: 997.4358; IR (ATR): 2955, 1679, 1363, 832 cm⁻¹.

- Compound 203

Compound **202** (212 mg, 0.22 mmol) and 2,3,4,5-tetrakis-(*p*-*tert*-butyl)phenylcyclopentadienone (265 mg, 0.43 mmol) were placed into a Schlenk tube and dissolved with Ph₂O (2 mL). The reaction mixture was placed into a sand bath and heated to reflux for 10 h. The crude material was purified by flash column chromatography (SiO₂, hexane/CH₂Cl₂ 3:2) affording **203** (210 mg, 45%) as a yellow solid. ¹H NMR (400 MHz, CD₂Cl₂): δ = 9.06 (s, 1H), 8.50 (s, 1H), 8.39 (s, 1H), 8.36 – 8.28 (m, 2H), 7.75 – 7.68 (m, 2H), 6.98 – 6.69 (m, 20H), 1.70 (s, 9H), 1.16 – 1.11 (m, 27H), 0.71 (s, 18H). ¹³C NMR (101 MHz, CD₂Cl₂): δ = 202.67 (C), 150.28 (C), 148.62 (C), 148.40 (C), 142.56 (C), 141.71 (C), 141.45 (C), 141.18 (C), 140.21 (C), 140.05 (C), 138.41 (C), 138.39 (C), 131.63 (CH), 131.61 (CH), 131.59 (CH), 131.51 (CH), 131.46 (CH), 131.43 (CH), 130.22 (C), 130.14 (C), 128.98 (C), 128.13 (CH), 127.62 (CH), 127.52 (C), 127.42 (C), 126.78 (CH), 125.86 (CH), 124.97 (C), 124.04 (CH), 123.91 (CH), 123.70 (CH), 123.35 (C), 122.76 (C), 122.73 (C), 121.31 (C), 119.52 (CH), 118.74 (CH), 35.95 (C), 34.43 (C), 34.16 (C), 32.11 (CH₃), 31.35 (CH₃), 30.96 (CH₃). HR-MS (ESI-TOF): *m/z* calc. for C₁₆₃H₁₆₃O⁺ [M+H]⁺: 2136.2698; found: 2136.2722; IR (ATR): 2959, 2903, 1682, 1362, 831 cm⁻¹.

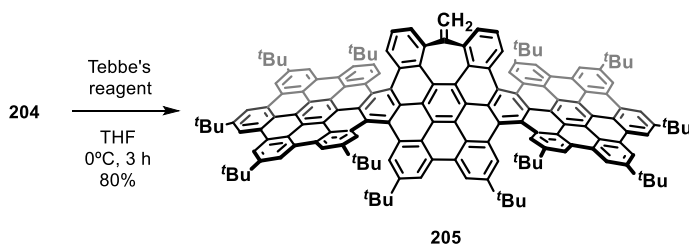
- Compound 204

Compound **203** (105 mg, 0.05 mmol) and DDQ (161 mg, 0.71 mmol) were placed into a round bottom flask, capped properly and purged with Ar. The solids were suspended with dry CH₂Cl₂ (6

4. Experimental section

mL) and the mixture placed into an ice-water bath at 0°C. Then, CF₃SO₃H (0.15 mL) was added dropwise and the reaction mixture stirred at 0°C during 10 min. Silica gel was added to the mixture and the solvent removed under vacuum. The crude was purified by flash column chromatography (SiO₂, CH₂Cl₂/hexane 4:1) affording **204** (34mg, 33%) as a dark red solid. ¹H NMR (500 MHz, C₄D₈O): δ = 9.88 (s, 1H), 9.86 (s, 1H), 9.81 (s, 1H), 9.56 – 9.50 (m, 5H), 9.48 (s, 1H), 9.41 (s, 1H), 9.39 (s, 1H), 9.32 – 9.26 (m, 2H), 7.81 (dd, *J*=7.1, 1.3, 1H), 7.55 (dd, *J*=8.6, 7.2, 1H), 1.92 (s, 9H), 1.90 (s, 9H), 1.88 (s, 9H), 1.59 (s, 9H), 1.55 (s, 9H), 1.38 (s, 9H). ¹³C NMR (126 MHz, C₄D₈O): δ = 200.29 (C), 150.55 (C), 150.39 (C), 150.34 (C), 149.76 (C), 149.52 (C), 149.44 (C), 144.62 (C), 135.23 (C), 132.19 (C), 132.11 (CH), 131.83 (C), 131.63 (C), 131.58 (C), 131.55 (C), 131.37 (C), 131.25 (C), 131.11 (C), 130.80 (C), 128.69 (CH), 128.31 (CH), 127.97 (CH), 127.68 (C), 127.28 (C), 127.25 (C), 127.02 (C), 126.98 (C), 126.87 (C), 126.71 (C), 125.90 (CH), 125.55 (CH), 124.87 (C), 124.72 (C), 124.59 (C), 124.47 (C), 124.35 (C), 124.00 (C), 123.71 (C), 122.61 (C), 121.94 (C), 121.75 (C), 121.65 (C), 121.56 (C), 121.49 (C), 121.24 (CH), 120.85 (CH), 120.26 (CH), 120.13 (CH), 120.09 (CH), 119.97 (CH), 119.23 (C), 36.42 (C), 36.39 (C), 36.35 (C), 36.09 (C), 35.79 (C), 32.10 (CH₃), 32.06 (CH₃), 31.85 (CH₃), 31.66 (CH₃). HR-MS (ESI-TOF): *m/z* calc. for C₁₆₃H₁₃₉O⁺ [M+H]⁺: 2112.0820; found: 2112.0857; IR (ATR): 2953, 2864, 1681, 1362, 869 cm⁻¹.

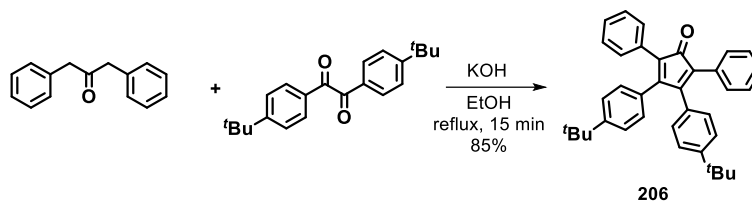
- Compound 205



Compound **204** (30 mg, 0.014 mmol) was dissolved in freshly distilled THF (5 mL) in a flame dried round bottom flask, cooled down to 0°C in an ice-water bath. Then, Tebbe's reagent solution 0.5 M (0.15 mL, 0.075 mmol) was added dropwise to the solution. The reaction mixture was stirred for 3 h at room temperature before being quenched with NaOH 1 M (5 mL). The reaction mixture was diluted with CH₂Cl₂ (50 mL) and washed with NaOH 1 M (2 × 50 mL), the organic layer was separated, dried over Na₂SO₄, filtered and the solvent removed under reduced pressure. The crude was purified by flash column chromatography (SiO₂, hexane/CH₂Cl₂, 3:2) affording **205** (24

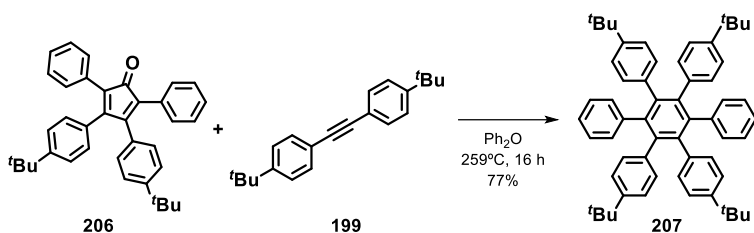
mg, 80%) as a dark red solid. ^1H NMR (500 MHz, $\text{C}_4\text{D}_8\text{O}$): δ = 9.88 (s, 1H), 9.86 (s, 1H), 9.80 (s, 1H), 9.54 – 9.48 (m, 5H), 9.46 (s, 1H), 9.40 (s, 1H), 9.36 (s, 1H), 9.26 (s, 1H), 9.06 (d, $J=8.8$, 1H), 7.58 (d, $J=7.0$, 1H), 7.46 – 7.42 (m, 1H), 5.12 (s, 1H), 1.91 (s, 9H), 1.89 (s, 9H), 1.87 (s, 9H), 1.60 (s, 9H), 1.53 (s, 9H), 1.37 (s, 9H). ^{13}C HSQC and ^{13}C HMBC (126 MHz, $\text{C}_4\text{D}_8\text{O}$): δ = 150.33 (C), 150.31 (C), 149.58 (C), 149.28 (C), 149.16 (C), 145.48 (C), 135.25 (C), 131.69, 128.19 (C), 127.72, 126.93, 124.62, 124.50, 124.39, 124.33, 124.14, 124.01, 123.91, 123.69, 121.05, 120.18, 120.03, 119.83, 119.79 (CH), 36.36 (C), 36.29 (C), 36.09 (C), 36.02 (C), 35.74 (C), 31.71 (CH_3), 31.63 (CH_3), 31.48 (CH_3), 31.32 (CH_3), 31.30 (CH_3). HR-MS (ESI-TOF): m/z calc. For $\text{C}_{164}\text{H}_{141}$ $[\text{M}+\text{H}]^+$: 2110.1033; found: 2110.1011; IR (ATR): 2921, 2855, 1362, 870 cm^{-1} .

- Compound 206

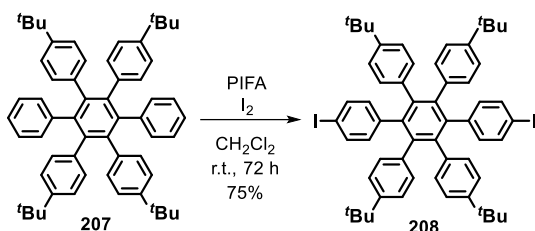


Procedure modified from literature.⁶ In a round bottom flask were placed 1,3-*bis*-phenyl-2-propanone (290 mg, 1.39 mmol) and 1,2-*bis*-(*p*-*tert*-butyl)phenylethane-1,2-dione (450 mg, 1.39 mmol) and dissolved with EtOH absolute (10 mL). The reaction mixture was heated to reflux and then a KOH 2 M solution in EtOH absolute (0.5 mL) was added. The reaction mixture was refluxed for 15 min and then cooled to 0°C. The solid is filtered affording **206** (600 mg, 85%) as a deep purple solid. The obtained spectroscopic data is in concordance with that reported in bibliography.²⁵⁴

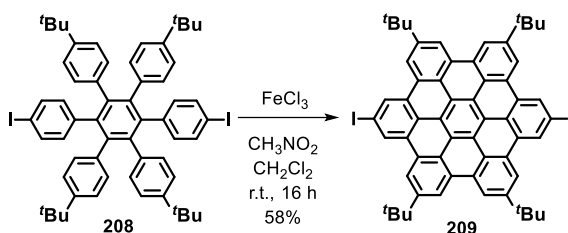
²⁵⁴ M. M. Martin, D. Lungerich, P. Haines, F. Hampel, N. Jux, *Angew. Chem. Int. Ed.* **2019**, *58*, 8932-8937.

- Compound 207

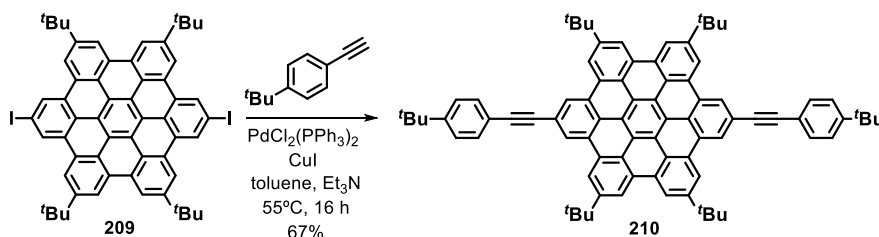
An equimolar amount of **206** (120 mg, 0.24 mmol) and **199** (70 mg, 0.24 mmol) were placed in a Schlenk tube, dissolved in diphenyl ether (2 mL) and bubbled with Ar. The reaction mixture was placed in a sand bath and refluxed for 16 h. The crude material was allowed to cool to room temperature and diluted with hexane (10 mL) and purified by flash column chromatography (SiO_2 , hexane) to afford **207** (146 mg, 77%) as a white solid. The obtained spectroscopic data is in concordance with that reported in bibliography.²⁵⁴

- Compound 208

Compound **207** (120 mg, 0.16 mmol) was dissolved in CH_2Cl_2 (10 mL) and degassed with Ar. PIFA (172 mg, 0.40 mmol) and iodine (102 mg, 0.40 mmol) were added and the mixture was stirred for 72 h at r.t. without light exposure. The reaction mixture was washed with 10% $\text{Na}_2\text{S}_2\text{O}_3$ solution (20 mL) and dried over anhydrous Na_2SO_4 . After removal of the solvent, the residue was purified by flash column chromatography (SiO_2 , hexane) affording **208** (121 mg, 75%) as a white solid. The obtained spectroscopic data is in concordance with that reported in bibliography.²⁵⁴

- Compound 209

Compound **208** (40 mg, 40 μmol) was dissolved in CH_2Cl_2 (20 mL) and degassed via bubbling Ar through the solution for 15 min. A solution of dry FeCl_3 (206 mg, 1.27 mmol) in CH_3NO_2 (0.6 mL) was added and the Ar bubbling was maintained for further 30 min. The reaction was stirred for 16 h at r.t., quenched via the addition of MeOH (20 mL) and the solvent removed under vacuum. The residue was purified by flash column chromatography (SiO_2 , hexane/ CH_2Cl_2 , 8:2) giving rise to **209** (23 mg, 58%) as a pale yellow solid. The obtained spectroscopic data is in concordance with that reported in bibliography.²⁵⁴

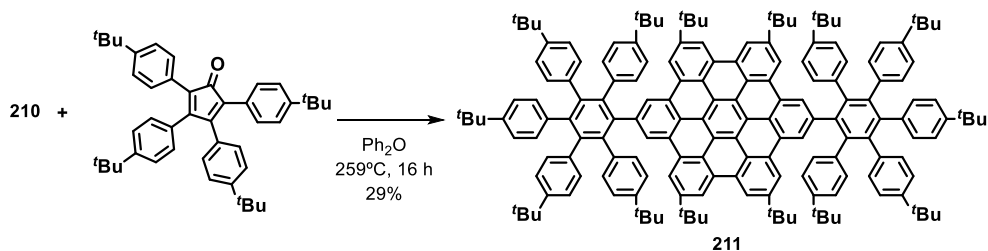
- Compound 210

Compound **209** (70 mg, 0.07 mmol), $\text{PdCl}_2(\text{PPh}_3)_2$ (7 mg, 0.01 mmol) and CuI (2 mg, 0.01 mmol) were dissolved in dry toluene (5 mL) under an Ar atmosphere. The resulting solution was heated to 50°C and NEt_3 (1.25 mL) was added. After 10 min, a solution of *p-tert*-butylphenylacetylene (133 mg, 0.84 mmol) in dry toluene (2 mL) was added slowly for 1 h. The reaction was heated to 55°C and stirred for 16 h. The mixture was diluted with CH_2Cl_2 (60 mL) and washed with $\text{NH}_4\text{Cl}_{\text{aq}}$ (15 mL) and brine (15 mL), the organic layer was separated and dried with anhydrous Na_2SO_4 and the solvent removed under reduced pressure. The crude was purified by flash column chromatography (SiO_2 , CH_2Cl_2 /hexane, 9:1) affording **210** (50 mg, 67%) as a yellow solid; $^1\text{H NMR}$ (400 MHz, CD_3Cl): $\delta = 9.00$ (s, 4H), 8.66 (s, 4H), 8.59 (s, 4H), 7.95 (d, $J=8.2$, 4H), 7.66 (d, $J=8.3$, 4H),

4. Experimental section

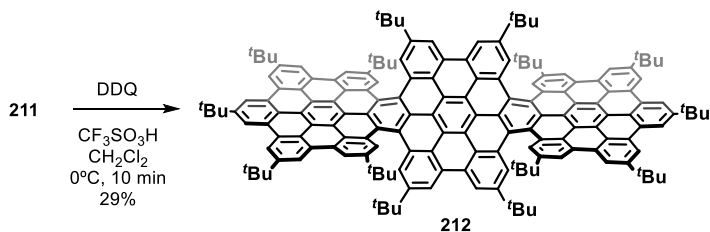
2.00 (s, 36H), 1.52 (s, 18H). HR-MS (ESI-TOF): m/z calc. for $C_{82}H_{75}$ $[M+H]^+$: 1059,5869; found 1059,5817. IR (ATR): 2960, 2921, 1363, 833 cm^{-1} .

- Compound 211



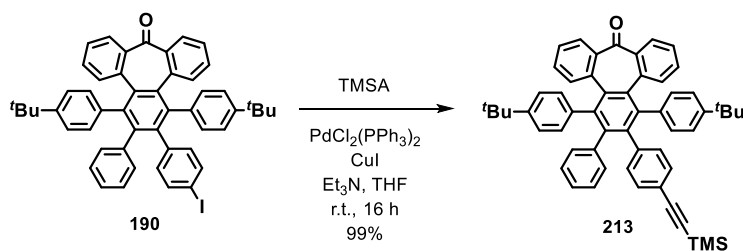
In a 50 mL Schlenk tube, **210** (50 mg, 0.05 mmol) and 2,3,4,5-tetrakis-(*p*-*tert*-butyl-phenyl)-cyclopentadienone (86 mg, 0.14 mmol) were dissolved in Ph_2O (2 mL) under inert atmosphere. The resulting solution was heated to $250^\circ C$ for 16 h. The crude was diluted with hexane and purified by flash column chromatography (SiO_2 , hexane/ CH_2Cl_2 , 17:3) affording **211** (30mg, 29%) as a white solid. 1H NMR (400 MHz, $CDCl_3$): δ = 9.11 (s, 4H), 8.73 (s, 4H), 8.70 (s, 4H), 7.00 (d, $J=8.1$, 8H), 6.94 – 6.79 (m, 24H), 6.75 (d, $J=8.2$, 8H), 1.72 (s, 36H), 1.17 (s, 18H), 1.15 (s, 36H), 0.68 (s, 36H). ^{13}C NMR (101 MHz, $CDCl_3$): δ = 148.67 (C), 147.99 (C), 147.77 (C), 141.43 (C), 141.28 (C), 141.12 (C), 140.66 (C), 138.94 (C), 138.24 (C), 138.15 (C), 138.11 (C), 131.50 (CH), 131.42 (CH), 131.37 (CH), 130.49 (C), 130.31 (C), 129.34 (C), 126.69 (CH), 123.78 (CH), 123.67 (C), 123.37 (CH), 123.28 (C), 120.63 (C), 120.60 (C), 119.02 (CH), 118.22 (CH), 35.76 (C), 34.28 (C), 34.01 (C), 32.25 (C), 31.40 (CH_3), 30.91 (CH_3), 25.64 (C), 22.83 (CH_3). HR-MS (ESI-TOF): m/z calc. for $C_{170}H_{179}$ $[M+H]^+$: 2220,4007; found: 2220,3992. IR (ATR): 2957, 1738, 1363, 831 cm^{-1} .

- Compound 212



In a round bottom flask, compound **211** (30mg, 0.014 mmol) and DDQ (40mg, 0.18 mmol) were dissolved in dry CH_2Cl_2 (5 mL) under inert atmosphere. The mixture was cooled to 0°C , then trifluoromethanesulfonic acid (0.15 mL) was added and the mixture was allowed to warm to room temperature and stirred for 10min. The mixture was diluted with CH_2Cl_2 (40 mL) and washed with $\text{NaHCO}_3(\text{aq})$ (2×15 mL) and brine (15 mL), the organic layer was separated and dried with anhydrous Na_2SO_4 and the solvent was removed under reduced pressure. The crude was purified by column chromatography (SiO_2 , hexane/ CH_2Cl_2 , 9:1) affording **212** (5 mg, 16 %) as a red solid. ^1H NMR A (600 MHz, $\text{THF}-d_8$): $\delta = 9.68$ (s, 4H), 9.57 (s, 4H), 9.54 (s, 4H), 9.53 (s, 4H), 9.49 (s, 4H), 9.35 (s, 4H), 9.33 (s, 4H), 1.91 (s, 18H), 1.90 (s, 36H), 1.46 (s, 36H), 1.41 (s, 36H). ^1H NMR B (600 MHz, $\text{THF}-d_8$): $\delta = 9.71$ (s, 4H), 9.60 (s, 4H), 9.54 (s, 8H), 9.52 (s, 4H), 9.38 (s, 8H), 1.91 (s, 54H), 1.50 (s, 36H), 1.44 (s, 36H). $^1\text{H}-^{13}\text{C}$ HSQC (151 MHz, $\text{THF}-d_8$): $\delta = 131.21$ (CH), 131.50 (CH), 123.70 (CH), 123.64 (CH), 124.31 (CH), 35.81 (C), 35.51 (C), 35.46 (C). HR-MS (ESI-TOF): m/z calc. for $\text{C}_{170}\text{H}_{155}$ $[\text{M}+\text{H}]^+$: 2196,2129; found: 2196,2068. IR (ATR): 2957, 1720, 1260, 727 cm^{-1} .

- Compound 213

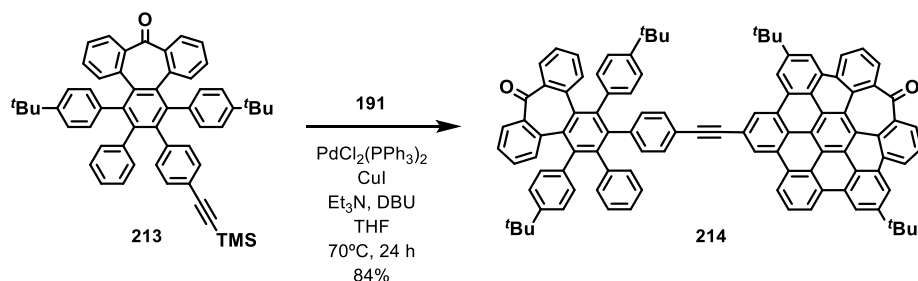


Trimethylsilylacetylene (53 μL , 0.38 mmol) was added dropwise to a degassed suspension of **190** (100 mg, 0.125 mmol), $\text{PdCl}_2(\text{PPh}_3)_2$ (20 mg, 0.028 mmol), CuI (5 mg, 0.028 mmol) in a mixture of $\text{THF}/\text{Et}_3\text{N}$ (1:2, 9 mL). The reaction was stirred at room temperature for 16 h. The mixture was diluted with CH_2Cl_2 (50 mL) and washed with $\text{NH}_4\text{Cl}(\text{aq})$ (2×50 mL) the organic layer was separated and dried over anhydrous Na_2SO_4 and the solvent was removed under reduced pressure. The crude was purified by flash column chromatography (SiO_2 , hexane/ CH_2Cl_2 , 7:3) affording **33** (95 mg, 99%) as a white solid. M. p.: $301-302^\circ\text{C}$. ^1H NMR (500 MHz, CDCl_3): $\delta = 7.39 - 7.37$ (m, 2H), 7.33 - 7.28 (m, 2H), 7.14 (dd, $J=7.9, 1.5$, 1H), 7.08 - 7.03 (m, 2H), 7.02 - 6.96 (m, 3H), 6.96 - 6.88 (m, 3H), 6.82 - 6.72 (m, 7H), 6.68 - 6.64 (m, 1H), 6.39 - 6.33 (m, 4H), 1.16 (s, 9H), 1.12 (s, 9H), 0.17 (s, 9H). ^{13}C NMR (126 MHz, CDCl_3): $\delta = 200.5$ (C), 148.7 (C), 148.5 (C), 146.2 (C), 142.7 (C),

4. Experimental section

141.9 (C), 141.6 (C), 141.3 (C), 141.2 (C), 140.2 (C), 137.5 (C), 137.4 (C), 136.0 (C), 135.9 (C), 135.10 (C), 135.07 (C), 133.2 (CH), 133.1 (CH), 132.3 (CH), 132.2 (CH), 131.63 (CH), 131.58 (CH), 130.9 (CH), 130.53 (CH), 130.46 (CH), 130.4 (CH), 130.3 (CH), 129.9 (CH), 128.45 (CH), 128.42 (CH), 127.2 (CH), 127.0 (CH), 126.9 (CH), 126.2 (CH), 125.7 (CH), 124.33 (CH), 124.32 (CH), 124.1 (CH), 123.6 (CH), 123.4 (CH), 119.9 (C), 105.7 (C), 93.3 (C), 34.4 (C), 34.3 (C), 31.34 (CH₃), 31.32 (CH₃), 0.1 (CH₃). HR-MS (MALDI-TOF DCTB+PPGNa790): m/z calc. for C₅₆H₅₂OSi [M]⁺: 768.3782; found: 768.3757; IR (ATR): 2960, 2160, 1680, 1594 cm⁻¹.

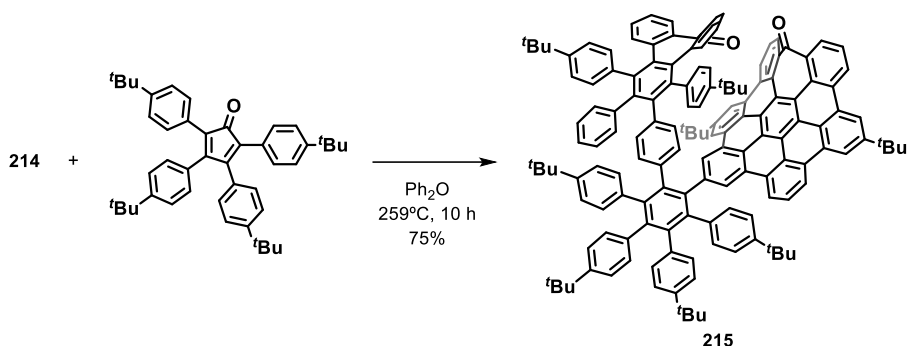
- Compound 214



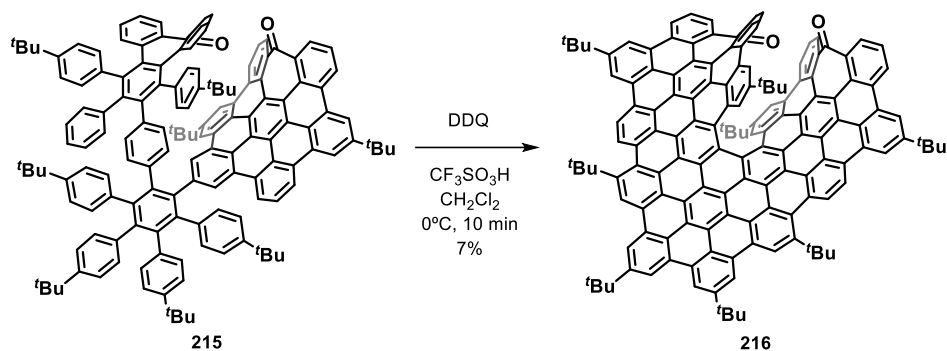
An equimolar amount of **213** (112 mg, 0.146 mmol) and **191** (115 mg, 0.146 mmol), PdCl₂(PPh₃)₂ (10 mg, 0.014 mmol) and CuI (5 mg, 0.028 mmol) were placed into a 25 mL round bottom flask, capped properly and purged with Ar. Then freshly distilled THF (6 mL), Et₃N (0.1 mL) and DBU (0.2 mL) were added and the suspension was bubbled with Ar. Finally, H₂O (3 drops) was added and the mixture was stirred at reflux for 24 h. The crude was diluted with CH₂Cl₂ (50 mL) and washed with NH₄Cl_(aq) (2 × 50 mL) the organic layer was separated and dried over anhydrous Na₂SO₄ and the solvent was removed under reduced pressure. The crude was purified by flash column chromatography (SiO₂, hexane/CH₂Cl₂, 1:1) affording **214** (80 mg, 84%) as a yellow solid. M. p. > 300°C. ¹H NMR (400 MHz, CD₂Cl₂): δ = 8.73–8.63 (m, 5H), 8.50 (s, 1H), 8.44 (s, 1H), 8.22 (d, *J* = 7.9, 1H), 8.06 (s, 1H), 8.01 (d, *J* = 8.0, 1H), 7.82–7.76 (m, 2H), 7.66–7.56 (m, 4H), 7.48–7.43 (m, 2H), 7.37 (dd, *J* = 7.9, 0.8, 1H), 7.32–7.15 (m, 7H), 7.10 (dd, *J* = 8.2, 1.5, 1H), 7.07–6.97 (m, 5H), 6.95–6.84 (m, 4H), 6.70 (dd, *J* = 7.9, 0.9, 1H), 6.65 (d, *J* = 7.7, 1H), 6.59 (dd, *J* = 8.2, 1.2, 1H), 6.52 (dd, *J* = 8.2, 1.3, 1H), 1.68 (s, 9H), 1.62 (s, 9H), 1.24 (s, 9H), 1.23 (s, 9H). ¹³C NMR (126 MHz, CD₂Cl₂): δ = 202.8 (C), 200.2 (C), 150.2 (C), 149.9 (C), 149.3 (C), 149.1 (C), 146.6 (C), 142.9 (C), 142.6 (C), 142.3 (C), 141.8 (C), 141.7 (C), 141.5 (C), 140.9 (C), 138.1 (C), 136.5 (C), 136.3 (C), 135.39 (C), 135.35 (C),

133.40 (CH), 133.36 (CH), 132.9 (CH), 132.4 (CH), 132.3 (CH), 131.5 (C), 131.3 (C), 131.1 (CH), 130.94 (CH), 130.88 (CH), 130.8 (CH), 130.6 (CH), 130.1 (CH), 129.7 (C), 129.5 (C), 129.3 (C), 129.0 (C), 128.8 (CH), 128.6 (C), 128.44 (C), 128.42 (C), 127.7 (CH), 127.6 (CH), 127.5 (CH), 127.3 (CH), 127.0 (CH), 126.7 (CH), 126.5 (CH), 126.4 (CH), 126.1 (CH), 125.1 (C), 124.8 (CH), 124.5 (CH), 124.2 (CH), 124.12 (CH), 124.09 (CH), 124.0 (CH), 123.9 (CH), 123.79 (C), 123.76 (CH), 123.5 (C), 123.2 (C), 123.02 (C), 122.96 (C), 122.8 (C), 121.9 (CH), 121.7 (C), 121.11 (CH), 121.09 (CH), 121.0 (CH), 120.6 (C), 120.5 (CH), 120.3 (C), 118.9 (CH), 118.7 (C), 90.6 (C), 90.2 (C), 35.9 (C), 35.8 (C), 34.6 (C), 34.5 (C), 32.0 (CH₃), 32.0 (CH₃), 31.5 (CH₃), 31.4 (CH₃). HR-MS (MALDI-TOF DCTB+PEGNa1500): m/z calc. for C₁₀₄H₇₆O₂ [M]⁺: 1356.5840; found: 1356.5874. IR (ATR): 2954, 1732, 1681, 1591 cm⁻¹.

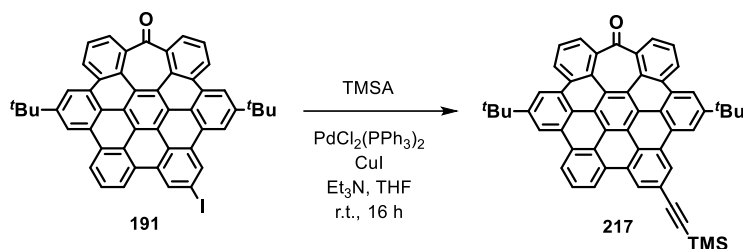
- Compound 215



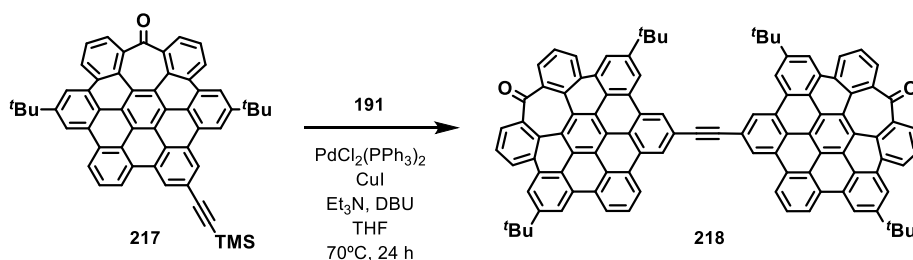
An equimolar amount of **214** (100 mg, 0.074 mmol) and 2,3,4,5-tetrakis(*p*-*tert*-butylphenyl)-cyclopentadienone (45 mg, 0.074) were placed into a Schlenk tube and dissolved in Ph₂O (2 mL). The reaction mixture was placed into a sand bath and heated to reflux over 10 h. The crude was purified by flash column chromatography (SiO₂, hexane/CH₂Cl₂, 1:1) affording **215** (108 mg, 75%) as a yellow solid. M. p. > 300°C. ¹H and ¹³C NMR signals were not listed, the obtained spectra is quite complex due to a mixture of atropisomers. HR-MS (MALDI-TOF DCTB+PEGMeNa2000): m/z calc. for C₁₄₈H₁₂₈O₂ [M]⁺: 1936.9909; found: 1936.9943. IR (ATR): 2959, 2906, 2865, 1681 cm⁻¹.

- Compound 216

A solution of compound **215** (38 mg, 0.02 mmol) and DDQ (60 mg, 0.264 mmol) in dry CH_2Cl_2 (5 mL) was cooled to 0 – 4°C in an ice-water bath, then trifluoromethanesulfonic acid was added (0.15 mL, 1.96 mmol) and the mixture was stirred for 10 min. The solution was diluted with CH_2Cl_2 (3 mL) and silica gel was added. The solvent was removed under vacuum and the crude was purified by flash column chromatography (SiO_2 , hexane/ CH_2Cl_2 , 3:7) affording **216** (2.7 mg, 7%) as a dark red solid. $[\alpha]_D^{25} = -5695^\circ$ (c 1.72×10^{-3} , CH_2Cl_2) (*M*)-1. ^1H NMR (500 MHz, CD_2Cl_2): $\delta = 10.40$ (s, 1H), 9.96 (d, $J=8.6$, 1H), 9.93 (s, 1H), 9.84 (s, 1H), 9.80 (d, $J=8.6$, 1H), 9.60 (s, 1H), 9.32 (d, $J=7.6$, 1H), 9.24 (s, 1H), 8.30 (s, 1H), 8.24 (d, $J=7.2$, 1H), 8.19–8.11 (m, 3H), 7.96 (t, $J=7.5$, 2H), 7.82 (s, 1H), 2.22 (s, 9H), 2.08 (s, 9H), 1.83 (s, 9H), 0.01 (s, 9H). ^{13}C NMR (126 MHz, CD_2Cl_2): $\delta = 203.3$ (C), 150.70 (C), 150.67 (C), 148.5 (C), 147.7 (C), 143.8 (C), 142.8 (C), 133.4 (CH), 132.6 (C), 131.7 (C), 130.9 (C), 130.8 (C), 129.9 (CH), 129.3 (C), 129.24 (C), 129.16 (C), 128.6 (C), 128.4 (C), 128.2 (C), 128.1 (CH), 128.0 (CH), 126.9 (C), 126.8 (C), 126.6 (C), 126.2 (CH), 125.7 (C), 125.5 (C), 125.4 (C), 125.1 (CH), 125.0 (CH), 124.8 (C), 124.5 (C), 124.4 (C), 124.2 (CH), 123.7 (C), 123.5 (C), 123.1 (CH), 122.73 (C), 122.65 (C), 122.3 (C), 122.1 (C), 121.8 (C), 121.6 (C), 120.8 (C), 120.7 (C), 120.69 (CH), 120.6 (C), 120.4 (CH), 120.0 (CH), 119.4 (CH), 118.8 (CH), 117.6 (CH), 40.1 (C), 36.6 (C), 36.2 (C), 35.7 (CH_3), 34.3 (C), 32.5 (CH_3), 32.1 (CH_3), 30.3 (CH_3). HR-MS (MALDI-TOF DCTB+PPGNa2000): m/z calc. for $\text{C}_{148}\text{H}_{102}\text{O}_2$ [M] $^+$: 1910.7874; found: 1910.7810. IR (ATR): 2955, 2921, 2852, 1660, 1633 cm^{-1} .

- Compound 217

Trimethylsilylacetylene (53 μL , 0.38 mmol) was added dropwise to a degassed suspension of **191** (172 mg, 0.218 mmol), $\text{PdCl}_2(\text{PPh}_3)_2$ (20 mg, 0.028 mmol), CuI (5 mg, 0.028 mmol) in a mixture of $\text{THF}/\text{Et}_3\text{N}$ (1:2, 9 mL). The reaction was stirred at room temperature for 16 h. The mixture was diluted with CH_2Cl_2 (50 mL) and washed with $\text{NH}_4\text{Cl}_{(\text{aq})}$ (2×50 mL) the organic layer was separated and dried over anhydrous Na_2SO_4 and the solvent was removed under reduced pressure. The crude was directly used in the next reaction, however, purification could be done by flash column chromatography (SiO_2 , hexane/ CH_2Cl_2 , 6:4) affording **217** as a yellow solid.

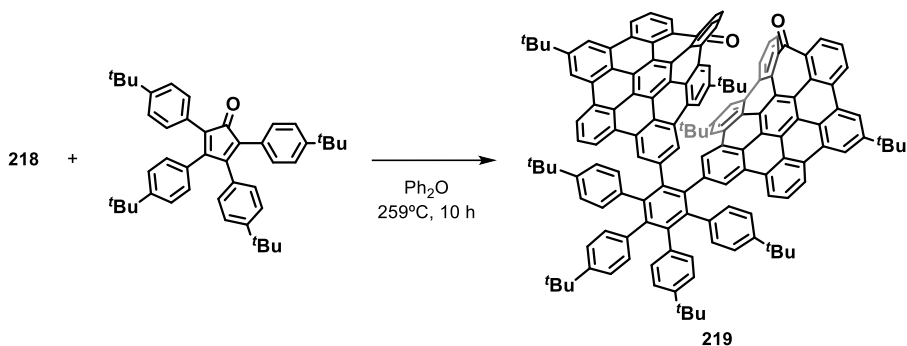
- Compound 218

An equimolar amount of **217** (112 mg, 0.146 mmol) and **191** (115 mg, 0.146 mmol), $\text{PdCl}_2(\text{PPh}_3)_2$ (10 mg, 0.014 mmol) and CuI (5 mg, 0.028 mmol) were placed into a 25 mL round bottom flask, capped properly and purged with Ar. Then freshly distilled THF (6 mL), Et_3N (0.1 mL) and DBU (0.2 mL) were added and the suspension was bubbled with Ar. Finally, H_2O (3 drops) was added and the mixture was stirred at 70°C for 24 h. The crude was diluted with CH_2Cl_2 (50 mL) and washed with $\text{NH}_4\text{Cl}_{(\text{aq})}$ (2×50 mL) the organic layer was separated and dried over anhydrous Na_2SO_4 and the solvent was removed under reduced pressure. The crude was used without further

4. Experimental section

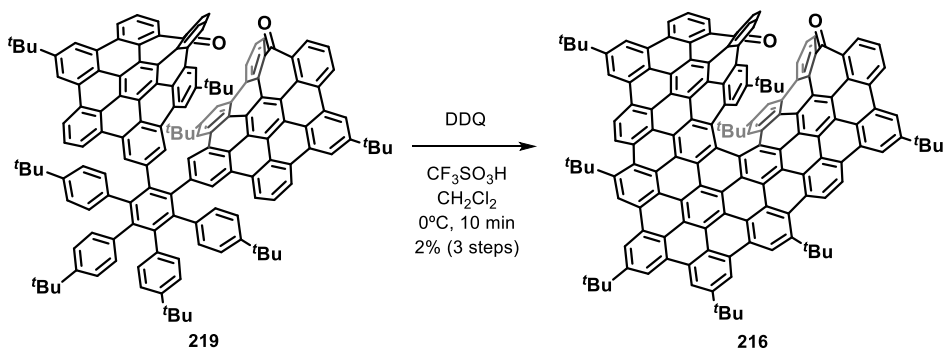
purification due to its low solubility. HR-MS (MALDI-TOF DCTB+PEGNa1500): m/z calc. for $C_{104}H_{66}O_2$ $[M]^+$: 1346.5057; found: 1346.5050.

- Compound 219



An equimolar amount of **218** (150 mg, 0.111 mmol) and 2,3,4,5-*tetrakis*-(*p*-*tert*-butyl-phenyl)-cyclopentadienone (68 mg, 0.111) were placed into a Schlenk tube and dissolved in Ph_2O (2 mL). The reaction mixture was placed into a sand bath and heated to reflux over 10 h. The crude was purified by flash column chromatography (SiO_2 , hexane/ CH_2Cl_2 , 1:1) affording **219** as a yellow solid. 1H and ^{13}C NMR signals were not listed, the obtained spectra is quite complex.

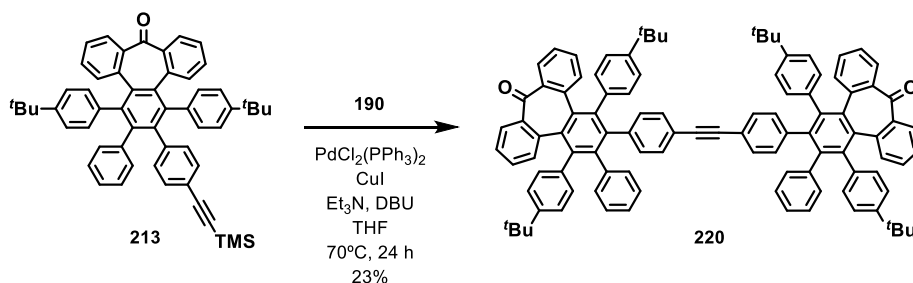
- Compound 216 (from 219)



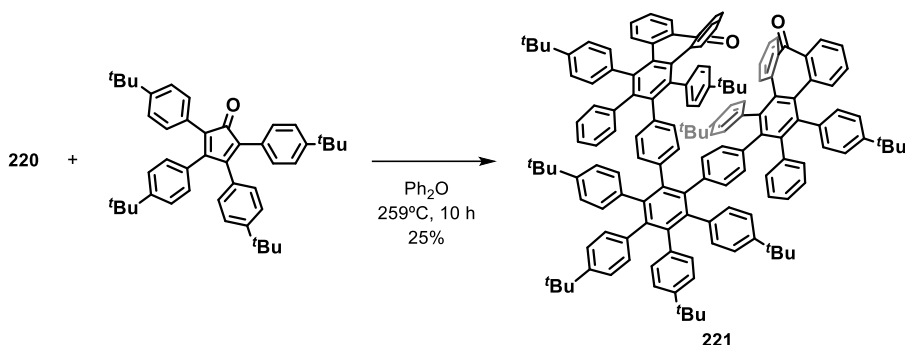
A solution of compound **219** (30 mg, 0.016 mmol) and DDQ (32 mg, 0.137 mmol) in dry CH_2Cl_2 (5 mL) was cooled to $0 - 4^\circ C$ in an ice-water bath, then trifluoromethanesulfonic acid was added (0.15 mL, 1.96 mmol) and the mixture was stirred at this temperature for 10 min. The solution was diluted with CH_2Cl_2 (3 mL) and silica gel was added. The solvent was removed under vacuum

and the crude was purified by flash column chromatography (SiO₂, hexane/CH₂Cl₂, 3:7) affording **216** (5 mg, 16%, 2% for the last 3 steps) as a dark red solid. The spectroscopic data obtained matched with that previously obtained.

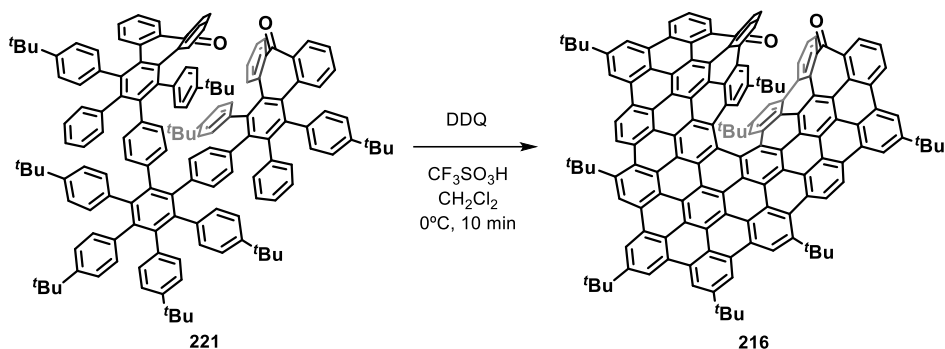
- Compound 220



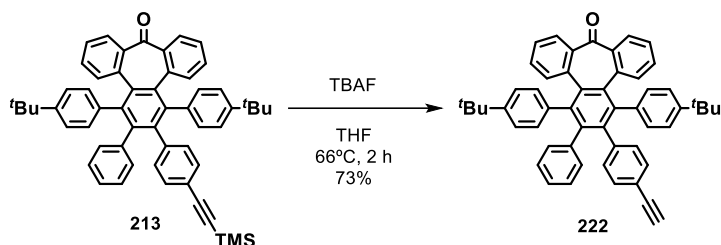
An equimolar amount of **213** (49 mg, 0.064 mmol) and **190** (51 mg, 0.064 mmol), PdCl₂(PPh₃)₂ (10 mg, 0.014 mmol) and CuI (5 mg, 0.028 mmol) were placed into a 25 mL round bottom flask, capped properly and purged with Ar. Then, freshly distilled THF (6 mL), Et₃N (0.1 mL) and DBU (0.2 mL) were added and the suspension was bubbled with Ar. Finally, H₂O (3 drops) was added and the mixture was stirred at 70°C for 24 h. The crude was diluted with CH₂Cl₂ (50 mL) and washed with NH₄Cl_(aq) (2 × 50 mL) the organic layer was separated and dried over anhydrous Na₂SO₄ and the solvent was removed under reduced pressure. The mixture was purified by flash column chromatography (SiO₂, hexane/CH₂Cl₂, 1:1) affording **220** (20 mg, 23%) as a white solid. ¹H NMR (500 MHz, CD₂Cl₂): δ = 7.40 – 7.31 (m, 4H), 7.18 – 7.14 (m, 1H), 7.08 (m, 4H), 7.00 (m, 3H), 6.94 (m, 2H), 6.88 – 6.75 (m, 6H), 6.73 – 6.68 (m, 1H), 6.45 – 6.35 (m, 4H), 1.15 (s, 9H), 1.15 (s, 9H). ¹³C NMR (126 MHz, CD₂Cl₂): δ = 200.1 (C), 149.3 (C), 149.0 (C), 146.5 (C), 142.62 (C), 142.59 (C), 142.0 (C), 141.7 (C), 141.4 (C), 140.6 (C), 138.0 (C), 137.8 (C), 136.5 (C), 136.1 (C), 135.3 (C), 135.2 (C), 133.3 (CH), 132.8 (CH), 132.7 (CH), 132.4 (CH), 132.1 (CH), 131.2 (CH), 131.1 (CH), 130.71 (CH), 130.66 (CH), 130.5 (CH), 128.7 (CH), 127.3 (CH), 126.6 (CH), 126.0 (CH), 124.5 (CH), 124.4 (CH), 124.4 (CH), 123.9 (CH), 123.7 (CH), 118.8 (C), 81.8 (C), 34.50 (C), 34.47 (C), 31.3 (CH₃).

- Compound 221

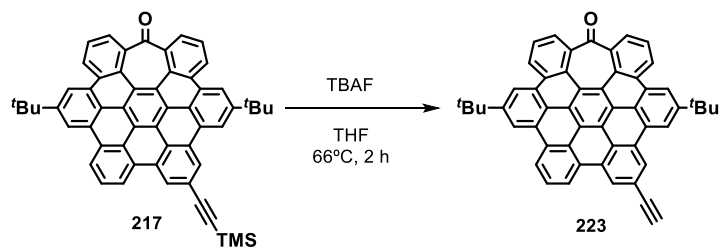
An equimolar amount of **220** (20 mg, 0.015 mmol) and 2,3,4,5-tetrakis-(*p*-*tert*-butyl-phenyl)-cyclopentadienone (10 mg, 0.015) were placed into a Schlenck tube and dissolved in Ph_2O (2 mL). The reaction mixture was placed into a sand bath and heated to reflux over 10 h. The crude was purified by flash column chromatography (SiO_2 , hexane/ CH_2Cl_2 , 7:3) affording **221** (7 mg, 25%) as a white solid. ^1H and ^{13}C NMR signals were not listed, the obtained spectra was quite complex.

- Compound 216 (from 221)

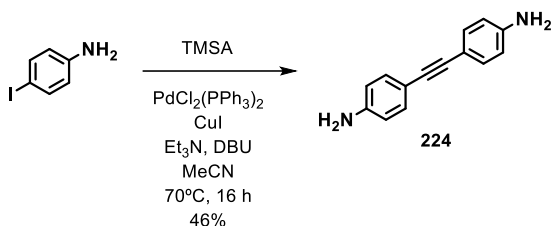
A solution of compound **221** (7 mg, 0.004 mmol) and DDQ (15 mg, 0.067 mmol) in dry CH_2Cl_2 (5 mL) was cooled to 0 – 4°C in an ice-water bath, then trifluoromethanesulfonic acid was added (0.15 mL, 1.96 mmol) and the mixture was stirred at this temperature for 10 min. The solution was diluted with CH_2Cl_2 (3 mL) and silica gel was added. The solvent was removed under vacuum and the crude was purified by flash column chromatography (SiO_2 , hexane/ CH_2Cl_2 , 3:7) affording **216** that was only detected by TLC. No enough product was obtained for a proper characterization.

- Compound 222

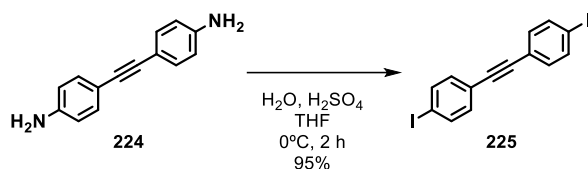
Into a round bottom flask, compound **213** (118 mg, 0.153 mmol) was placed and dissolved with THF (5 mL). Then, *tetra-n*-butylammonium fluoride (145 mg, 0.460 mmol) was added. The flask was capped tightly and the reaction mixture stirred at 66°C for 2 h. After this time, the mixture was allowed to cool to room temperature, the solvent removed under reduced pressure and the crude purified by flash column chromatography (SiO₂, hexane/CH₂Cl₂, 7:3). Compound **222** (79 mg, 73%) was obtained as a white solid. ¹H NMR (300 MHz, CDCl₃): δ = 7.40 (d, *J*=7.5, 2H), 7.36 – 7.29 (m, 2H), 7.16 (dd, *J*=7.9, 1.4, 1H), 7.10 – 6.90 (m, 9H), 6.86 – 6.72 (m, 7H), 6.67 (t, *J*=7.5, 1H), 6.38 (d, *J*=7.8, 3H), 2.89 (s, 1H), 1.15 (s, 9H), 1.13 (s, 9H).

- Compound 223

Into a round bottom flask, compound **217** (118 mg, 0.153 mmol) was placed and dissolved with THF (5 mL). Then, *tetra-n*-butylammonium fluoride (145 mg, 0.460 mmol) was added. The flask was capped tightly and the reaction mixture stirred at 66°C for 2 h. After this time, the mixture was allowed to cool to room temperature, the solvent removed under reduced pressure and the crude purified by flash column chromatography (SiO₂, hexane/CH₂Cl₂, 6:4). Compound **223** was obtained as a yellow solid. ¹H NMR (300 MHz, CD₂Cl₂): δ = 8.98 – 8.61 (m, 1H), 7.83 (d, *J* = 14.5 Hz, 0H), 3.39 (s, 0H), 1.67 (s, 1H), 1.61 (s, 1H).

- Compound 224

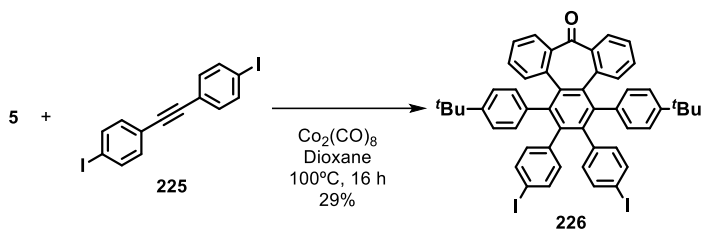
Prepared according procedure described on literature.⁸ 4-iodoaniline (2.00 g, 9.13 mmol), $\text{PdCl}_2(\text{PPh}_3)_2$ (90 mg, 0.13 mmol) and CuI (90 mg, 0.47 mmol) were placed in a round bottom flask and degassed with Ar. Then, acetonitrile (20 mL) and DBU (8 mL) were added and the suspension bubbled with Ar before adding H_2O (5 drops). The reaction mixture was placed in a reaction block at 70°C and TMSA (0.64 mL, 4.57 mmol) was added quickly and stirred overnight at that temperature. The mixture was allowed to cool to room temperature, diluted with CH_2Cl_2 (100 mL) and washed with $\text{NH}_4\text{Cl}_{(\text{sat})}$ (2×100 mL). The organic layer was separated and dried over anhydrous Na_2SO_4 , gravity-filtered and the solvent removed in vacuo. The crude material was purified by flash column chromatography (SiO_2 , CH_2Cl_2 /hexane, 8:2) affording **224** (868 mg, 46%) as a yellowish solid. ^1H NMR (400 MHz, CDCl_3): $\delta = 7.30$ (d, $J=8.5$, 4H), 6.62 (d, $J=8.5$, 4H), 3.77 (s, 4H). The obtained spectroscopic data matched with that reported on literature.

- Compound 225

The diamine **224** (600 mg, 2.88 mmol) was suspended in a mixture of H_2SO_4 (2 mL) and water (8 mL). The reaction mixture was cooled down to 0°C and then sodium nitrite (427 mg, 6.19 mmol) in water (4 mL) was added dropwise and the reaction stirred for 30 min at this temperature. The resulting solution was added to a well-stirred solution of potassium iodide (4.90 g, 29.50 mmol) in water (10 mL) contained in a large round bottom flask to accommodate foaming. After 2 h the precipitate was filtered off and washed with water and with $\text{Na}_2\text{S}_2\text{O}_3(\text{aq})$. Finally, the solid was dried in the oven at 90°C overnight yielding compound **225** (1.18 g, 95%) as a yellow powder. ^1H

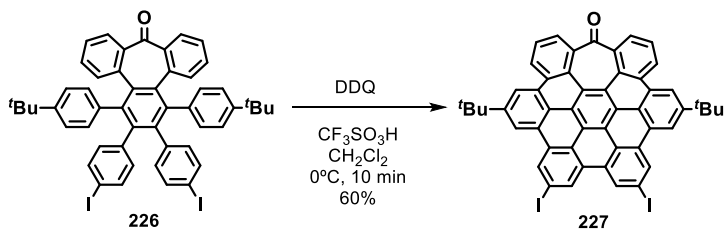
NMR (400 MHz, CDCl₃): δ = 7.69 (d, J =8.5, 1H), 7.24 (d, J =8.5, 1H). The obtained spectroscopic data matched with that reported on literature.

- Compound 226



In a glovebox, **185** (270 mg, 0.55 mmol) and cobalt carbonyl (242 mg, 0.71 mmol) were placed into a 25 mL round bottom flask and capped properly. Anhydrous 1,4-dioxane (6 mL) was added and the solution stirred at 100°C during 30 min. Then a degassed solution of compound **225** (350 mg, 0.81 mmol) in anhydrous 1,4-dioxane (2 mL) was added dropwise during 30 min. The reaction was stirred 16 h under inert atmosphere at 100°C . The mixture was then cooled down to room temperature and the solvent removed under reduced pressure. The residue was adsorbed on silica gel and purified by flash column chromatography (SiO_2 , hexane/ CH_2Cl_2 , 3:2) affording **226** (147 mg, 29%) as a white solid. ^1H NMR (400 MHz, CDCl₃): δ = 7.39 (d, J =7.7, 4H), 7.11 – 7.05 (m, 4H), 7.05 – 6.91 (m, 8H), 6.78 (t, J =7.8 Hz, 4H), 6.35 (d, J =8.0 Hz, 2H), 6.14 (d, J =7.2 Hz, 2H), 1.17 (s, 18H).

- Compound 227

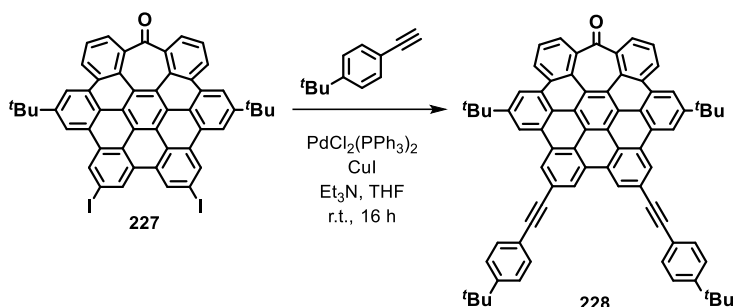


In a round bottom flask, compound **226** (45 mg, 0.05 mmol) and DDQ (67 mg, 0.30 mmol) were dissolved in dry CH_2Cl_2 (5 mL) under Ar atmosphere. The mixture was cooled down to 0°C , then trifluoromethanesulfonic acid (0.10 mL) was added and the mixture stirred at 0°C for 10 min. The mixture was then diluted with CH_2Cl_2 (10 mL) and silica gel was added. The solvent was removed

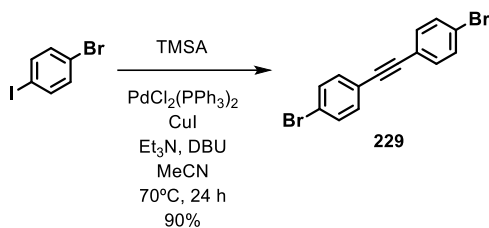
4. Experimental section

in vacuo and the crude material purified by flash column chromatography (SiO₂, CH₂Cl₂/hexane 3:2) affording **227** (27 mg, 60%) as a yellow solid. ¹H NMR (400 MHz, CDCl₂): δ = 8.71 (s, 2H), 8.63 – 8.54 (m, 6H), 8.36 (s, 2H), 7.70 (d, *J*=7.2, 2H), 7.51 (t, *J*=7.7, 2H), 1.67 (s, 18H).

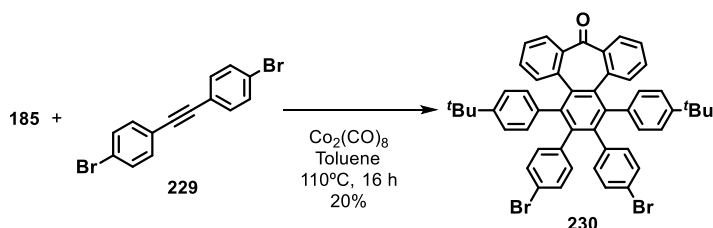
- Compound **228** (from **227**)



In a round bottom flask, compound **227** (95 mg, 0.10 mmol), PdCl₂(PPh₃)₂ (50 mg, 0.075 mmol), CuI (50 mg, 0.26 mmol) were placed and purged with Ar. Then suspended with THF (5 mL) and Et₃N (5 mL) and bubbled with Ar. *p*-*tert*-Butylphenylacetylene (112 μL, 0.62 mmol) was added dropwise and the reaction mixture stirred at room temperature overnight, then diluted with CH₂Cl₂ (50 mL) and washed with NH₄Cl_{sat} (2 × 50 mL). The organic layer was separated, dried over anhydrous Na₂SO₄, filtered and the solvent removed under vacuum. The resulting crude material was purified by flash column chromatography (SiO₂, hexane/CH₂Cl₂, 1:1) giving rise to **228** as a yellow solid. ¹H NMR (500 MHz, CD₂Cl₂): δ = 8.69 (s, 2H), 8.54 (s, 2H), 8.49 (s, 2H), 8.44 (d, *J*=7.7, 2H), 8.27 (s, 1H), 7.67 (d, *J*=7.2, 2H), 7.52 (d, *J*=8.0, 4H), 7.40 (d, *J*=8.0, 4H), 7.33 (t, *J*=7.1, 2H), 1.68 (s, 9H), 1.33 (s, 9H). ¹³C NMR (126 MHz, CD₂Cl₂): δ = 202.37 (C), 152.13 (C), 150.06 (C), 142.45 (C), 131.95 (CH), 131.12 (C), 130.49 (C), 129.05 (C), 129.00 (C), 128.34 (C), 127.32 (C), 127.00 (C), 125.93 (CH), 124.89 (C), 124.71 (CH), 124.28 (CH), 124.04 (CH), 123.70 (C), 123.11 (C), 123.09 (C), 122.24 (C), 121.12 (CH), 120.64 (C), 120.39 (C), 118.91 (CH), 90.92 (C), 89.74 (C), 35.94 (C), 35.13 (C), 32.12 (CH₃), 31.36 (CH₃).

- Compound 229

Prepared according to procedure described on literature.²⁵⁵ In a properly dried and degassed flask charged with PdCl₂(PPh₃)₂ (90 mg, 0.13 mmol), CuI (90 mg, 0.47 mmol) and 1-bromo-4-iodobenzene (2.00 g, 7.07 mmol), acetonitrile (20 mL) and DBU (8 mL) were added. The solution was bubbled with Ar. Then trimethylsilylacetylene (0.50 mL, 3.53 mmol) was added by syringe, followed immediately by distilled water (0.20 mL). The flask was covered with aluminum foil and the reaction stirred overnight. The reaction mixture was diluted with CH₂Cl₂ (100 mL) and washed with NH₄Cl_(sat) (2 × 100 mL). The organic layer was dried over anhydrous Na₂SO₄, gravity-filtered and the solvent removed in vacuo. The crude was purified by flash column chromatography (SiO₂, hexane) affording **229** (1.07 g, 90%) as a white solid. ¹H NMR (400 MHz, CDCl₃): δ = 7.49 (d, *J*=8.5, 4H), 7.38 (d, *J*=8.5, 4H).

- Compound 230

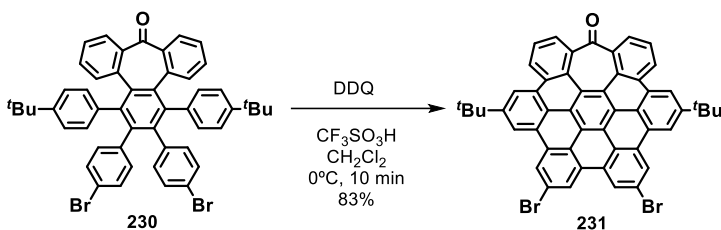
In a glovebox, compound **185** (350 mg, 0.71 mmol) and Co₂(CO)₈ (315 mg, 0.92 mmol) were placed in a round bottom flask and capped properly, the solids were dissolved in dry toluene (6 mL) and the reaction mixture placed in an oil bath at 110°C for 30 min. Then a degassed suspension of **229** (350 mg, 1.04 mmol) in dry toluene (2 mL) was added dropwise over the

²⁵⁵ M. J. Mio, L. C. Kopel, J. B. Braun, T. L. Gadzikwa, K. L. Hull, R. G. Brisbois, C. J. Markworth, P. A. Grieco, *Org. Lett.* **2002**, *4*, 3199-3202.

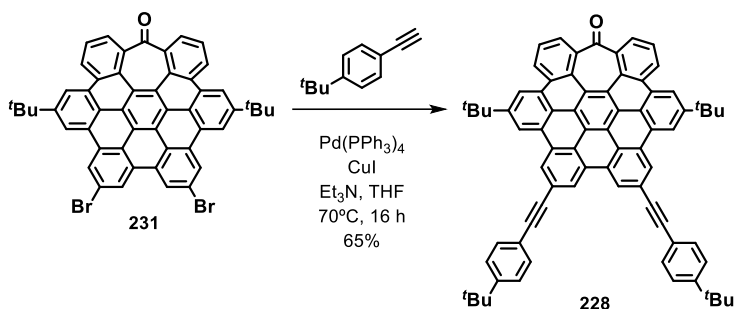
4. Experimental section

reaction mixture and the resulting solution was stirred at 110°C overnight. The solvent was removed in the rotavapor and the crude material purified by flash column chromatography (SiO₂, hexane/CH₂Cl₂, 7:3) affording **230** (120 mg, 20%) as a white solid. ¹H NMR (500 MHz, CD₂Cl₂): δ = 7.35 (d, *J*=7.5, 2H), 7.25 (d, *J*=8.1, 2H), 7.21 (d, *J*=7.9, 2H), 7.09 (t, *J*=7.4, 2H), 7.03 (s, 4H), 6.93 (d, *J*=7.7, 2H), 6.84 (t, *J*=7.9, 4H), 6.79 (t, *J*=7.6, 2H), 6.36 (d, *J*=8.0, 2H), 6.32 (d, *J*=7.9, 2H), 1.17 (s, 14H). ¹³C NMR (126 MHz, CD₂Cl₂): δ = 200.04 (C), 149.30 (C), 146.48 (C), 141.78 (C), 141.46 (C), 139.86 (C), 137.71 (C), 136.45 (C), 135.09 (C), 133.72 (CH), 133.29 (CH), 132.66 (CH), 132.54 (CH), 130.45 (CH), 129.80 (CH), 128.75 (CH), 127.39 (CH), 124.54 (CH), 124.45 (CH), 123.97 (CH), 120.10 (C), 34.52 (C), 31.33 (CH₃).

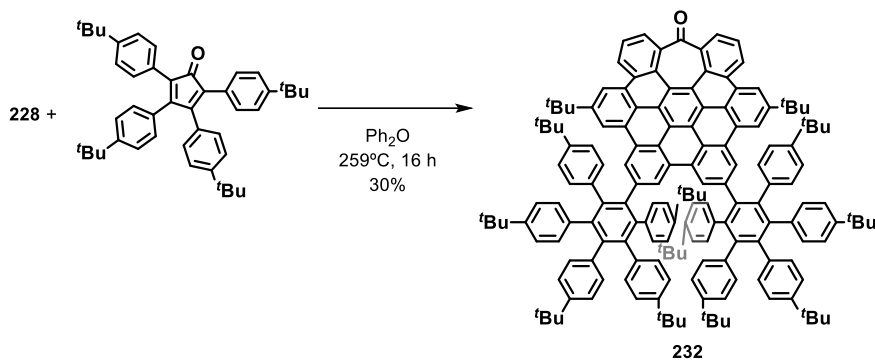
- Compound 231



To a solution of polyphenylene **230** (110 mg, 0.13 mmol) and DDQ (170 mg, 0.75 mmol) in dry CH₂Cl₂ (6 mL) placed in an ice-water bath, then trifluoromethanesulfonic acid (0.15 mL) was slowly added and the reaction mixture stirred for 10 min under Ar atmosphere. The mixture was then diluted with CH₂Cl₂ (10 mL) and silica gel was added. The solvent was removed in the rotavapor and the crude material purified by flash column chromatography (SiO₂, hexane/CH₂Cl₂, 3:2) giving rise to **231** (89 mg, 83%) as a yellow solid. ¹H NMR (400 MHz, CDCl₃) δ = 8.69 (d, *J*=9.4, 2H), 8.68 (s, 2H), 8.65 (s, 2H), 8.63 (s, 2H), 8.47 (s, 2H), 7.79 (d, *J*=7.1, 2H), 7.63 (t, *J*=7.4, 2H), 1.67 (s, 18H).

- Compound 228 (from 231)

Compound **231** (270 mg, 329 μmol), $\text{Pd}(\text{PPh}_3)_4$ (50 mg, 0.04 mmol) and CuI (15 mg, 0.08 mmol) were placed into a round bottom flask, capped properly and purged with Ar. The solids were suspended with a mixture of freshly distilled THF (2 mL) and NEt_3 (4 mL) and bubbled with Ar. The reaction mixture was placed at 70°C and *p*-*tert*-butylphenylacetylene (0.18 mL, 0.99 mmol) was added dropwise. The reaction mixture was kept at this temperature for 16 h. Once cooled to room temperature, the crude was diluted with CH_2Cl_2 (100 mL) and washed with $\text{NH}_4\text{Cl}_{(\text{sat})}$ (2 \times 100 mL). The organic layer was separated, dried with anhydrous Na_2SO_4 , filtered and the solvent removed at the rotavapor. The crude was purified by flash column chromatography (SiO_2 , hexane/ CH_2Cl_2 , 1:1) affording **228** (208 mg, 65%) as a yellow solid. The obtained spectroscopic data matched with that previously reported.

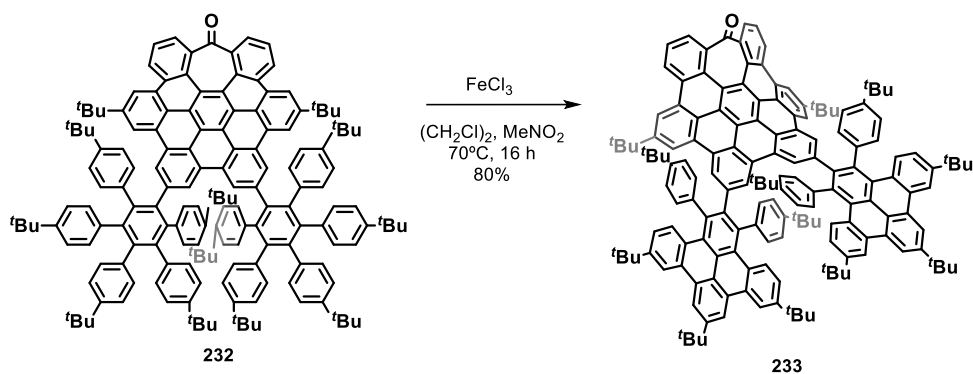
- Compound 232

A solution of **228** (67 mg, 68.70 μmol) and 2,3,4,5-tetrakis(*p*-*tert*-butyl-phenyl)cyclopentadienone (84 mg, 137.4 μmol) in Ph_2O (2 mL) was placed in a sand bath and refluxed

4. Experimental section

overnight. The reaction mixture was cooled down to room temperature, diluted with hexane (10 mL) and purified by flash column chromatography (SiO₂, hexane/CH₂Cl₂, 3:2) giving rise to **232** (44 mg, 30%) as a glassy yellow solid. ¹H NMR (500 MHz, CD₂Cl₂): δ = 8.62 (d, *J*=7.7, 2H), 8.49 (s, 2H), 8.32 (s, 5H), 7.92 (s, 2H), 7.62 (d, *J*=7.0, 2H), 7.54 (t, *J*=7.5, 2H), 7.05 (d, *J*=7.9, 4H), 6.99 – 6.90 (m, 14H), 6.89 – 6.78 (m, 17H), 6.75 (d, *J*=7.9, 4H), 6.61 (d, *J*=7.8, 4H), 1.54 (s, 18H), 1.17 (s, 18H), 1.16 (s, 36H), 0.69 (s, 36H). ¹³C NMR (126 MHz, CD₂Cl₂): δ = 202.64 (C), 149.99 (C), 148.46 (C), 148.38 (C), 148.35 (C), 142.49 (C), 141.61 (C), 141.36 (C), 141.04 (C), 140.36 (C), 140.00 (C), 138.62 (C), 138.60 (C), 138.36 (C), 131.89 (CH), 131.81 (CH), 131.57 (CH), 131.50 (CH), 131.42 (CH), 129.78 (C), 129.50 (C), 128.79 (C), 128.44 (C), 127.56 (CH), 127.36 (C), 127.05 (CH), 126.90 (CH), 126.22 (CH), 124.49 (C), 123.80 (CH), 123.71 (CH), 123.13 (C), 123.03 (C), 122.28 (C), 121.06 (C), 120.57 (CH), 117.88 (CH), 35.74 (C), 34.46 (C), 34.13 (C), 31.96 (CH₃), 31.40 (CH₃), 31.00 (CH₃).

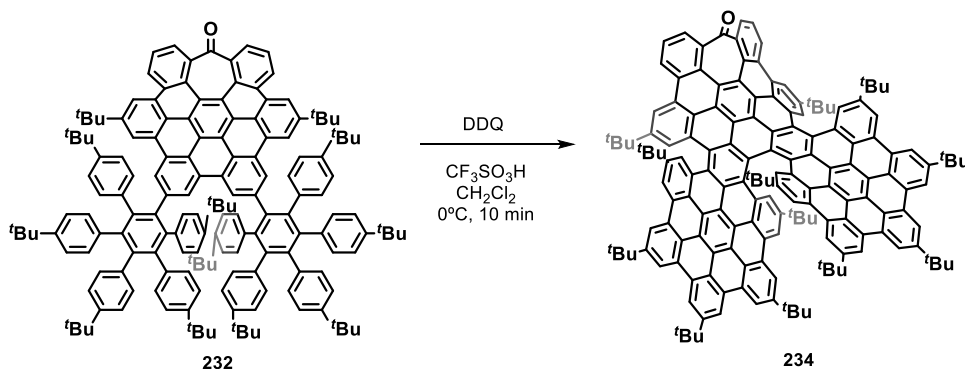
- Compound 233



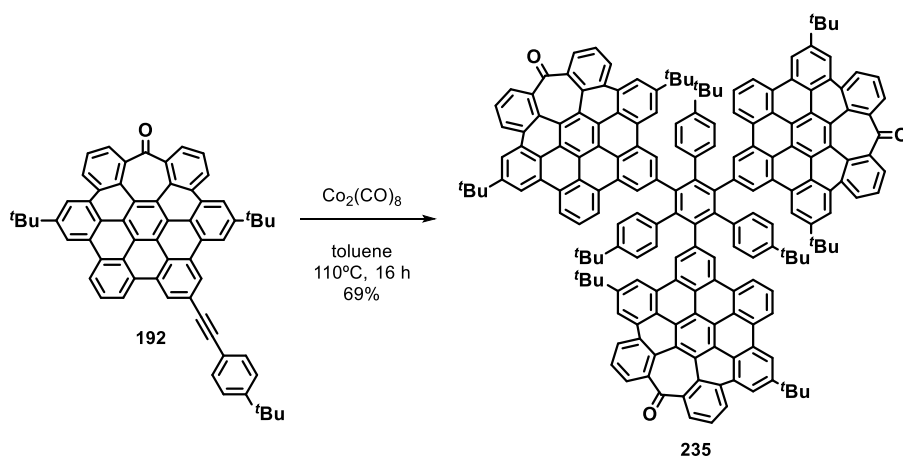
Compound **232** (40 mg, 0.019 mmol) was placed in a round bottom flask, dissolved with 1,2-dichloroethane (10 mL) and bubbled with Ar. In parallel, iron trichloride (120 mg, 0.740 mmol) was dissolved in MeNO₂ (2 mL) and degassed with Ar. The solution of **232** was placed at 70°C and the iron trichloride solution was added dropwise during 1 h while bubbling Ar through the reaction mixture. After addition, the reaction mixture was kept at 70°C overnight before allow it to cool to room temperature. Then diluted with CH₂Cl₂ (50 mL) and washed with H₂O (2 × 50 mL), the organic layer was separated and dried over anhydrous Na₂SO₄, filtered and the solvent removed under vacuum. The crude was purified by flash column chromatography (SiO₂, hexane/CH₂Cl₂, 3:2) affording **233** (32 mg, 80%) as a dark green solid. ¹H NMR (400 MHz, CD₂Cl₂):

$\delta = 9.33$ (d, $J=1.4$, 1H), 9.23 (dd, $J=8.2$, 1.5, 1H), 8.89 (d, $J=1.0$, 1H), 8.67 (d, $J=1.8$, 1H), 8.08 – 7.95 (m, 3H), 7.75 (d, $J=9.0$, 1H), 7.51 (d, $J=9.1$, 1H), 7.45 (d, $J=2.1$, 1H), 7.32 (dd, $J=7.6$, 1.5, 1H), 7.15 – 7.10 (m, 1H), 7.05 – 6.93 (m, 5H), 6.85 (dd, $J=8.2$, 2.1, 1H), 6.74 (dd, $J=7.9$, 1.9, 2H), 6.57 (dd, $J=9.1$, 1.9, 1H), 6.50 (dd, $J=8.1$, 2.0, 1H), 1.40 (s, 9H), 1.37 (s, 9H), 1.34 (s, 9H), 1.20 (s, 9H), 1.01 (s, 9H), -0.02 (s, 9H). HR-MS (ESI-TOF): m/z calc. for $C_{163}H_{154}O$ $[M]^+$: 2127.2000; found: 2127.2056.

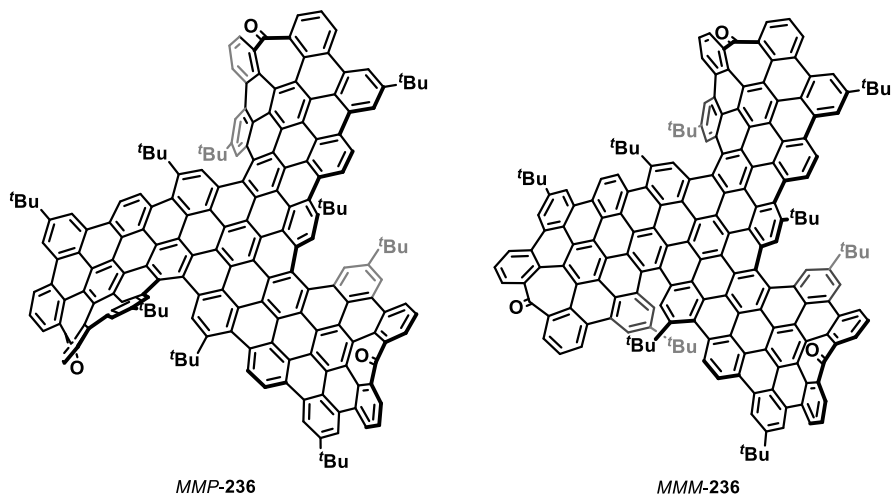
- Compound 234



In a round bottom flask, compound **232** (34 mg, 16 μmol) and DDQ (50 mg, 0.22 mmol) were purged with Ar and dissolved with dry CH_2Cl_2 (6 mL). The reaction mixture was placed in an ice-water bath and trifluoromethanesulfonic acid (0.15 mL) were added dropwise and stirred for 10 min. The mixture was diluted with CH_2Cl_2 (10 mL), silica gel was added and the solvent removed under vacuo. The crude material was purified by flash column chromatography (SiO_2 , CH_2Cl_2 /hexane, 3:2) affording **234** as a dark green solid. *MMP/PPM-234*: ^1H NMR (400 MHz, CDCl_2): $\delta = 9.71$ (s, 1H), 9.48 – 9.22 (m, 13H), 9.15 (d, $J=6.7$, 3H), 9.01 (s, 1H), 8.84 (s, 1H), 8.78 (s, 1H), 8.49 (s, 1H), 8.29 – 8.04 (m, 7H), 8.00 (s, 1H), 7.68 (s, 1H), 1.94 (s, 9H), 1.90 (s, 18H), 1.89 (s, 9H), 1.59 (s, 9H), 1.55 (s, 9H), 1.45 (s, 9H), 1.43 (s, 9H), 1.41 (s, 9H), 0.13 (s, 9H), -0.26 (s, 9H). HR-MS (ESI-TOF): m/z calc. for $C_{163}H_{138}O$ $[M]^+$: 2111.0748; found: 2111.0806. Fraction D: ^1H NMR (400 MHz, CD_2Cl_2): $\delta = 9.61$ (s, 2H), 9.47 (s, 2H), 9.46 – 9.41 (m, 6H), 9.33 (s, 2H), 9.31 – 9.26 (m, 4H), 9.17 (s, 2H), 8.93 (s, 2H), 8.45 (s, 2H), 8.23 (s, 2H), 8.15 – 8.02 (m, 4H), 7.93 (s, 2H), 1.92 (s, 18H), 1.86 (s, 18H), 1.50 (s, 18H), 1.49 (s, 18H), 1.31 (s, 18H), -0.22 (s, 18H). HR-MS (ESI-TOF): m/z calc. for $C_{163}H_{138}O$ $[M]^+$: 2111.0748; found: 2111.0757.

- Compound 235

Under argon atmosphere, compound **192** (160 mg, 0.195 mmol) and $\text{Co}_2(\text{CO})_8$ (27 mg, 78 μmol) were placed into a round bottom flask, capped properly and dissolved in toluene (6 mL). The reaction was stirred at 110°C for 16 h. The solvent was removed under reduced pressure and the crude was purified by flash column chromatography (SiO_2 , hexane/ CH_2Cl_2 3:2) affording **235** (110 mg, 69%) as a yellow solid. M.p. $> 300^\circ\text{C}$; ^1H NMR and ^{13}C NMR signals were not listed, the obtained spectra is quite complex due to a mixture of atropisomers; HR-MS (MALDI DCTB+PPGNa 2000): m/z calc. for $\text{C}_{189}\text{H}_{138}\text{O}_3$ $[\text{M}]^+$: 2455.0640; found: 2455.0653; IR (ATR): 2958, 1737, 1680, 1612 cm^{-1} .

- Compound 236

A solution of compound **235** (40 mg, 0.016 mmol) and DDQ (36 mg, 0.158 mmol) in dry CH_2Cl_2 (5 mL) was cooled to $0-4^\circ\text{C}$ in an ice-water bath, then trifluoromethanesulfonic acid was added (0.1 mL, 1.306 mmol) and the mixture was stirred for 10 min. The solution was diluted with CH_2Cl_2 (3 mL), then silica gel was added and the solvent removed. The crude was purified by flash column chromatography (SiO_2 , hexane/ CH_2Cl_2 , 1:4) to afford **236** (9.4 mg, 24% (22% (*M,M,P/P,P,M*)-**236** and 2% (*M,M,M/P,P,P*)-**236**)). M. p.: $> 300^\circ\text{C}$; HR-MS (MALDI-TOF DCTB+PEGNa 2000): m/z calc. for $\text{C}_{189}\text{H}_{120}\text{O}_3$ [M] $^+$: 2436.9232; found: 2436.9218. (*M,M,P/P,P,M*)-**236**: $[\alpha]_{\text{D}}^{25} = +3843^\circ$ ((*M,M,P*)-**236**, 6.245×10^{-6} M); ^1H NMR (500 MHz, $\text{C}_2\text{D}_2\text{Cl}_4$): $\delta = 11.08$ (s, 1H), 11.03 (s, 1H), 10.66 (s, 1H), 10.28 (d, $J=8.4$, 1H), 10.21 (d, $J=8.5$, 2H), 10.02 (d, $J=8.4$, 1H), 9.96–9.90 (m, 2H), 9.75 (s, 1H), 9.71–9.67 (m, 3H), 9.52 (d, $J=8.4$, 1H), 9.47 (d, $J=8.3$ Hz, 1H), 9.42–9.34 (m, 3H), 9.31 (s, 1H), 9.29 (s, 1H), 9.21 (s, 1H), 8.44 (s, 1H), 8.41–8.38 (m, 2H), 8.38–8.34 (m, 1H), 8.33–8.30 (m, 2H), 8.28–8.16 (m, 8H), 8.05–7.98 (m, 2H), 7.87 (s, 1H), 7.84 (s, 1H), 2.47 (s, 9H), 2.34 (s, 9H), 1.98 (s, 9H), 1.90 (s, 18H), 1.71 (s, 9H), 1.51 (s, 9H), 0.08 (s, 9H), -0.09 (s, 9H). $^1\text{H}-^{13}\text{C}$ HSQC and $^1\text{H}-^{13}\text{C}$ HMBC (600 MHz, 151 MHz, $\text{C}_2\text{D}_2\text{Cl}_4$): $\delta = 150.06$ (C), 149.85 (C), 148.81 (C), 148.18 (C), 147.84 (C), 147.55 (C), 146.99 (C), 144.40 (C), 142.69 (C), 142.62 (C), 140.83 (C), 133.08 (CH), 132.86 (CH), 132.72 (CH), 131.56 (CH), 128.79 (CH), 128.19 (CH), 127.79 (CH), 127.77 (CH), 127.74 (CH), 127.68 (CH), 126.6 (CH), 125.53 (CH), 125.31 (CH), 124.81 (CH), 124.53 (CH), 124.37 (CH), 123.57 (CH), 123.42 (CH), 122.72 (CH), 122.57 (CH), 122.28 (CH),

121.43 (CH), 120.16 (CH), 119.02 (CH), 118.86 (CH), 118.76 (CH), 118.75 (CH), 118.01 (CH), 117.52 (CH), 116.28 (CH), 116.20 (CH), 39.97 (C), 39.93 (C), 39.23 (C), 35.70 (C), 35.64 (C), 35.59 (CH₃), 35.51 (CH₃), 35.19 (C), 34.81 (CH₃), 33.80 (C), 33.65 (C), 31.83 (CH₃), 31.74 (CH₃), 31.33 (CH₃), 29.89 (CH₃), 29.72 (CH₃). IR (ATR): 2957, 2921, 2852, 1666 cm⁻¹. (*M,M,M/P,P,P*)-**56**: ¹H NMR (600 MHz, C₂D₂Cl₄): δ = 10.67 (s, 1H), 10.08 (d, *J*=7.9, 1H), 10.00 (d, *J*=9.0, 1H), 9.76 (s, 1H), 9.59 (s, 1H), 9.51 (d, *J*=8.6, 1H), 9.41 (d, *J*=8.0, 1H), 9.34 (s, 1H), 9.19 (s, 1H), 8.33 (t, *J*=7.5, 1H), 8.29 – 8.20 (m, 3H), 1.95 (s, 9H), 1.67 (s, 9H), 1.47 (s, 9H). ¹H-¹³C HSQC and ¹H-¹³C HMBC (600 MHz, 151 MHz, C₂D₂Cl₄): δ = 149.9 (C), 148.7 (C), 143.4 (C), 133.2 (CH), 132.8 (CH), 128.4 (CH), 128.2 (CH), 128.0 (CH), 127.8 (CH), 126.5 (CH), 124.8 (CH), 123.5 (CH), 120.2 (CH), 118.8 (CH), 117.0 (CH), 39.0 (C), 35.6 (C), 35.0 (C), 34.7 (CH₃), 31.8 (CH₃), 31.2 (CH₃). IR (ATR): 2957, 2921, 2852, 1666 cm⁻¹.

4.3. X-Ray diffraction structures

- Compounds **194a** and **194b**

Single crystals suitable for X-ray diffraction crystallography of **194a** were grown by slow diffusion of methanol vapor into a solution of **194a** in chlorobenzene. We have also grown X-ray diffraction quality crystals of **194b** by slow evaporation of a solution of the compound in a CH₂Cl₂/hexane mixture. The X-ray diffraction data were collected on a Bruker D8 Venture diffractometer equipped with a Photon 100 detector. The structures were solved with the SHELXT²⁵⁶ software (direct methods) and refined using the full-matrix least-squares against F² procedure with SHELX 2016²⁵⁷ using the WinGX32²⁵⁸ software. Hydrogen atoms were placed in idealized positions ($U_{\text{eg}}(\text{H}) = 1.2U_{\text{eg}}(\text{C})$ or $U_{\text{eg}}(\text{H}) = 1.5U_{\text{eg}}(\text{C})$) and were allowed to ride on their parent atoms. A summary of the X-ray diffraction measurement and refinement data is given in Table 7. During the refinement of **194a** the structure of the molecule was established unambiguously and obtained with reasonable thermal ellipsoids. However large residual electron density, located mainly in the voids between the ribbon-shaped nanographene molecules, remained present and could not be modeled. This is probably due to the presence of disordered chlorobenzene molecules that occupy that space, as other two other solvent molecules in the asymmetric unit

²⁵⁶ G. M. Sheldrick, *Acta Cryst.* **2015**, A71, 3-8.

²⁵⁷ G. M. Sheldrick, *Acta Cryst.* **2008**, A64, 112-122.

²⁵⁸ L. J. Farrugia, *J. Appl. Cryst.* **2012**, 45, 849-854.

that could be modelled were present in the structure. To tackle this issue, the SQUEEZE²⁵⁹ routine included in PLATON²⁶⁰ was applied and a density of 426 e⁻ in an approximately 1400 Å³ volume was identified. This density fits reasonably well with the presence of 7 molecules of chlorobenzene and possibly one extra molecule of methanol in the unit cell, solvents used in the crystallization. This density was removed and the data refined against the model. These solvent molecules removed with SQUEEZE were added to the cell unit contents and a last cycle of refinement was performed. Additionally, SIMU, DELU and ISOR instructions were used to model the disorder associated with a molecule of chlorobenzene present in the crystal of **194a** and that of one of the *tert*-butyl groups in **194b**. Both compounds have crystallized as a racemic mixture of the *P* and *M* enantiomers.

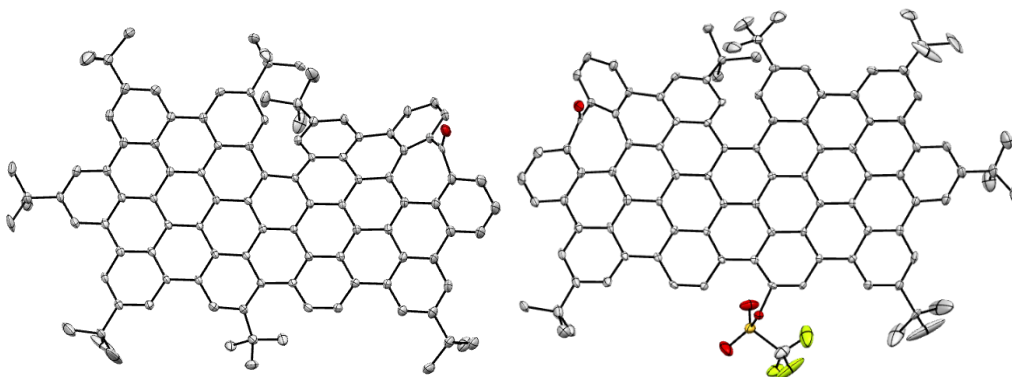


Figure 87. ORTEP drawing showing the thermal displacement ellipsoids (50% probability) of the crystal structure of: **194a** (left) and **194b** (right). Hydrogen atoms and solvent molecules have been omitted for clarity.

- Compound 203

Suitable crystals for X-ray diffraction analysis of precursor **203** were grown by slow evaporation of a solution of the compound in CH₂Cl₂/MeOH. The X-ray diffraction data were collected on a Bruker D8 Venture diffractometer equipped with a Photon 100 detector using Cu radiation source. The structure was solved with SHELXT and refined using the full-matrix least-squares against F^2 procedure with SHELX 2018 using the WinGX32 software. C–H hydrogen atoms were

²⁵⁹ A. L. Spek, *Acta Cryst.* **2015**, *C71*, 9-18.

²⁶⁰ A. L. Spek, *Acta Cryst.* **2009**, *D65*, 148-155.

4. Experimental section

placed in idealized positions ($U_{\text{eg}}(\text{H}) = 1.2U_{\text{eg}}(\text{C})$ or $U_{\text{eg}}(\text{H}) = 1.5U_{\text{eg}}(\text{C})$) and were allowed to ride on their parent atoms.

One of the t-butyl groups was found to be disordered between two positions. This disorder was modeled using the PART instruction to split the corresponding methyl groups between those two positions.

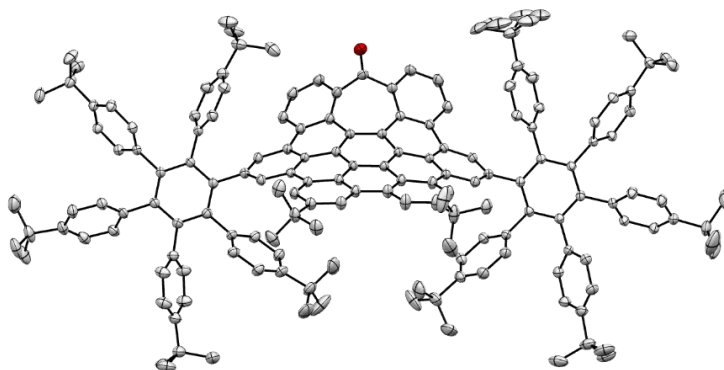


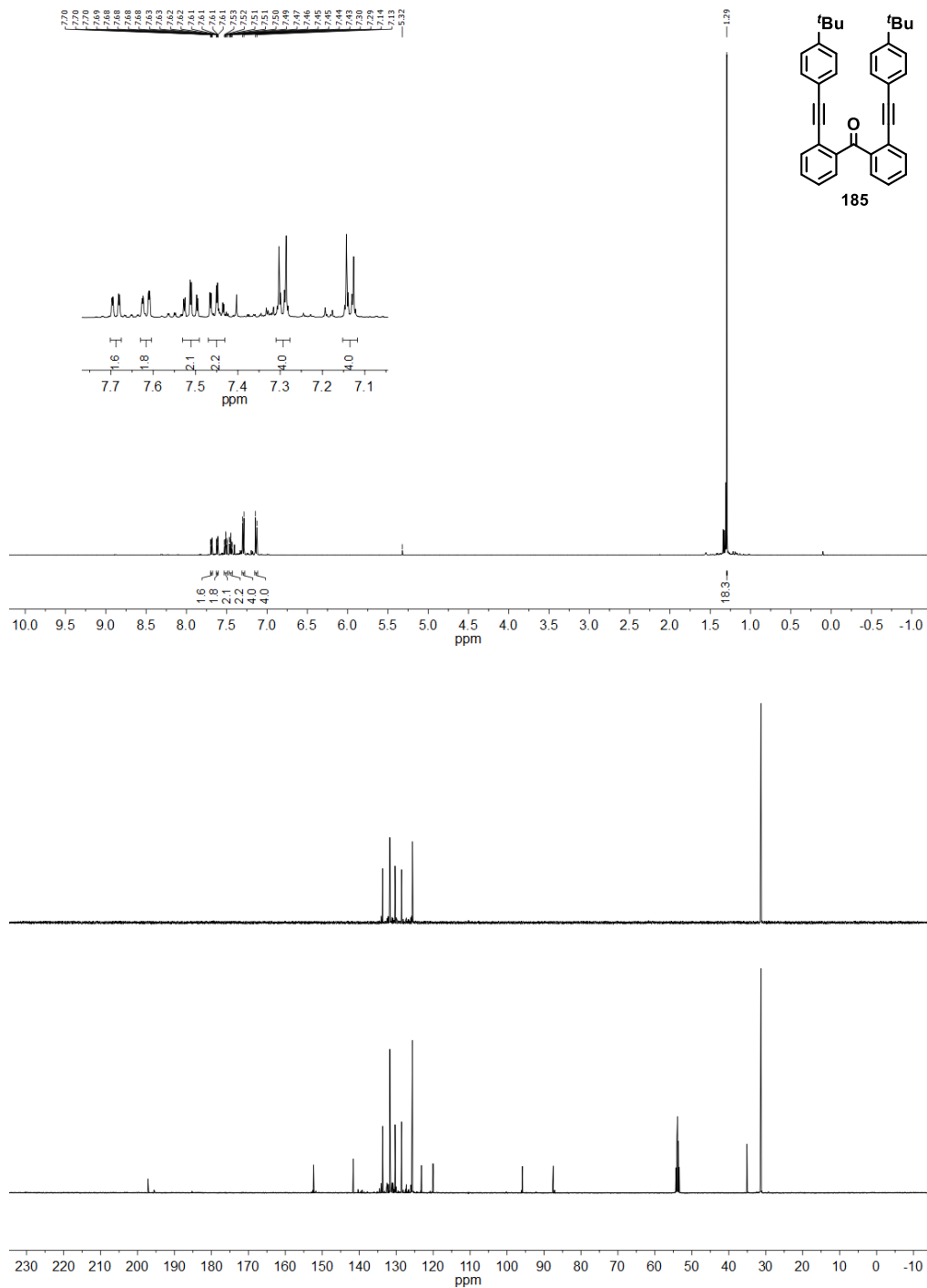
Figure 88. ORTEP drawing showing the thermal displacement ellipsoids (50% probability) of the crystal structure of: **203**. Hydrogen atoms and solvent molecules have been omitted for clarity.

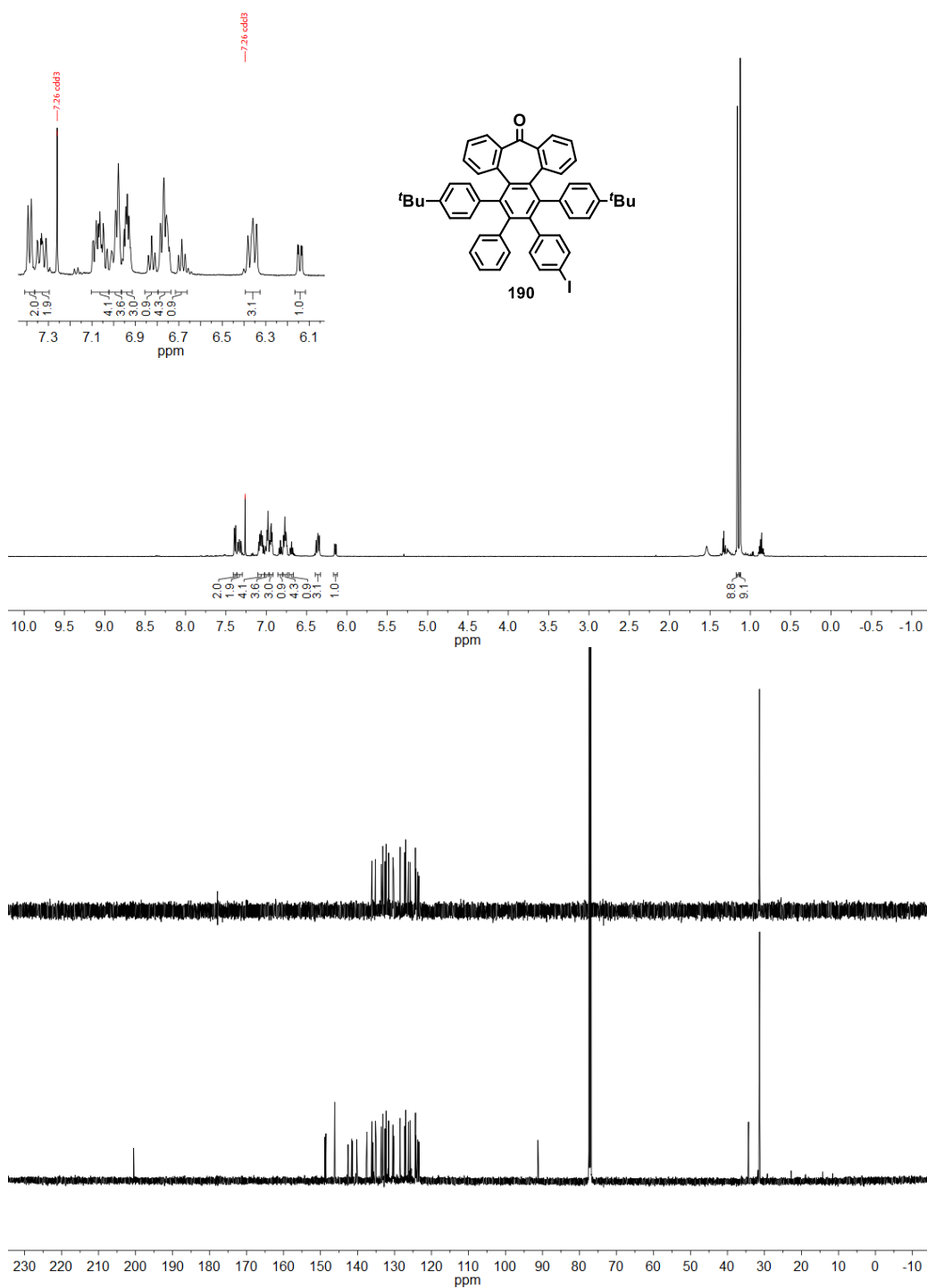
Table 7. Summary of X-ray diffraction crystallography measurement and refinement data for compounds **194a**, **194b** and **203**^a

| | 194a ·4.5C ₆ H ₅ ·0.5CH ₃ OH | 194b ·2C ₆ H ₁₄ | 203 |
|--|--|---|---|
| Chemical formula | C _{140.5} H _{113.5} Cl _{5.5} O _{1.5} | C ₁₁₆ H ₁₀₃ F ₃ O ₄ S | C ₁₆₆ H ₁₆₈ OC ₁₆ |
| <i>M</i> _r | 2020.78 | 1650.04 | 2391.69 |
| Crystal size [mm ³] | 0.444 x 0.140 x 0.040 | 0.453 x 0.088 x 0.038 | 0.460 x 0.279 x 0.174 |
| Crystal system | Triclinic | Triclinic | Monoclinic |
| Space group | <i>P</i> -1 | <i>P</i> -1 | <i>P</i> 21/ <i>n</i> |
| <i>a</i> [Å] | 15.3025(6) | 14.3675(8) | 18.7015(6) |
| <i>b</i> [Å] | 16.0955(6) | 17.3718(11) | 21.6095(7) |
| <i>c</i> [Å] | 22.2445(9) | 18.9206(12) | 35.5723(12) |
| α [°] | 94.998(2) | 67.525(3) | 90 |
| β [°] | 108.991(2) | 86.143(3) | 104.981(2) |
| γ [°] | 92.221(2) | 89.598(3) | 90 |
| <i>V</i> [Å ³] | 5147.8(4) | 4352.9(5) | 13887.2(8) |
| <i>Z</i> | 2 | 2 | 4 |
| ρ_{calcd} [Mg m ⁻³] | 1.304 | 1.259 | 1.144 |
| μ [mm ⁻¹] | 1.845 | 0.835 | 1.520 |
| F(000) | 2124 | 1748 | 5096 |
| ϑ range [°] | 2.112 to 59.291 | 2.533 to 50.604 | 2.415 to 79.050 |
| <i>hkl</i> ranges | -16,17/-17,17/-24,24 | -14,14/-17,17/-18,18 | -23,23/-24,27/-45,43 |
| Reflections collected | 64348 | 41843 | 174605 |
| Independent reflections | 14785 | 9165 | 29641 |
| <i>R</i> _{int} | 0.0391 | 0.0523 | 0.0512 |
| Completeness [%] | 98.9 | 99.7 | 99.7 |
| Absorption correction | Numerical | Multi-scan | Numerical |
| Final <i>R</i> indices [<i>I</i> > 2 σ (<i>I</i>)] | <i>R</i> ₁ = 0.0996 <i>wR</i> ₂ = 0.2829 | <i>R</i> ₁ = 0.0720 <i>wR</i> ₂ = 0.1869 | <i>R</i> ₁ = 0.0971 <i>wR</i> ₂ = 0.2721 |
| <i>R</i> indices (all data) | <i>R</i> ₁ = 0.1171 <i>wR</i> ₂ = 0.3003 | <i>R</i> ₁ = 0.0872 <i>wR</i> ₂ = 0.2004 | <i>R</i> ₁ = 0.1117 <i>wR</i> ₂ = 0.2871 |
| Goodness-of-fit on <i>F</i> ² | 1.054 | 1.036 | 1.045 |

^aIn common: Temperature, 100 K. Wavelength, 1.54178 Å (Cu-K α). Refinement method, full-matrix least-squares on *F*².

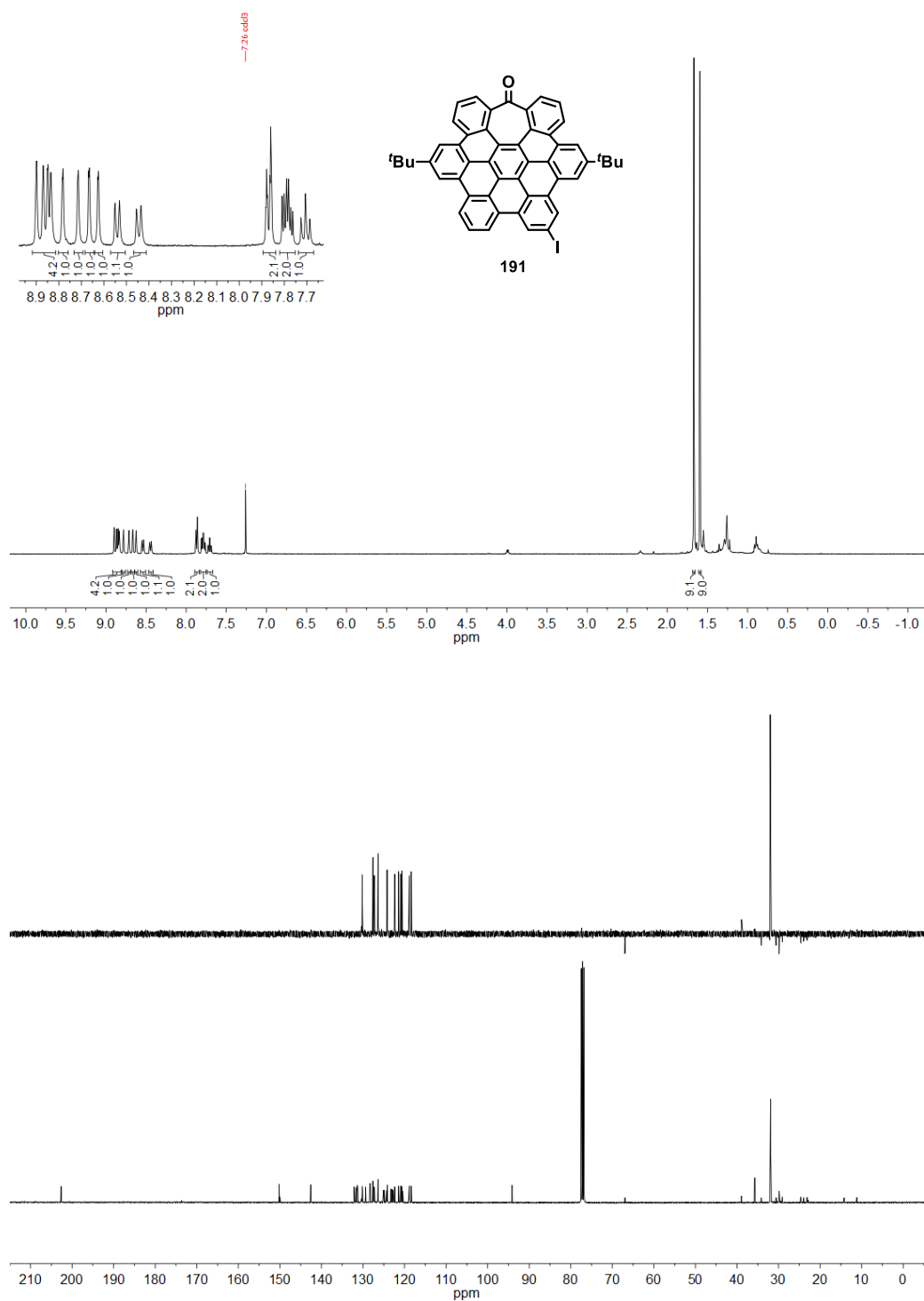
4.4. Representative NMR spectra of prepared compounds



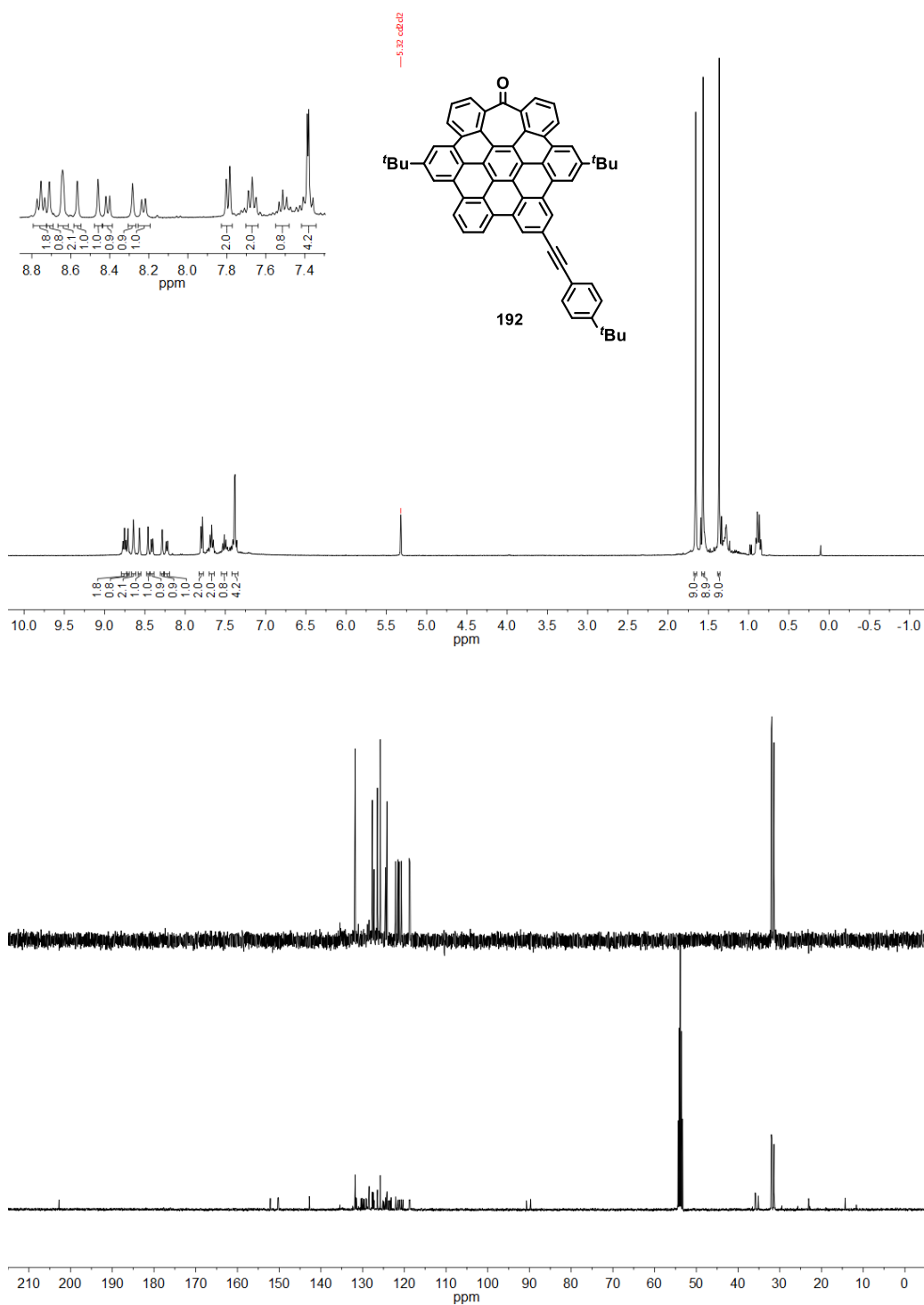


^1H NMR (500 MHz, CDCl_3) and ^{13}C NMR (126 MHz, CDCl_3) spectra of compound **190**.

4. Experimental section

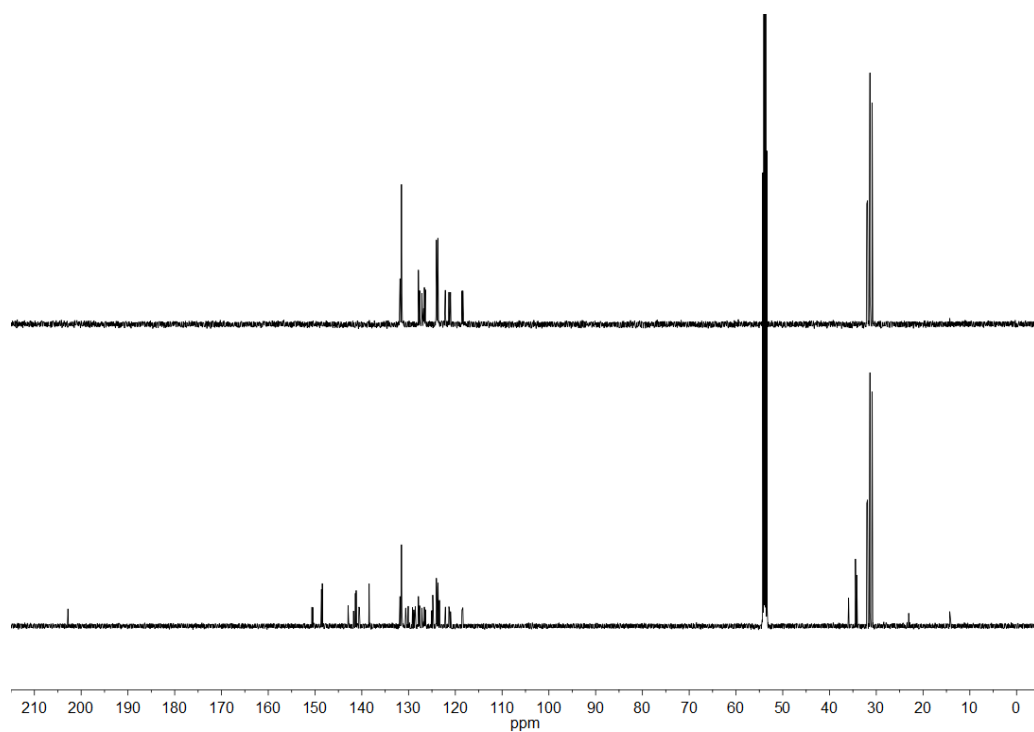
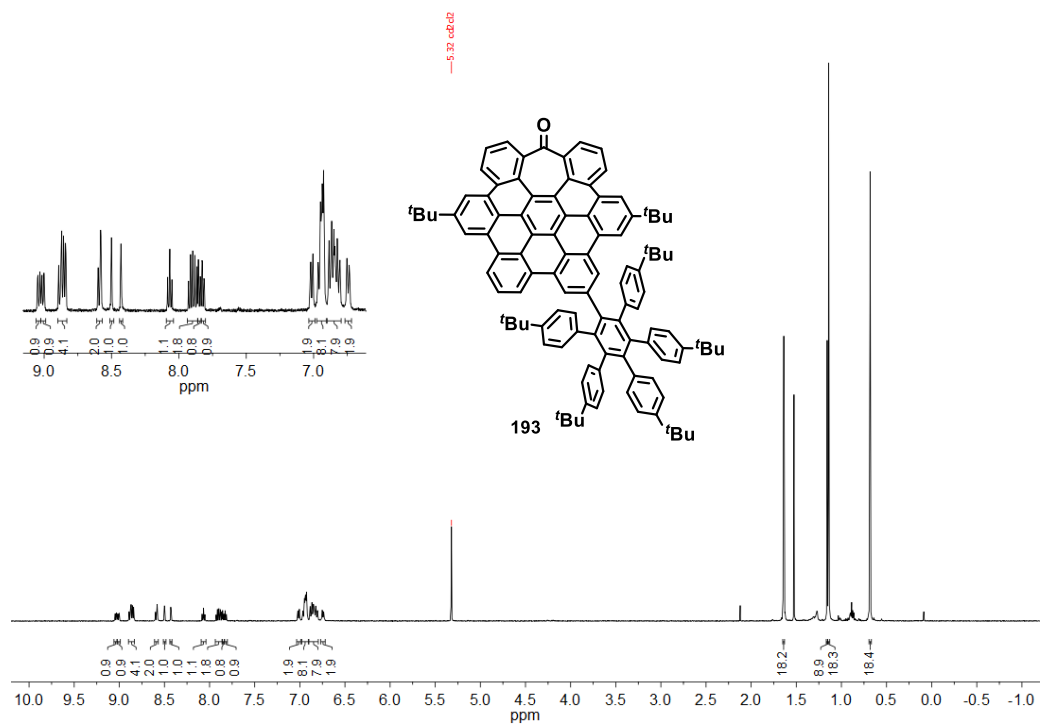


^1H NMR (400 MHz, CDCl_3) and ^{13}C NMR (101 MHz, CDCl_3) spectra of compound **191**.

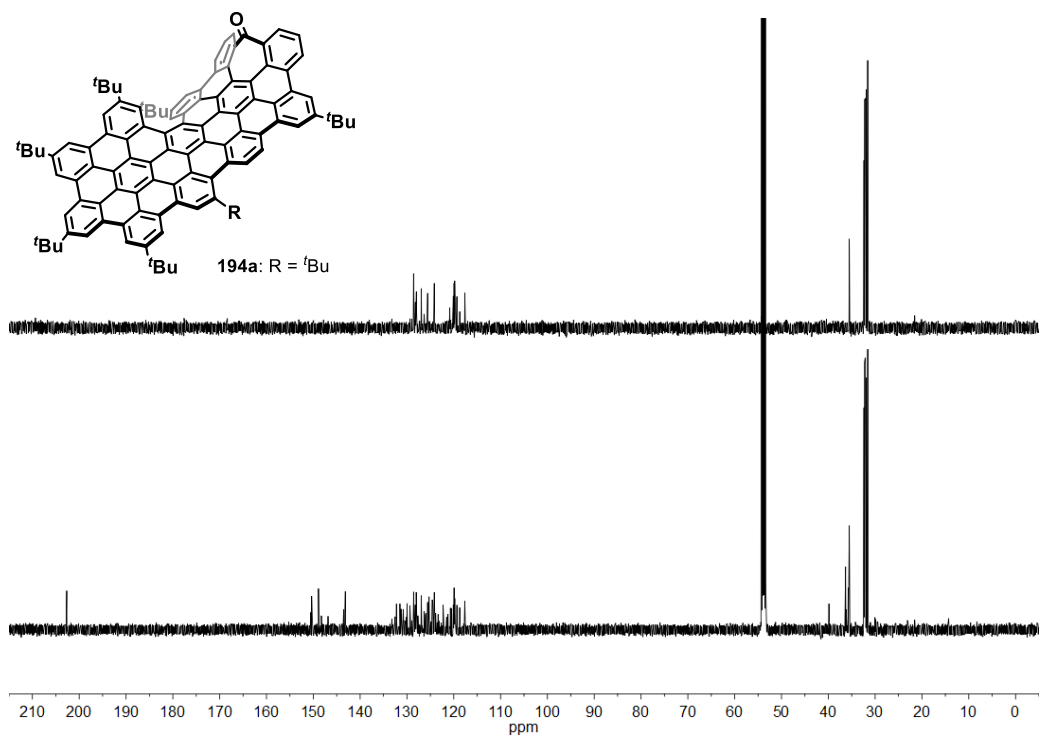
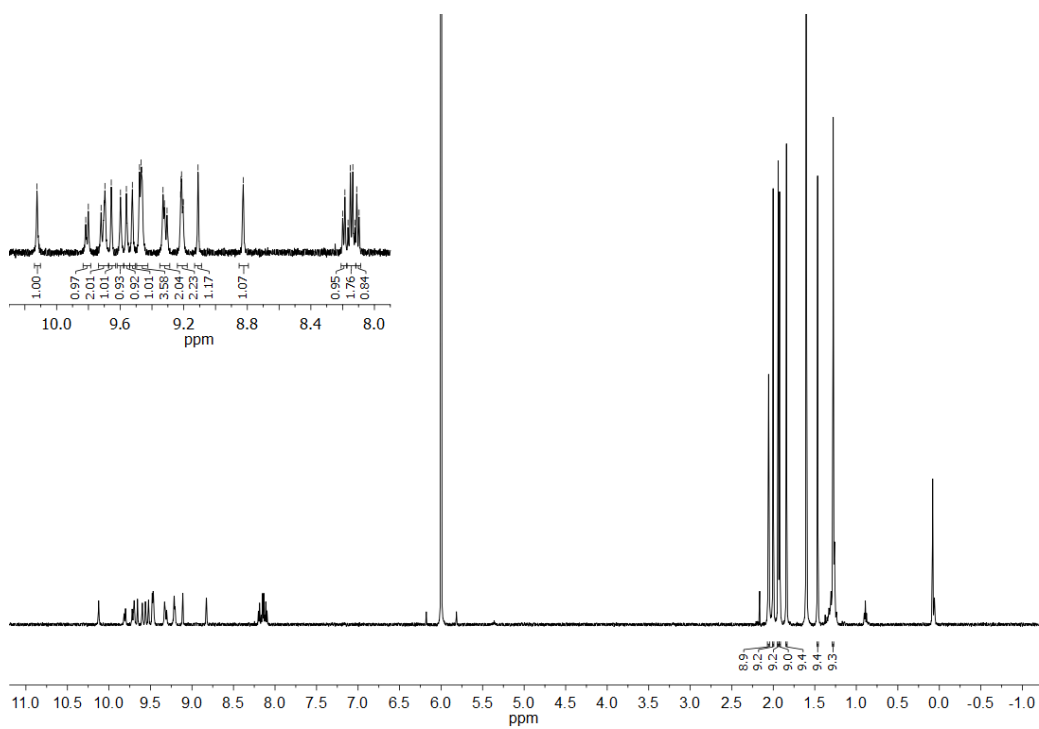


^1H NMR (400 MHz, CD_2Cl_2) and ^{13}C NMR (101 MHz, CD_2Cl_2) spectra of compound **192**.

4. Experimental section

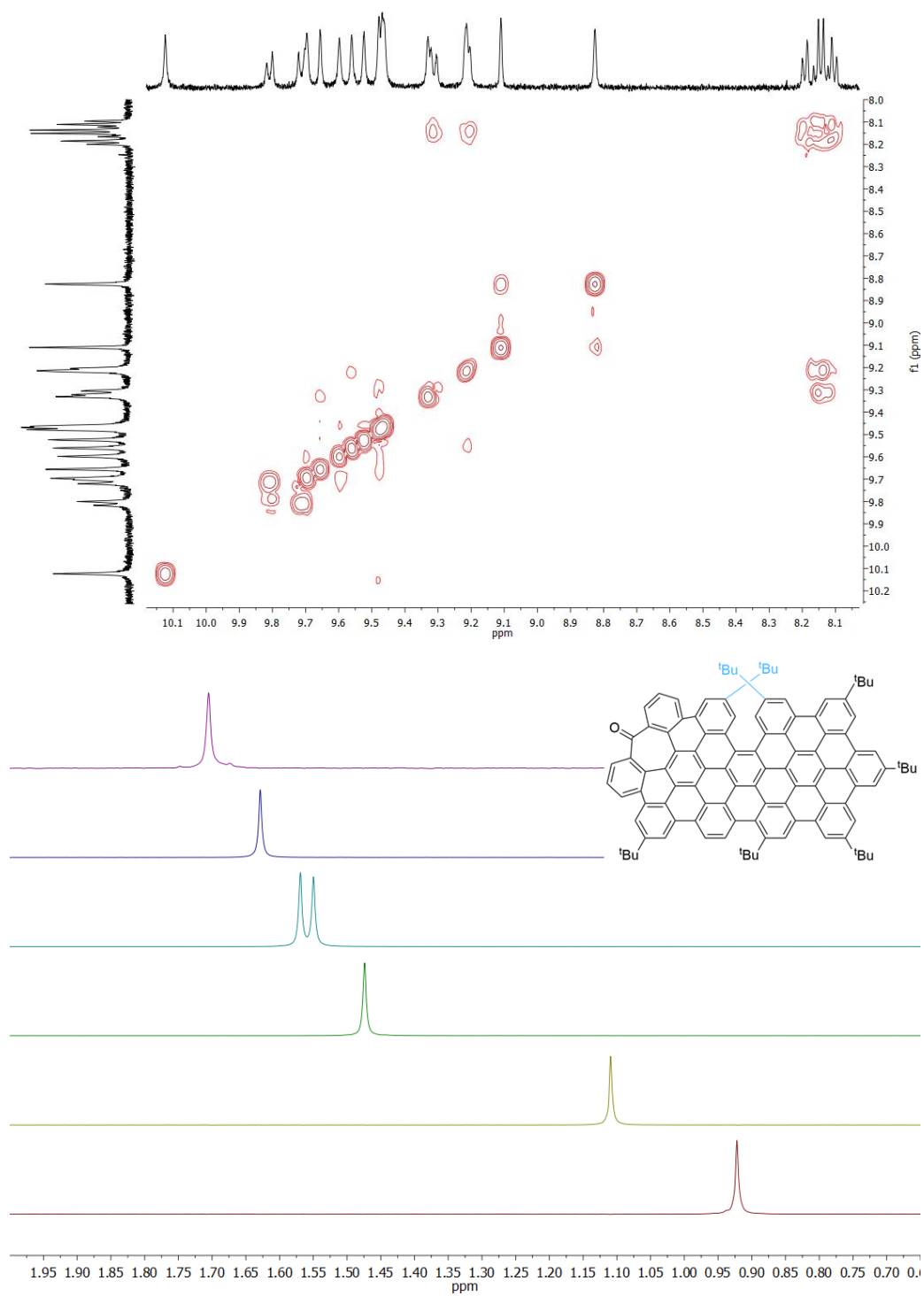


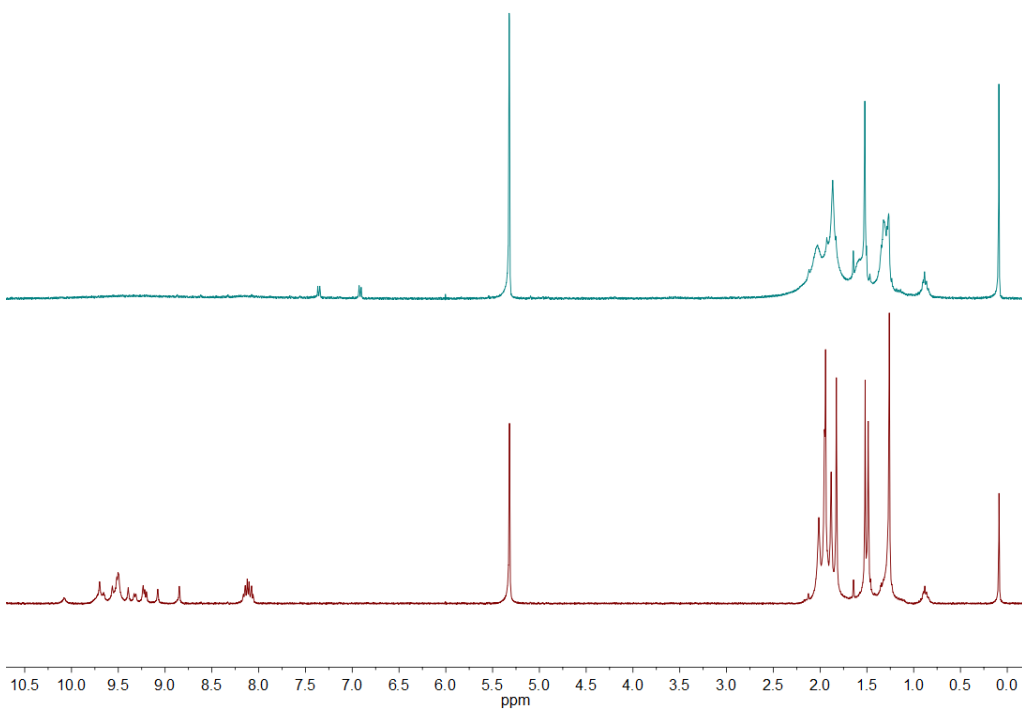
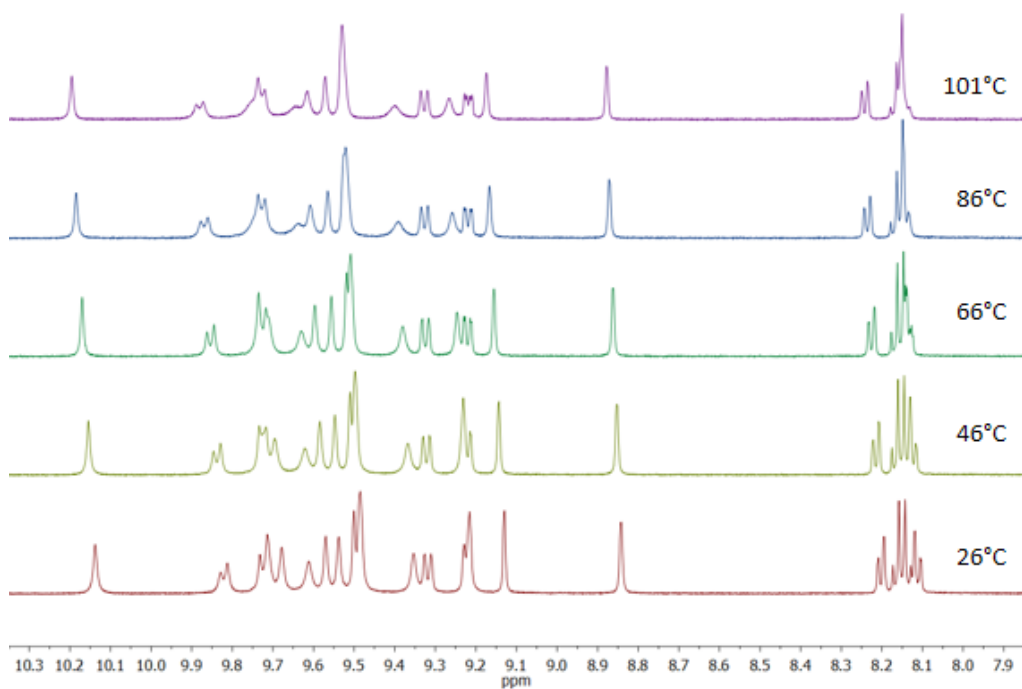
¹H NMR (500 MHz, CD₂Cl₂) and ¹³C NMR (126 MHz, CD₂Cl₂) spectra of compound **193.**



^1H NMR (500 MHz, CDCl_2), ^{13}C NMR and DEPT135 (126 MHz, CD_2Cl_2) spectra of compound **194a**.

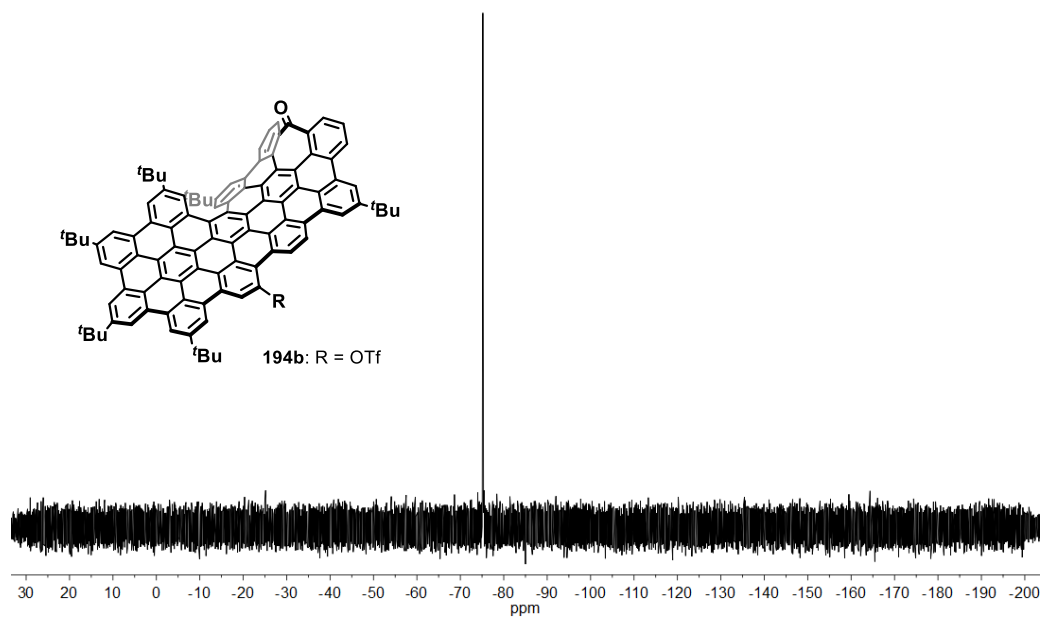
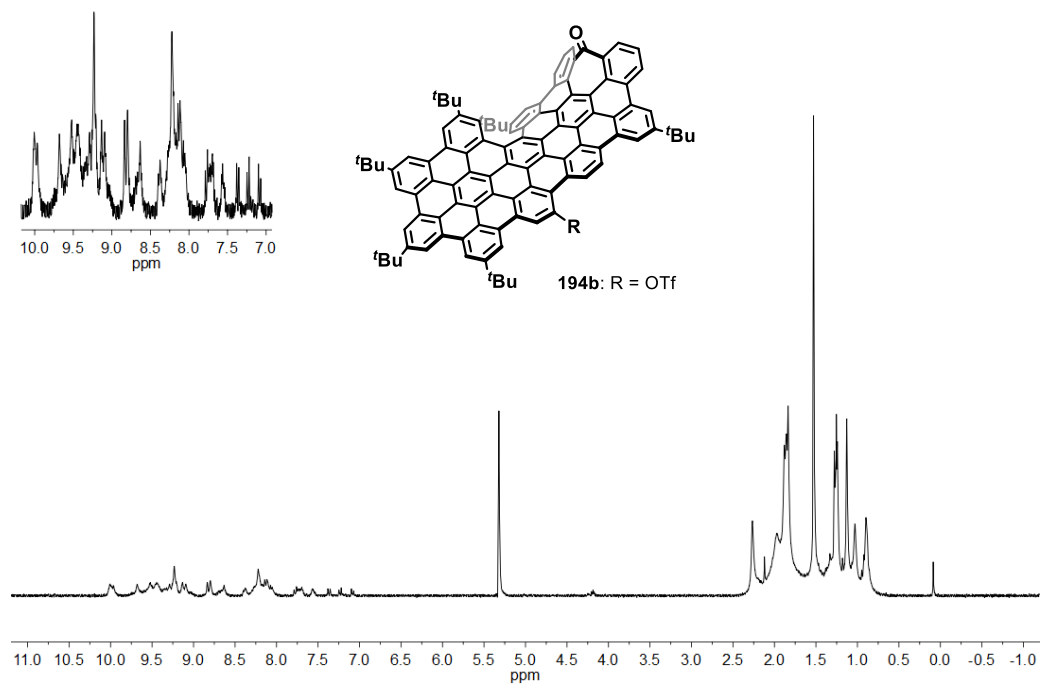
4. Experimental section



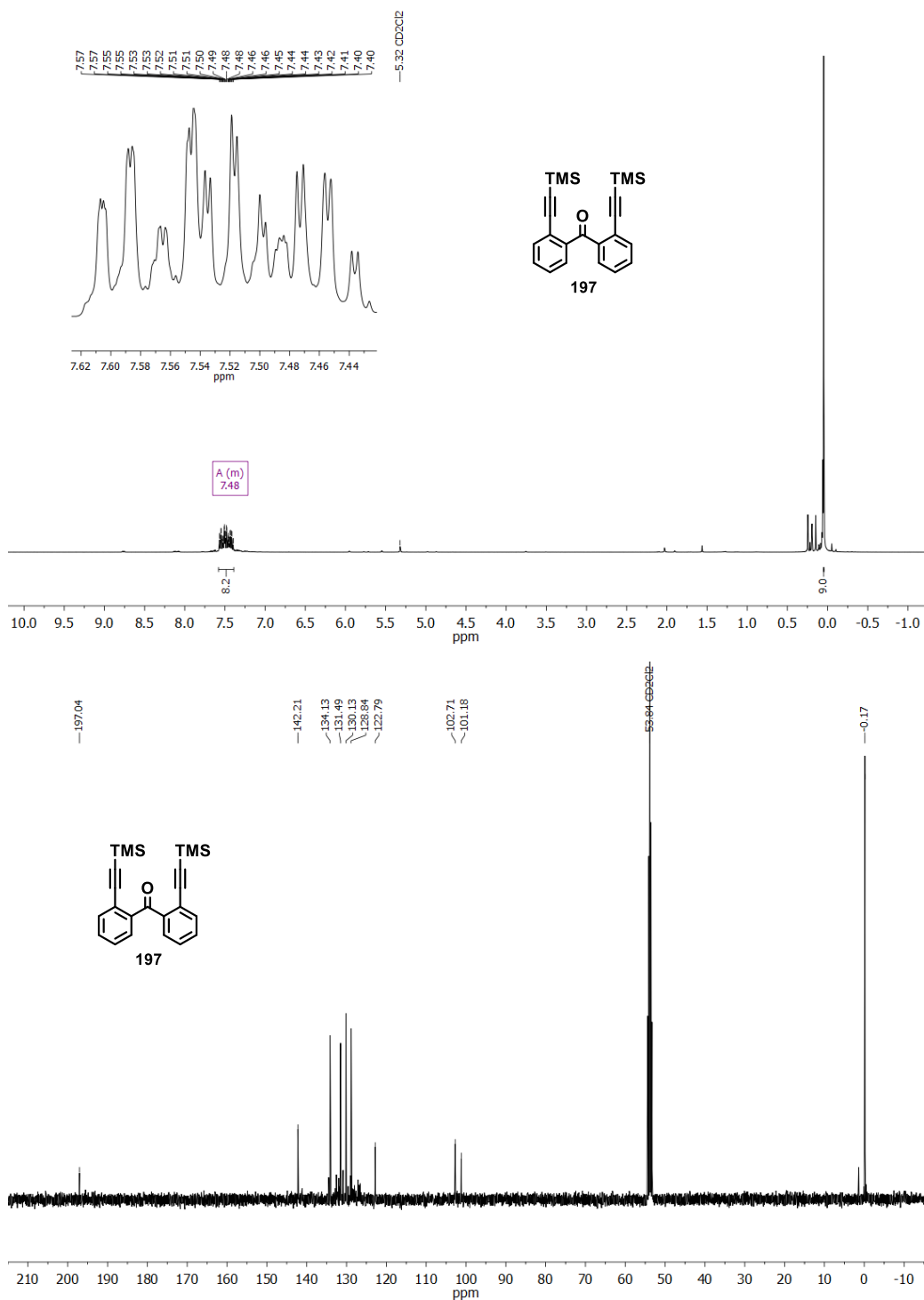


Partial VT ^1H NMR (500 MHz, CDCl_2) spectrum of compound **194a** and ^1H NMR (400 MHz, CD_2Cl_2) spectrum of compound **194a** before (bottom, red) and after addition of 1 eq. of "magic blue" (bottom, blue).

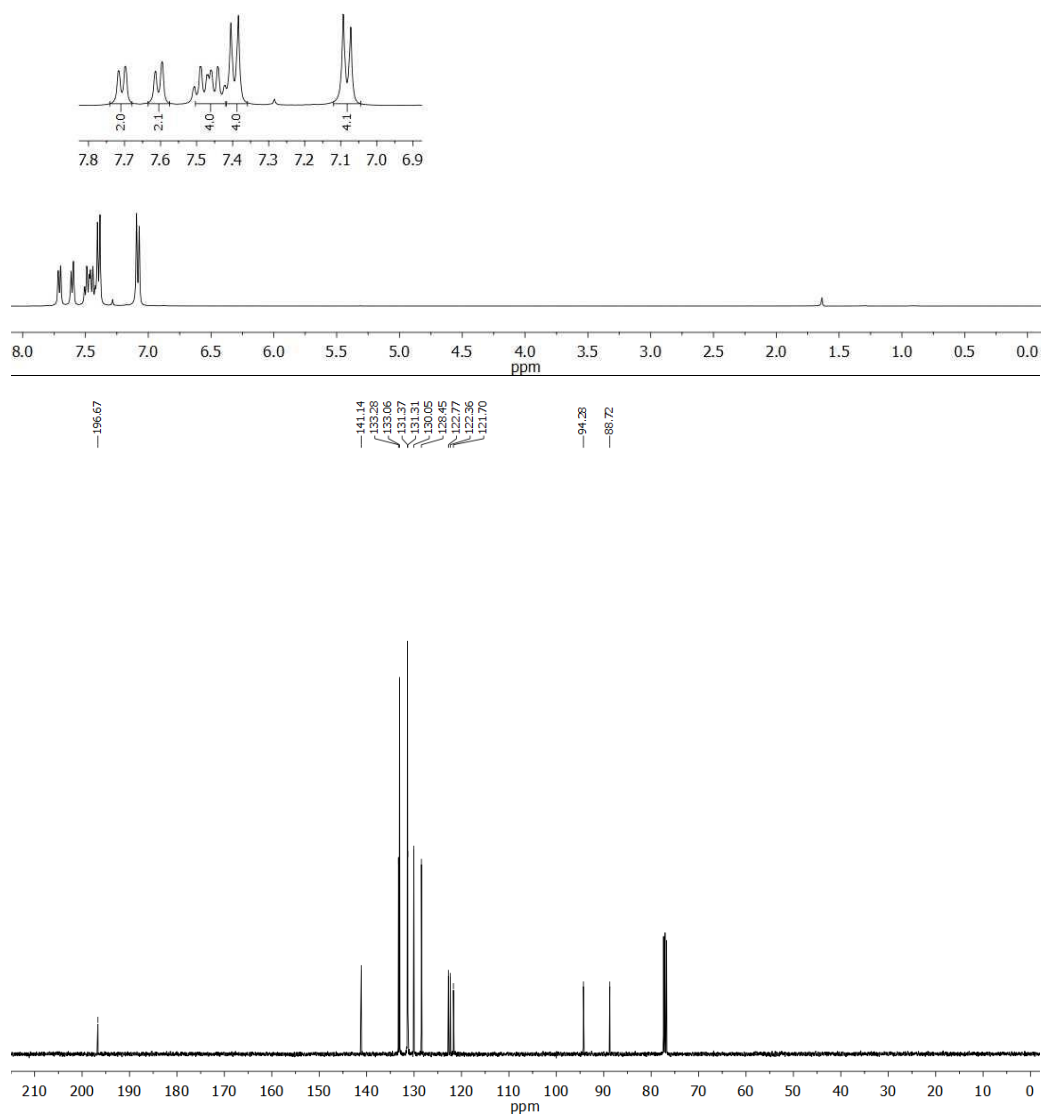
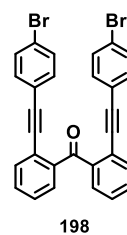
4. Experimental section

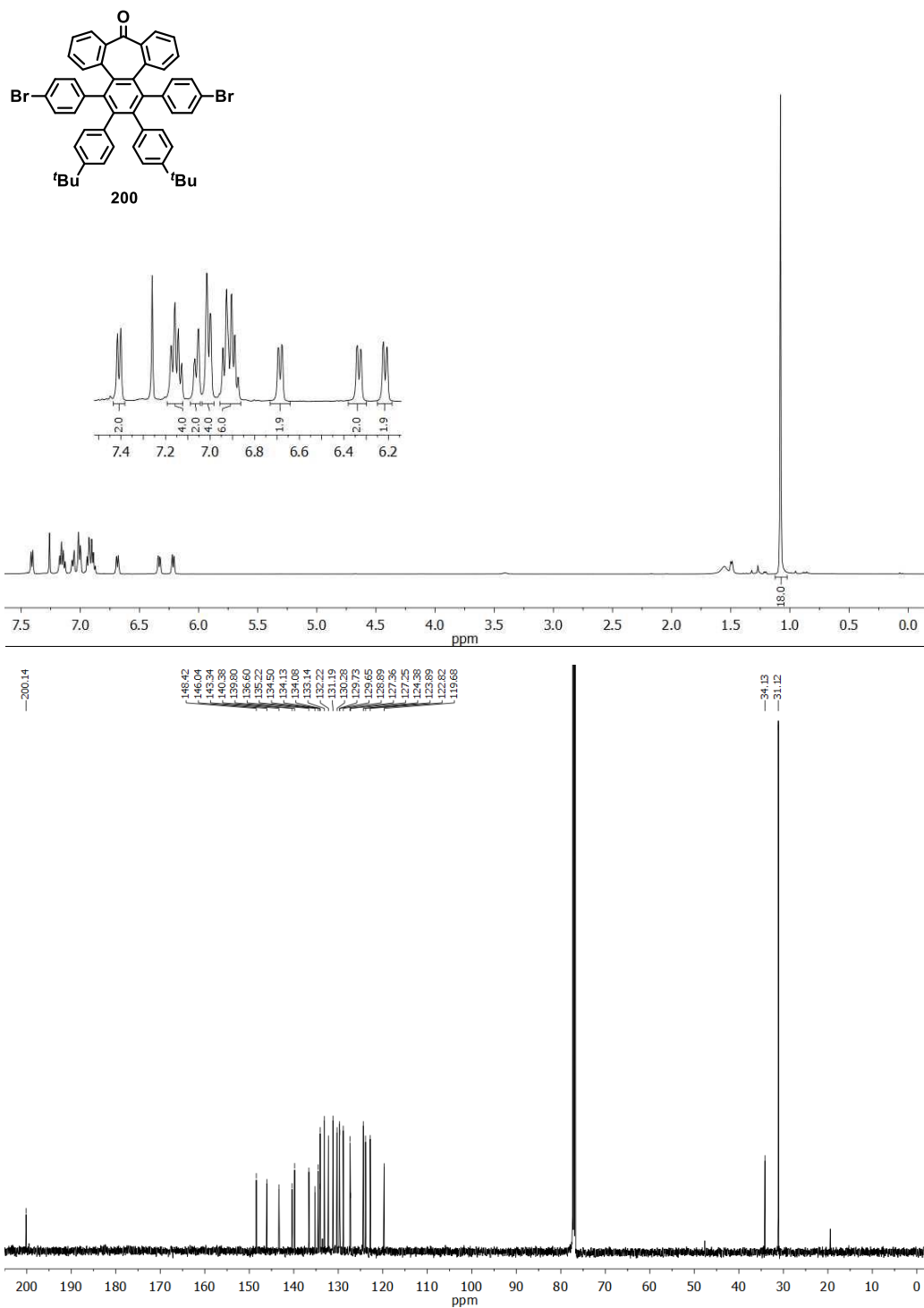


^1H NMR (300 MHz, CD_2Cl_2) and ^{19}F NMR (377 MHz, $(\text{CD}_2\text{Cl}_2)_2$) spectra of compound **194b**.

 ^1H NMR (500 MHz, CD_2Cl_2) and ^{13}C NMR (126 MHz, CD_2Cl_2) spectra of compound **197**.

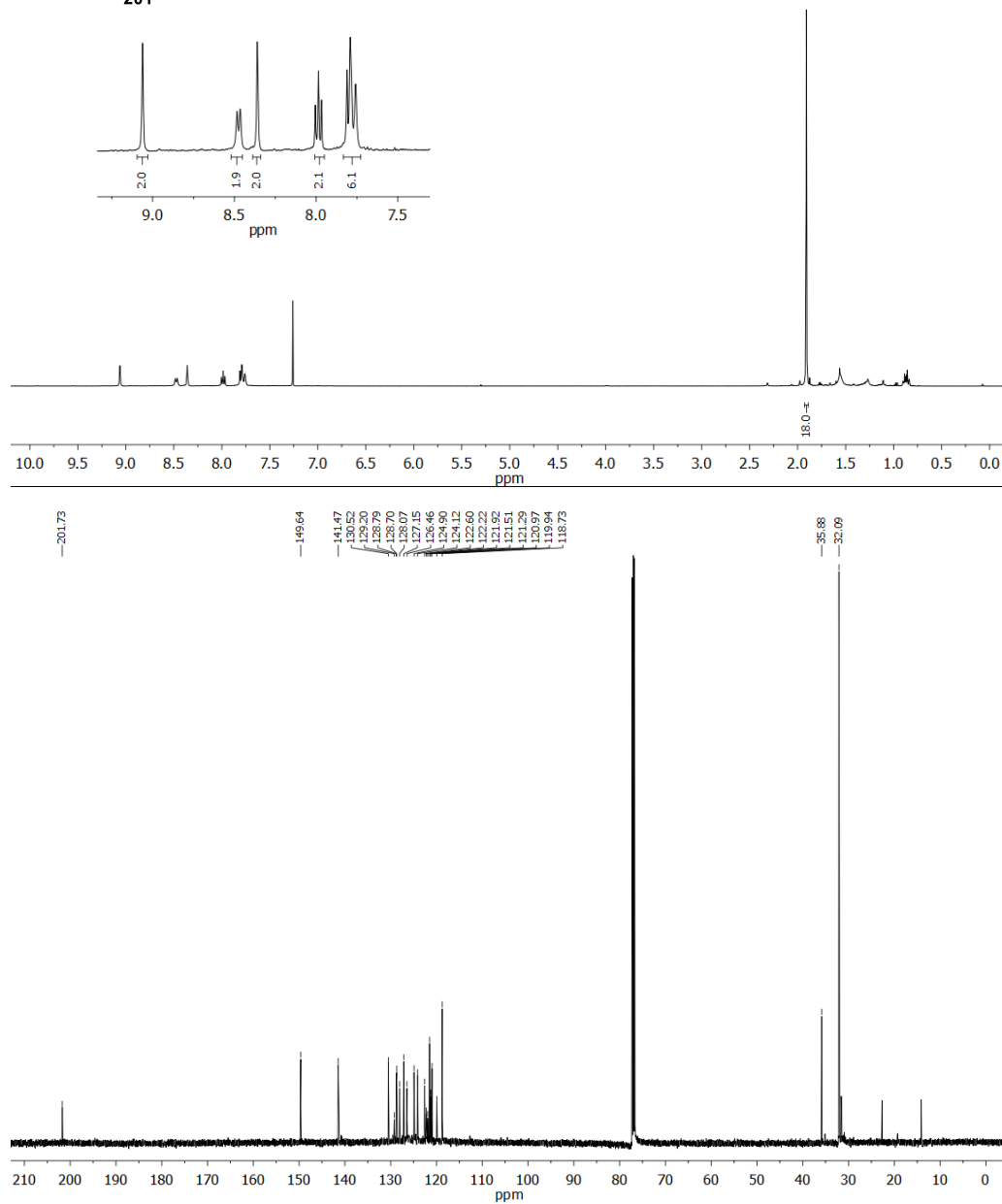
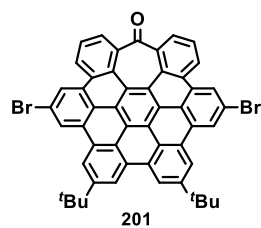
4. Experimental section



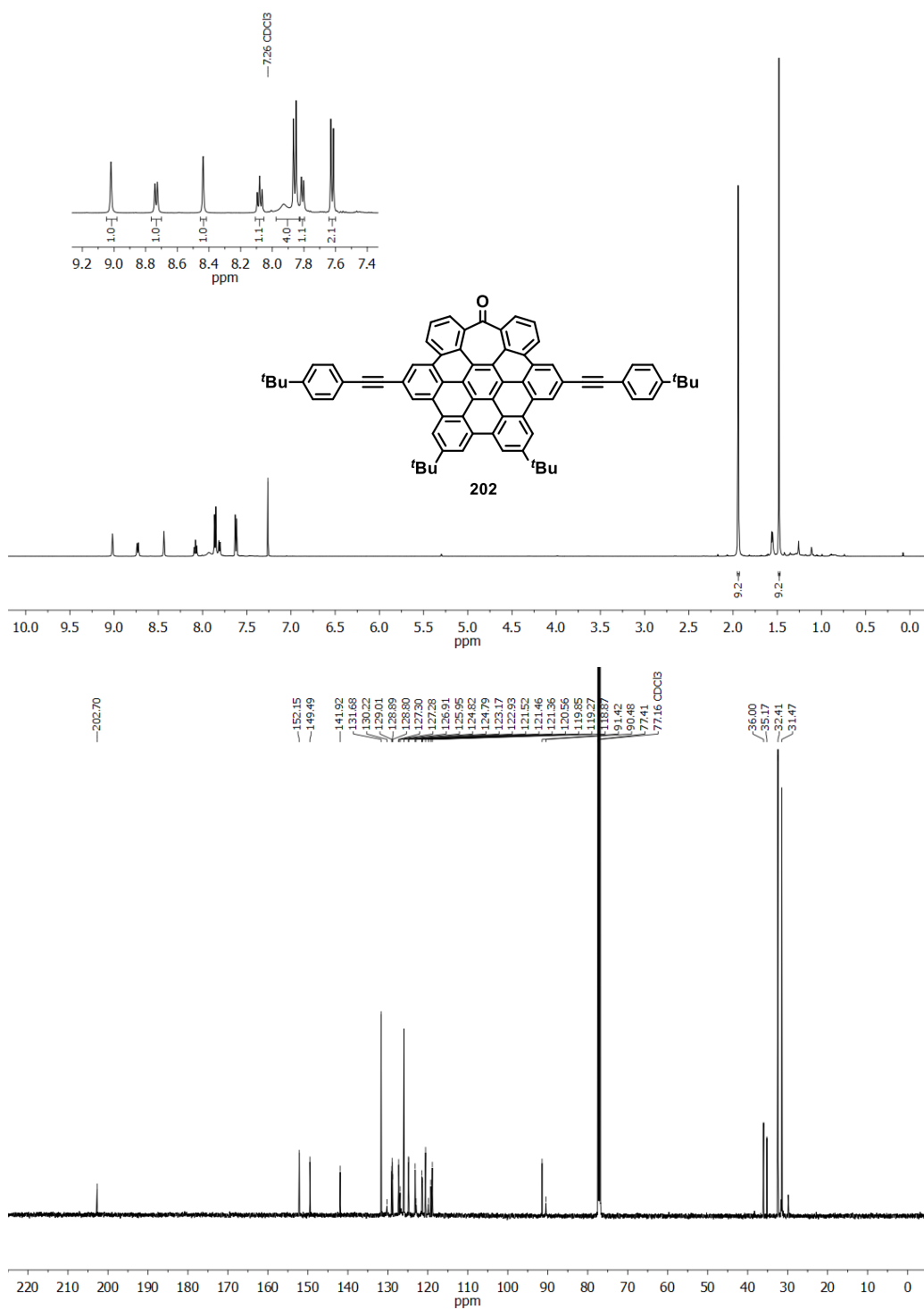


^1H NMR (500 MHz, CDCl_3) and ^{13}C NMR (126 MHz, CDCl_3) spectra of compound **200**.

4. Experimental section

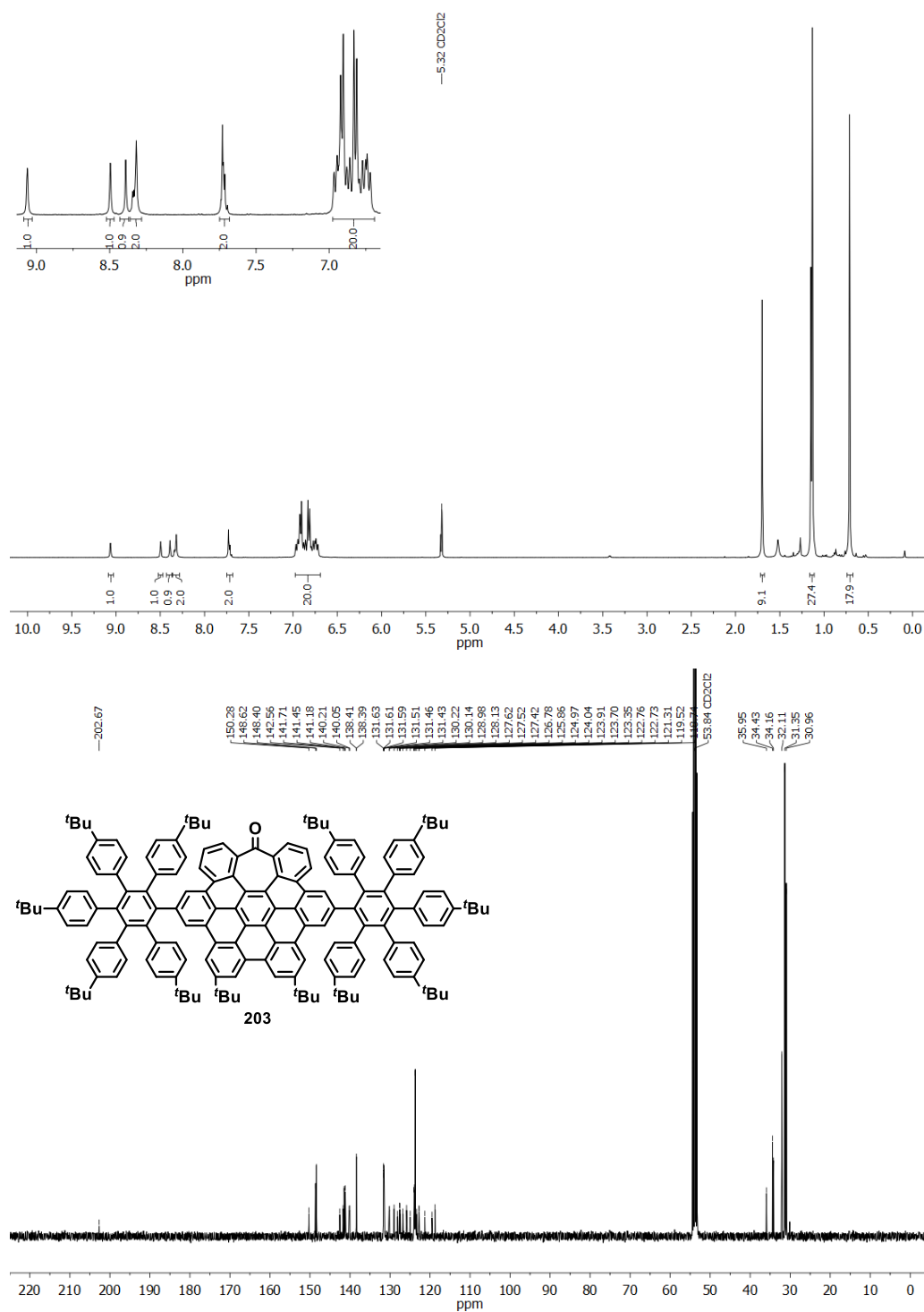


¹H NMR (400 MHz, CDCl₃) and ¹³C NMR (101 MHz, CDCl₃) spectra of compound **201**.

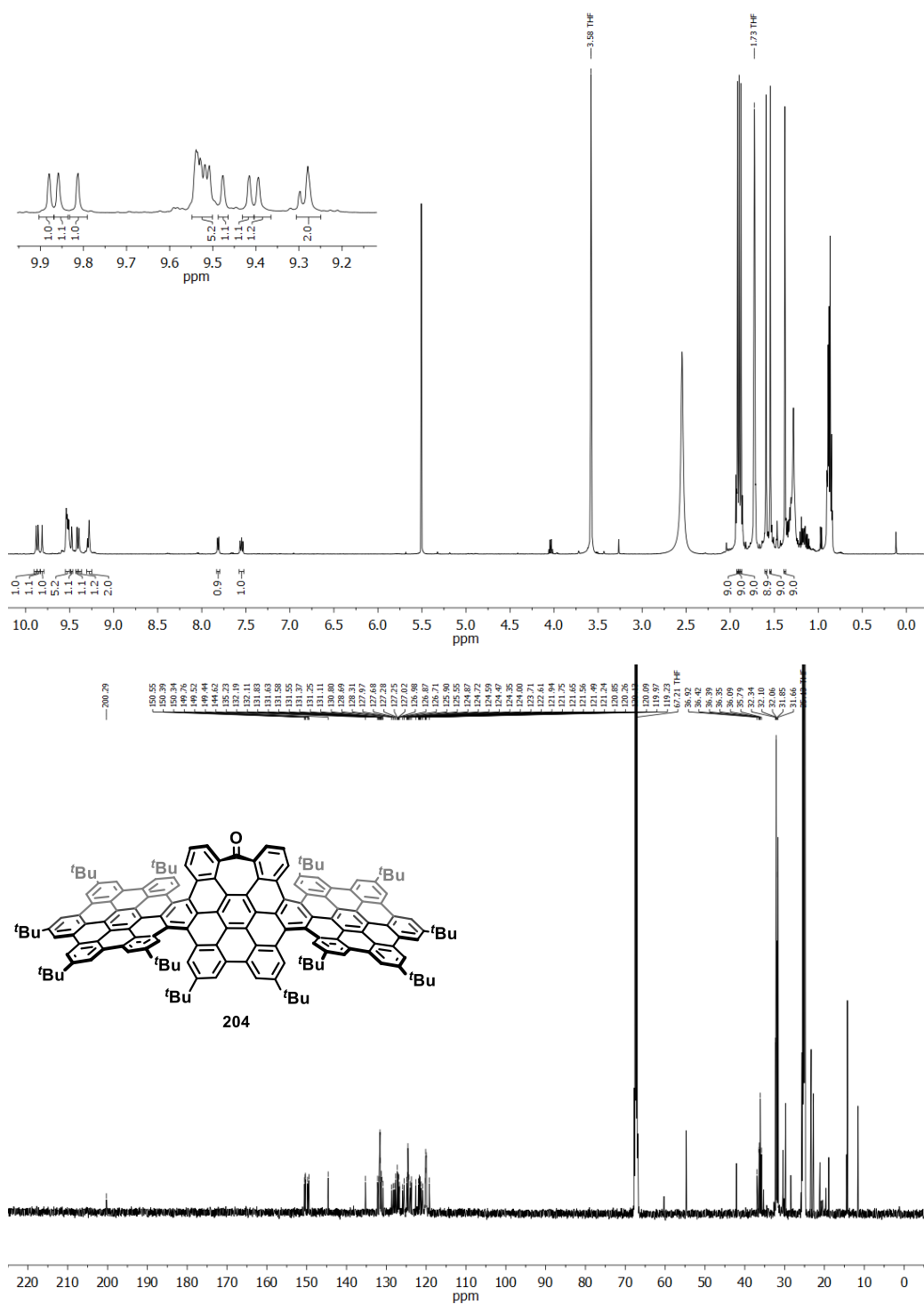


¹H NMR (500 MHz, CDCl₃) and ¹³C NMR (126 MHz, CDCl₃) spectra of compound **202.**

4. Experimental section

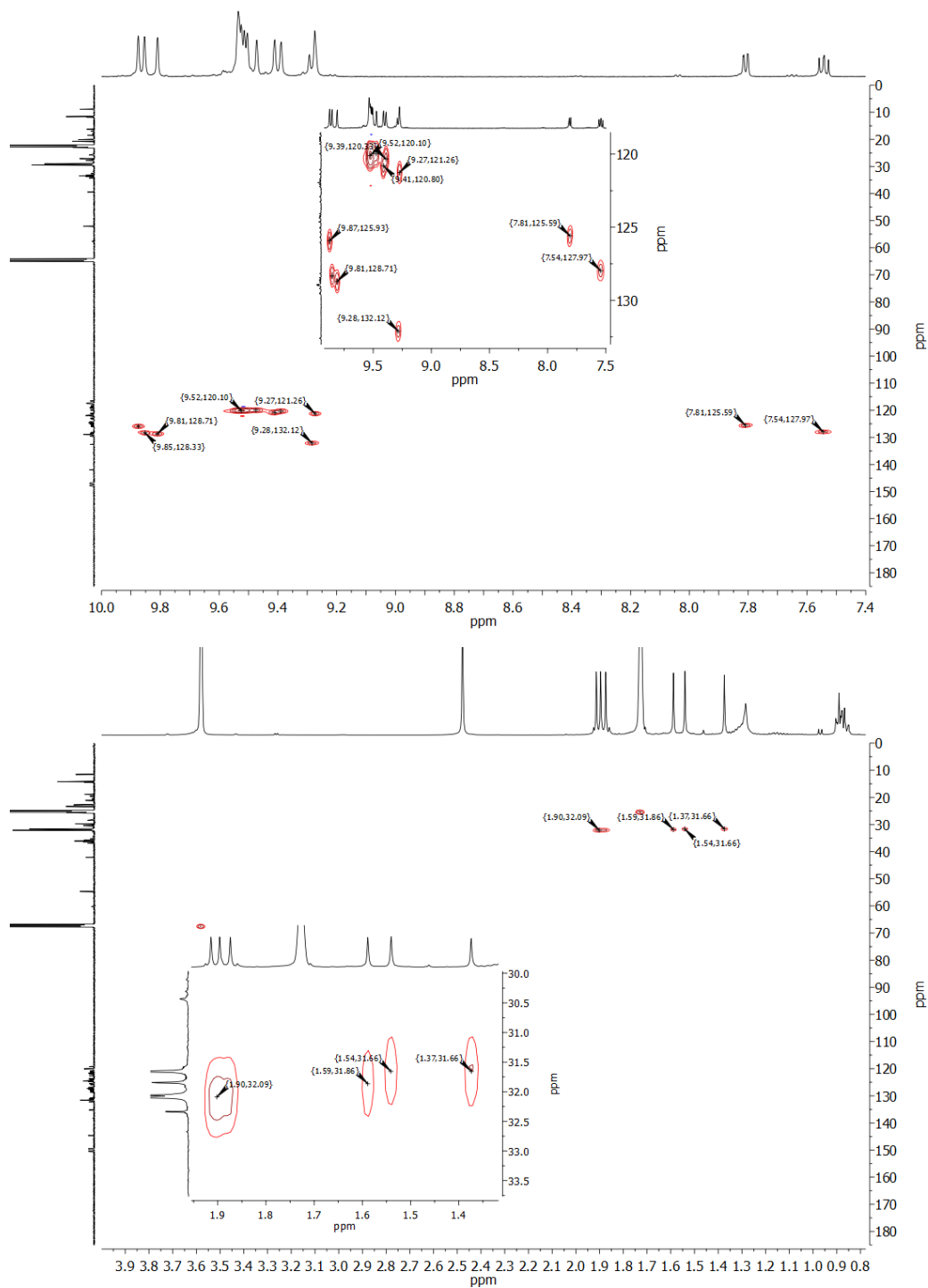


¹H NMR (400 MHz, CD₂Cl₂) and ¹³C NMR (101 MHz, CD₂Cl₂) spectra of compound **203**.

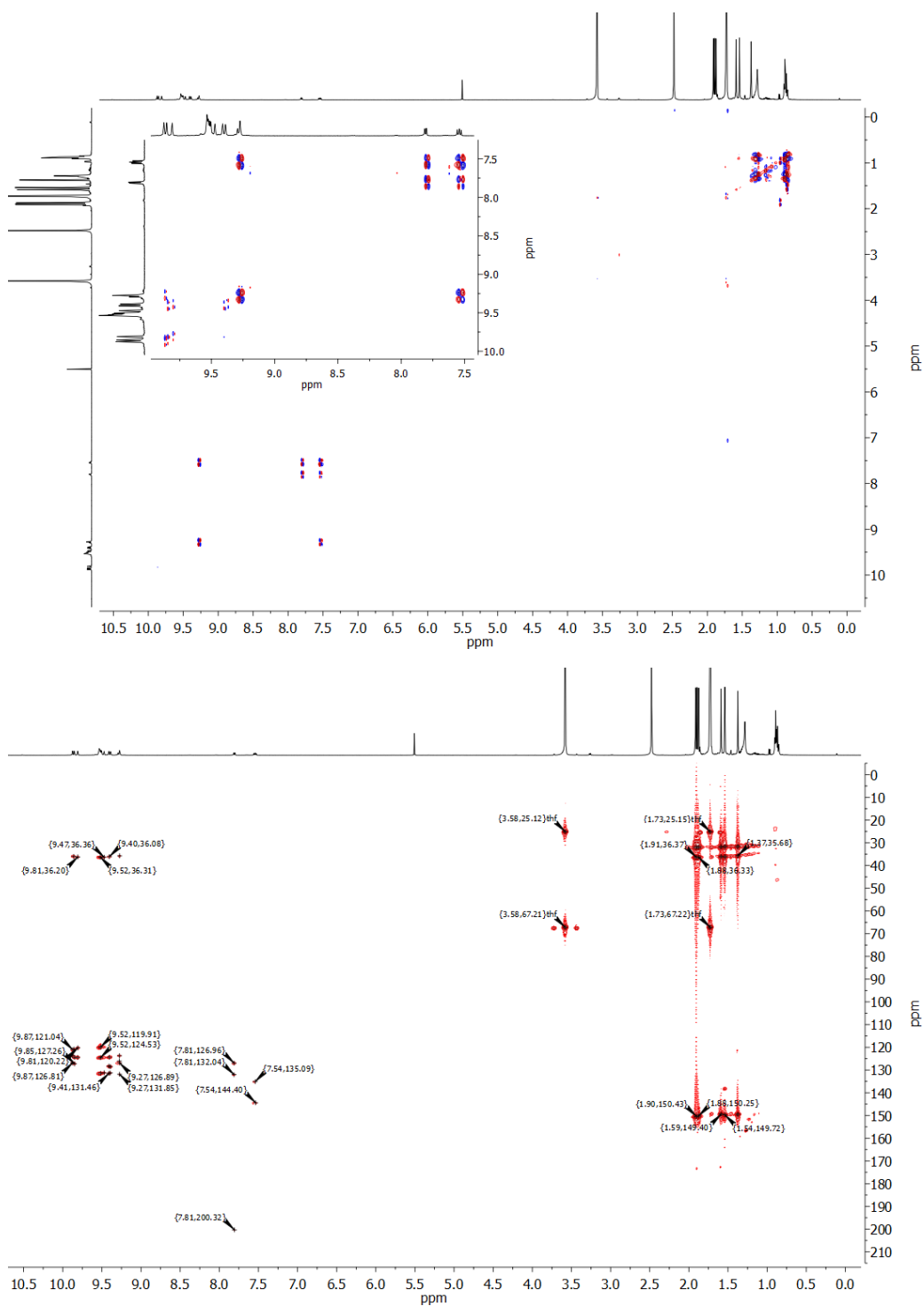


¹H NMR (500 MHz, C₄D₈O) and ¹³C NMR (126 MHz, C₄D₈O) spectra of compound **204.**

4. Experimental section

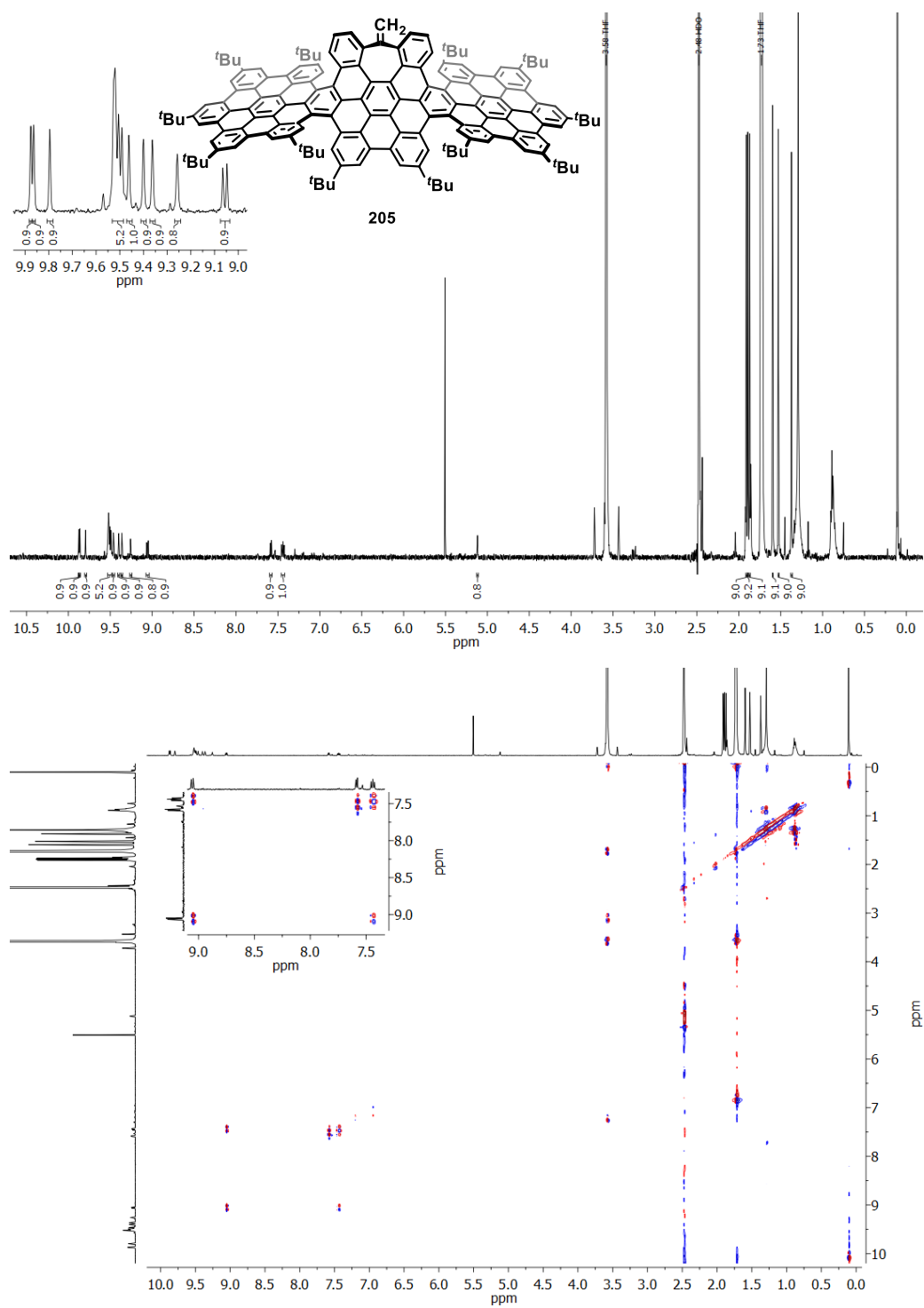


Partial ^1H ^{13}C HSQC (500 MHz, $\text{C}_4\text{D}_8\text{O}$) spectra of compound **204**.

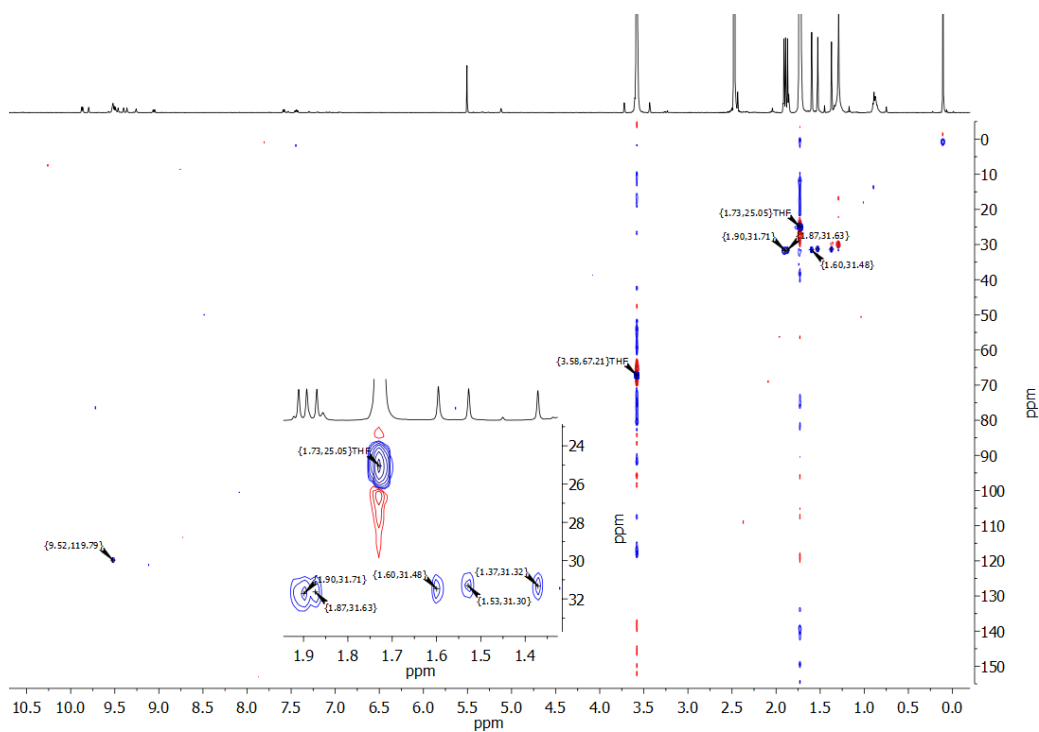


^1H ^1H COSY (500 MHz, $\text{C}_4\text{D}_8\text{O}$) and ^1H ^{13}C HMBC (500 MHz, 126 MHz, $\text{C}_4\text{D}_8\text{O}$) spectra of compound **204**.

4. Experimental section

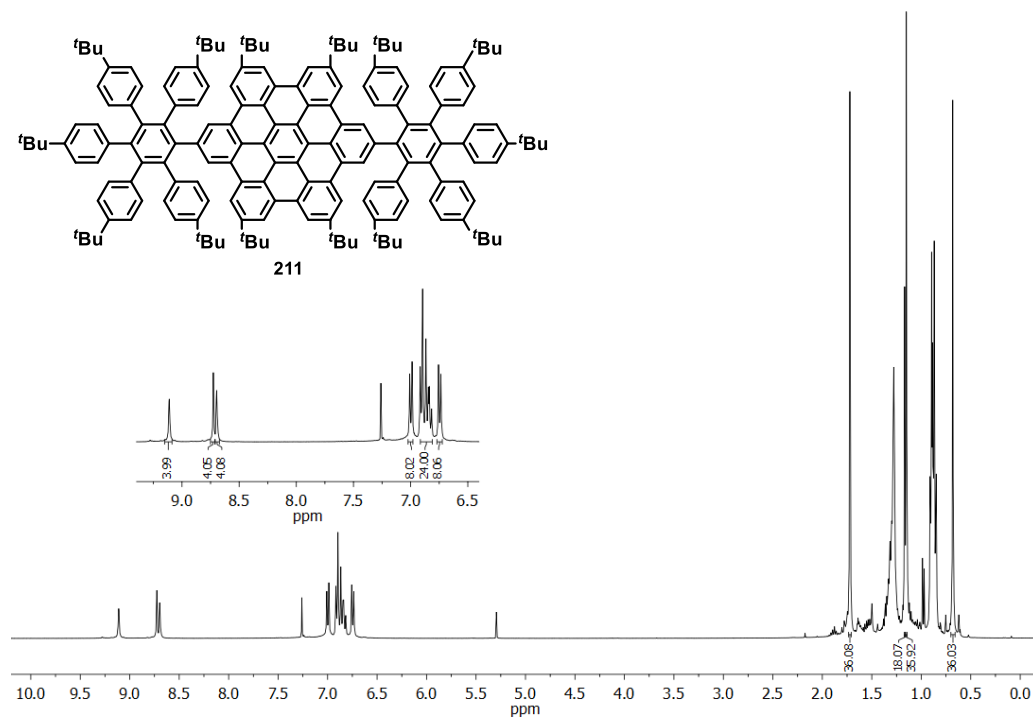
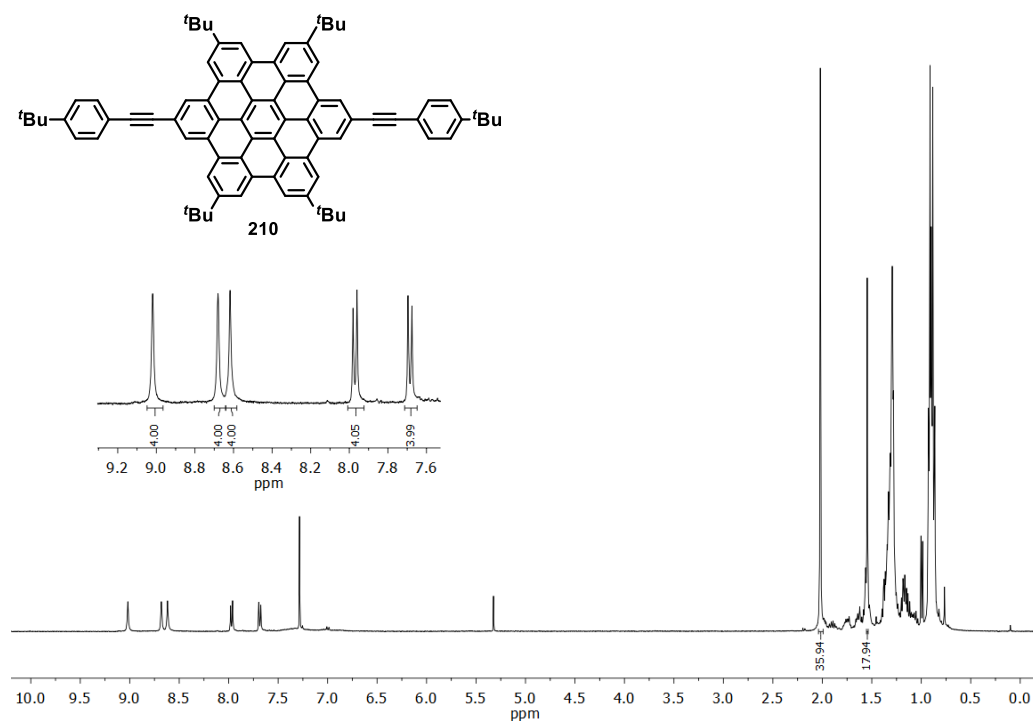


¹H NMR (500 MHz, C₄D₈O) and ²D COSY (500 MHz, C₄D₈O) spectra of compound **205**.

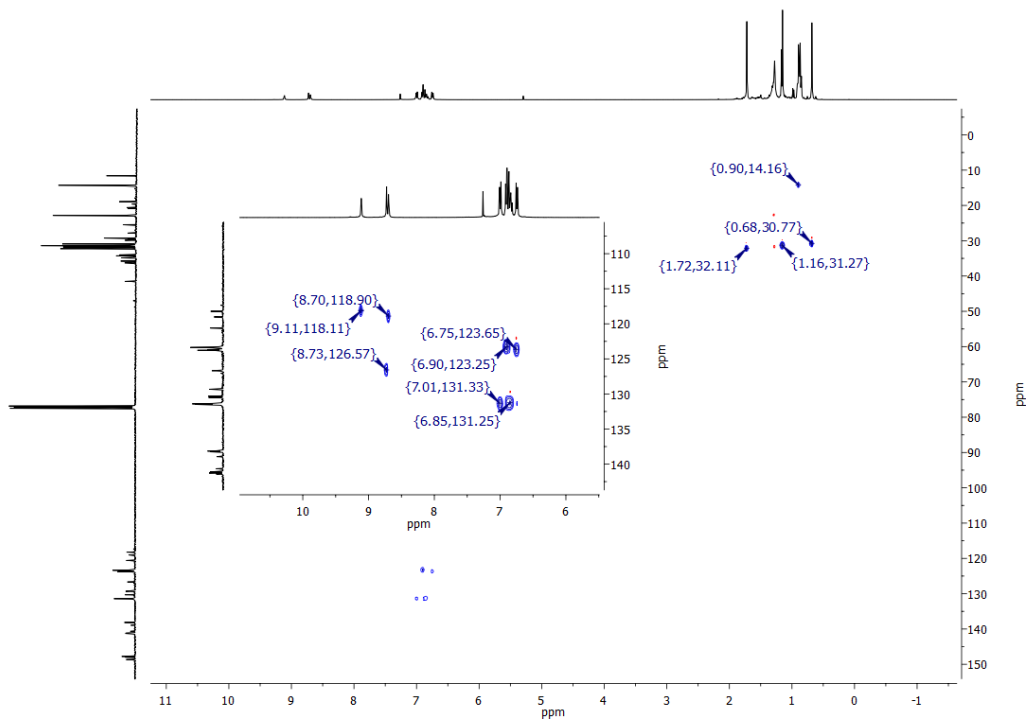
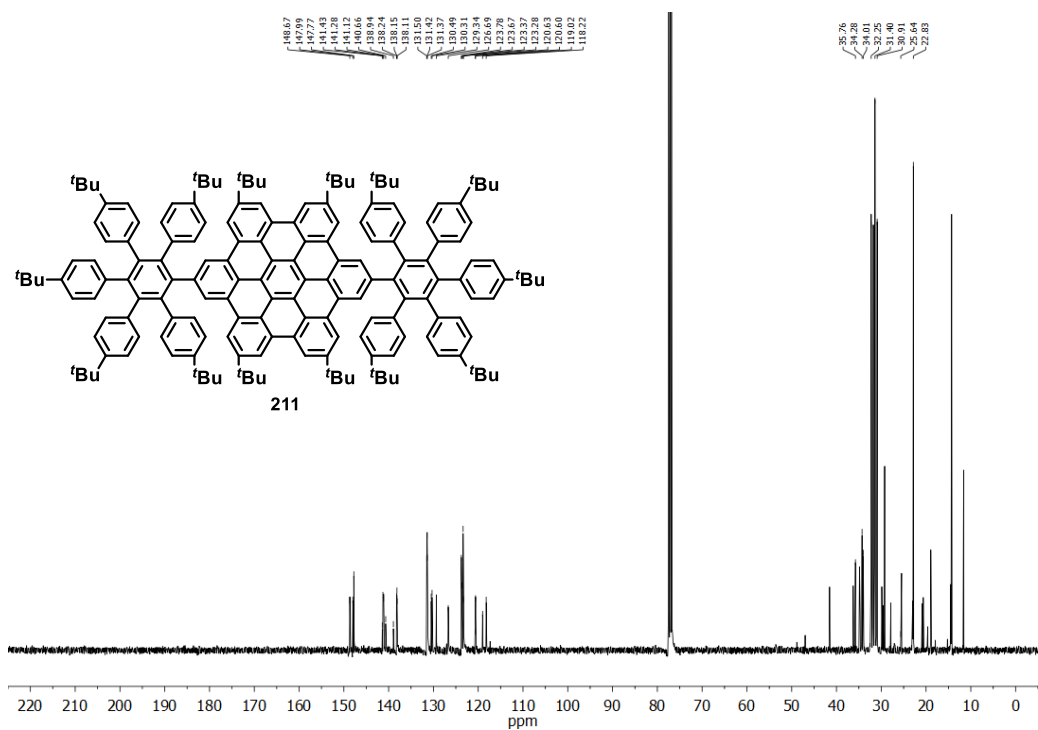


^1H ^{13}C HSQC and ^1H ^{13}C HMBC (500 MHz, 126 MHz, $\text{C}_4\text{D}_8\text{O}$) spectra of compound **205**.

4. Experimental section

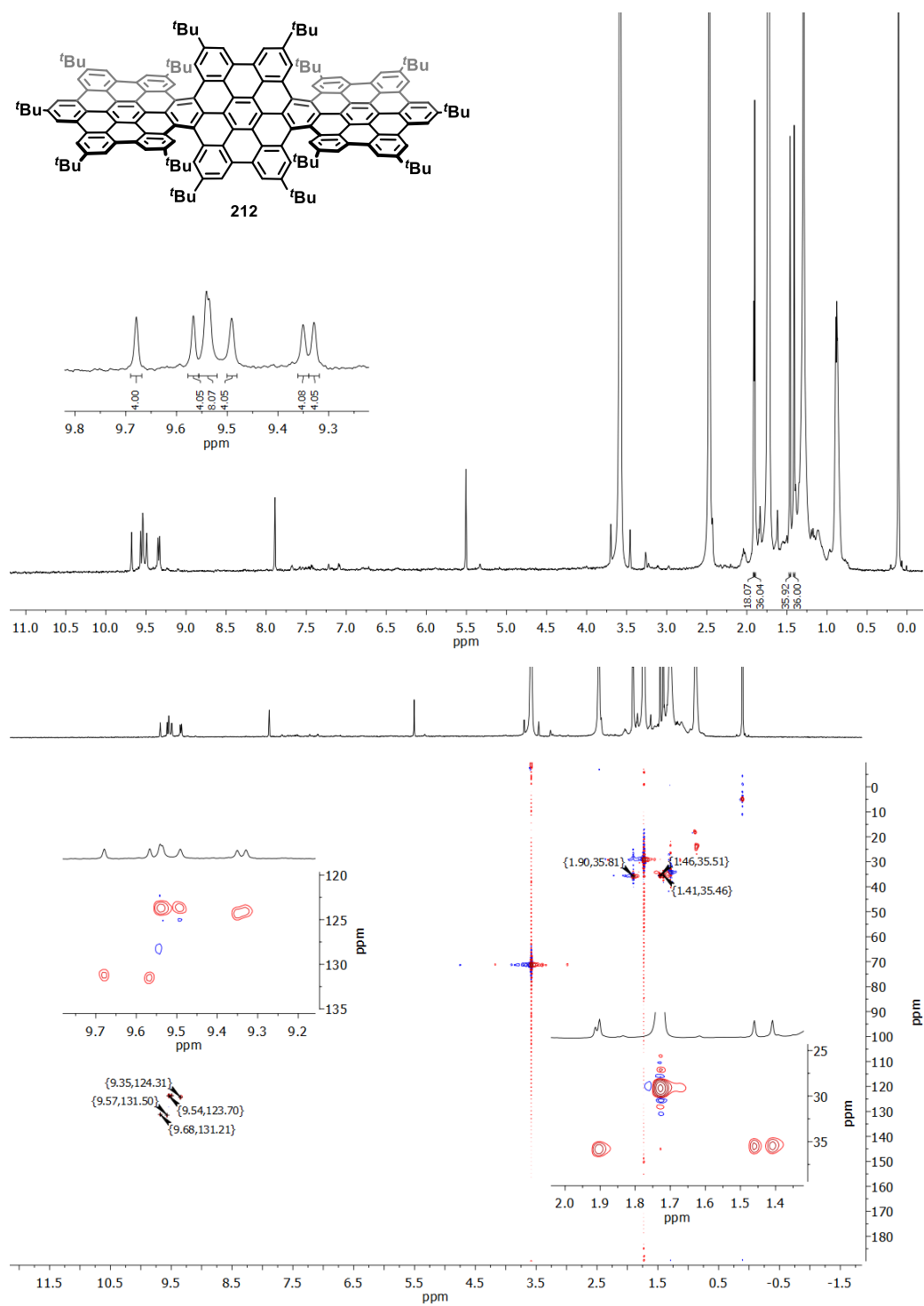


$^1\text{H NMR}$ (400 MHz, CDCl_3) spectrum of compound **210** and $^1\text{H NMR}$ (400 MHz, CDCl_3) spectrum of compound **211**.

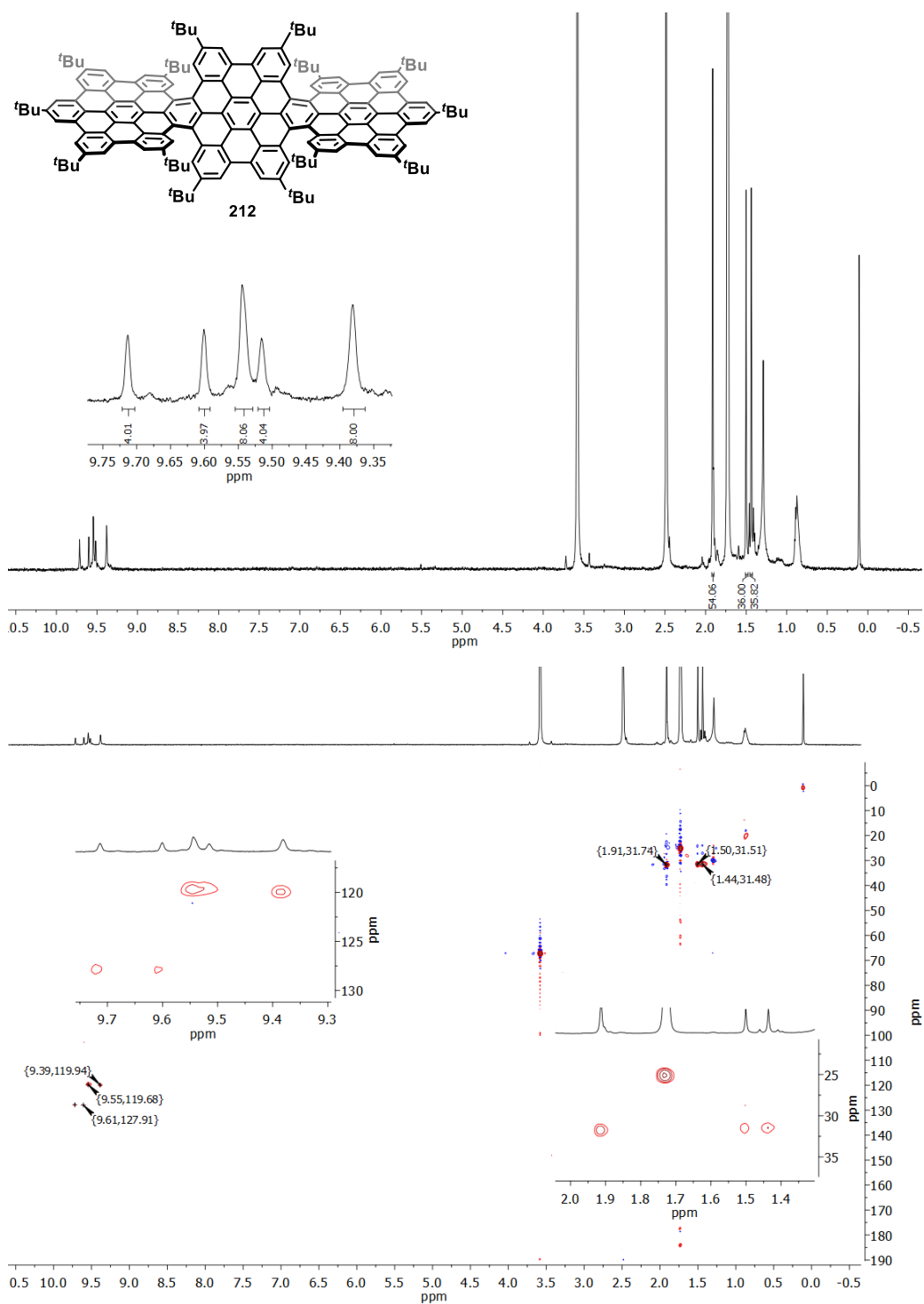


^{13}C NMR (101 MHz, CDCl_3) and ^1H ^{13}C HSQC (400 MHz, 101 MHz, CDCl_3) spectrum of compound **211**.

4. Experimental section

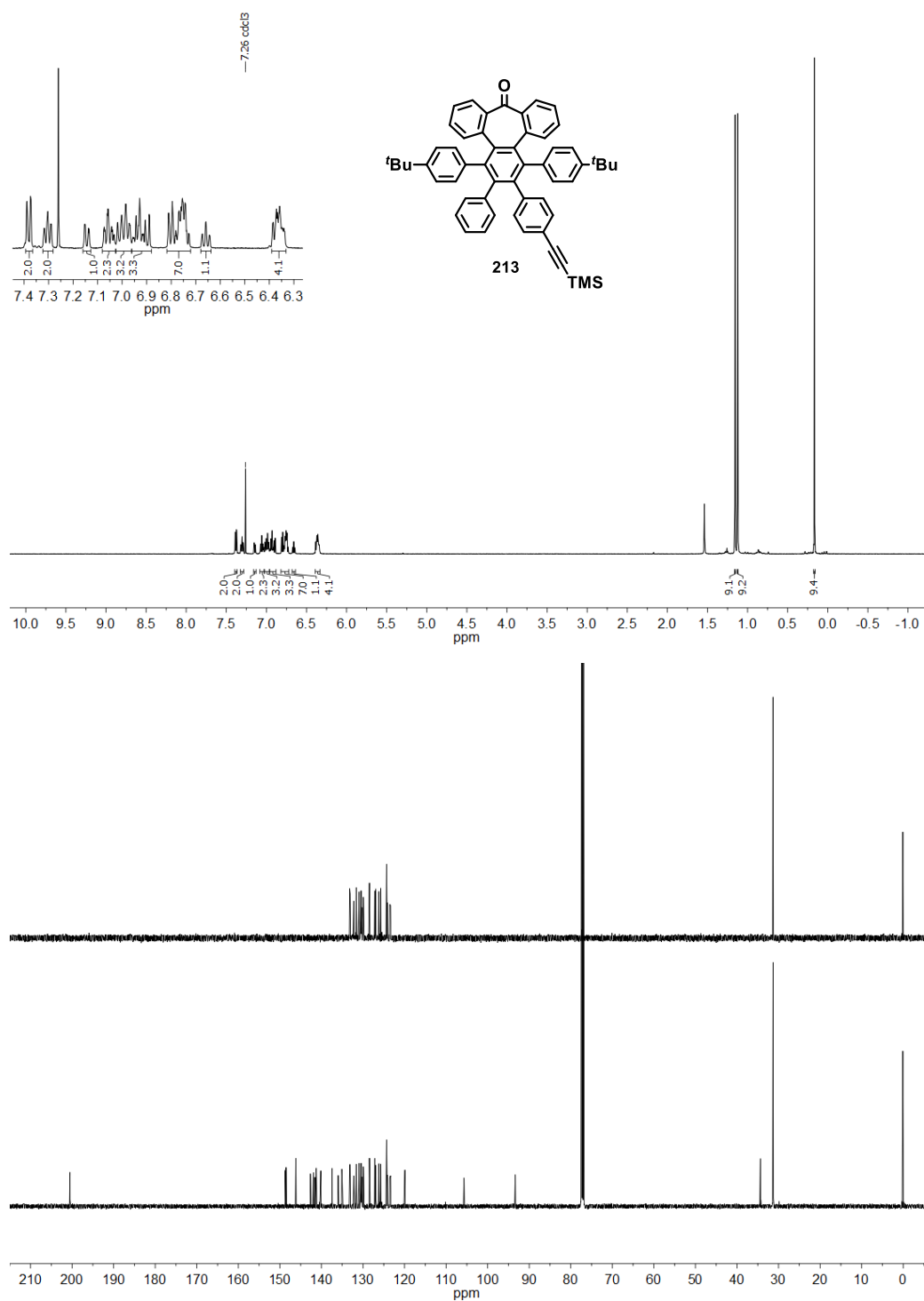


¹H NMR (600 MHz, C₄D₈O) and ¹H ¹³C HSQC (600 MHz, 151 MHz, C₄D₈O) spectra of compound **212a**.

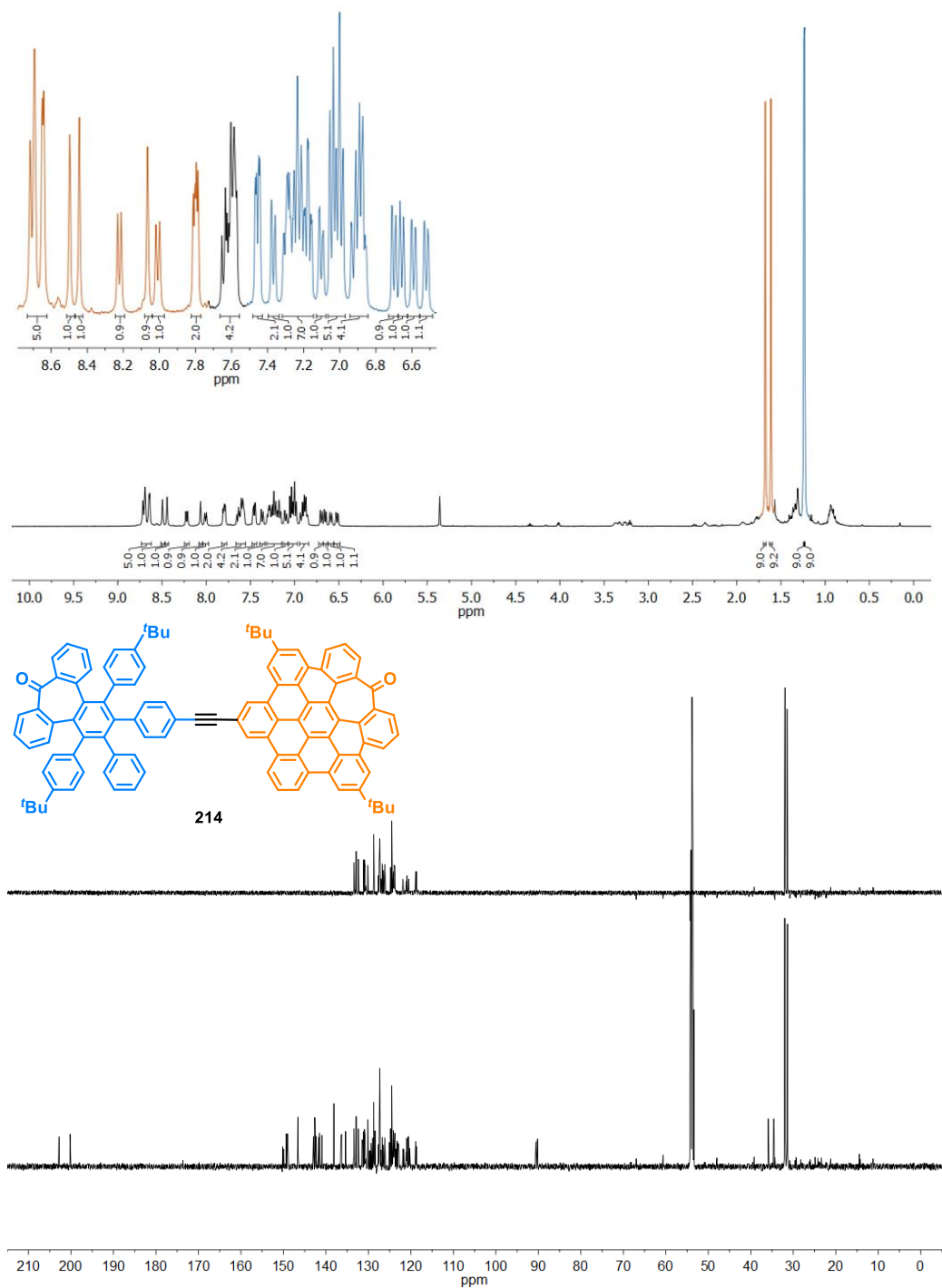


^1H NMR (600 MHz, $\text{C}_4\text{D}_8\text{O}$) and ^1H ^{13}C HSQC (600 MHz, 151 MHz, $\text{C}_4\text{D}_8\text{O}$) spectra of compound **212b**.

4. Experimental section

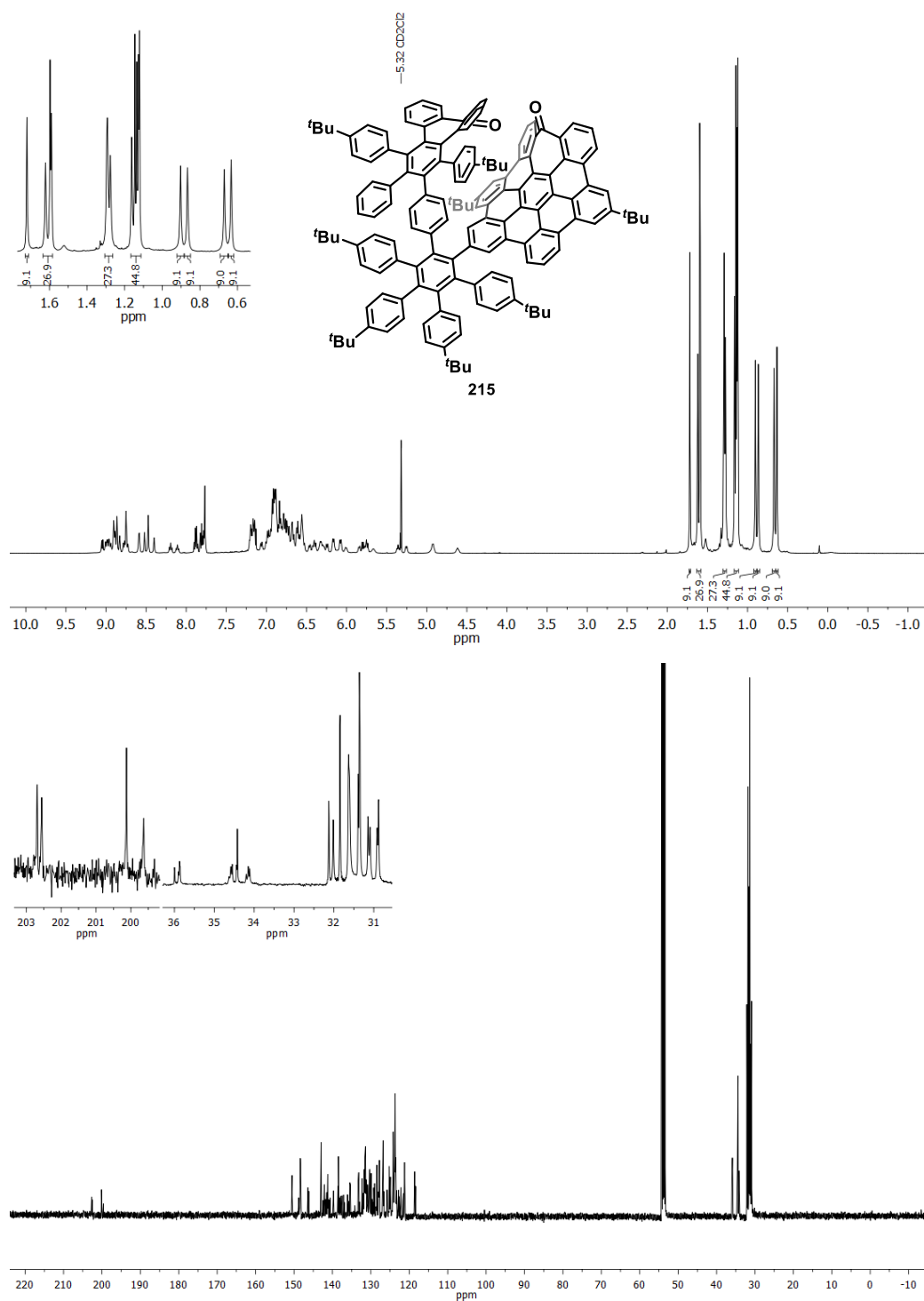


^1H NMR (500 MHz, CDCl_3), ^{13}C NMR and DEPT135 (126 MHz, CDCl_3) spectra of compound **213**.

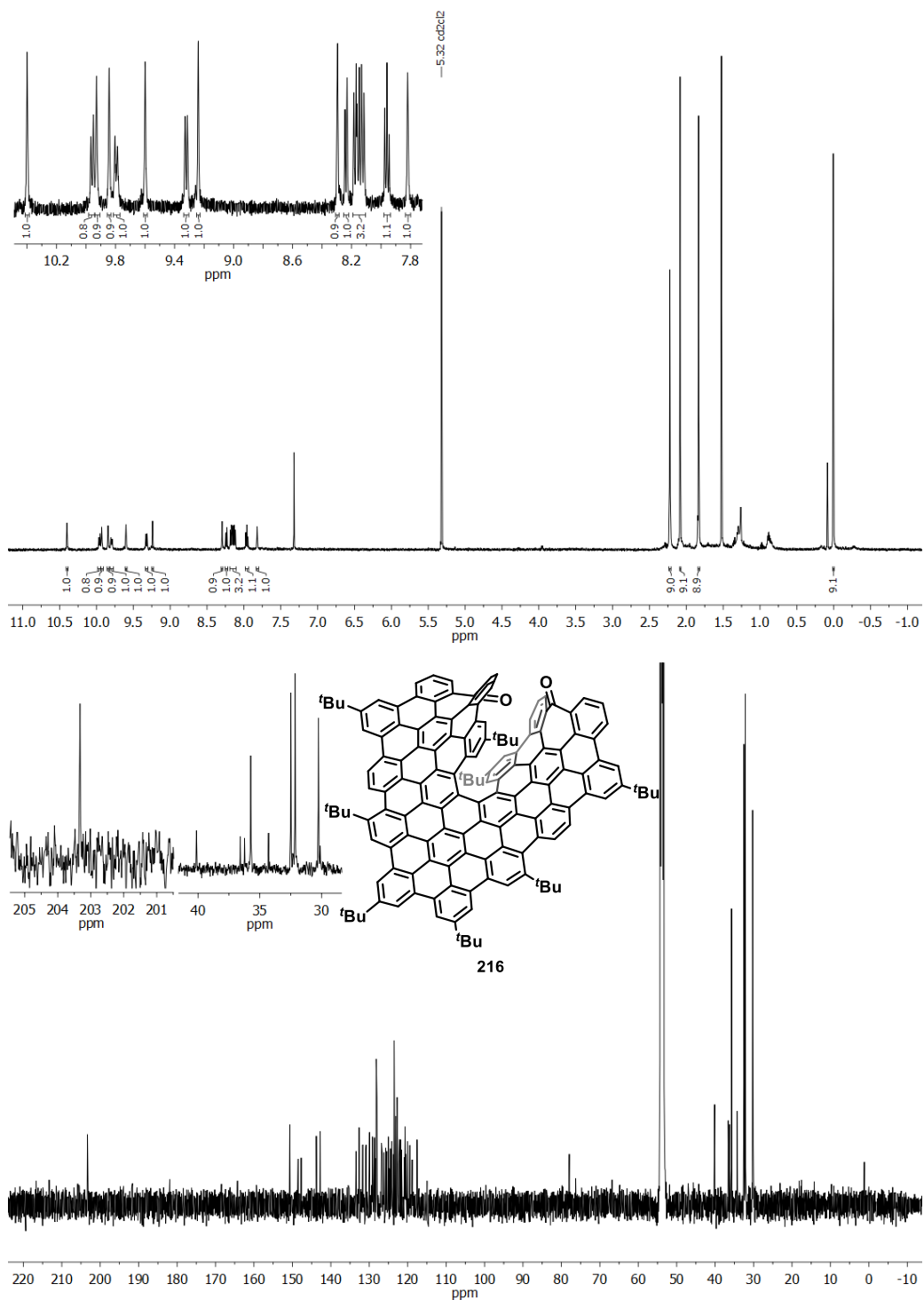


^1H NMR (400 MHz, CD_2Cl_2), ^{13}C NMR and DEPT135 (126 MHz, CD_2Cl_2) spectra of compound **214**.

4. Experimental section

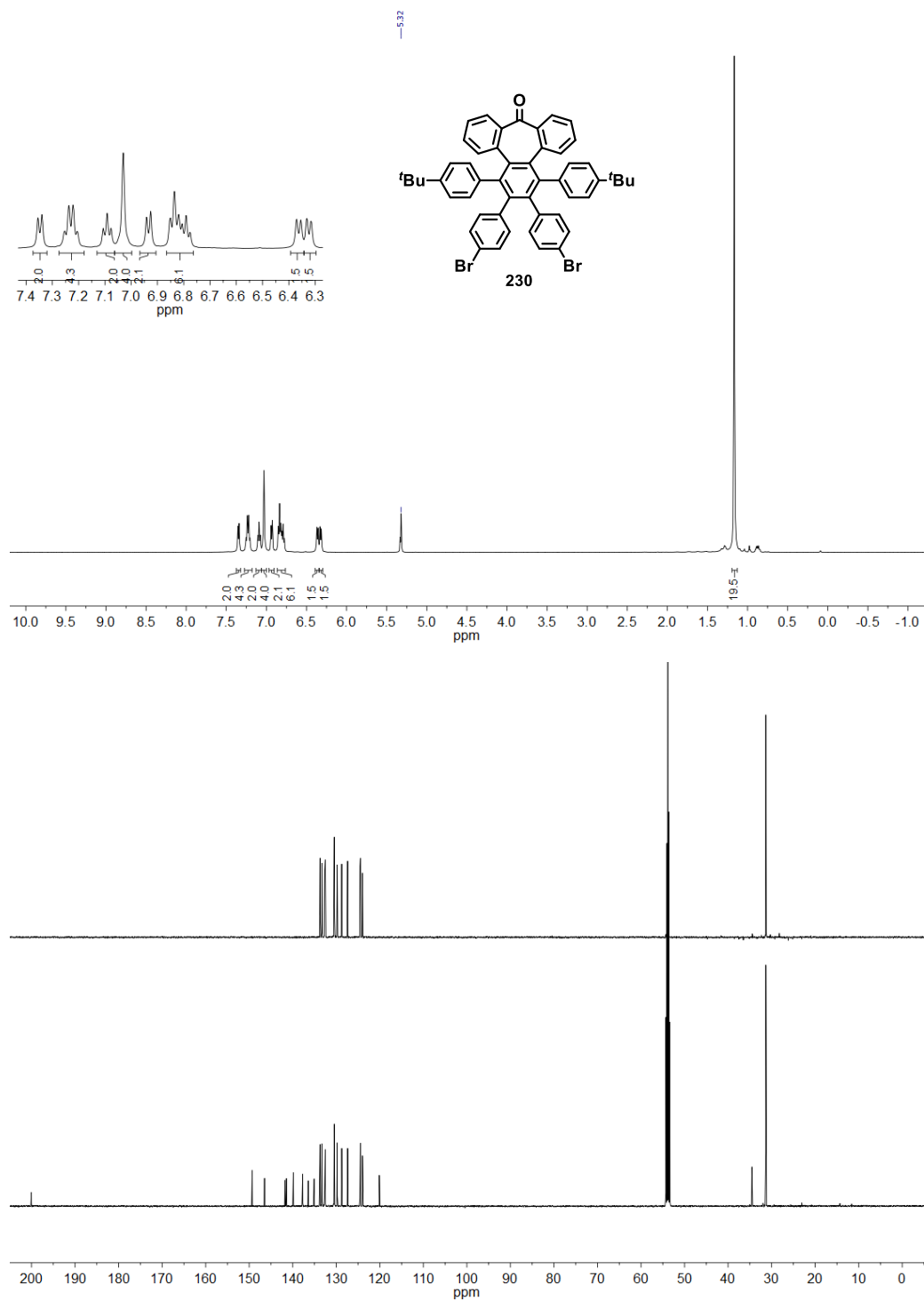


¹H NMR (400 MHz, CD₂Cl₂) and ¹³C NMR (101 MHz, CD₂Cl₂) spectra of compound **215**.

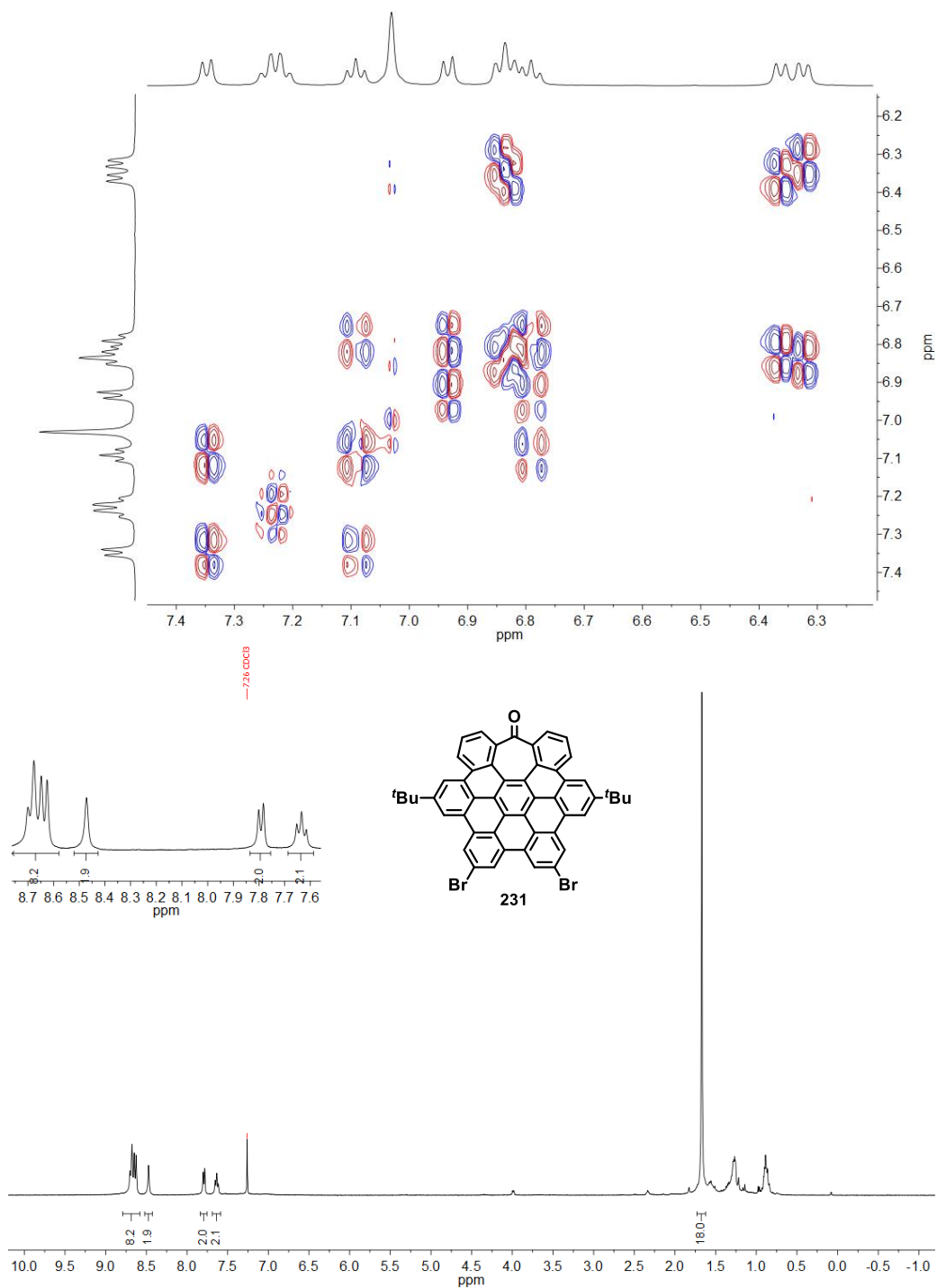


^1H NMR (500 MHz, CD_2Cl_2) and ^{13}C NMR (126 MHz, CD_2Cl_2) spectra of compound **216**.

4. Experimental section

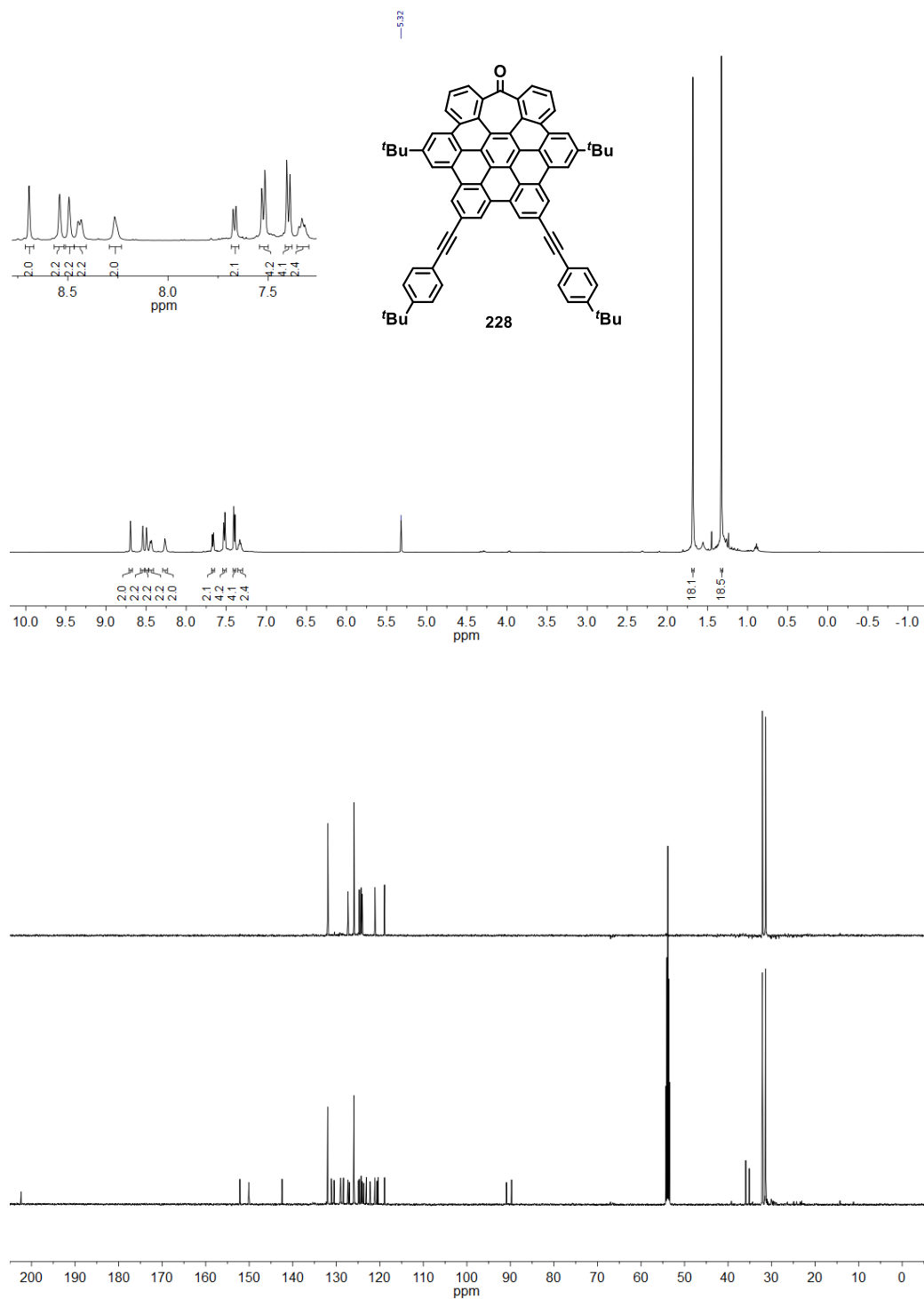


^1H NMR (500 MHz, CD_2Cl_2), ^{13}C NMR and DEPT135 (126 MHz, CD_2Cl_2) spectra of compound **230**.

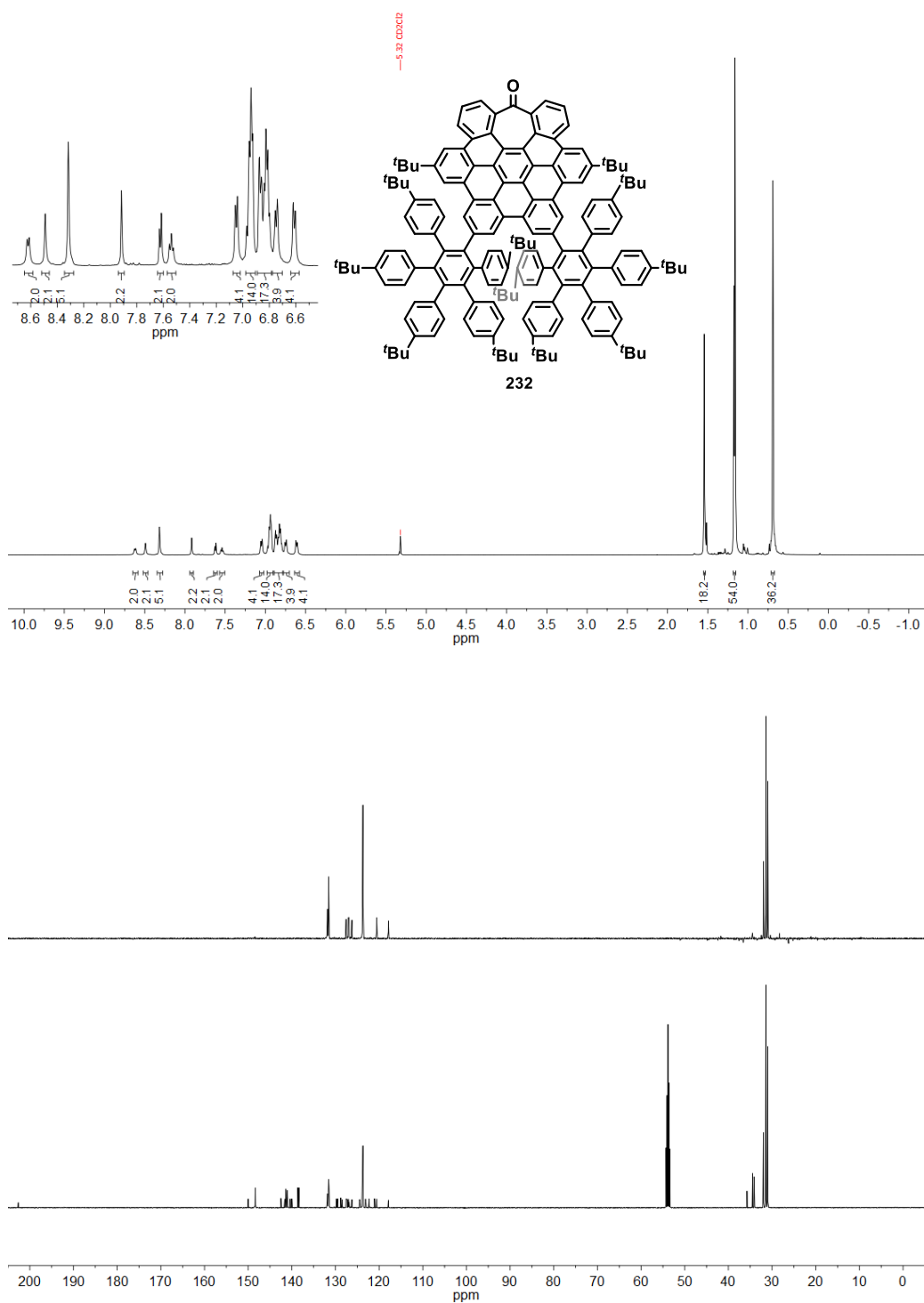


Partial ^1H ^1H COSY (500 MHz, CD_2Cl_2) spectrum of compound **230** and ^1H NMR (400 MHz, CDCl_3) spectrum of compound **231**.

4. Experimental section

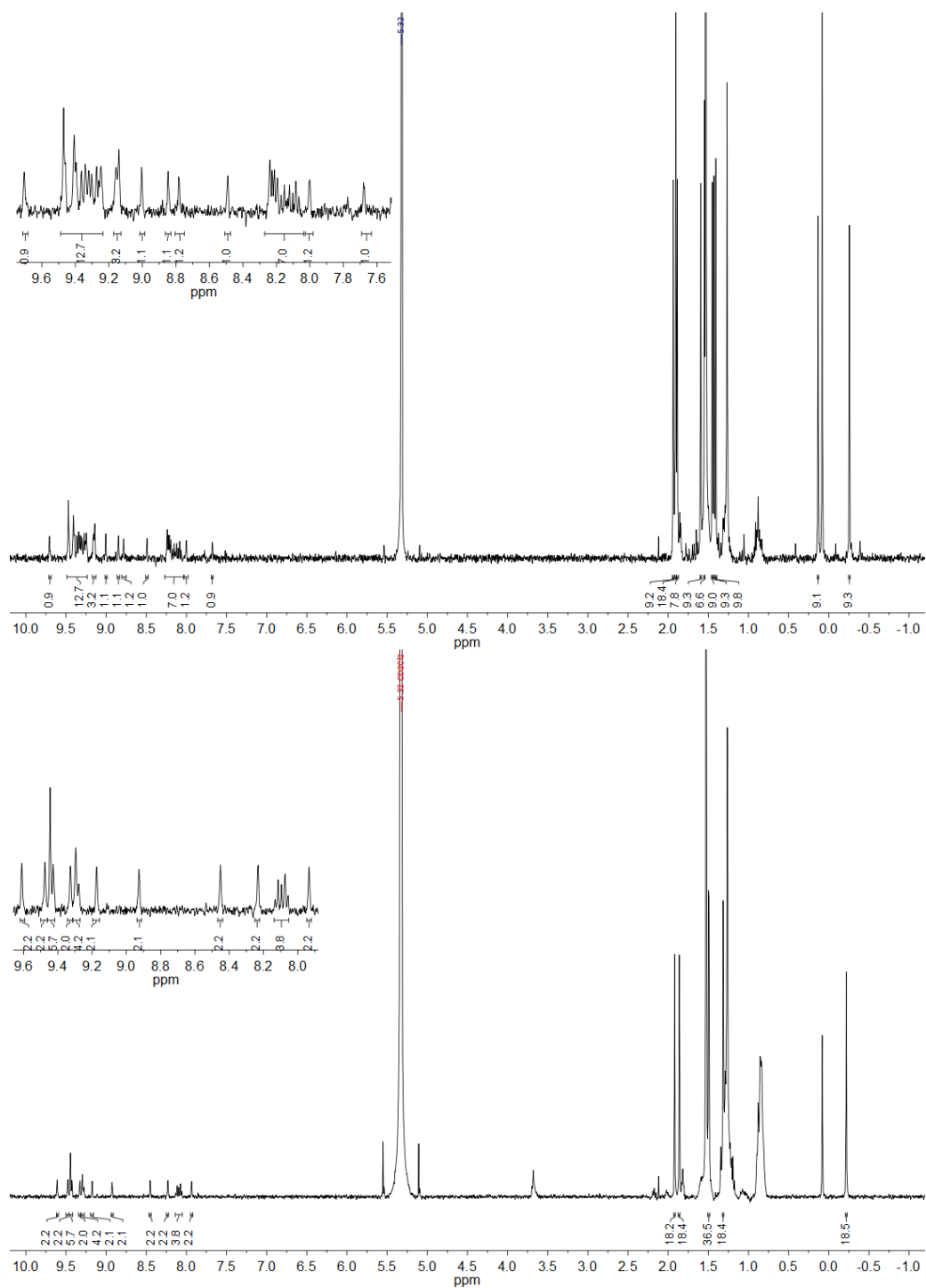


¹H NMR (500 MHz, CD₂Cl₂), ¹³C NMR and DEPT135 (126 MHz, CD₂Cl₂) spectra of compound **228**.

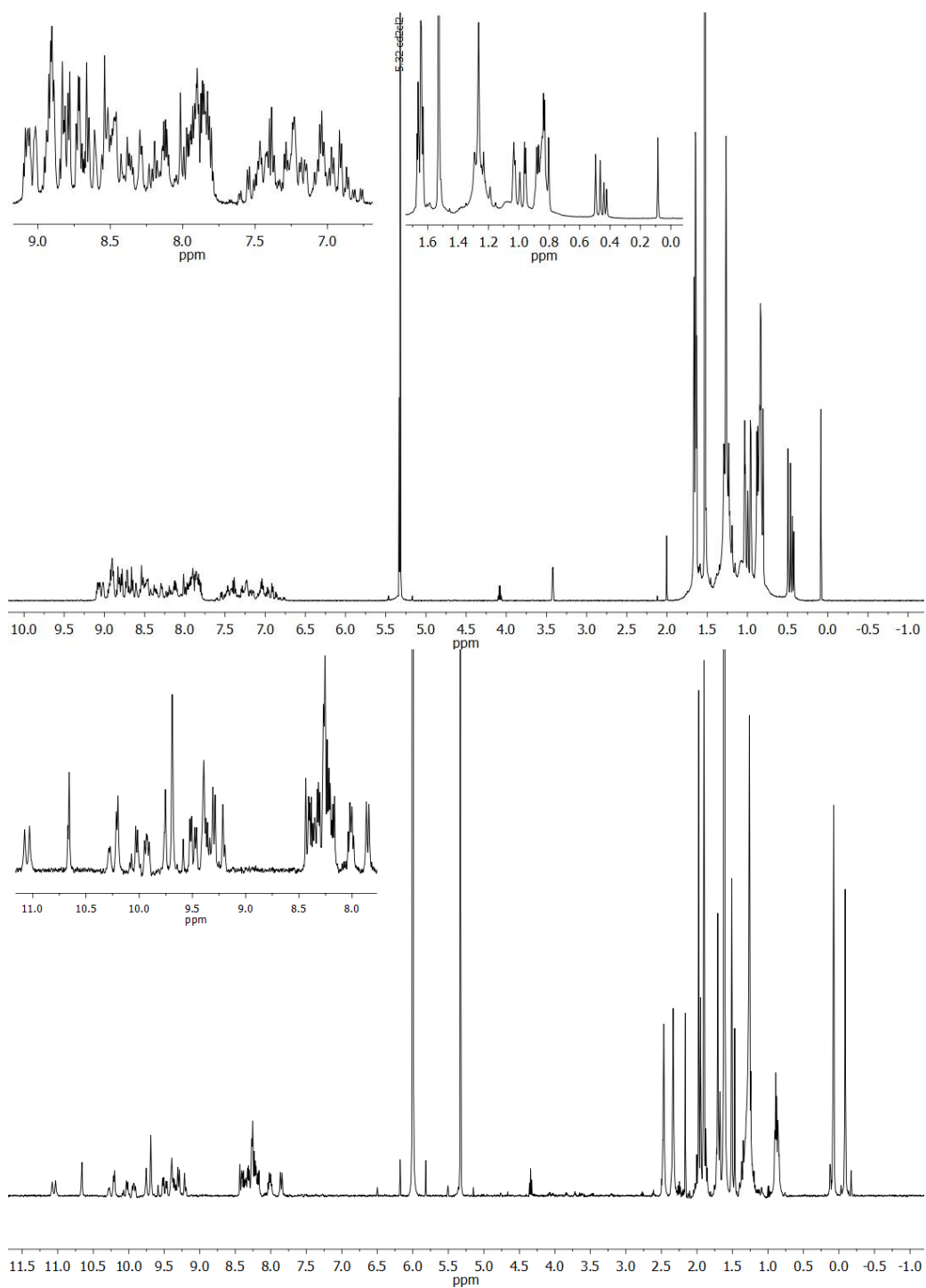


¹H NMR (500 MHz, CD₂Cl₂), ¹³C NMR and DEPT135 (126 MHz, CD₂Cl₂) spectra of compound **232**.

4. Experimental section

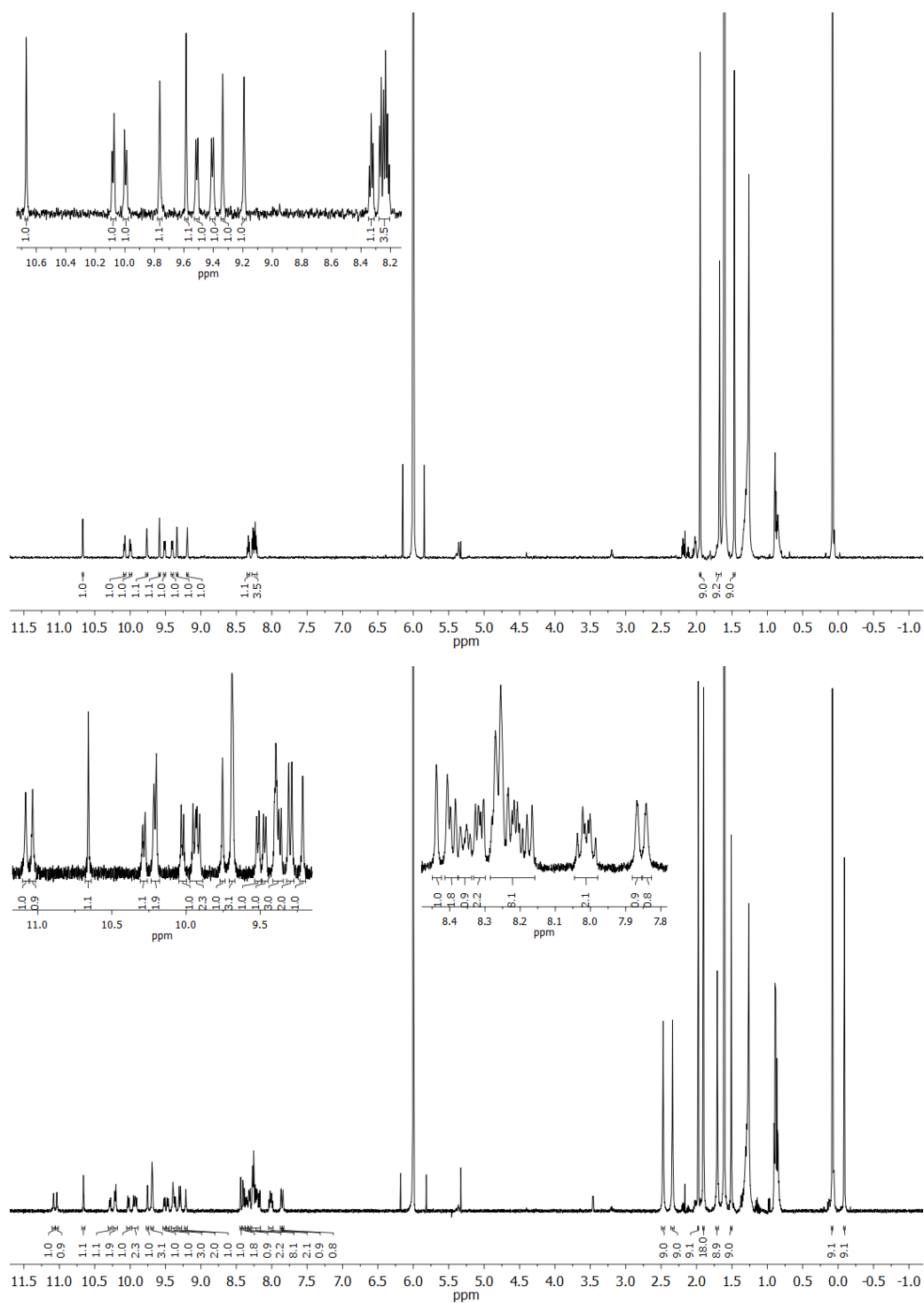


^1H NMR (400 MHz, CD_2Cl_2) and ^1H NMR (400 MHz, CD_2Cl_2) spectra of compound MMP/PPM-234 (top) and fraction D (bottom).

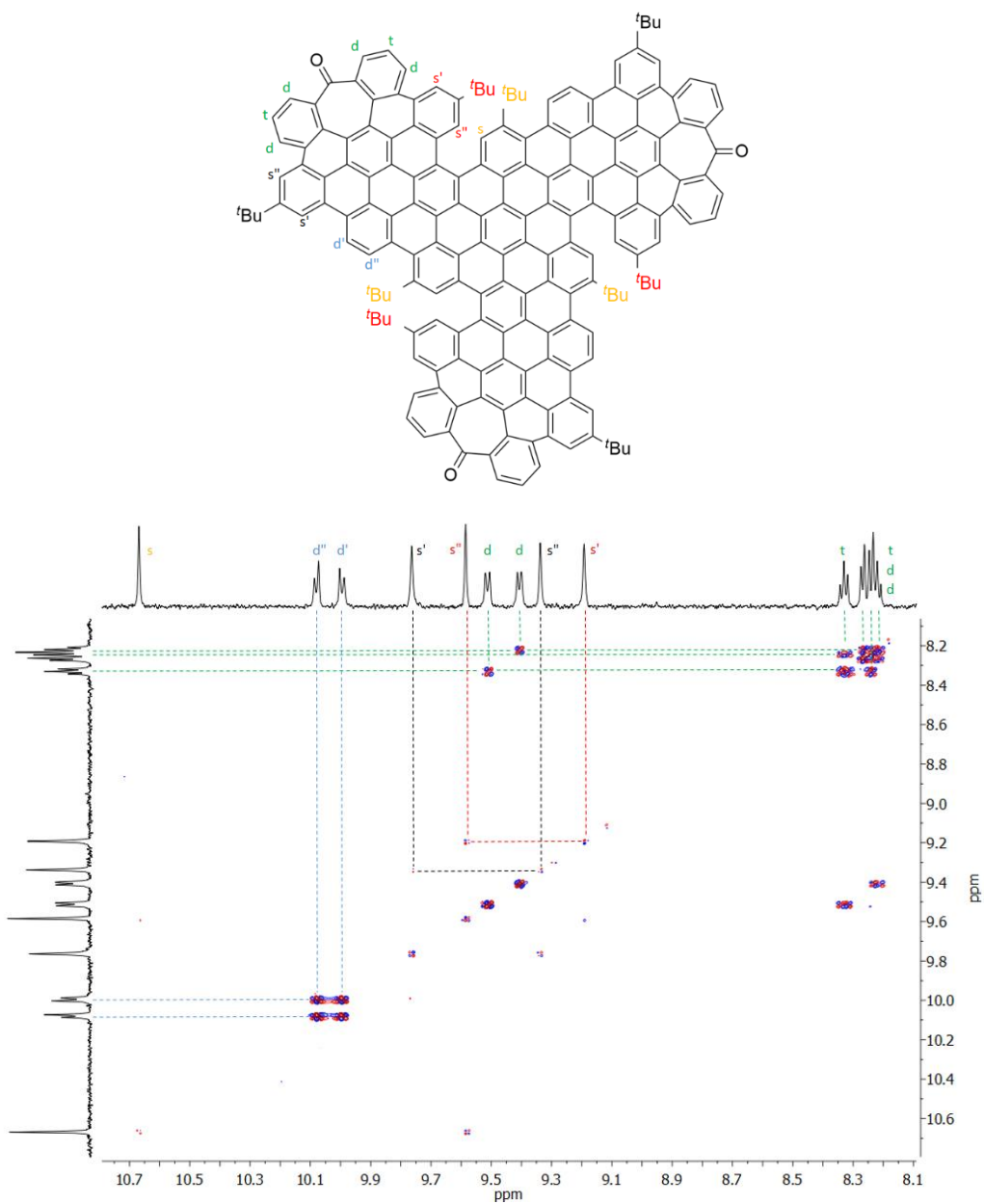


^1H NMR (600 MHz, CD_2Cl_2) spectrum of compound **235** (top) and ^1H NMR (500 MHz, $(\text{CDCl}_2)_2$) spectrum of compound **236** (bottom, mixture of diastereoisomers).

4. Experimental section

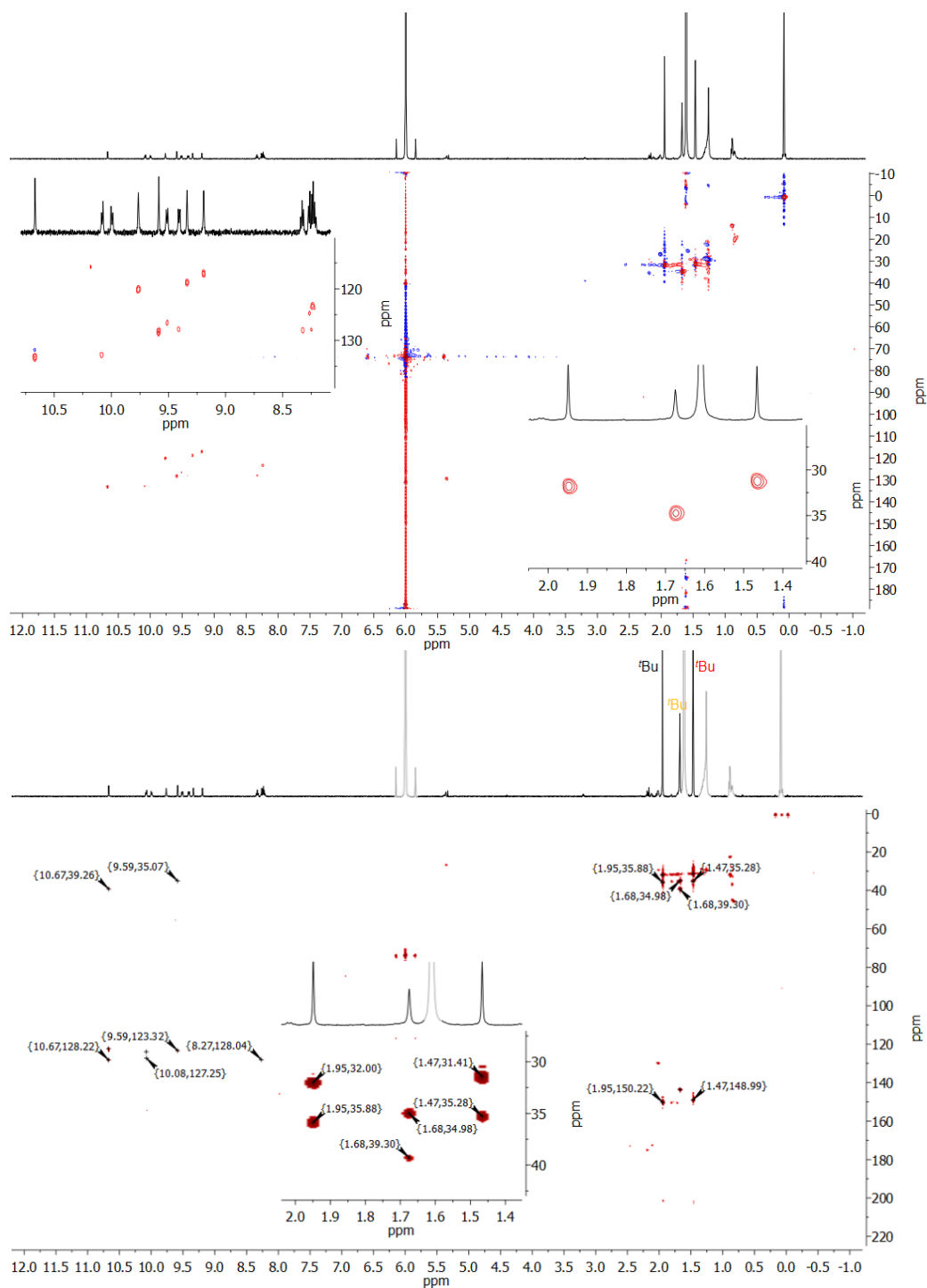


^1H NMR (600 MHz, CDCl_2) spectra of compounds *MMM/PPP-236* (top) and *MMP/PPM-236* (bottom).

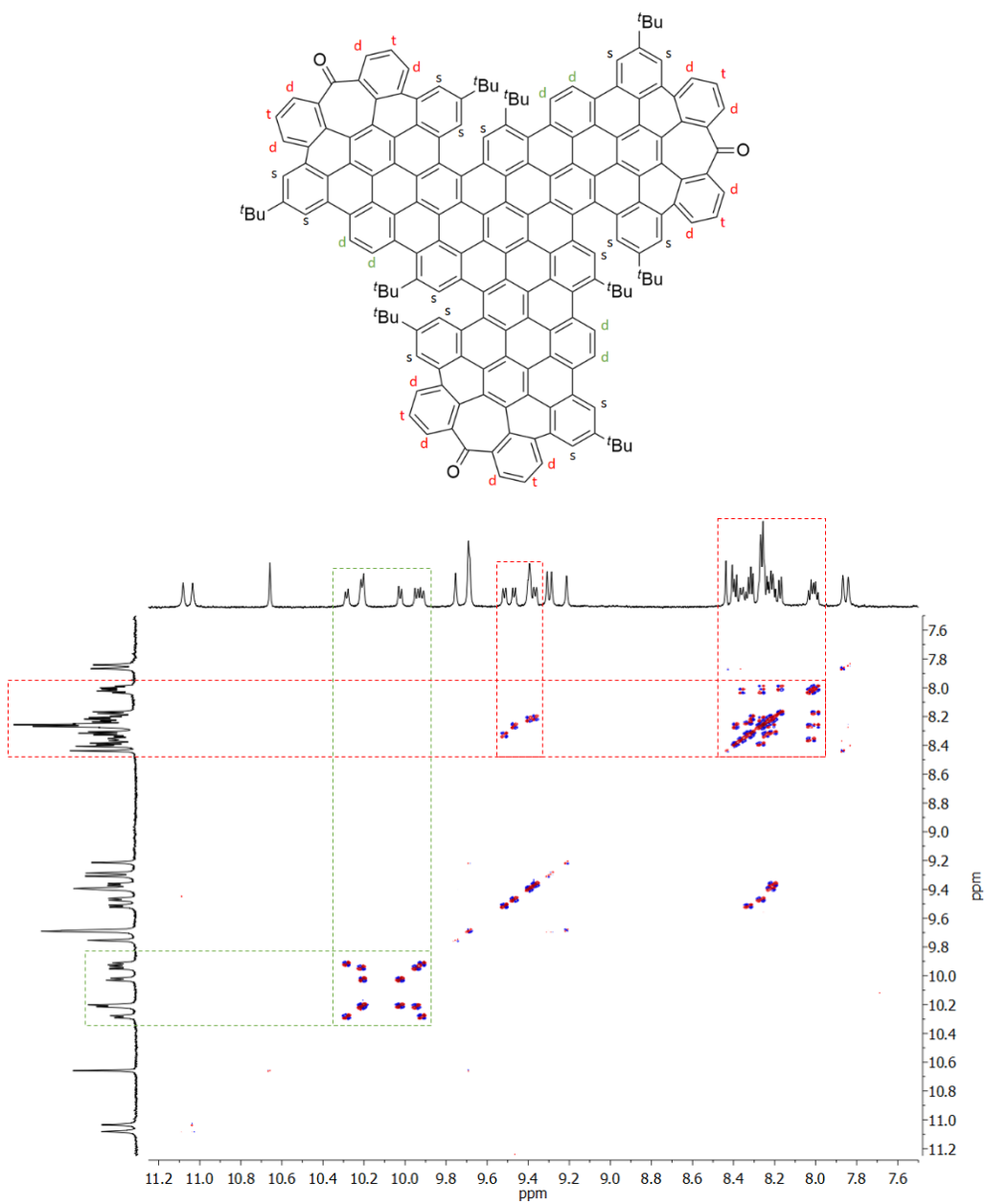


Multiplet analysis and partial ^1H ^1H COSY (600 MHz, $(\text{CDCl}_2)_2$) spectrum of compound MMM/PPP-236.

4. Experimental section

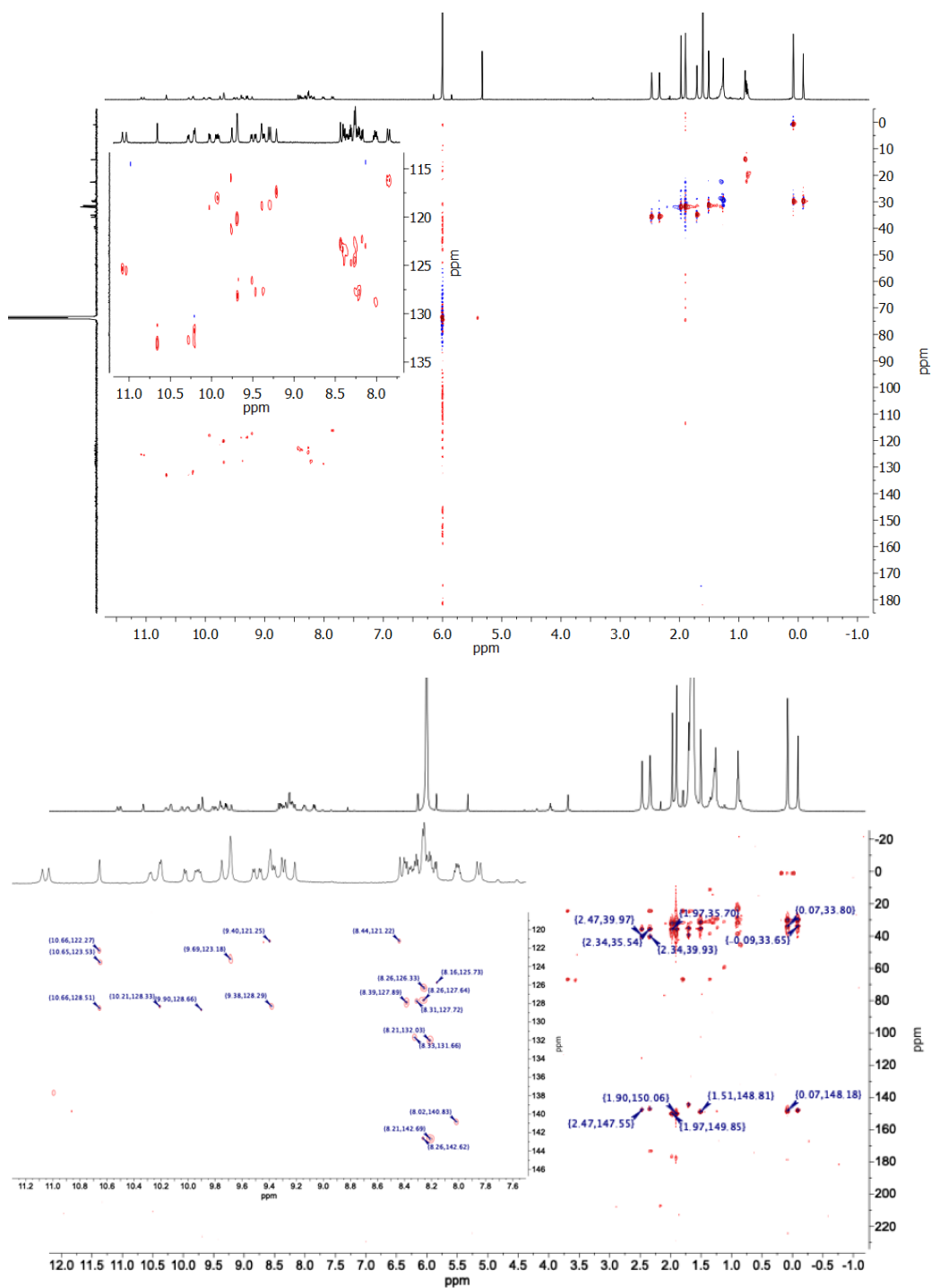


^1H ^{13}C HSQC (600 MHz, 151 MHz, CDCl_2) (top) and ^1H ^{13}C HMBC (600 MHz, 151 MHz, CDCl_2) spectra of compound *MMM/PPP-236*.



Multiplet analysis and partial ^1H ^1H COSY (600 MHz, $(\text{CDCl}_2)_2$) spectrum of compound MMP/PPM-236.

4. Experimental section



^1H ^{13}C HSQC (600 MHz, 151 MHz, CDCl_2) spectrum of compound *MMP/PPM-236* (top). ^1H ^{13}C HMBC (600 MHz, 151 MHz, CDCl_2) spectrum of compound *MMM/PPP-236* (bottom).

5. CONCLUSIONS

Based on the obtained results after the experimental work carried out during this thesis, we draw the following conclusions:

- We have successfully prepared a ribbon-shaped nanographene consisting on two HBC units, one of them presenting a heptagonal ring as a tropone unit. The arrangement of these two HBC units created a carbo[5]helicene moiety that induces chiroptical properties to the molecule. The prepared nanographene was reported as the first nanographene combining TPA-UC and CPL.
- We have demonstrated the effect of the saddle geometry on the TPA response in nanographenes. This fact could be extended to GQDs and might be one of the cause of their high TPA levels.
- We have prepared the first undecabenzo[7]helicene ever reported as a constituent of a distorted nanographene. This nanographene shows improved TPA response and CPL levels than the previously reported one. The studied electrochemical properties showed promising features for its use as an extraordinary electron acceptor.
- We have prepared a saddle-helix hybrid nanographene combining carbo[5]helicenes and a carbo[7]helicene along with a seven membered ring. Both, their nonlinear and chiroptical properties have been studied showing promising CPL values with red shifted emission wavelengths.
- We have successfully prepared a triskelion-shaped nanographene consisting of 153 conjugated carbon atoms. This graphene molecule shows improved solubility than previously reported flat analogues. Their chiroptical properties showed high CPL for such extended nanographene.

To sum up, as a **general conclusion**, we can say that our methodology can be exploited for the preparation and extension of heptagon containing nanographenes, thus creating a new family of well-defined curved PAHs with high solubility and an outstanding combination of optical, chiroptical and electrochemical properties.

6. ANNEXES

LIST OF PUBLICATIONS

Most of the results presented in this thesis have been published and listed below:

“Enantiopure distorted ribbon-shaped nanographene combining two-photon absorption-based upconversion and circularly polarized luminescence”, Carlos M. Cruz, Irene R. Márquez, Inês F. A. Mariz, Victor Blanco, Carlos Sánchez-Sánchez, Jesús M. Sobrado, José A. Martín-Gago, Juan M. Cuerva, Ermelinda Maçôas, Araceli G. Campaña, *Chem. Sci.* **2018**, *9*, 3917-3924.

Article featured on the **INSIDE BACK COVER** of the journal *Chemical Science* and selected among the **MOST IMPACTFUL NANOSCIENCE ARTICLES** published in *Chemical Science*.

“Undecabenz[7]superhelicene: A Helical Nanographene Ribbon as a Circularly Polarized Luminescence Emitter”, Carlos M. Cruz, Silvia Castro-Fernández, Ermelinda Maçôas, Juan M. Cuerva, Araceli G. Campaña, *Angew. Chem. Int. Ed.* **2018**, *57*, 14782-14786.

Article highlighted as **VERY IMPORTANT PAPER**.

“Combining Defects in a Single Nanographene: A Fully Helical Saddle Ribbon”, Carlos M. Cruz, Silvia Castro-Fernández, Ermelinda Maçôas, Alba Millán, Araceli G. Campaña, *Synlett*, **2019**, *30*, 997-1002.

Article highlighted on the **FRONT COVER** of *Synlett*.

“A triskelion-shaped saddle-helix hybrid nanographene”, Carlos M. Cruz, Irene R. Márquez, Silvia Castro-Fernández, Juan M. Cuerva, Ermelinda Maçôas, Araceli G. Campaña, *Angew. Chem. Int. Ed.*, **2019**, *58*, 8068-8072.

Article highlighted as **HOT PAPER**.

“Two-photon absorption enhancement by the inclusion of saddle curvature in distorted nanographene ribbons”, Silvia Castro-Fernández, Carlos M. Cruz, Inês F. A. Mariz, Irene R. Márquez, Vicente G. Jiménez, Lucía Palomino-Ruiz, Juan M. Cuerva, Ermelinda Maçôas, Araceli G. Campaña, *Submitted to Angew. Chem. Int. Ed.*